Robert Jeffrey
Merton College, Oxford

# The Remarkable Outflows from the Galactic Microquasar SS433

A thesis submitted in candidature for the degree of
Doctor of Philosophy
at the
University of Oxford

Trinity Term 2016

The Remarkable Outflows from the Galactic Microquasar SS433

Robert Jeffrey
Merton College, Oxford

This Thesis was submitted in successful candidature for the degree of Doctor of Philosophy at the University of Oxford in Trinity Term 2016.

Submitted on 29$^{th}$ September 2016
Examined on 5$^{th}$ December 2016, by Dr Garret Cotter (Oxford) and Professor Ralph Spencer (Manchester)
Corrected Version submitted on 20$^{th}$ December 2016
Leave to Supplicate granted on 9$^{th}$ February 2017
Degree awarded on 16$^{th}$ September 2017

Supervised by Professor Katherine Blundell, OBE.

# Declaration

The work described in the thesis is believed to be original, except where explicit references are made to the work of other authors. It is the result of my own research, and includes nothing which is the outcome of work done in collaboration, except as specifically indicated below. No part of this thesis has been, or is being, submitted for any other qualification, other than the degree of Doctor of Philosophy at the University of Oxford.

The work described in Chapter 4 has been published as:

> Robert M. Jeffrey, Katherine M. Blundell, Sergei A. Trushkin, and Amy J. Mioduszewski
> **Fast launch speeds in radio flares, from a new determination of the intrinsic motions of SS 433's jet bolides**
> Monthly Notices of the Royal Astronomical Society (September 01, 2016)
> Vol. 461 312-320 doi:10.1093/mnras/stw1322

Sergei Trushkin provided radio monitoring data from the RATAN telescope (see Figure 4.8). Amy Mioduszewski provided the reduced images from her 2003 VLBA observations of SS 433 (Mioduszewski et al. (2004); see Figure 4.2). All authors offered comments on the completed manuscript. The argument, analyis and manuscript are the result of my own work.

I also acknowledge the sources for Figure 7.1, which is taken from figure 2 in Fender and Belloni (2012), and for Figure 7.26, which is taken from figure 3 of Seifina and Titarchuk (2010). Citations are given at the appropriate points in the text. For copyright reasons, these figures have been omitted from the online version of the thesis.

With the above exceptions, I declare that this thesis is the result of my own work.

---

Robert Jeffrey

September 2016

# Abstract

In this thesis, I present 4 new, high-resolution observations of the Galactic microquasar SS 433, obtained from the Very Long Baseline Array (VLBA). I show that we can resolve the same ejecta in successive observations separated by $\sim 35$ d. I will demonstrate a method to uniquely determine launch vectors of the jet bolides, and I use this unprecedented baseline in time to show that the expansion rate of these bolides may reach $0.03c$.

I also present the first scientific results from the study of the radio jets in a unique set of historic observations of SS 433: the 39 images that comprise the 2003 VLBA movie of Mioduszewski et al. (2004). This unmatched time sampling allows us to see daily changes in the dynamics of SS 433's jets. I present evidence that these observations caught SS 433 as it transitioned from quiescence into a flare, and I show that this manifests itself as an increase in both the jet launch speed and the brightness of the jet bolides.

Using these data, I examine the evolution of the particle energies, densities and magnetic fields within the bolides. We see that the estimates of the mass-loss rates via the jets cannot be reconciled with the those inferred from X-ray or optical data, if we posit equipartition of energy in synchrotron emitting plasma. The time resolution of the 2003 data allows us to observe the flux evolution of the jet bolides, and I show that the bolides undergo a power law decay as $t^{-2.8}$.

Lastly, I examine X-ray monitoring data from the Swift/BAT satellite and the MAXI All-Sky-Monitor. From these lightcurves, I examine the geometry of the X-ray emission from close to the compact object itself, and I discuss SS 433's place within the current paradigm of accretion in microquasars.

Throughout, we will see that it is the accessible time scales of the SS 433 phenomenon that allow us to learn about its exciting, complex physics.

---

# Resources

This thesis was supported by a PhD Studentship from the Science and Technologies Facilities Council. Additional travel funding was awarded by the Steve Rawlings Memorial Prize and from Merton College, Oxford.

The VLBA is a facility of the National Radio Astronomy Observatory, operated by Associated Universities, Inc., under a cooperative agreement with the National Science Foundation.

Data from the RATAN telescope microquasar monitoring program were provided by Sergei Trushkin and co-workers. Further details of their monitoring of SS 433 may be obtained from Trushkin et al. (2003).

The MAXI All-Sky-Monitor data products were provided by the MAXI team. Details of the MAXI mission may be found at Matsuoka et al. (2009), and the date products may be obtained from the web portal at `maxi.riken.jp.`.

Swift/BAT transient monitor results were provided by the Swift/BAT team. Details are available at Krimm et al. (2013), while the data may be obtained via the web portal at `swift.gsfc.nasa.gov/results/transients/SS433/`.

Much of the data analysis was performed using the Python programming language, and in particular the Numpy, Scipy and Astropy packages. The figures were produced using the Matplotlib plotting package (Hunter (2007)).

This work has made extensive use of the AIPS package for the reduction of interferometry data (Greisen (2003)). Use has also been made of the Parseltongue package for interfacing between AIPS and Python (Kettenis et al. (2006)).

This thesis was prepared and typeset using LaTeX.

# Acknowledgements

I would not have made it this far without the support and guidance of a great many individuals, both in Oxford and beyond. I have tried to learn from the superior wisdom and insight of the outstanding astronomers I have had the privilege to meet over the last four years. In particular I owe my thanks to Tony Beasley, Tony Bell, Sam Doolin, Ian Heywood, Robert Laing, Amy Mioduszewski, Alison Peck, Rick Perley, David Roberts, Sasha Tchekovskoy, Craig Walker, and John Wardle. I am indebted to Eric Greisen, for his lessons in AIPS wrangling. Many of these conversations occurred during my visits in 2014 to the NRAO sites in Socorro and Charlottesville and to Brandeis University. These trips would not have been possible through the support of Merton College, and most especially without the award of the Steve Rawlings Memorial Prize.

I have been fortunate in the friends I have had around me over past four years. I thank my office-mates, for reminding me that there is a universe beyond AIPS. And I thank Michael, Catherine, James, Niall, Chris, Diane, and the many other friends who have striven to keep me optimistic and sane over the last few years.

I thank my parents and family for their love, support, and care, and for the timely supplies of parental cuisine.

But more than anyone else, I must thank my supervisor, Katherine Blundell, for her unwavering patience and support, which has been both enlightening and inspiring. I have enjoyed the problems on which we have worked together, and I wish that we had time to continue to develop and explore them.

---

Robert Jeffrey

September 2016

# Contents

# List of Figures

# The Remarkable Outflows from the Galactic Microquasar SS433

# Chapter 1

# Scientific Background – SS 433: An Overview

## 1.1 Introduction

The Universe is shaped by the *accretion* of matter. This is the process by which a massive body (a protoplanet, a star, a black hole, or a galaxy) gains mass from the surrounding medium. As matter becomes more tightly bound, gravitational energy is released and converted into other forms of energy: kinetic energy, thermal energy, and radiation.

Accretion, and this associated release of energy, drives many other processes in astrophysics. For example, it is the gravitational energy released in the collapse of a protostar that ignites hydrogen fusion. As massive stars die, the gravitational energy released in the final collapse can outshine distant galaxies. And at the centres of galaxies, super-massive black holes accrete gas from their surroundings, releasing energy which then shapes the evolution of their host galaxies and the surrounding cluster (active galactic nuclei (AGN), or quasars).

In each of the above cases, accretion energy is used to drive powerful outflows. That is, some of the energy released by matter as it falls towards the massive object is used to expel some fraction of the accreting matter from the system, often with tremendous energy. The most dramatic examples of this are the relativistic jets that are seen from accreting black holes and neutron stars, in which particles are accelerated to significant fractions of the speed of light. These energetic outflows

illuminate the accreting object; understanding them can allow us to study the accretion engine itself.

There is a class of these accreting objects which is particularly helpful for astronomers: the microquasar. These are (often Galactic) compact objects (neutron stars or black holes), with masses from a few to a few tens of solar masses. They offer the great benefit that their comparatively small scale, their proximity, and their energetic outflows mean they can be resolved both spatially and temporally, allowing us to study their physics in detail. In this thesis, we will study one remarkable such object: SS 433.

## 1.2 SS 433

One of the most powerful probes of accretion processes available to astronomers is the Galactic microquasar SS 433 (Stephenson and Sanduleak (1977)). This is a binary system consisting of a black hole accreting from an optical companion star – the accretion rate exceeds the Eddington limit (at which radiation pressure would disrupt a spherical accretion flow) by as much as 3 orders of magnitude. Its orientation, its mildly relativistic jets, and its regular and persistent precession combine to make this object a singularly powerful example with which to study the physics of accreting compact bodies.

SS433's remarkable nature was first identified in 1978 by three groups working on supernova remnants and their progenitors. Clark and Murdin (1978), Seaquist et al. (1978), and Ryle et al. (1978) observed a source lying near the centre of the W50 supernova remnant with peculiarly strong radio and X-ray emission, and with an anomalous and varying optical spectrum.[1] Its main physical attributes (a binary system launching "precessing" jets) were established within the first 3 years, but 40 years, and 1000 papers later,[2] there are still many questions to be answered about SS 433's complex physics.

A recent review of the general observational and theoretical phenomenology in SS 433 is given in Fabrika (2004). In this Chapter, we will give a brief overview of the system's key properties, with an emphasis on work from the 21$^{st}$ Century.

Before proceeding, a brief word on observational terminology will be helpful. SS 433 is observed:

[1] For the history of the competition between parallel groups that lead to SS 433's discovery, see *The Quest For SS433*, by Clark (1985).

[2] At least 963, according to the NASA Astrophysics Data System in September 2016.

in optical (e.g., Goranskii et al. (1998)), X-ray, (e.g., Antokhina et al. (1992)), and radio (e.g., Vermeulen et al. (1993a)) photometry; in optical (e.g., Eikenberry et al. (2001)), X-ray (e.g., Kotani et al. (1996)), and infrared (Perez and Blundell (2009)) spectroscopy; and in radio (e.g., Blundell and Bowler (2004)), infrared (Blundell and Hirst (2011)), and X-ray (e.g., Migliari et al. (2002)) images. In spectroscopic observations, an individual spectral line is usually resolved into a "stationary" line (associated with emission tied to the compact object/accretion disc (King et al. (2000))) and two "moving" lines (emitted in the jet and counterjet, and which are red and blueshifted depending on whether they are receding from or approaching the observer). In images of the system, the jets lie almost East-West on the plane of the sky, rotated by about 10° counter-clockwise from the East-West axis. Throughout this work, we will use *jet* to refer to the eastern jet, and *counterjet* to refer to the western jet. We will see later that the (eastern) jet points towards the observer for most of the precession period, and the (western) counterjet points away from the observer, but, for about a third of the precession period, the (eastern) jet passes through the plane of the sky and points away from the observer, while the (western) counterjet points slightly towards the observer.

## 1.3 The nature of the SS 433 phenomenon

### 1.3.1 The binary system & the W50 remnant

The determination of the orbital period of the SS 433 binary was a relatively simple task – there is a 13.082 d periodicity that appears as a variation of radial velocity of the stationary line (e.g., Crampton et al. (1980), Crampton and Hutchings (1981)), and which appears as primary eclipses (corresponding to the eclipse of the compact object by the companion star) in optical photometric monitoring (e.g., Goranskii et al. (1998)). We will use the ephemerides of Goranskii et al. (1998) as reported in Fabrika (2004).

Determination of the component parts of the binary system has proven less straightforward. As discussed below (Section 1.4.2), there is little consistency between estimates of the mass ratio of the components, hindering attempts to determine the nature of the compact object. More recent work using observations of matter orbitting outside the binary system points to a relative massive binary system containing a large, stellar-mass black-hole with $M_{\rm bh} \gtrsim 16\,{\rm M}_{\odot}$ (Blundell et al. (2008), Bowler (2010b)). The same data indicate that the companion star is likely to have

a mass $M_* \gtrsim 22\,\mathrm{M}_\odot$.

The binary system sits near the centre of the W50 supernova remnant. This remnant consists of a shell of radius 45 pc (i.e., $1.4 \times 10^{18}$ m), with asymmetric lobes which lie along the axes of the precessing jets in SS 433 (the Eastern lobe has a length of approximately 120 pc and the Western has length 80 pc) The shell is the expanding shock from the supernova explosion that created the black-hole in the binary system, while the lobes are relics of an earlier period of jet activity. Hydrodynamic simulations by Goodall et al. (2011) indicate that the asymmetries in the lobes are due to the density gradient of the ISM as a function of distance from the Galactic Plane – i.e., the shorter, Western jet which is propagating towards the Galactic Plane has to travel through denser matter, and so undergoes greater deceleration[3] than the Eastern lobe. From their simulations, Goodall et al. (2011) argue for at least three distinct phases of jet activity, with the supernova remnant having an age 17, 000–20, 000 yr, and with the current phase of jet activity having gone on for no more than 1500 yr.

### 1.3.2 The relativistic jets

The most striking feature of the SS 433 system is its pair of precessing, mildly relativistic jets. These are observed at x-ray, optical and radio frequencies, with the precession (i.e., the periodic rotation of the jet launch vector about a fixed precession axis, analogously to a spinning top) made manifest in radio maps as the variation of the orientation of the jet on the plane of the sky, and in optical spectra as "moving lines" whose positions appear to change as the velocity component along the line-of-sight of freshly launched plasma increases and decreases. Both the (ballistic) jet motions and the redshifts of emission from the jets can be described approximately by the "kinematic model" (Abell and Margon (1979), Hjellming and Johnston (1981)), in which they propagate freely with mean launch speeds of $0.26c$. This will be discussed in much greater detail in Chapter 2.

Here we will briefly summarise some of the characteristics and properties of the jets. The jets begin as continual, outflows, producing thermal X-ray radiation, as well as spectral lines from iron and silicon (e.g., Marshall et al. (1979), Watson et al. (1986); see Chapter 7 for more details). The jets cool and fragment into discrete clouds (Brinkmann et al. (1988)). These clouds are often referred to as "bullets" and give rise to spectral lines from the the recombination series of hydrogen

[3] On scales comparable with the supernova remnant – i.e., 1000 times greater than the scale of the corkscrew jets we discuss elsewhere

(e.g., Goranskii et al. (1998)). The jets of SS 433 are unusual among microquasar jets in that we know that they contain baryons, as seen from the presence of these emission lines.

As well as spectral properties, the jets can be imaged directly using radio interferometers at arcsecond scales (with, e.g., the Very Large Array (VLA; Hjellming and Johnston (1981)) or the Multi-Element Radio Linked Interferometer Network (MERLIN; Spencer (1979), Spencer (1984))), and at milli-arcsecond scales (with e.g., the Very Long Baseline Array(VLBA; Paragi et al. (1999), Jeffrey et al. (2016)), MERLIN (Stirling et al. (2004)), or the European VLBI Network (Paragi et al. (2002))). At arcsecond-scales, the precession of the jet launch vector means the jets appear to trace out a pair of corkscrew-like structures. At milliarcsecond-scales, the jets appear as a series of clumpy knots (often referred to as "bolides" or "plasmons"), sometimes superimposed on a smooth flow. The exact relationship between the "bullets" (which give rise to the optical emission lines) and the "bolides" that we can image in these high-resolution maps of the system remains unclear. We will discuss some of the similarities between the two flows in Chapter 4, but there are currently no simultaneous observations that allow us to unambiguously relate the two.

It is worth pausing to emphasise the length scales involved here. A jet speed of $0.26c$ corresponds to a motion of $6.7 \times 10^{12}\,\mathrm{m\,d^{-1}}$. Models of the X-ray jets indicate that the length of the X-ray jets is $10^{10}$–$10^{11}\,\mathrm{m}$ (e.g., Kotani et al. (1996), Brinkmann et al. (2005)), and that its base radius is $\sim 10^{6}\,\mathrm{m}$ (Marshall et al. (2002); for reference, the Schwarzschild radius of a $16\,\mathrm{M_\odot}$ black-hole is $5 \times 10^{4}\,\mathrm{m}$). The X-ray emission therefore occurs within the first 100–1000 seconds after launch. The optical lines appear at a distance of $\sim 4 \times 10^{12}\,\mathrm{m}$, or about 16 hours post-launch, and are visible for typically about 2 days (Vermeulen et al. (1993b), Fabrika (2004)).

VLBI observations have detected the jet out to $\gtrsim 400\,\mathrm{mas}$ (i.e., to $\sim 3 \times 10^{14}\,\mathrm{m}$, or about 50 d post launch; e.g., Paragi et al. (1999), Stirling et al. (2002)). Vermeulen et al. (1993c) determine that the jets reach their peak brightness at about 50 mas away from the core ($\sim 4 \times 10^{13}\,\mathrm{m}$, or about 6 d after launch), before fading. With the VLA, the jets are detected out to $\sim 4''$ either side of the core, or a distance of $3 \times 10^{15}\,\mathrm{m}$ (e.g., Blundell and Bowler (2004)). This allows the jets to be resolved over almost 3 complete precession periods.

Lastly, we note that resolved X-ray images (Migliari et al. (2002)) indicate that the jets undergo reheating at about 200 d after launch, based on resolving X-ray bremsstrahlung and Iron lines at distances $\sim 10^{15}\,\mathrm{m}$ from the jet base. Beyond this though, the jets are undetected until their interaction with the W50 shell is observed at distances of $\sim 10^{18}\,\mathrm{m}$.

### 1.3.3 Winds & the circumbinary outflow

The main mode of mass loss is through winds. Though some workers have identified these winds with a stellar wind from the companion (e.g., Fuchs et al. (2002), Crampton and Hutchings (1981)), Blundell et al. (2008) show that the width of the broad H$\alpha$ line associated the winds (which is related to the winds' line-of-sight velocity components) varies both with the nutation of the jet and with precession phase, and so establish that the winds blow polloidally from the accretion disc. Blundell and Hirst (2011) observed that these winds are approximately poloidal and perpendicular to the precessing accretion disc. The winds have speeds that are $\gtrsim 1000\,\mathrm{km\,s^{-1}}$, but the relativistic jets can sweep up wind ejecta as they pass.

Recent work has supplemented this accretion disc wind with a circumbinary, equatorial outflow (Paragi et al. (1999), Blundell et al. (2001), Paragi et al. (2002), Doolin and Blundell (2009)). The exact nature of this remains uncertain, though certain observational details are known. The outflow is observed as a "ruff" that appears in radio maps with an angular extent of $\sim 50\,\mathrm{mas}$. The spectral index of this emission ($\alpha = 0.12 \pm 0.02$ where $S_\nu \propto \nu^{-\alpha}$; Blundell et al. (2001)) is consistent with the emission being due to thermal bremsstrahlung, though Blundell et al. (2001) also find that the radio ruff's brightness requires a rather high temperature ($\gtrsim 10^7\,\mathrm{K}$). The ruff is observed to undergo a precession with a possible periodicity of $\sim 552\,\mathrm{d}$ (Doolin and Blundell (2009)).

Analysis of the optical H$\alpha$ emission lines (Blundell et al. (2008)) and the Brackett-$\gamma$ emission lines in the infra-red (Perez and Blundell (2009)) reveal the presence of a circumbinary ring of matter, orbiting the binary centre of mass at a speed of $\sim 200\,\mathrm{km\,s^{-1}}$ and at about twice the binary separation. This is believed to represent the inner edge of an excretion disc, through which the radio ruff is ultimately fed. Its dynamics are discussed in Doolin and Blundell (2011).

The source of the excretion flow remains unclear. There is some evidence (e.g., from the variation of the intensities of the emission lines from the circumbinary disc as a function of the orbital phase; Bowler (2010b)) that the ring is fed by overflow through the outer Lagrange points of the binary system, though equatorial or stellar winds present possible alternatives (Fabrika (2004)).

## 1.4 Determination of the system's properties

### 1.4.1 Distance

We can now say with a high degree of confidence that SS 433 lies at a distance of 5.5 kpc from Earth. This was the earliest distance measurement (Hjellming and Johnston (1981), from fitting the kinematic model (see Chapter 2) to early VLA maps of the arcsecond-scale radio jets), but was challenged over the subsequent decades.

There have been two approaches taken to determine SS 433's distance. One is to measure the radial velocity (via observations of neutral H I) to attempt to locate SS 433 and the W50 remnant within the Galaxy rotation curves. Most notably, Dubner et al. (1998) used this method to determine a distance of 3 kpc. Lockman et al. (2007) instead found that the distance to W50/SS 433 was consistent with 5.5 kpc: they observed the presence of fainter neutral hydrogen in both emission and absorption moving at a radial velocity of $75\,\mathrm{km\,s^{-1}}$, which when combined with the Galactic rotation curves of Dickey et al. (1983) constrains the distance to be at least 5.5 kpc.

The second method for distance determination uses the proper motions of the jets to calculate the distance, either assuming a fixed speed (chosen to match the speed of the optical jet), or fitting distance and speed within the context of the kinematic model. VLBI observations using this technique have yielded distances of e.g. $4.8 \pm 0.35$ kpc (Vermeulen et al. (1993c)), $4.61 \pm 0.35$ kpc (Stirling et al. (2002)), or $4.5 \pm 0.2$ kpc (Marshall et al. (2013)). On the other hand, the angular size of the arcsecond-scale jet constrains the jet to be at a distance of 5.5 kpc. The observed angular separation between successive coils of the precessing jet 'corkscrew' fixes the combination $(\beta c\, P_{\mathrm{pre}})\ /\ D$, and since $P_{\mathrm{pre}}$ (the precession period) is known from the periodicity of the redshift variations, this constrains $\beta c/D$ – i.e. if the jet lies closer than 5.5 kpc, the jets must either be slower or must decelerate.

The value we will use throughout this work is $5.5 \pm 0.2$ kpc, as determined by Blundell and Bowler (2004) from fitting the kinematic model to their deep VLA map of the system. The consistency with the value derived from the completely independent method of Lockman et al. (2007) gives us further confidence in this choice. We will see (Chapter 4) that this choice, together with natural variation in launch speeds, describes the jets well.

### 1.4.2 The system mass, the mass ratio, & the nature of the compact object

The question of the determination of the masses of the binary components has proved challenging. Fabrika (2004) (§7.2) outlines some of the challenges involved and some of the "many contradictory reports of its mass" that have been published, but for extreme illustration we point to Lopez et al. (2006), who claim $M_* = 35 \pm 7\,\mathrm{M}_\odot$ and $M_{\rm bh} = 20 \pm 5\,\mathrm{M}_\odot$ (from a model of the eclipse of a cooled jet by a companion that does not fill its Roche lobe), and to Goranskij (2011), who argues that "And yet, it is a neutron star", with the compact object having a mass as low as $1.5\,\mathrm{M}_\odot$ and a A7-type companion star with mass $10\,\mathrm{M}_\odot$ (based on a low estimate of the mass ratio and an attempt to model the photometry of the companion). These are, admittedly, outliers, but they demonstrate the wildly divergent views that exist within the community.

There are two general approaches to this problem (Cherepashchuk et al. (2013)): either (a) by estimating the mass function[4] using spectroscopy to find the orbital speeds of the companion or the compact object; and (b) by estimating the total mass in the binary system using the properties of the circumbinary ring.

The challenge in the first case is the determination of the mass ratio $q := M_{\rm bh}/M_*$, where $M_{\rm bh}$ and $M_*$ are the masses of the compact object (black hole) and the companion star respectively. In principle, this can be done from the shape of the eclipses of the compact object/accretion disc by the companion, but, as we will find in Chapter 7, the complex and uncertain geometry of the inner binary system makes this difficult. Existing mass ratio estimates from X-ray lightcurves (e.g., Antokhina et al. (1992): $q \sim 0.15$) are generally lower than those estimated from optical light curves (which are consistent with $q \gtrsim 0.4$; Gies et al. (2002b)). There are, however, exceptions to this rule: e.g., the X-ray lightcurves of Brinkmann et al. (2005) point to a mass ratio $q = 0.57$.

[4]The mass function is used to set a lower limit on the mass of an (unseen) companion in a spectroscopic binary system where only the radial velocity can only be estimated (from absorption or emission lines) for one component (see e.g., Carroll and Ostlie (2014), §7). If $K_1$ is the half-amplitude of the radial velocity curve for component 1, then the mass function for the companion $m_2$ is:

$$f\left(m_2; m_1, \eta\right) := \frac{m_2\,\sin^3\eta}{\left(1+\left(m_1/m_2\right)\right)^2} \equiv \frac{P_{\rm orb}}{2\pi G}\,K_1^3\left(1-e^2\right)^{3/2}$$

where $P_{\rm orb}$ is the orbital period, $e$ is the binary eccentricity, $\eta$ is the angle between the normal to the orbital plane and the line-of-sight, and $m_1$ and $m_2$ are the masses. Typically, $\eta$ and $m_1/m_2$ are unknown, but as $\sin^3\eta \in (0,1]$ for $\eta \in (0, \pi/2]$ and $\left(1+\left(m_1/m_2\right)\right)^{-2} \in (0,1)$, we can see that $m_2 \leq f$. This can be rewritten in a more helpful form as:

$$\frac{m_2}{\mathrm{M}_\odot}\,\frac{\sin^3\eta}{\left(1+\left(m_1/m_2\right)\right)^2} = 37.86\left(\frac{P_{\rm orb}}{\rm yr}\right)\left(\frac{K_1}{100\,\mathrm{km\,s^{-1}}}\right)^3\left(1-e^2\right)^{3/2}.$$

Estimating the mass function for the companion star requires the radial component of the orbital velocity of the compact object. Estimates of the half-amplitude of the radial velocity curve for the compact object, $K_{\rm bh}$, are consistent at $\sim 175\,{\rm km}\,s^{-1}$. For instance, Crampton and Hutchings (1981) find $K_{\rm bh} = 195 \pm 19\,{\rm km\,s^{-1}}$ from singly-ionised helium recombination lines; Fabrika and Bychkova (1990) and Gies et al. (2002b) find $K_{\rm bh} = 175 \pm 20\,{\rm km\,s^{-1}}$ and $K_{\rm bh} = 162 \pm 29\,{\rm km\,s^{-1}}$ from He II and C II emission lines respectively. The accretion disc itself is only directly observed during flares (Blundell et al. (2011)); Bowler (2010a) finds that H$\alpha$ emission seen from the disc in a flare displays an orbital variation that is consistent with $175\,{\rm km\,s^{-1}}$. Hence, we can estimate:

$$f\left(M_*; M_{\rm bh}, i_0\right) = \frac{M_*\,\sin^3 i_0}{\left(1 + \left(M_{\rm bh}/M_*\right)\right)^2} = 7.3\,{\rm M}_\odot \tag{1.1}$$

(note that we know the angle between the binary orbital plane and the line-of-sight – $i_0 = 79^\circ$ – assuming that the orbital plane is the mid-plane of the precessing jets). This implies that the compact object is a black hole (i.e., has a mass greater than $\sim 2.5{\rm M}_\odot$) if the mass ratio is greater than 0.2.

Attempts to lift this degeneracy have been made by looking for absorption features associated with the companion. If a value could be found for the radial component of the orbital velocity of the companion, $K_*$, then the mass ratio would be uniquely determined by $q = M_{\rm bh}/M_* = K_{\rm bh}/K_*$. Using different candidate absorption features, estimates include: $q = 0.72$ (Gies et al. (2002b)); $q = 0.57$ (Gies et al. (2002a)); $q = 0.28$ (Hillwig et al. (2004)); and $q = 0.35$ (Hillwig and Gies (2008); Kubota et al. (2010)). In all cases, these point to a black hole as the relativistic object, but the mass estimates vary from $M_{\rm bh} = 4.3 \pm 0.8\,{\rm M}_\odot$ (Hillwig and Gies (2008)), to $M_{\rm bh} = 16 \pm 6\,{\rm M}_\odot$ (Gies et al. (2002b)).

The second case was outlined by Blundell et al. (2008), who observed that the "stationary" Balmer H$\alpha$ line in SS 433's spectrum could be decomposed into a component that varied with the orbital period (identified tentatively with the wind outflow), and two actually stationary H$\alpha$ lines, which they identified with a circumbinary ring – a quasi-stable keplerian ring (or the inner edge of a disc) of matter orbiting the binary system with a speed of $\sim 200\,{\rm km\,s^{-1}}$. They show that the mass ratio is determined by the ratio of the velocity of one binary component (which is most easily supplied by the compact object) to the speed of the circumbinary ring, and that the orbital speed of the circumbinary ring can be related to the total mass of the binary. Hence, they estimate the total mass of the system as $38\,{\rm M}_\odot$, and the mass ratio as $q \simeq 0.7$.

The major advantage of this method is that it allows the measurement of the mass ratio without the challenges involved in finding the orbital velocity of the companion.

### 1.4.3 Mass loss rates & the super-Eddington accretion rate

Estimates are available for two of the three mass-loss mechanisms. The mass loss rate in the jet is estimated from models of the X-ray jets (Kotani et al. (1996)) as $\dot{M}_{\rm jet} > 5 \times 10^{-7}\,{\rm M}_\odot\,{\rm yr}^{-1}$. The wind loss rate is estimated to be $\dot{M}_{\rm wind} \simeq 10^{-4}\,{\rm M}_\odot\,{\rm yr}^{-1}$, with a final outflow speed of about $1500\,{\rm km\,s}^{-1}$. These are determined from the luminosities and the linewidths of the Brackett-$\gamma$ lines in the wind (Perez and Blundell (2009); see also Fabrika (1997), Fabrika (2004)). The mass loss rate via the cicumbinary outflow is as yet unknown.

Importantly, these estimates place the accretion rate well in excess of the Eddington limit for such a stellar-mass black-hole accretor (Perez and Blundell (2009), Fabrika (2004)). The Eddington criterion says that a spherical accretion flow will be disrupted by radiation pressure if the accretion rate exceeds the Eddington accretion rate $\dot{M}_{\rm Edd}$, where:

$$\dot{M}_{\rm Edd} = \frac{4\pi G M_{\rm bh} m_p}{\eta \sigma_T c} = \frac{2.2 \times 10^{-9}}{\eta} \left( \frac{M_{\rm bh}}{{\rm M}_\odot} \right) {\rm M}_\odot\,{\rm yr}^{-1} \tag{1.2}$$

where $\eta \sim 0.1$ is the efficiency with which gravitational potential energy is converted into radiation and $\sigma_T$ is the Thomson cross-section (see Frank et al. (2002)). For a $16\,{\rm M}_\odot$ black hole, this corresponds to an accretion rate of $\dot{M}_{\rm edd} \simeq 4 \times 10^{-7}\,{\rm M}_\odot\,{\rm yr}^{-1}$. We can see that $\dot{M}_{\rm SS\ 433} \sim 1000 \dot{M}_{\rm Edd}$ – i.e., the accretion rate is highly super-Eddington. This is not a problem if the accretion flow is aspherical or the radiation output is collimated. However, it does set SS 433 apart from the rest of the Galactic microquasar population, whose accretion rates are typically on the order of $0.01\,\dot{M}_{\rm Edd}$.

## 1.5 Further complexities

### 1.5.1 Flaring & variability

SS 433 displays variability in both optical and radio wavebands. At times, it can enter an active state in which its radio brightness may rise by more than 50-100%. It can remain in this fluctuating

state for as long as 90 days (Fabrika (2004)). There are also shorter radio and optical flares, in which the system's radio photometric brightness rises, accompanied by a massive ejection, either through the accretion-disc wind or through the radio jets. Contemporaneous optical and radio observations of a flare in 2004 (Blundell et al. (2011)) revealed the coupled, multi-wavelength behaviour of the flaring phenomenon, and pointed to a picture in which flares consist of (a) enhanced mass loss through a faster and increased accretion disc wind; (b) faster launch speeds as determined from the optical jets; and (c) a two-part radio flare with a first peak due to the enhanced wind, and a second due to the appearance of jet bolides. In particular, from archival radio photometry and optical spectroscopy, Blundell et al. (2011) report that faster optical jets always precede radio flares by a couple of days. We will return to this in Chapter 4.

### 1.5.2 Eccentricity

Although the orbit is generally assumed to be circular, there are several pieces of evidence for a non-zero eccentricity. These are outlined in §3.1 of Blundell et al. (2011). For instance, Blundell and Bowler (2005) show that the mean jet speed (determined from the sum of redshifts in the jet and counterjet) varies sinusoidally as a function of orbital phase with an amplitude of $0.0066c$ about a mean of $0.2581c$. The direct observations of H$\alpha$ emission from the accretion disc by Blundell et al. (2011) allow them to determine line-of-sight velocity of the compact object over more than an orbital period. They find that the phases of maximum and minimum speed are not consistent with $\Phi_{\rm orb} = 0.75$ and $\Phi_{\rm orb} = 0.25$ respectively, as would be the case in a circular orbit. Thirdly, the relatively rapid precession of the circumbinary ruff as determined by Doolin and Blundell (2009) requires a non-zero eccentricity.

## 1.6 Summary

The 21$^{\rm st}$ Century has seen significant advances in our understanding of the SS 433 phenomenon, with recent determinations of distance and mass of particular relevance. The discovery of the circumbinary ring and equatorial outflow has added an important new component to our conception of SS 433's physical structure.

There remain many questions, especially to do with SS 433's temporal evolution and variation, how its outflows vary, and about the nature of flares. But it is the ability to make temporally-

resolved (as well as spatially-resolved) studies of the system that will give us insights into the physics of the object.

Throughout this thesis, we will exploit this ability to observe SS 433's variations on practical time scales: in Chapter 4, we will use time-resolved, spatially-resolved observations to determine the dynamics of the jets; in Chapter 6, we will use time-resolved observations to explore the evolution of the internal properties of the jet bolides; and in Chapter 7, we will use X-ray monitoring data to examine both SS 433's flaring behaviour and the composition of the binary system.

# Chapter 2

# Scientific Background – The Kinematic Model

## 2.1 Introduction

SS 433's most striking features are its twin, precessing jets. It was through observations of two different manifestations of these jets that SS 433 first drew the attention of the astronomical community, namely its moving emission lines, and its shape as seen in radio images. It became clear swiftly that a precessing jet model, referred as the Kinematic Model, could explain both of these as manifestations of the same phenomenon. It was used first by Abell and Margon (1979) to describe the redshifts of pairs of moving emission lines that arise from hydrogen (and other) atoms moving in the relativistic jets. The model was then developed by Hjellming and Johnston (1981) to account for the proper motions of the jet plasma seen in early VLA maps of the system, by properly incorporating the effect on observations of the finite speed of light.

In its simplest form, the Kinematic Model treats the jet and counterjet of SS 433 as anti-parallel jets precessing with a period of 162 days at constant precession frequency around the surface of cones of fixed orientation and opening angle. This basic model gives a remarkably good first-order description of the jets' behaviour. We will derive its various elements over the course of this Chapter. The geometry is outlined in Section 2.2 and its observational manifestation in terms of proper motions and the redshift of emission lines is developed in Section 2.3; and these are

combined to give the Kinematic Model in Section 2.4.

It is not, however, the complete picture. There is a significant nutational component to the motion with periodicity of $\sim 6$ d (Newsom and Collins (1981)), which is believed to arise from the interaction between the 13.08 d orbital and 162 d precessional periods (Katz et al. (1982)). There are also other variations both in the jet launch speeds and their directions, some of which are stochastic in nature, and some associated with flaring (Blundell and Bowler (2005), Blundell et al. (2007), Blundell et al. (2011), Jeffrey et al. (2016)). We will discuss these briefly in Section 2.5.

## 2.2 Geometry and Coordinate Systems

First, we need to develop an appropriate description of the geometry of the precessing jets.

The most practical coordinate system for us to describe observations in is usually a local version of the Equatorial Coordinate System, in which one of the basis vectors is parallel to the line of sight, and the other two lie in the plane of the sky aligned with Right Ascension and Declination. We will refer to this as the Observer's Reference Frame, which we can define more rigorously as follows:

**Definition 2.2.1** (The Observer's Reference Frame)**.** The Observer's Reference Frame can be (locally) described using 3 Cartesian basis vectors, $\{\boldsymbol{e}_{\tilde{x}}, \boldsymbol{e}_{\tilde{y}}, \boldsymbol{e}_{\tilde{z}}\}$, where we set the origin in the plane of the sky, and:

- $\boldsymbol{e}_{\tilde{x}}$ is the vector pointing towards the observer along the line-of-sight
- $\boldsymbol{e}_{\tilde{y}}$ is the vector in the plane of the sky, pointing North (i.e., aligned with increasing Declination, $\delta$)
- $\boldsymbol{e}_{\tilde{z}}$ is the vector in the plane of the sky, pointing East (i.e., aligned with increasing Right Ascension, $\alpha$)

Although this reference frame is the most convenient in which to make observations, it is not the most convenient frame to describe the physics of the system. To calculate the orientation of the vector along which the jet points at a given epoch, it is more convenient to choose a coordinate system aligned with the precession cone of the jet.

**Definition 2.2.2** (Jet Precession Cone Coordinate System)**.** We define the jet precession cone coordinate system using an orthonormal, right-handed set of cartesian basis vectors, $\{\boldsymbol{e}_x, \boldsymbol{e}_y, \boldsymbol{e}_z\}$, such that:

- $\boldsymbol{e}_z$ is the vector aligned with the axis of the jet precession cone
- $\boldsymbol{e}_x$ is the vector in the plane containing $\boldsymbol{e}_z$ and the line-of-sight, $\boldsymbol{e}_{\tilde{x}}$, and is orthogonal to $\boldsymbol{e}_z$
- $\boldsymbol{e}_y$ is the vector in the plane of the sky, orthogonal to $\boldsymbol{e}_x$ and $\boldsymbol{e}_z$

If $\chi_0$ is the position angle of the jet precession cone axis, and $i_0$ is the angle between it and the line of sight, then these two sets of basis vectors can be related by two rotations:

1. a rotation through $\chi_0$ counter-clockwise about the line-of-sight; and,
2. a rotation through $\frac{\pi}{2} - i_0$ counter-clockwise in the plane containing the jet precession cone axis and the line-of-sight (i.e., about the vector $\boldsymbol{e}_y$).

These rotations can be expressed in matrix form as follows.

**Result 2.2.3** (Transformation between Frames)**.** The basis vectors of the Jet Precession Cone coordinate system can be related to the basis vectors of the Observer's coordinate system using:

$$\begin{pmatrix} \boldsymbol{e}_x \\ \boldsymbol{e}_y \\ \boldsymbol{e}_z \end{pmatrix} = \begin{pmatrix} \sin i_0 & 0 & -\cos i_0 \\ 0 & 1 & 0 \\ \cos i_0 & 0 & \sin i_0 \end{pmatrix} \begin{pmatrix} 1 & 0 & 0 \\ 0 & \cos\chi_0 & \sin\chi_0 \\ 0 & -\sin\chi_0 & \cos\chi_0 \end{pmatrix} \begin{pmatrix} \boldsymbol{e}_{\tilde{x}} \\ \boldsymbol{e}_{\tilde{y}} \\ \boldsymbol{e}_{\tilde{z}} \end{pmatrix} \tag{2.1}$$

$$\Rightarrow \begin{pmatrix} \boldsymbol{e}_x \\ \boldsymbol{e}_y \\ \boldsymbol{e}_z \end{pmatrix} = \begin{pmatrix} \sin i_0 & \cos i_0 \sin\chi_0 & -\cos i_0 \cos\chi_0 \\ 0 & \cos\chi_0 & \sin\chi_0 \\ \cos i_0 & -\sin i_0 \sin\chi_0 & \sin i_0 \cos\chi_0 \end{pmatrix} \begin{pmatrix} \boldsymbol{e}_{\tilde{x}} \\ \boldsymbol{e}_{\tilde{y}} \\ \boldsymbol{e}_{\tilde{z}} \end{pmatrix} \tag{2.2}$$

In Figure (2.2), we sketch the Jet Coordinate System (panel (a)), and the two rotations required to obtain the Observer's Coordinate System (panels (b) and (c)).

### 2.2.1 Vector components in polar coordinates

Let us now consider the transformation between polar coordinate systems in these two reference frames.

We can represent a vector centred on the origin using spherical polar coordinates, given by a length and two angles with respect to this cartesian basis. Working in the Observer's coordinates, it is convenient to choose the angle to the line-of-sight, $\eta$, as the polar angle, and the position angle

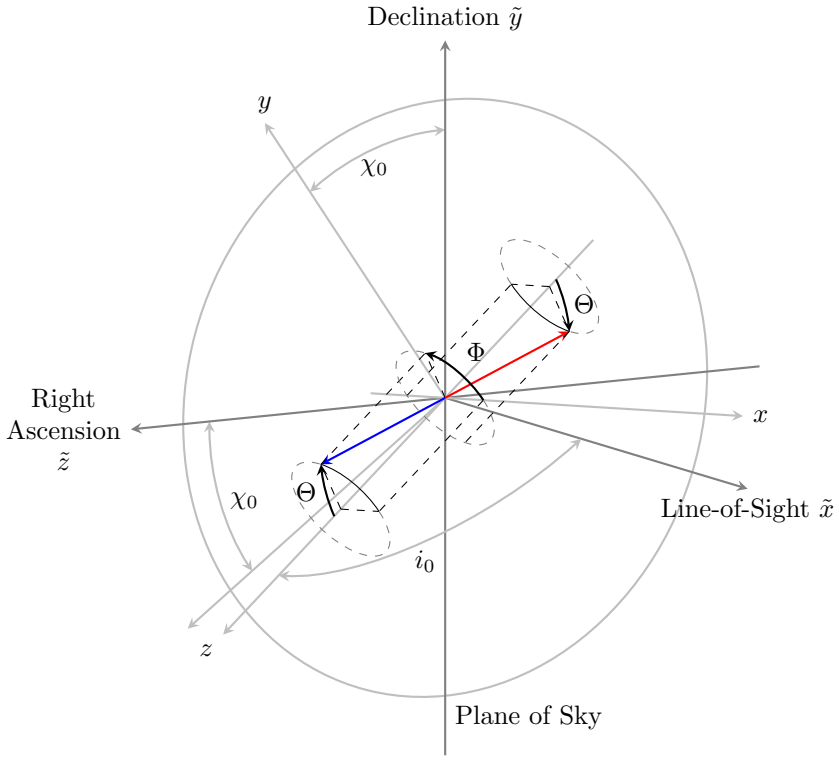


Figure 2.1: The angles needed to describe the precessing jet model. $\chi_0$ and $i_0$ denote the position angle and the angle to the line-of-sight of the axis of the jet precession cone respectively. $\Theta$ is the opening angle of the jet precession cone, and $\Phi$ is the angle between the jet and the point of maximum blueshift as projected onto the mid plane of the system (the $x$-$y$ plane). This is the closely related to the precession phase. The jet and counterjet are shown in blue and red respectively, and the jet cone and equatorial coordinate systems are marked (axes $\{x, y, z\}$ and $\{\tilde{x}, \tilde{y}, \tilde{z}\}$ respectively).

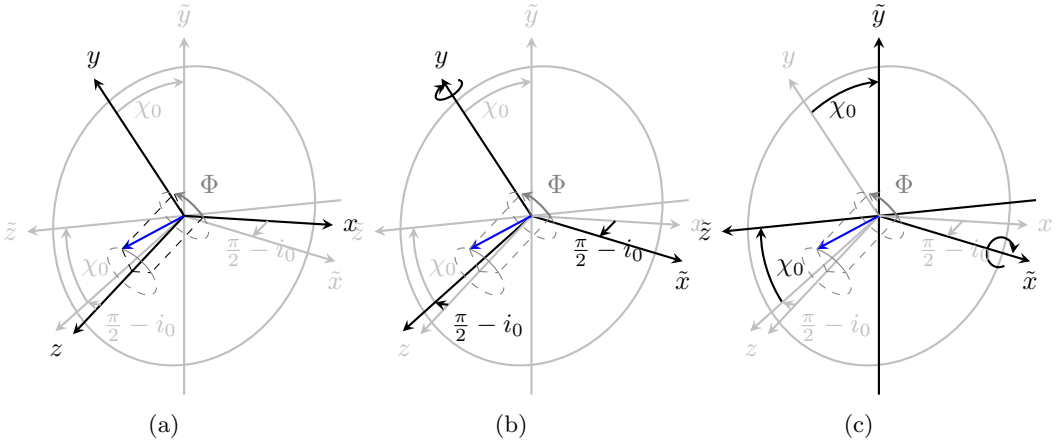


Figure 2.2: The Jet Cone Coordinate System and the sequence of rotations required to relate it to the Observer's Coordinate System: (a) the Jet Cone System; (b) projections onto the plane-of-sky and line-of-sight by a rotation through angle $\frac{\pi}{2} - i_0$ about the $y$-axis; (c) projections onto N-S and E-W by rotating through angle $\chi_0$ about the line-of-sight (i.e., $\tilde{x}$-axis).

(i.e., the angle counter-clockwise from East[1]), $\chi$, as the azimuthal angle. With these choices, a vector $\boldsymbol{a}$ can be written:

$$\boldsymbol{a} = a\cos\eta\,\boldsymbol{e}_{\tilde{x}} - a\sin\eta\sin\chi\,\boldsymbol{e}_{\tilde{y}} + a\sin\eta\cos\chi\,\boldsymbol{e}_{\tilde{z}} \tag{2.3}$$

where $a = |\boldsymbol{a}|$.

Notice that the angular dependences of the basis vector $\boldsymbol{e}_z$ in Result (2.2.3) are the same as in Equation (2.3). Our rotations between coordinate frames amount to describing the vector $\boldsymbol{e}_z$ in spherical polar coordinates, and we have used $\chi_0$ and $i_0$ as position angle and angle to the line-of-sight in the same sense as we used $\chi$ and $\eta$ in (2.3).

With respect to the jet precession cone coordinate system, we can again define spherical polar coordinates. Now we choose to use $\theta$ and $\phi$ in their conventional uses as the polar and azimuthal angles, measured from $\boldsymbol{e}_z$ (the jet precession cone axis) and counter-clockwise from $\boldsymbol{e}_x$ respectively. We will see later how these angles correspond to the jet cone opening angle and the precession phase.

A vector can be described in these spherical polar coordinates as:

$$\boldsymbol{a} = a\sin\theta\cos\phi\,\boldsymbol{e}_x + a\sin\theta\sin\phi\,\boldsymbol{e}_y + a\cos\theta\,\boldsymbol{e}_z \tag{2.4}$$

We will need to transform these to the most useful coordinates for the observer, namely $\{\boldsymbol{e}_{\tilde{x}}, \boldsymbol{e}_{\tilde{y}}, \boldsymbol{e}_{\tilde{z}}\}$. The change of basis is Result (2.2.3).

[1]Note the unusual choice of convention used here, in which position angle is defined from East, not North. We have chosen this convention to suit the particular orientation of SS 433.

**Result 2.2.4** (Vector Components in the Observer's Reference Frame)**.** The equatorial frame components of the vector $\boldsymbol{a}$ that is described in the jet precession cone frame by polar coordinates $\{\theta, \phi\}$ are:

$$a_{\tilde{x}} = a\sin\theta\cos\phi\sin i_0 + a\cos\theta\cos i_0 \tag{2.5}$$

$$a_{\tilde{y}} = a\sin\theta\cos\phi\cos i_0\sin\chi_0 + a\sin\theta\sin\phi\cos\chi_0 - a\cos\theta\sin i_0\sin\chi_0 \tag{2.6}$$

$$a_{\tilde{z}} = -a\sin\theta\cos\phi\cos i_0\cos\chi_0 + a\sin\theta\sin\phi\sin\chi_0 + a\cos\theta\sin i_0\cos\chi_0 \tag{2.7}$$

where $a_{\tilde{x}}$ is the vector component along the line-of-sight, and $a_{\tilde{y}}$ and $a_{\tilde{z}}$ are the vector components in the directions of increasing Declination and Right Ascension respectively, and angles $i_0$ and $\chi_0$ describe the angle to the line-of-sight and the position angle of the jet precession cone axis.

*Proof.* We simply insert the transformation between the two bases given by Result (2.2.3) into $\boldsymbol{a}$. Thus:

$$\boldsymbol{a} = a\begin{pmatrix}\sin\theta\cos\phi\\ \sin\theta\sin\phi\\ \cos\theta\end{pmatrix}^{\mathsf{T}}\begin{pmatrix}\boldsymbol{e}_x\\ \boldsymbol{e}_y\\ \boldsymbol{e}_z\end{pmatrix} \tag{2.8}$$

$$= a\begin{pmatrix}\sin\theta\cos\phi\\ \sin\theta\sin\phi\\ \cos\theta\end{pmatrix}^{\mathsf{T}}\begin{pmatrix}\sin i_0 & \cos i_0\sin\chi_0 & -\cos i_0\cos\chi_0\\ 0 & \cos\chi_0 & \sin\chi_0\\ \cos i_0 & -\sin i_0\sin\chi_0 & \sin i_0\cos\chi_0\end{pmatrix}\begin{pmatrix}\boldsymbol{e}_{\tilde{x}}\\ \boldsymbol{e}_{\tilde{y}}\\ \boldsymbol{e}_{\tilde{z}}\end{pmatrix} \tag{2.9}$$

$$= a\begin{pmatrix}\sin\theta\cos\phi\sin i_0 + \cos\theta\cos i_0\\ \sin\theta\cos\phi\cos i_0\sin\chi_0 + \sin\theta\sin\phi\cos\chi_0 - \cos\theta\sin i_0\sin\chi_0\\ -\sin\theta\cos\phi\cos i_0\cos\chi_0 + \sin\theta\sin\phi\sin\chi_0 + \cos\theta\sin i_0\cos\chi_0\end{pmatrix}^{\mathsf{T}}\begin{pmatrix}\boldsymbol{e}_{\tilde{x}}\\ \boldsymbol{e}_{\tilde{y}}\\ \boldsymbol{e}_{\tilde{z}}\end{pmatrix} \tag{2.10}$$

$$= a_{\tilde{x}}\boldsymbol{e}_{\tilde{x}} + a_{\tilde{y}}\boldsymbol{e}_{\tilde{y}} + a_{\tilde{z}}\boldsymbol{e}_{\tilde{z}} \tag{2.11}$$

from which we can read off the components in the Observer's Reference Frame. □

The inverse of this process is also useful.

**Result 2.2.5** (Vector Components in the Jet Cone Frame)**.** The jet precession cone frame components of a vector $\boldsymbol{a}$ that is described by an angle to the line-of-sight, $\eta$, and a position angle, $\chi$, are:

$$a_x = a\cos\eta\sin i_0 - a\sin\eta\cos i_0\cos(\chi_0 - \chi) \tag{2.12}$$

$$a_y = a\sin\eta\sin(\chi_0 - \chi) \tag{2.13}$$

$$a_z = a\cos\eta\cos i_0 + a\sin i_0\sin\eta\cos(\chi_0 - \chi) \tag{2.14}$$

where $a_z$ is the vector component along jet precession cone axis, $a_y$ is the vector component in the mid-plane of the jet system parallel to the plane of the sky, and $a_x$ is the vector component in the mid-plane of the jet system pointing out of the plane of the sky. Angles $i_0$ and $\chi_0$ describe the angle to the line-of-sight and the position angle of the jet precession cone axis respectively.

*Proof.* We insert the inverse of the transformation between the two bases given by Result (2.2.3) into $\boldsymbol{a}$. Thus:

$$\boldsymbol{a} = a\begin{pmatrix}\cos\eta\\ -\sin\eta\sin\chi\\ \sin\eta\cos\chi\end{pmatrix}^{\intercal}\begin{pmatrix}\boldsymbol{e}_{\tilde{x}}\\ \boldsymbol{e}_{\tilde{y}}\\ \boldsymbol{e}_{\tilde{z}}\end{pmatrix} \tag{2.15}$$

$$= a\begin{pmatrix}\cos\eta\\ -\sin\eta\sin\chi\\ \sin\eta\cos\chi\end{pmatrix}^{\intercal}\begin{pmatrix}1 & 0 & 0\\ 0 & \cos\chi_0 & -\sin\chi_0\\ 0 & \sin\chi_0 & \cos\chi_0\end{pmatrix}\begin{pmatrix}\sin i_0 & 0 & \cos i_0\\ 0 & 1 & 0\\ -\cos i_0 & 0 & \sin i_0\end{pmatrix}\begin{pmatrix}\boldsymbol{e}_x\\ \boldsymbol{e}_y\\ \boldsymbol{e}_z\end{pmatrix} \tag{2.16}$$

$$= a\begin{pmatrix}\cos\eta\\ -\sin\eta\sin\chi\\ \sin\eta\cos\chi\end{pmatrix}^{\intercal}\begin{pmatrix}\sin i_0 & 0 & \cos i_0\\ \sin\chi_0\cos i_0 & \cos\chi_0 & -\sin\chi_0\sin i_0\\ -\cos\chi_0\cos i_0 & \sin\chi_0 & \cos\chi_0\sin i_0\end{pmatrix}\begin{pmatrix}\boldsymbol{e}_x\\ \boldsymbol{e}_y\\ \boldsymbol{e}_z\end{pmatrix} \tag{2.17}$$

$$= a\begin{pmatrix}\cos\eta\sin i_0 - \sin\eta\cos i_0\cos(\chi_0 - \chi)\\ \sin\eta\sin(\chi_0 - \chi)\\ \cos\eta\cos i_0 + \sin i_0\sin\eta\cos(\chi_0 - \chi)\end{pmatrix}^{\intercal}\begin{pmatrix}\boldsymbol{e}_x\\ \boldsymbol{e}_y\\ \boldsymbol{e}_z\end{pmatrix} \tag{2.18}$$

$$= a_x\boldsymbol{e}_x + a_y\boldsymbol{e}_y + a_z\boldsymbol{e}_z \tag{2.19}$$

□

To complete our geometrical results, it is helpful to identify expressions explicitly relating the

angles $\{\theta, \phi\}$ in the Jet Cone Frame to the angles $\{\eta, \chi\}$ in the Observer's frame.

**Result 2.2.6.** A vector with polar and azimuthal angles $\{\theta, \phi\}$ (in the Jet Cone frame) can be written in terms of an angle to the line-of-sight, $\eta$, and a position angle, $\chi$ (measured counter-clockwise from East), where:

$$\cos\eta = \sin\theta\cos\phi\sin i_0 + \cos\theta\cos i_0 \tag{2.20}$$

$$\tan\chi = -\frac{\sin\theta\cos\phi\cos i_0\sin\chi_0 + \sin\theta\sin\phi\cos\chi_0 - \cos\theta\sin i_0\sin\chi_0}{-\sin\theta\cos\phi\cos i_0\cos\chi_0 + \sin\theta\sin\phi\sin\chi_0 + \cos\theta\sin i_0\cos\chi_0} \tag{2.21}$$

Similarly, a vector with angle to the line-of-sight, $\eta$, and position angle, $\chi$, can be written in terms of polar angles $\theta$ and $\phi$ in the Jet Cone frame, where:

$$\cos\theta = \cos\eta\cos i_0 + \sin i_0\sin\eta\cos(\chi_0 - \chi) \tag{2.22}$$

$$\tan\phi = \frac{\sin\eta\sin(\chi_0 - \chi)}{\cos\eta\sin i_0 - \sin\eta\cos i_0\cos(\chi_0 - \chi)} \tag{2.23}$$

*Proof.* First, we notice that, from Equation 2.3, we have

$$\cos\eta = \frac{a_{\tilde{x}}}{a} \qquad\qquad \tan\chi = -\frac{a_{\tilde{y}}}{a_{\tilde{z}}} \tag{2.24}$$

and, from Equation 2.4, we have:

$$\cos\theta = \frac{a_z}{a} \qquad\qquad \tan\phi = \frac{a_y}{a_x} \tag{2.25}$$

Then, using Results 2.2.4 and 2.2.5, we obtain the desired results. □

## 2.3 Observing light from relativistic sources

### 2.3.1 Proper Motions & Light Travel Time Effects

Due to the finite travel time of light signals, the proper motion, $\mu$, of a light source across the sky (i.e., its observed change in angular displacement per unit of astronomer's time), is a function of the orientation of the source's motion with respect to the observer.

**Result 2.3.1** (Proper Motion)**.** The proper motion of a moving source is given by:

$$\mu = \frac{\mathrm{d}\xi}{\mathrm{d}T} = \frac{\beta_{\text{apparent}} c}{D} = \frac{c}{D} \frac{\beta \sin \eta}{1 - \beta \cos \eta} \tag{2.26}$$

where $D$ is the distance to the source, $c$ is the speed of light, $\eta$ is the angle of the source's intrinsic velocity to line-of-sight, and $v = \beta c$ is its speed. $\xi$ is the angular displacement on the sky, and $T$ denotes time elapsed according to the observer's clock (the epoch of observation).

*Proof.* The geometry is sketched in Figure 2.3. All times are measured in the rest frame of the observer, but times $t$ and $t + \Delta t$ correspond to the times at which light rays *leave* the source, and times $T$ and $T + \Delta T$ represent the times at which those light rays *reach* the observer on Earth. The key insight is that the emission and observation of light are *different events*, related by the light cone connecting source and observer. Hence, using the geometry of Figure 2.3, the observation times can be written in terms of the emission times as:

$$T = t + \left( \frac{D - \beta_{\parallel} ct}{c} \right)$$
$$T + \Delta T = t + \Delta t + \left( \frac{D - \beta_{\parallel} c\,(t + \Delta t)}{c} \right)$$

Rearranging these and subtracting the first equation from the second, we get:

$$\frac{\Delta T}{\Delta t} = \left(1 - \beta_{\parallel}\right)$$

The angular distance travelled between the two observations is $\Delta\xi = \xi\,(T + \Delta T) - \xi\,(T) = \beta_{\perp} c \Delta t / D$. Dividing through by $\Delta T$, using the above relation for $\Delta T / \Delta t$, and noting that $\beta_{\parallel} = \beta \cos \eta$ and $\beta_{\perp} = \beta \sin \eta$, we obtain the Result. □

This is a textbook result (see e.g., Longair (2011), Mirabel and Rodríguez (1994) for other examples of the derivation), and follows from the same reasoning underlying the apparent superluminal motions seen in the jets associated with some AGN and microquasars (Rees (1966)). The apparent speed, of the source $\beta_{\text{apparent}} c$, will be greater than its projected intrinsic speed, $\beta c \sin \eta$, if the source is approaching the observer ($\eta < \frac{\pi}{2}$), and will be reduced if the source travels away from the observer ($\eta > \frac{\pi}{2}$).

Using the Observer coordinate system set out in Definition 2.2.1, where $\tilde{z}$ and $\tilde{y}$ correspond to the directions of Right Ascension and Declination, we can resolve the proper motion into changes of

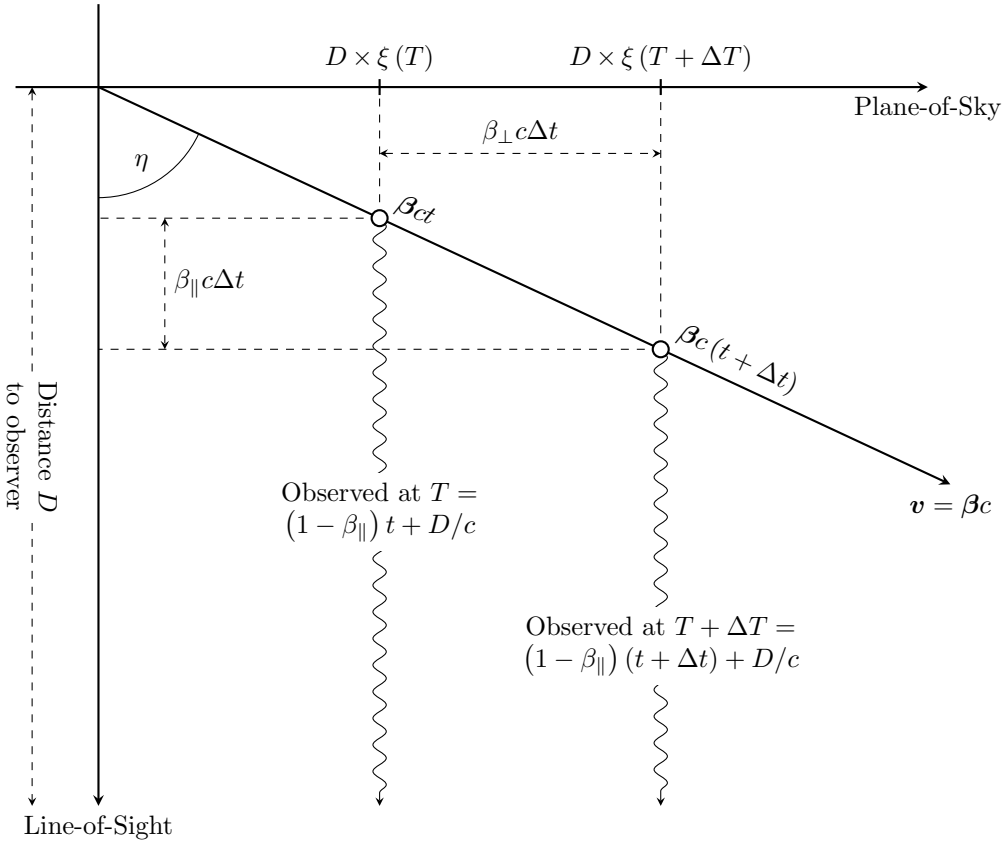


Figure 2.3: Schematic showing the role of light travel time effects in determining proper motions. It shows light pulses leaving a source that moves at $\boldsymbol{v} = \boldsymbol{\beta} c$ to be observed by a distant ($D \gg \beta c \Delta t$) astronomer on Earth. The events corresponding to emission of a light pulse occur at *coordinate* times $t$ and $t + \Delta t$ in the observer's rest frame, while the events corresponding to those pulses reaching Earth occur at coordinate times $T$ and $T + \Delta T$ respectively. From the geometry shown here, the time steps are related by $\Delta T / \Delta t = \left(1 - \beta_\parallel\right)$, since the second ray has to travel a shorter distance from position at emission to observation on Earth. At these two observations, the source's angular displacements from the core are $\xi\,(T)$ and $\xi\,(T + \Delta T)$. The proper motion measured by the astronomer on Earth is $\mu = \left[\xi\,(T + \Delta T) - \xi\,(T)\right] / \Delta T$, where $\xi\,(T + \Delta T) - \xi\,(T) = \beta_\perp c \Delta t / D$. By eliminating $\Delta t$, Equation 2.26 follows simply.

RA and Dec:

**Result 2.3.2.** In terms of change in Right Ascension, $\mathrm{d}\alpha$, and Declination, $\mathrm{d}\delta$, the proper motions in radians of relativistically moving plasma are:

$$\frac{\mathrm{d}\alpha}{\mathrm{d}T} = \frac{c}{D\cos\delta}\frac{\beta_{\tilde{z}}}{1-\beta_{\tilde{x}}} \tag{2.27}$$

$$\frac{\mathrm{d}\delta}{\mathrm{d}T} = \frac{c}{D}\frac{\beta_{\tilde{y}}}{1-\beta_{\tilde{x}}} \tag{2.28}$$

where $\delta$ is the source Declination, $\chi$ is the position angle measured from east, $D$ is the distance from the observer to the source, and $dT$ is change in observer time.

We will return to the question of analysing proper motions of jet bolides in greater detail in Chapter 4.

### 2.3.2 Redshifts

The highest precision probes of the SS 433 jets come from spectroscopic redshifts. As well as emission lines from the Lyman and Balmer series of hydrogen (Clark and Murdin (1978), Blundell and Bowler (2005)), the SS 433 jets are the almost unique examples of microquasar jets from which X-ray emission lines of high-$Z$ elements are observed (for instance, from silicon and iron (e.g., Marshall et al. (1979), Watson et al. (1986), Kotani et al. (1996)); the other candidate is 4U1630-47, in which possible red and blue-shifted iron lines were detected by Díaz Trigo et al. (2013)).

The redshift of emission from the jet and the counterjet is determined by the component of jet velocity along the line-of-sight.

**Result 2.3.3.** Suppose a source moving at $\boldsymbol{v} = \boldsymbol{\beta}c$ radiates a photon at wavelength $\lambda_{\mathrm{em}}$ in its rest frame. The photon is observed by a stationary, distant observer at wavelength $\lambda_{\mathrm{obs}}$. Then, the redshift is given by:

$$z := \frac{\lambda_{\mathrm{obs}} - \lambda_{\mathrm{em}}}{\lambda_{\mathrm{em}}} = \frac{1-\beta_{\parallel}}{\sqrt{1-\beta^2}} - 1 \tag{2.29}$$

where $\beta_{\parallel} = \beta_{\tilde{x}} = \boldsymbol{\beta}\cdot\boldsymbol{e}_{\tilde{x}}$ is the velocity component along the line-of-sight, and $\boldsymbol{e}_{\tilde{x}}$ is the unit vector pointing towards the observer along the line-of-sight.

Blundell and Bowler (2005) noted that the assumption of antisymmetric jet launch in precessing jet models (i.e., $\boldsymbol{\beta}_{\mathrm{jet}} = -\boldsymbol{\beta}_{\mathrm{cjt}}$) allows the unique determination of the jet Lorentz factor $\gamma$, jet

speed $\beta$, and the launch angle $\eta$ with respect to the line-of-sight. They obtain these by taking the sum and the difference of the two redshifts:

$$\gamma = \frac{z_{\rm jet} + z_{\rm cjt}}{2} + 1 \tag{2.30}$$

$$\cos\eta = \frac{z_{\rm jet} - z_{\rm cjt}}{2\gamma\beta} \tag{2.31}$$

where $\gamma := \left(1-\beta^2\right)^{-1/2}$.

In the next section we will use the kinematic model to find a functional form for $\beta_{\tilde{x}} = \boldsymbol{\beta}\cdot\boldsymbol{e}_{\tilde{x}} = \beta\cos\eta$. There exists a substantial archive of high precision redshift measurements, which can then be used to determine the parameters of the model.

## 2.4 The Kinematic Model

In Section 2.2, we developed the geometrical machinery needed for the Kinematic Model, and in Sections 2.3.1 and 2.3.2, we summarised the key physics needed for observational probes. Now we consider the actual precessing jet itself.

The remaining assumptions we need to make about the jet motions are:

1. that the jet and counterjet bolides are launched simultaneously;
2. that the jet and counterjet launch vectors are anti-parallel $\boldsymbol{\beta}_{\rm jet} = -\boldsymbol{\beta}_{\rm cjt}$;
3. that the launch vector precesses at a constant rate ($\dot{\Phi}$ = constant) and with a fixed cone-opening angle, $\Theta$;
4. that, following launch, the jet ejecta proceed ballistically (i.e., without acceleration or deceleration).

From these, we can integrate $\dot{\Phi}$ = constant to get the precessional phase as a function of time:

$$\Phi\left(T\right) = s_{\rm rot}\frac{2\pi}{P}\left(T - T_{\rm ref}\right) \tag{2.32}$$

where $s_{\rm rot} = \pm 1$ denotes counter-clockwise or clockwise rotation, $P$ is the precessional period, and $T_{\rm ref}$ is a reference epoch at which the jet is maximally blue-shifted (i.e. at which $\Phi = 0$). In SS 433, the precession is in a left-handed sense; i.e., the jet precesses in a clockwise fashion, and

$s_{\rm rot} = -1$.

In terms of the $\{\boldsymbol{e}_x, \boldsymbol{e}_y, \boldsymbol{e}_z\}$ basis vectors, the velocity of the jet is:

$$\boldsymbol{\beta} = \beta \sin\Theta \cos\Phi\, \boldsymbol{e}_x + \beta \sin\Theta \sin\Phi\, \boldsymbol{e}_y + \beta \cos\Theta\, \boldsymbol{e}_z \tag{2.33}$$

(c.f., Equation 2.4) where $\Theta$ is the cone opening angle (i.e., the angle between the jet and the precession cone axis), and $\Phi = \Phi\left(T_{\rm launch}\right)$ is the precession phase (i.e., the angle projected onto the midplane of the system between the jet and the vector $\boldsymbol{e}_x$) at the epoch of launch.

We can rewrite this vector in terms of components along the axes of the equatorial coordinate system by the change of basis in Result 2.2.4.

**Result 2.4.1** (Velocity Components of Mean Jet Motion)**.** If a jet precesses around a cone of opening angle $\Theta$ with the precession axis having angle $i_0$ to the line-of-sight and angle projected on the plane of the sky $\chi_0$ measured counter-clockwise from East, then in the Observer's coordinate frame, the components of the launch velocity vector at precession phase $\Phi$ are

$$\beta_{\tilde{x}} = \beta \sin\Theta \cos\Phi \sin i_0 + \beta \cos\Theta \cos i_0 \tag{2.34a}$$

$$\beta_{\tilde{y}} = \beta \sin\Theta \cos\Phi \cos i_0 \sin\chi_0 + \beta \sin\Theta \sin\Phi \cos\chi_0 - \beta \cos\Theta \sin i_0 \sin\chi_0 \tag{2.34b}$$

$$\beta_{\tilde{z}} = -\beta \sin\Theta \cos\Phi \cos i_0 \cos\chi_0 + \beta \sin\Theta \sin\Phi \sin\chi_0 + \beta \cos\Theta \sin i_0 \cos\chi_0 \tag{2.34c}$$

where $\beta_{\tilde{x}}$ is the velocity component along the line-of-sight, and $\beta_{\tilde{y}}$ and $\beta_{\tilde{z}}$ are the velocity components in the directions of increasing Declination and Right Ascension respectively.

Lastly, we can write down expressions for the angular displacements of the jet and counterjet.

**Result 2.4.2** (Angular Displacements in the Kinematic Model)**.** Assuming ballistic motion and that the jet and counterjet possess antisymmetry, the angular displacements of components launched at $T_{\rm launch}$ as seen at some later time $T_{\rm obs} > T_{\rm launch}$ are:

$$\begin{aligned} \Delta\alpha_{\rm jet} &= \frac{c}{D\cos\delta}\frac{\beta_{\tilde{z}}}{1-\beta_x}\left(T_{\rm obs} - T_{\rm launch}\right) & \Delta\alpha_{\rm cjt} &= -\frac{c}{D\cos\delta}\frac{\beta_{\tilde{z}}}{1+\beta_x}\left(T_{\rm obs} - T_{\rm launch}\right) \\ \Delta\delta_{\rm jet} &= \frac{c}{D}\frac{\beta_{\tilde{y}}}{1-\beta_x}\left(T_{\rm obs} - T_{\rm launch}\right) & \Delta\delta_{\rm cjt} &= -\frac{c}{D}\frac{\beta_{\tilde{y}}}{1+\beta_x}\left(T_{\rm obs} - T_{\rm launch}\right) \end{aligned} \tag{2.35}$$

where $\beta_i = \beta_i\left(T_{\rm launch}\right)$ are the Observer's frame components of the velocity launch vector.

These expressions are obtained by integration of the equations in Result 2.3.2, using the assumption of antisymmetry to write $\boldsymbol{\beta}_{\rm jet} = -\boldsymbol{\beta}_{\rm cjt}$ and the assumption of ballistic motion to write $\boldsymbol{\beta}\left(T\right) = \boldsymbol{\beta}\left(T_{\rm launch}\right)$ for times $T > T_{\rm launch}$.

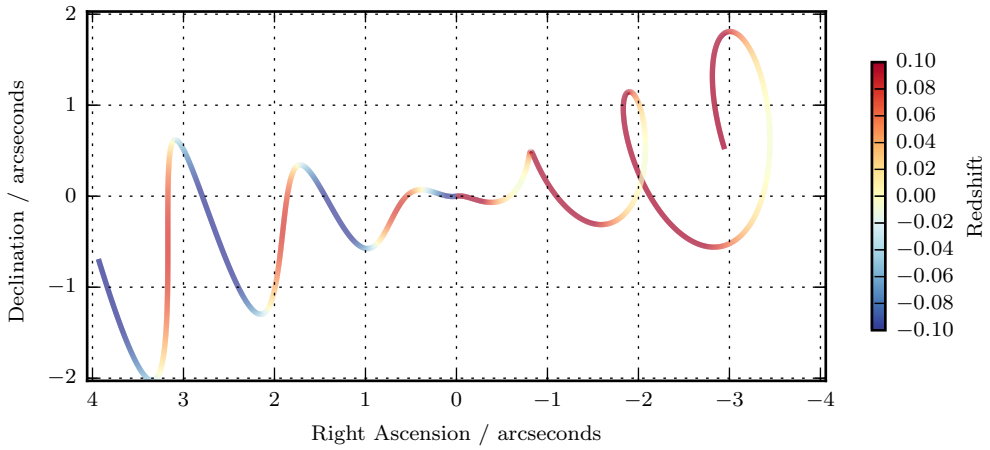


Figure 2.4: The loci of the jets as predicted by the kinematic model. Shown here are 3 complete precession periods, as seen when the jet is at zero-phase (i.e., the jet orientation is at its closest to the line of sight and a bolide launched at this epoch would be maximally blue-shifted, while its corresponding counterjet bolide would be maximally red-shifted). The apparent assymmetry between jet and counterjet that arises from the finite speed of light is clear. The colourscale shows the redshift associated with each point on the jet.

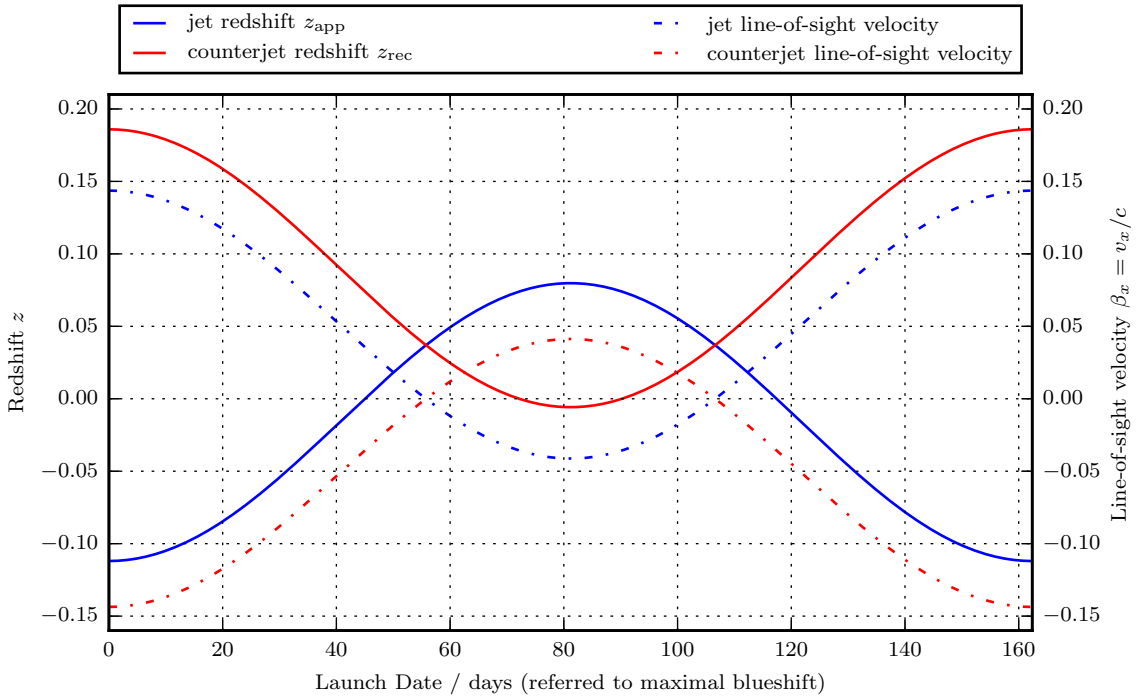


Figure 2.5: The predicted line-of-sight velocity components derived from the kinematic model (Equation A.11a) and their associated redshifts. The (eastern) jet and the (western) counterjet are plotted in blue and red respectively. Note the non-zero redshift when the jets are in the plane of the sky – this is the transverse doppler effect: $z_{\text{plane of sky}} = \gamma - 1$.

### 2.4.1 Best Fitting Parameter Values

The kinematic model well describes both the moving optical emission lines, and the characteristic corkscrew shape of the SS 433 jets, and a number of workers have performed fits to its basic parameters. In the simplest model, there are 7 parameters:

- the speed $\beta_0$;
- the cone opening angle $\Theta_0$;
- the precession phase parameters, namely precessional period $P_{\rm jet}$ and a reference epoch $T_{\rm ref}$ corresponding to zero phase;
- the jet cone orientation parameters, i.e., the angle $i_0$ between the jet cone axis and the line-of-sight, and the position angle $\chi_0$ of the jet cone axis as projected onto the plane of the sky;
- the distance $D$ to SS 433.

As can be seen from an inspection of Result 2.3.3 and Equation A.11a for the redshift $z$ and line-of-sight velocity $\beta_{\tilde{x}}$, neither position angle nor distance enter into the model when used to describe redshifts of the moving lines. Accordingly, some workers omit these and, somewhat confusingly refer to this as the 5 parameter model.

Note also that one should include the sense of the rotation (i.e., whether the jet precesses in a right or left handed sense). This can be given as $s_{\rm jet} = \pm 1$, corresponding to right and left handed rotations respectively, and where observationally SS 433's precession is in the left-handed, or negative sense (i.e., $s_{\rm jet} = -1$).[2]

The parameters that we will take as canonical throughout this work are presented in Table 2.1, together with their sources.

The majority of these values were obtained by Eikenberry et al. (2001) using fits to optical spectra over the first twenty years of observations of SS 433. It is worth noticing that, with an archive extending over multiple decades, the precision obtained by fits to optical spectra is much greater than that arising from fits to radio maps. Hence, the 5 parameters which appear in the model describing redshifts $\beta_0$, $\Theta_0$, $i_0$, $P_{\rm jet}$, and $T_{\rm ref}$ are known to much greater position than the position angle $\chi_0$, which comes only from the mean orientation of the radio maps.

[2] Of course, one can avoid introducing $s_{\rm jet}$ if one allows for a negative precession period!

| | | |
|---|---|---|
| $\beta$ | average bulk speed | $0.2647 \pm 0.0008$ |
| $P_{\rm jet}$ | precessional period | $(162.375 \pm 0.011)$ days |
| $T_{\rm ref}$ | reference epoch (see below) | MJD $(43563.23 \pm 0.11)$ |
| $\Theta$ | jet cone opening angle | $(20.92 \pm 0.08)^\circ$ |
| $i_0$ | angle between jet cone axis and line of sight | $(78.05 \pm 0.05)^\circ$ |
| $\chi_0$ | orientation of jet cone on the plane of the sky | $10 \pm 2^\circ$ |

Table 2.1: Best Fitting Kinematic Model Parameters. The values for $\beta$, $P_{\rm jet}$, $T_{\rm ref}$, $\Theta$, and $i_0$ are from Eikenberry et al. (2001). $\chi_0$ is taken from Hjellming and Johnston (1981). Care is needed to ensure the correct reference epoch is chosen for the phase convention. This is discussed further in Section 2.4.1.1.

#### 2.4.1.1 A note on conventions

There are a number of phase conventions in use in the literature, depending on whether one measures the jet precession from its closest point to the observer (maximal blueshift), its furthest point from the observer (maximal redshift), or measured from the plane of the sky. This directly affects the meaning of the reference epoch (Blundell and Bowler (2005)). For our purposes, it is important to note that the convention used by Eikenberry et al. (2001) (namely, zero-phase defined to be the point at which the jet passes through the plane of the sky going away from the observer) is different from the convention we use here (namely, the maximal blueshift convention). The conversion between these conventions is as follows.

$$\Rightarrow T_0 = T_{\rm Eik} - \frac{P_{\rm jet}}{2\pi} \arccos\left(-\cot\Theta_0 \cot i_0\right) \tag{2.36}$$

*Proof.* Let $T_{\rm Eik}$ be the reference epoch in the Eikenberry convention, and let $T_0$ be the reference epoch in the maximal blueshift convention used here. i.e., at $T_{\rm Eik}$, the jet is in the plane of the sky, with $\eta = \frac{\pi}{2}$, and at $T_0$, the jet is at phase 0. Inserting $\eta = \frac{\pi}{2}$ into Equation 2.20, we can find the precession phase in the maximal blueshift convention such that the jet lies in the plane of the sky:

$$\begin{aligned} \cos\eta &= \sin\Theta_0 \cos\Phi \sin i_0 + \cos\Theta_0 \cos i_0 = 0 \\ \Rightarrow \cos\Phi &= -\cot\Theta_0 \cot i_0 \\ \Rightarrow \Phi &= \pm \arccos\left(-\cot\Theta_0 \cot i_0\right) \end{aligned}$$

where $\Phi = -\frac{2\pi}{P_{\rm jet}}\left(T_{\rm Eik} - T_0\right)$ is the precession phase in the maximal blue shift convention at the Eikenberry reference epoch. The sign represents the fact that there are two crossings of the plane

of the sky. We take the positive sign for a crossing above the $\tilde{x}$-$\tilde{z}$ plane, and a negative one for a crossing below; in our case, we take the negative sign. Then,

$$-\frac{2\pi}{P_{\rm jet}}\left(T_{\rm Eik}-T_0\right) = -\arccos\left(-\cot\Theta_0\cot i_0\right)$$
$$\Rightarrow T_0 = T_{\rm Eik} - \frac{P_{\rm jet}}{2\pi}\arccos\left(-\cot\Theta_0\cot i_0\right)$$

□

## 2.5 Deviations from the Kinematic Model

The kinematic model provides a remarkably stable description of the average behaviour of the jets. It is not the complete picture. Careful analysis, particularly of the residuals between the observed redshifts and those predicted by the kinematic model reveal that there are other processes at work. We outline some of these briefly below.

### 2.5.1 Nodding

As well as the orbital periodicity $P_{\rm orb} = 13.1\,{\rm d}$ and the jet precession period $P_{\rm jet} = 162.375\,{\rm d}$, the system also displays a significant periodic behaviour at about 6 d, closely associated with the beat between the orbital and precessional periods. This was first reported by Newsom and Collins (1980). Subsequently, models were developed identifying this period as the nutation (nodding) of the jet due to small perturbations around its mean, driven motion in a slaved disc model (e.g., Katz et al. (1982), Matese and Whitmire (1982), Collins et al. (1981), Collins and Newsom (1986)).

In this work, we will adopt the formalism of Katz et al. (1982) and Vermeulen (1989). This approach considers small perturbations about the mean precessional motion of the jet. Hence, instead of describing the launch vector of the jet by a fixed cone opening angle $\Theta_0$ and a precession angle $\Phi$ advancing at a fixed precession rate, we suppose that the launch vector is described by two angles $\{\theta, \phi\}$ which are related to the mean motions by small corrections. i.e.,

$$\theta = \Theta_0 + \delta\theta = \Theta_0 + \varepsilon_\theta \cos 2\left(\psi - \phi\right) \tag{2.37a}$$
$$\phi = \bar{\phi} + \delta\phi \;\; = \bar{\phi} + \varepsilon_\phi \sin 2\left(\psi - \phi\right) \tag{2.37b}$$

where $\psi$ is the orbital phase of the companion, $\theta$ and $\phi$ are the jet cone opening angle and the precession angle (compare these to the use of polar coordinates in Figure 2.1), and the mean precessional motion is

$$\bar{\phi} = \Omega_{\rm pre} T + \phi_0 = s_{\rm rot} \frac{2\pi}{P_{\rm pre}} \left(T - T_{\rm ref}\right) \tag{2.38}$$

These are motivated mathematically by a slaved disc model. As formalised by Katz et al. (1982), the disc is modelled as a rigid, rapidly rotating ring, at an angle to the orbital plane, and sitting in the (time-dependent) gravitational potential of the orbiting companion. Tidal forces then cause the ring to precess and nutate like a spinning top. By linearising the equations of motion for this system, solutions of the above form are obtained (see Appendix A for a derivation using Lagrangian mechanics). Physically, it makes sense for the functional form to be related to twice the synodic period[3], since the force exerted by the point mass on the ring will be the same twice in each synodic period (e.g., the two occasions in each synodic period at which the companion mass is aligned with the line along which the ring intersects the orbital plane).

By inserting Equations A.12 into Equations A.11 and expanding up to leading order in the small quantities $\varepsilon_\theta$ and $\varepsilon_\phi$, we obtain linearised equations for the perturbed velocity. These can be written as $\boldsymbol{\beta} = \boldsymbol{\beta}^{(0)} + \boldsymbol{\beta}^{(1)}$, where the components of the mean motion $\boldsymbol{\beta}^{(0)}$ are given by Equations A.11, and the components of the linear perturbation term are:

$$\beta_{\tilde{x}}^{(1)} = A_{63} \cos\psi_{63} + A_{58} \cos\psi_{58} \tag{2.39a}$$

$$\beta_{\tilde{y}}^{(1)} = \frac{A_{63}}{\sin i_0} \left(\cos\chi_0 \sin\psi_{63} + \cos i_0 \sin\chi_0 \cos\psi_{63}\right) - \frac{A_{58}}{\sin i_0} \left(\cos\chi_0 \sin\psi_{58} - \cos i_0 \sin\chi_0 \cos\psi_{58}\right) \tag{2.39b}$$

$$\beta_{\tilde{z}}^{(1)} = \frac{A_{63}}{\sin i_0} \left(\sin\chi_0 \sin\psi_{63} - \cos i_0 \cos\chi_0 \cos\psi_{63}\right) - \frac{A_{58}}{\sin i_0} \left(\sin\chi_0 \sin\psi_{58} + \cos i_0 \cos\chi_0 \cos\psi_{58}\right) \tag{2.39c}$$

where $A_{58}$ and $A_{63}$ are the amplitudes of oscillations at 5.83 d and 6.28 d, and the nodding phases

Equations 2.39 are almost as given in Vermeulen (1989). Note the different conventions for position angles – Vermeulen uses the more orthodox convention of measuring counter-clockwise from North, where here we measure counter-clockwise from East, such that $\chi$ in Vermeulen's equations corresponds to $\frac{\pi}{2} + \chi_0$ in these equations. There is also an overall sign error in Vermeulen (1989),

[3]The synodic period is the time interval such that the companion and the inclined disc have the same angular relation between them, $P_{\rm syn} = 2\pi \,/\, \left(\omega_{\rm orb} - \Omega_{\rm pre}\right)$

which contradicts Katz et al. (1982); we agree with the Katz result. For reference, the perturbative expansion is given in Appendix A.

The slaved-precession model of Katz et al. (1982) actually predicts contributions at 3 periodicities, namely:

$$5.83\,\mathrm{d} \equiv \frac{2\pi}{2\omega_{\mathrm{orb}} + 3\,|\omega_{\mathrm{pre}}|}$$
$$6.06\,\mathrm{d} \equiv \frac{2\pi}{2\omega_{\mathrm{orb}} + 2\,|\omega_{\mathrm{pre}}|}$$
$$6.28\,\mathrm{d} \equiv \frac{2\pi}{2\omega_{\mathrm{orb}} + |\omega_{\mathrm{pre}}|}\,,$$

where we note that $\omega_{\mathrm{orb}}$ and $\omega_{\mathrm{pre}}$ evolve in counter-clockwise and clockwise senses respectively, and hence have opposite signs. The true, physical variation is at 6.06 d, but the superposition of this onto the 162 d precession leads to the two offset periodicities. The amplitudes predicted by the Katz et al. (1982) model are not in agreement with observations: they predict that the variation at 6.28 d should be the largest term, with no significant variation at 5.83 d. In fact, their fits to the Kinematic Model residuals find no significant contribution at 6.06 d, with significant spectral power at 5.83 d. The same result is seen by Blundell and Bowler (2005). Importantly, their analysis of the power spectra of the sums and differences of the jet and counterjet redshifts confirm that the nutation is purely the result of changes in angle; there is *no* associated variation in the jet launch speed.

It should be noted, that no model has yet successfully predicted the amplitudes of the various nutational components. If this could be done, it would provide a powerful insight into the dynamics and structure of the accretion disc.

In Figure 2.6, we show the effect of this nutational motion on the cone opening angle and on the precession angle, as well as showing the resulting line-of-sight velocity components.

### 2.5.2 Decay of precession period

In early observations of the precession of the SS 433 jets, several workers (e.g. Collins and Newsom (1980), Margon et al. (1981)) found tentative evidence for a substantial decay term in the precessional period, with values of $\dot{P}_{\mathrm{jet}}$ possibly as large as $10^{-2}$ (that is, a decay time as short as perhaps 100 precession periods, or 40-50 years). This term was included phenomenologically in

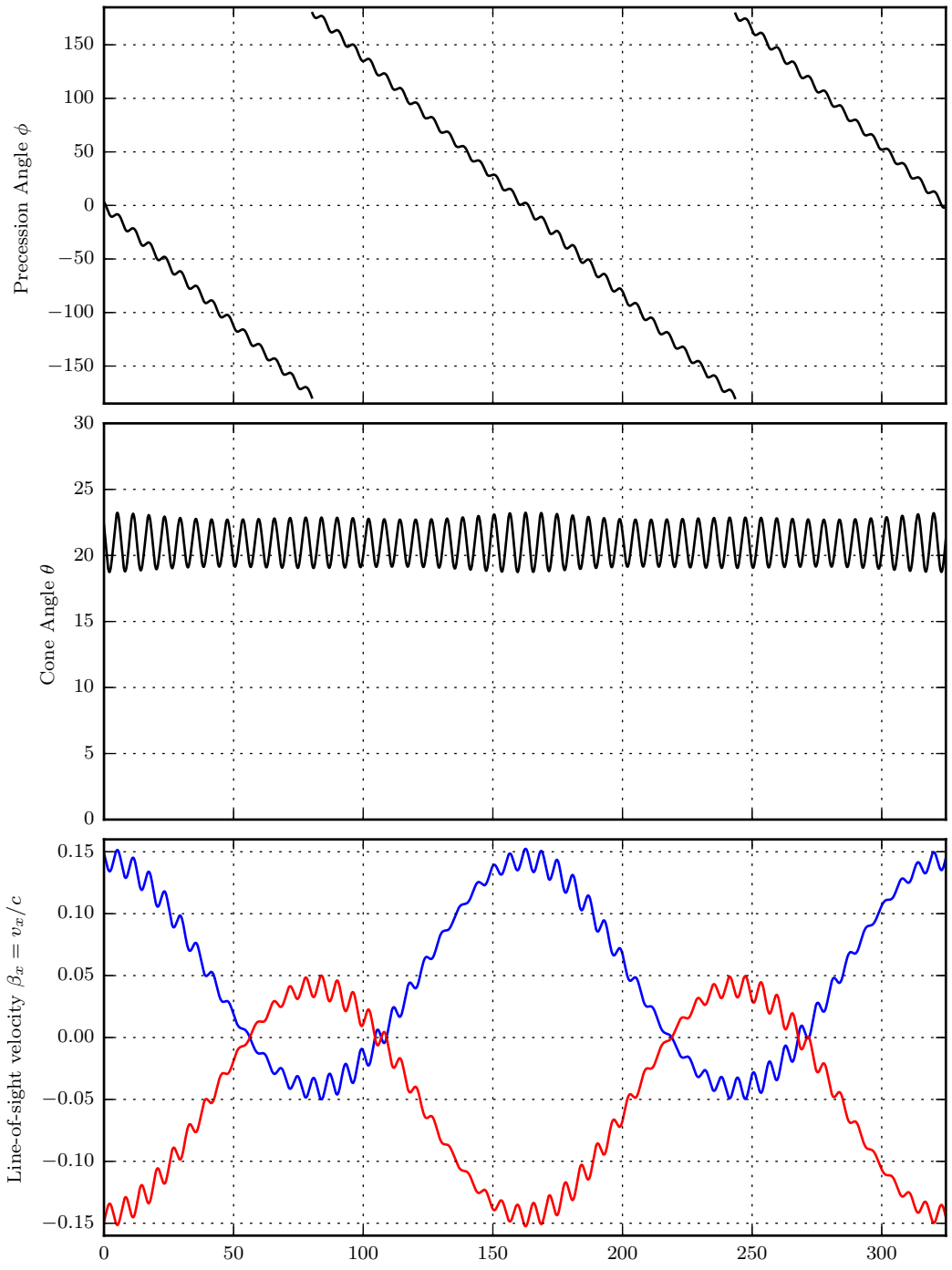


Figure 2.6: Nutation effects over 2 precession periods from point of zero-phase on 2011-10-13. (a) precession angle, i.e., azimuthal angle measured counter-clockwise from the point of maximal blueshift; (b) cone opening angle; and (c) line-of-sight velocity components for the jet (blue) and counterjet (red).

the precession models of Katz et al. (1982) and Newsom and Collins (1986). As the time baseline of observations of the jet lines grew, the limit on any long-term secular evolution could be brought down further. Anderson et al. (1983) concluded that, rather than a steady decay, the variation was either oscillatory (i.e., a constant, non-zero second derivative, $\ddot{P}_{\rm jet}$), or the result of random variations, while studies of the accumulated spectroscopy after 10 years (Margon and Anderson (1989)) and 20 years (Eikenberry et al. (2001)) found the data to be consistent with both $\dot{P}_{\rm jet} = 0$ and $\ddot{P}_{\rm jet} = 0$. Instead, the apparent variations were explained as being due to stochastic variations (Fabrika (2004)) in the properties of the precession cycle, which take place on timescales of up to a few months, and after which the system returns to its average behaviour.

Eikenberry et al. (2001) placed an upper limit on the rate of precessional decay at $\dot{P}_{\rm jet} < 5 \times 10^{-5}$ corresponding to a decay timescale on the order of 10,000 years. It is intriguing to note that, while this is a long timescale compared to the few decades over which we have observed this object, it is not long compared to the age of the W50 remnant.

### 2.5.3 Stochastic variations, flares, and other

The slaved nutation and the possiblity of a non-zero time-derivative of the precession period described in the previous two subsections are both deviations from the Kinematic Model that are deterministic (i.e., non-random) in character. There is evidence that the jets also display random or stochastic variability in both their launch speeds and in the orientation of the launch vector. In optical spectra, Katz and Piran (1982) and Margon and Anderson (1989) saw deviations of redshifts from the model predictions at a statistically significant level, and argued that these were due to variations in the pointing angle only. More recent work (Blundell and Bowler (2005)) has shown that random, uncorrelated variations in the cone opening angle, precession phase angle, and speed are indistinguishable from variations in the angles only. Indeed, using both fits to the arcsecond scale radio jets (Blundell and Bowler (2004)) and determinations of the speed in optical spectra (Blundell and Bowler (2005)), they show that there must be deviations in speed from the mean value of $\beta_0 c = 0.26c$ by as much as $\pm 0.06c$. Furthermore, these variations appear to be anticorrelated with the jet cone opening angle – i.e., faster ejections are launched at a smaller angle to the axis of the precession cone than slow ejections.

The other quasi-random variability is associated with flaring activity. Blundell et al. (2011) observed SS 433 in the optical and radio in the weeks leading up to and including a large flare.

Preceding the flare, the optical jet speed is observed to decline, while during the massive ejection associated with the flare itself possesses an elevated speed. We will return to this behaviour at greater length in Chapter 4.

Lastly, we note that the analysis of jet speeds from the red- and blueshifts of hydrogen lines by Blundell and Bowler (2005) showed clear evidence for a variation in speed (but not in launch pointing angle) with the 13.08 d orbital period – giving further evidence in support of an eccentric orbit (1.5.2).

## 2.6 The origin of the precessional motion

There is a general consensus that the physics underlying the precessional motion in SS 433 (and other microquasars) are due to tidal forcing of an accretion disc that is inclined at an angle to the orbital plane of the binary system Katz (1973). The tidal gradients of the gravitational potential from the companion star across the disc work to reduce the inclination of the disc with respect to the orbital plane. The gyroscopic stability of the rapidly rotating disc acts to preserve its inclination. These combine to give a stable retrograde precession. This is the basis of the slaved disc model of Whitmire and Matese (1980).

As applied to a simple model consisting of a rapidly rotating ring in the time varying potential of the companion star (Katz et al. (1982)), we have already seen that this model is semi-successful in predicting the relationships between the orbital and precessional motions and the nodding perturbation. It is not, however, able to accurately predict the amplitudes of these perturbations, or to predict a value for the periodicity of the 163 d precessional motion.

The validity of approximating a fluid, possibly thick, accretion disc by a thin, rigid ring is also open to question. Several workers have applied the same basic physics to more complex models. For instance, the dynamical models of Collins and Newsom (1986) and Collins and Scher (2002) relax the requirement that the precession be due to a ring, considering geometrically thick, but still rigid, bodies, though their treatment seems more applicable to the case where the compact object is a neutron star, rather than a black hole.

More interesting is the role of fluid mechanics in these models, which several workers have shown to have complex effects. Here, the single inclined ring is replaced by a tilted (Charles et al. (2008)) or a warped accretion disc, which can similarly precess. In particular, Papaloizou and

Pringle (1983) demonstrate that the presence of viscosity (or equivalently, the precence of radial communication between concentric, Keplerian rings) tends to flatten warped or inclined accretion discs, while Ogilvie and Dubus (2001) show that this can be counteracted by radiation pressure, which can maintain a stable warp and a stable precession rate. However, Begelman et al. (2006) argue that these warps lie at radii much greater than the inner radius of the accretion disc, raising questions about how nutational and precessional motions are communicated to the jets, which must be launched from close to the black hole. The precession in these pictures can also be seen as a wave-like propagation of a distortion in the shape of the disc (e.g., Papaloizou and Terquem (1995) and Terquem (1998)). Thus far, however, these have not been used to explain the second order nodding motion described by Katz et al. (1982).

Non-disc based precession models are generally discounted. For instance, Whitmire and Matese (1980) argue that the compact object itself cannot be the cause of the precession – they argue that both Lens-Thirring precession (an effect arising from the dragging of space-time in the Kerr metric around a rotating black hole) and driven precession of the black hole would predict too slow a precession rate.

In summary, though more complicated models provide a more faithful and complete physical picture, they are unable to add much beyond the simple physical picture of Katz et al. (1982). The general picture of a slaved disc precessing under tidal forcing from the companion remains the most likely explanation.

## 2.7 Summary

In this Chapter, we have reviewed the Kinematic Model describing precessing, relativistic jets, outlining both the geometry and the observational signatures of the problem in terms of proper motions and redshifts. We have briefly discussed the underlying physics, using the Katz et al. (1982) prescription to explore the nodding motions, and discussing some of the elements of tidal mechanics and fluid dynamics that can feed into a description of the precession phenomenon.

In the coming Chapters, we will expand this machinery to allow us to use radio maps to fully determine the velocity vectors of the jet and counterjet.

# Chapter 3

# VLBA Observations of SS 433

## 3.1 Introduction

Our ability to make images of small or distant astrophysical objects is, ultimately, limited by the wave nature of light and the corresponding diffraction limit. This prevents us from resolving structures with an angular size less than $\vartheta \sim \lambda/d$, where $d$ is the size of our instrument's aperture, and $\lambda$ is the observing wavelength. When making observations at radio frequencies, $\lambda$ is large (at 1.6 GHz, $\lambda = 18$ cm), so we need a huge aperture to obtain the resolution needed. If we wish to make images with 10 milliarcsecond resolution at this frequency, we would need an aperture with a size of almost 4000 km. Constructing a single such telescope is obviously impractical. However, the techniques of *aperture synthesis* allow us to create an effective aperture of this size by correlating signals from distant antennas.

In this Chapter, we present new images of SS 433 from observations with the Very Long Baseline Array (VLBA) in 2011-12. We will first give a brief overview of the principles of Very Long Baseline Interferometry (VLBI), before summarising the reduction process used for calibrating the data and making images in AIPS (the Astronomical Image Processing System; Greisen (2003)).

This discussion closely follows that given in Taylor et al. (1999) (especially chapters 1, 2, 5, and 22), and in the AIPS Cookbook (NRAO (1990); in particular chapter 9 and appendix C), to which the reader is directed for more details.

## 3.2 Principles of long-baseline radio interferometry

### 3.2.1 Visibilities

To make images of the sky, our aim is to determine the values of the sky brightness distribution, $I_\nu(\boldsymbol{s})$, at points on the celestial sphere denoted by the unit vector $\boldsymbol{s}$. The brightness distribution is also known as the specific intensity or the spectral radiance; its S.I. units are $\mathrm{W\,m^{-2}\,Hz^{-1}\,sr^{-1}}$.

Consider two detectors, separated by a distance vector $\boldsymbol{b}$ (the *baseline*). Consider a ray coming from the point on the distant celestial sphere whose direction is given by the unit vector $\boldsymbol{s}$.[1] This will induce a voltage at each detector. However, distance the ray must travel to reach the two detectors will be different: consequently, there is a phase shift of $2\pi(\boldsymbol{b}\cdot\boldsymbol{s})/\lambda$ between the voltage responses at the two detectors. Let us denote the voltage responses at the two detectors due only to the rays from $\boldsymbol{s}$ by $V_1(t;\boldsymbol{s}) = v(\boldsymbol{s})\,\mathrm{e}^{2\pi i\,\nu t}\mathrm{e}^{2\pi i\,(\boldsymbol{b}\cdot\boldsymbol{s})/\lambda}$ and $V_2(t;\boldsymbol{s}) = v(\boldsymbol{s})\,\mathrm{e}^{2\pi i\,\nu t}$. We will adopt the complex exponential notation for convenience – this allows us to omit several details regarding the practical operation of the (complex) correlator.

How do these relate to the sky brightness at $\boldsymbol{s}$? The brightness is the power per unit frequency per unit unit effective collecting area per unit solid angle. The square of the voltage at each detector is proportional to the power received. Hence,

$$|v(\boldsymbol{s})|^2 \propto \text{power received} \equiv I_\nu(\boldsymbol{s})\,A(\boldsymbol{s})\,\Delta\nu\,\mathrm{d}\Omega\,, \tag{3.1}$$

where $A(\boldsymbol{s})$ is the effective collecting area of the antenna (this will combine both the projected area $\boldsymbol{A}\cdot\boldsymbol{s}$ and the response of the detector as a function of angle – this is also referred to as the *primary beam*), $\Delta\nu$ is the bandwidth of the detector, and $\mathrm{d}\Omega$ is the small area of solid angle about the vector $\boldsymbol{s}$.

Now let's correlate the two signals. This involves taking the time average of the product of the

[1] This can of course be described in terms of two angles, e.g., polar coordinate $\{\theta,\phi\}$, or Right Ascension and Declination.

two voltages. The response $\mathrm{d}\mathcal{R}$ due to emission from $\boldsymbol{s}$ is

$$\mathrm{d}\mathcal{R}\left(\boldsymbol{b};\boldsymbol{s}\right) = \left\langle V_1^*\left(t;\boldsymbol{s}\right) \times V_2\left(t;\boldsymbol{s}\right)\right\rangle \tag{3.2}$$

$$= \left|v\left(\boldsymbol{s}\right)\right|^2 \mathrm{e}^{-2\pi i\left(\boldsymbol{b}\cdot\boldsymbol{s}\right)/\lambda} \tag{3.3}$$

$$\propto I_\nu\left(\boldsymbol{s}\right) A\left(\boldsymbol{s}\right) \mathrm{e}^{-2\pi i\left(\boldsymbol{b}\cdot\boldsymbol{s}\right)/\lambda}\, \Delta\nu\, \mathrm{d}\Omega \tag{3.4}$$

where the asterisk denotes a complex conjugate, and $\left\langle f\left(t\right)\right\rangle := \frac{1}{T}\int_0^T \mathrm{d}t\, f\left(t\right)$, and we have used Equation 3.1 in the last line. To obtain the total response of the correlator for the two antennas separated by $\boldsymbol{b}$, we must now integrate over all solid angles (i.e., over all directions, $\boldsymbol{s}$), obtaining:

$$\mathcal{R}\left(\boldsymbol{b}\right) \propto \Delta\nu \int_\Omega \mathrm{d}\Omega\, I_\nu\left(\boldsymbol{s}\right) A\left(\boldsymbol{s}\right) \mathrm{e}^{-2\pi i\left(\boldsymbol{b}\cdot\boldsymbol{s}\right)/\lambda}\,. \tag{3.5}$$

(Note that we have omitted a subtlety: this integration can only be performed if the sky brightness distribution is spatially incoherent.)

Let's turn our generic detectors into antennas by developing the ideas of the effective collecting area and the antenna response. In practice, the antenna response will have a central peak and sidelobes. We will make observations by pointing our antennas (i.e., the central peak of the antenna response) at the object we wish to observe, and then keeping the antennas tracking this point by rotating them as the Earth turns beneath them. To represent this, let's define the *pointing centre*, $\boldsymbol{s}_0$ as a fixed point on the celestial sphere, with $\boldsymbol{b}$ as the time dependent baseline. Let some arbitrary other point on the sky be referred to the pointing centre by $\boldsymbol{s} = \boldsymbol{s}_0 + \boldsymbol{\sigma}$. Then, $\boldsymbol{\sigma}$ can replace $\boldsymbol{s}$ as our coordinates to describe $I_\nu$, and we introduce the normalised response of the detector, $\mathcal{A}\left(\boldsymbol{\sigma}\right) := A\left(\boldsymbol{\sigma}\right)/A_0$, where $A\left(\boldsymbol{\sigma}\right)$ is the effective collecting area of the antenna as introduced previously, and we normalise it to its value at the beam (pointing) centre $\boldsymbol{\sigma} = 0$. Then, we can rewrite the total correlator response (Equation 3.5) as:

$$\mathcal{R}\left(\boldsymbol{b};\boldsymbol{s}_0\right) \propto \mathrm{e}^{-2\pi i\left(\boldsymbol{b}\cdot\boldsymbol{s}_0\right)/\lambda}\, A_0\, \Delta\nu \int_\Omega \mathrm{d}\Omega\, I_\nu\left(\boldsymbol{\sigma}\right) \mathcal{A}\left(\boldsymbol{\sigma}\right) \mathrm{e}^{-2\pi i\left(\boldsymbol{b}\cdot\boldsymbol{\sigma}\right)/\lambda} \tag{3.6}$$

and hence, we define the *complex visibility*:

$$\mathcal{V}_\nu\left(\boldsymbol{b}\right) := \int_\Omega \mathrm{d}\Omega\, I_\nu\left(\boldsymbol{\sigma}\right) \mathcal{A}\left(\boldsymbol{\sigma}\right) \mathrm{e}^{-2\pi i\left(\boldsymbol{b}\cdot\boldsymbol{\sigma}\right)/\lambda} \tag{3.7}$$

such that $\mathcal{R}\left(\boldsymbol{b};\boldsymbol{s}_0\right) \propto \mathrm{e}^{-2\pi i\left(\boldsymbol{b}\cdot\boldsymbol{s}_0\right)/\lambda}\, A_0\, \Delta\nu\, \mathcal{V}_\nu\left(\boldsymbol{b}\right)$.

### 3.2.2 The Fourier inversion & incomplete sampling

We now show that under certain approximations, this can be reduced to the Fourier transform of the sky brightness distribution. Following Clark (1999), we consider the case where we only observe a small region of the sky – i.e., $|\boldsymbol{\sigma}| \ll 1$. In this case, we can make a local approximation of the celestial sphere as a flat plane. Then, we introduce a coordinate system such that $\boldsymbol{s}_0 := (0, 0, 1)$ and $\boldsymbol{\sigma} := (l, m, 0)$, where $\{l, m\}$ are direction cosines, and $\mathrm{d}\Omega = \mathrm{d}l\,\mathrm{d}m$. Letting $\boldsymbol{b} = \lambda\,(u, v, w)$ in this coordinate system, we can write the visibility as:

$$\mathcal{V}_\nu\,(u, v) = \iint \mathrm{d}l\,\mathrm{d}m\, I_\nu\,(l, m)\,\mathcal{A}\,(l, m)\,\mathrm{e}^{-2\pi i\,(ul+vm)}\,. \tag{3.8}$$

This is just a 2-dimensional Fourier transform, which can be inverted in principle to obtain the sky brightness distribution:

$$I_\nu\,(l, m)\,\mathcal{A}\,(l, m) = \iint \mathrm{d}u\,\mathrm{d}v\,\mathcal{V}_\nu\,(u, v)\,\mathrm{e}^{2\pi i\,(ul+vm)}\,. \tag{3.9}$$

The $u$-$v$ plane is referred to as the Fourier plane.

In practice, we don't have complete sampling of the $u$-$v$ plane. We have some finite number of antennas ($N = 10$, for the VLBA), giving a finite number of baselines $\boldsymbol{b}_{ij}$ (i.e., $N\,(N-1)\,/2$ baselines), sampled for a finite time. As we have already noted, the Earth's rotation means that, in the reference $(u, v, w)$ frame described above, the baselines are time dependent. This allows us to fill out more of the $u$-$v$ plane. However, we still only obtain finite samples of $\mathcal{V}_\nu$. We can represent this by a multiplying the visibility function by a sampling function $S\,(u, v)$ to obtain the sampled visibility function $\hat{\mathcal{V}}_\nu$. The Fourier transform of this sampled visibility function is the *dirty image*. As it is the Fourier transform of a product, the convolution theorem tells us that it can be written as the convolution of the two Fourier transforms. i.e., as the true sky brightness distribution convolved with the Fourier transform of the sampling function (the *dirty beam*). The art of radio imaging lies in deconvolving these two functions.

## 3.3 Imaging VLBA data in AIPS

### 3.3.1 Calibration

The correlator outputs a time series $\mathcal{R}_{ij}(t)$ for each baseline, representing the evolution traced by each baseline vector $\boldsymbol{b}(t)$. From this, we can extract the observed visiblities $\tilde{\mathcal{V}}_{ij}(t)$ for each baseline as a function of time. In principle, these should be smooth, complex functions of $t$. However, atmospheric, geometric, and instrumental uncertainties introduce errors into the observed visibilities. These errors can be represented by a baseline-dependent complex factor $\mathcal{G}_{ij}(t)$ (referred to as the *gain*), such that:

$$\tilde{\mathcal{V}}_{ij}(t) = \mathcal{G}_{ij}(t)\,\mathcal{V}_{ij}(t) + \text{random noise} \tag{3.10}$$

where $\mathcal{V}_{ij}(t)$ is the true visibility.

For calibration purposes, $\mathcal{G}_{ij}(t)$ can be divided into antenna-based amplitude and phase errors, and residual baseline based errors. The calibration procedures aim to determine these values.

There are also, often, bad data that cannot be calibrated (e.g., due to radio frequency interference (RFI) or issues at low elevations). These must be "flagged" and removed from the data set. AIPS includes several tasks (e.g., `WIPER` and `TVFLG`) to do this interactively. Data should be flagged where, for example, there are large deviations or dicontinuities in amplitude as a function of time along each baseline, or clear discontinuities between different frequency bands. We have also found it necessary to flag data at low elevations (15° was generally sufficient), and at the start and end of scans (the task `QUACK` enables this). However, this process is highly iterative – often, a data set will need to be flagged on more than one occasion throughout the calibration procedure.

The calibration recipe for VLBA data is set out in Appendix C of the AIPS CookBook (NRAO (1990)). There are several steps:

1. *a priori* geometric calibration, to correct errors in the model of the Earth's orientation (procedure `VLBAEOPS`) and path length differences introduced by the ionosphere (procedure `VLBATECR`);

2. *a priori* amplitude calibration, using system temperatures to correct each antenna (procedure `VLBACALA`);

3. bandpass calibration, using a bright reference source to remove degradation of amplitude at the edge of each IF due to finite bandwidth (task `BPASS`);

4. *a priori* phase calibrations, correcting for the orientation of the antennas (procedure `VLBAPANG`) and instrument phase delays (procedure `VLBAPCOR`);

5. fringe-fitting and phase calibration (see below); and finally

6. apply calibrations from reference source to the science data.

For VLBI, phase calibration is done using a phase reference source. This is a strong, scarcely resolved reference source close to the faint science target. Errors in the phase calibration appear as slopes along the frequency axis and with time, as well as an antenna-dependent phase residual. The phase reference source is used to calculate the corrections needed to remove each of these errors; these are then interpolated to apply the corrections to the weaker science target (see Cotton (1995)). This is done using the procedure `VLBAFRGP`.

### 3.3.2 Deconvolution & imaging

After these calibration steps the corrections are applied to the science target (task `SPLIT`), and the source is imaged. This is done using the AIPS task `IMAGR`, which uses the Cotton-Schwab CLEAN algorithm (Schwab (1984)) to deconvolve the dirty beam from the dirty image. This is described in Cornwell et al. (1999).

The key to the CLEAN algorithm is to consider the dirty image as the sum of many point sources, each convolved with the dirty beam. CLEAN then works by identifying the brightest points in the image plane, subtracting off some fraction of the dirty beam from that point (thereby removing the sidelobes associated with that point), iterating until some termination criterion (e.g., the noise level is reached), and then restoring a Gaussian *clean beam* to each point from which a clean component was previously subtracted.

It is also necessary at this point to perform hybrid imaging and self-calibration. In this process, the image generated from the visibility data is used as a model to improve the calibration of the visibility data. A new, improved image is then made, and the process repeated. This is performed using the AIPS task `CALIB`.

## 3.4 2011-12 Observations

SS 433 was observed with the VLBA on several occasions during 2011 and 2012. Images are shown here from 2011-Nov-05 (MJD 55871.0; Figure 3.1), 2011-Dec-24 (MJD 55919.83; Figure 3.2), 2012-Jan-28 (MJD 55954.75; Figure 3.3), and 2012-Sept-07 (MJD 56177.13; Figure 3.4).

These were *L*-Band observations at 1.6 GHz, giving a beam size of approximately 10 mas × 5 mas. The low frequency end of the band was grossly affected by radio frequency interference (RFI) and flagged. This gave us 6 contiguously spaced IFs of 16 MHz. After *a priori* amplitude and bandpass calibration, and fringe fitting to calibrate phase, these IFs were averaged down to a single channel, giving an image of the continuum for each epoch.

**Multi-scale CLEAN** The data were flagged, calibrated, and imaged using standard routines in the AIPS software package, following the recipes in Appendix C of the AIPS Cookbook (NRAO (1990)) as outlined above.

Each 11 hour observation consisted of alternating 7 minute scans of SS 433, and 2 minute scans of the phase calibrator J1929+0507 (4° from the science target). The source rises and sets at different times at each antenna, and it was found that the images were improved by using only the middle 8 hours of each epoch, when the array coverage is fullest. To handle the complex, extended structure present in the jets, we found it to be essential to use the multi-scale implementation of CLEAN available within the AIPS task `IMAGR` (Greisen et al. (2009)). We found the greatest success when using 2 CLEAN scales, at 1 and 5 times the beam size. Equally importantly, we used CLEAN boxes to restrict the algorithm only to areas of real emission – this was necessary to reveal the complex diffuse matter surrounding the core.

**Self-calibration** It was found that self-calibration was necessary to produce maps of the system. Many repeated iterations were needed to achieve a reasonable solution – typically $> 15$ manual phase calibration iterations, with one final amplitude and phase iteration at the end. At the $n^{\text{th}}$ iteration, the $n-1^{\text{th}}$ iteration calibrated data were used to generate a new model, which was then used to calibrate the un-selfcalibrated $0^{\text{th}}$ order data set. In the early iterations, large solution intervals (set to the full length of a scan) were used, while the AIPS adverb `UVRANGE` was used to down-weight the short baselines (typically, starting at a minimum baseline length of 10 mega$\lambda$, with `WTUV = 0.2`). We also limited the number of CLEAN components subtracted quite severely

in the early iterations, though this was soon relaxed. As the number of failed solutions reduced and the model improved, this was cutoff was slowly brought down.

With these, good images were achieved for the first and third epochs, and satisfactory solutions for the others. However, in no case did we achieve thermal-noise limited images; such is the difficulty of imaging a complex and varying structure.

**Time variability within the source** A significant challenge in imaging arises because of time variation in SS 433, and especially from the motion of the jet bolides during the course of the observations. With the sparse sampling of the Fourier plane given by an array with only ten antennas, we would like as long an observation as possible to improve our visibility sampling and hence our image quality. The length of these observations give us sufficient signal-to-noise to image the expanded jet bolides over an extended period after launch (up to 50 d). But, with proper motions of $\sim 8\,\mathrm{mas\,d^{-1}}$ and observations lasting almost half a day, the bolides move by almost a full beam in the course of the observations, violating the assumptions underlying the use of the Fourier transform in synthesis imaging. This is the principal cause of the spurious signals North and South of the main jet axis.

Attempts to mitigate this by imaging subsections of the full scan were only partially successful. The problem is most acute around the brightest and most compact points on the map. This is especially apparent in the 2011-Dec-24 epoch (Figure 3.2).

We divided each epoch into subscans of 2 hours. Then we used `IMAGR` to CLEAN the brightest, most compact points around the inner regions. These provided a model which was subtracted from the UV data file for the subscan with AIPS task `UVSUB`. The task `DBCON` was used to recombine the residual data sets, which we then subjected to a deep CLEAN to image more extended matter, both around the core and along the jet, and then to several self-calibration and hybrid imaging iterations. Finally, the model subtracted from the middle 2 hours was restored to the calibrated background data set. Ultimately, however, this failed to make a significant improvement to the resulting image. It was most helpful in allowing us to prepare CLEAN boxes around the more extended flux – but otherwise the images produced using the method above were no better than those produced using the same CLEAN boxes on the complete data set.

The solution to the problem of imaging a varying source (whether in amplitude or in structure) in interferometry remains unclear. Nonetheless, the images we obtained are of sufficient quality for

us to determine the locations of the jet bolides securely. In each figure, the lowest contour level is set at $\gtrsim 5\sigma$, where $\sigma$ is the rms background noise away from the artefacts north and south of the jet. Accordingly, we are able to confidently locate even the faint outer bolides in the third epoch.

**Other remarks** We experimented with different weighting schemes in `IMAGR` (using the adverb `ROBUST`). This is an implementation of the Briggs (1995) weighting scheme. The effects here were small, though we used `ROBUST = -1`, together with the Gaussian function provided by `UVBXFN = 4`, which calculates weights within the gridded visibilities with respect to neighbouring cells (A.J. Mioduszewski, private communication).

Ultimately, these made little systematic difference – the main source of error remains that introduced by time variation, and the resulting difficulties introduced in the calibration procedure.

## 3.5 Remarks on the images and the circumbinary ruff

Although in none of the epochs do we achieve thermal noise limited images, these maps still give new insights into this remarkable system. Most importantly, the maps from 2011-Dec-24 and 2012-Jan-28 are sufficiently closely spaced in time that the same ejecta can be seen in both maps. This will form the subject of the discussion in the next Chapter. We can also see in 2012-Jan-28 map the remarkable degree to which the ejecta have expanded in the 35 d between these two epochs. We will return to this in Chapter 5.

The data from 2011-Nov-06 and 2012-Jan-28 produce the best of the images here. In these two epochs, the extended equatorial emission (the circumbinary ruff) that is identified in the maps of Paragi et al. (1999) and Blundell et al. (2001) can be seen clearly. The evolution of this ruff can provide an important probe of the dynamics of the inner binary system (Doolin and Blundell (2011)). From previous observations of this ruff (notably the 2003 VLBA movie of Mioduszewski et al. (2004), which we will discuss in later chapters (see Figure 4.2)), Doolin and Blundell (2009) estimated a ruff precession period of 552.5 d, a mean position angle of 2° east of north, an amplitude of 34.5°, and a reference date (i.e., zero-phase) of MJD 52620. Their fits, however, are not particularly well constrained – the 2003 data they use only sample a small part of the precession cycle. From Figures 3.1 and 3.3, we can estimate angles of the precessing ruff. These are shown in Figure 3.5. That these new data points do not lie on the predicted curve

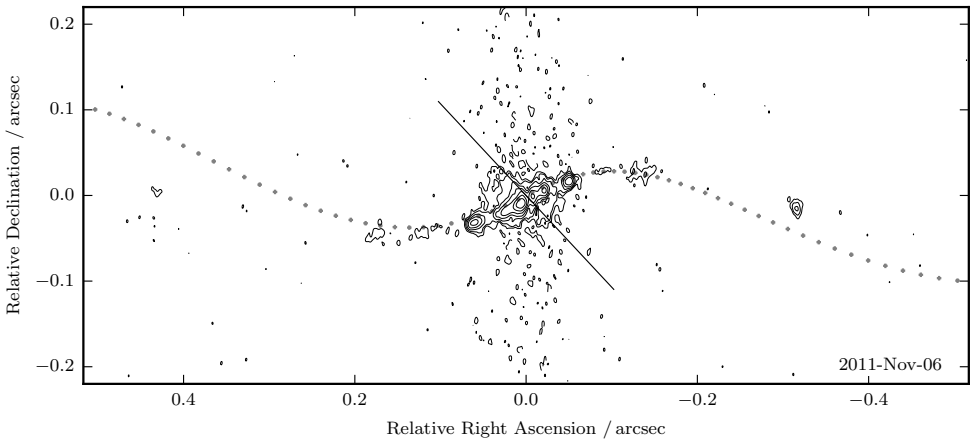


Figure 3.1: 1.6 GHz VLBA image of SS 433 from 2011-Nov-06. Contour levels are at $2^n \times 0.22\,\mathrm{mJy\,beam^{-1}}$. The kinematic model trace (grey dots) is shown, as is the approximate angle of the circumbinary ruff (43° east of north).

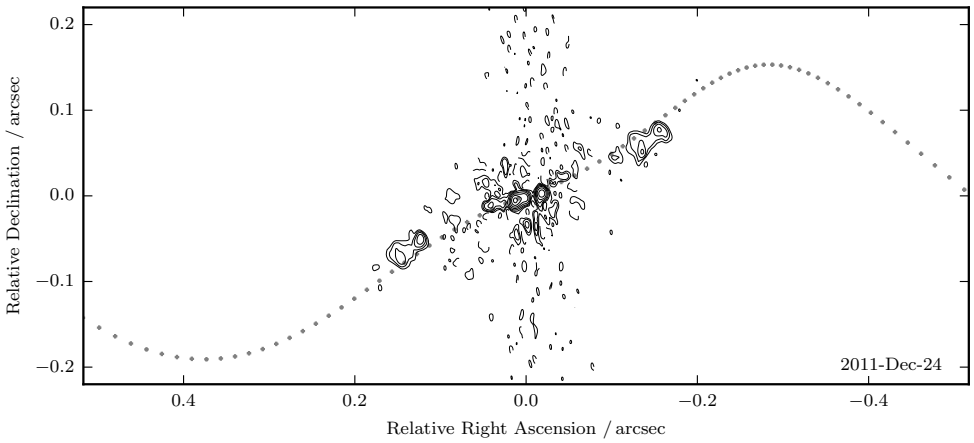


Figure 3.2: 1.6 GHz VLBA image of SS 433 from 2011-Dec-24. Contour levels are at $2^n \times 2.2\,\mathrm{mJy\,beam^{-1}}$. The kinematic model trace (grey dots) is shown.

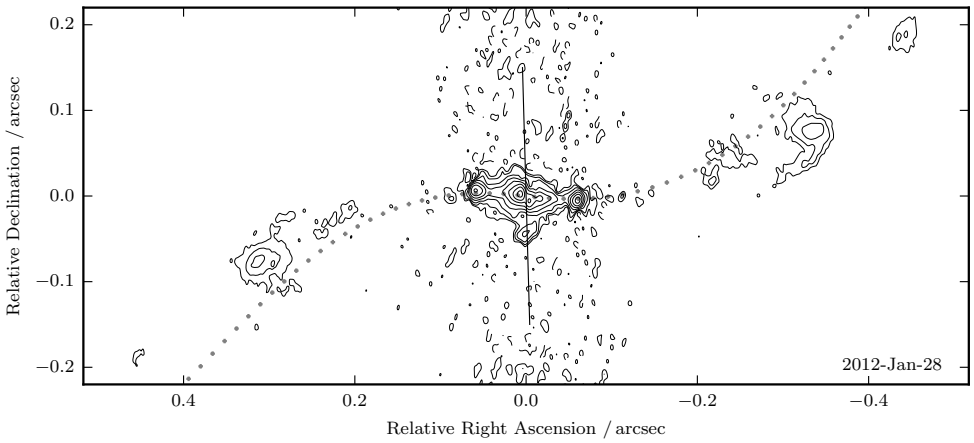


Figure 3.3: 1.6 GHz VLBA image of SS 433 from 2012-Jan-28. Contour levels are at $2^n \times 0.22\,\mathrm{mJy\,beam^{-1}}$. The kinematic model trace (grey dots) is shown, as is the approximate angle of the circumbinary ruff (1° east of north).

suggests that the Doolin and Blundell (2009) values may overestimate the period by perhaps 5% (tentatively, 525 d seems to give a reasonable fit), and underestimate the amplitude by perhaps 10°. It is unfortunate that the data in the other epochs are not sufficiently well behaved to provide additional constraints for this fit.

## 3.6 Summary

We have outlined the principles of radio interferometry and the methods for reducing VLBI data. We have presented 4 new maps of SS 433, two of which (2011-Dec-24 and 2012-Jan-28) are sufficiently close in time that the same ejecta can be resolved in both epochs. In the coming Chapters, we will examine some of the scientific results that can be extracted from these two maps.

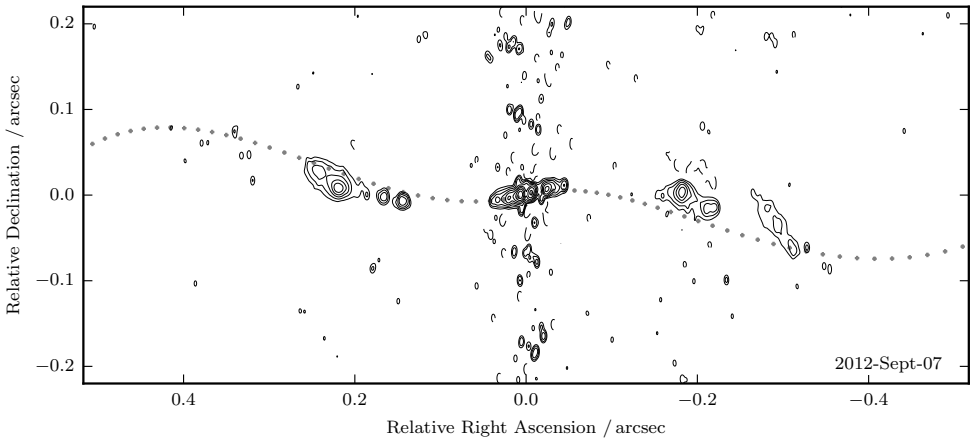


Figure 3.4: 1.6 GHz VLBA image of SS 433 from 2012-Sept-07. Contour levels are at $2^n \times 0.22\,\mathrm{mJy\,beam^{-1}}$. The kinematic model trace (grey dots) is shown.

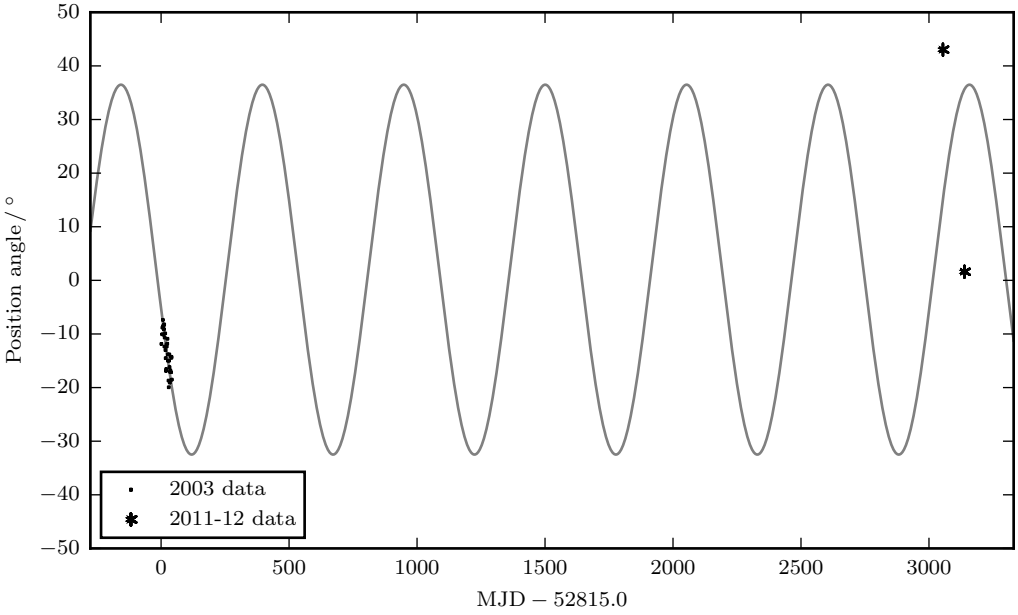


Figure 3.5: The angle of the equatorial outflow – the circumbinary ruff – as measured in the 2011-Nov-06 and 2012-Jan-28 epochs described here (43° and 1° respectively) together with the ruff angles as measured in the 2003 VLBA movie (see Doolin and Blundell (2009)). The light gray curve is the fit reported by Doolin and Blundell (2009). The new data do not match the historic fit, yet illustrate the significant change in position angle of this component as a function of time.

# Chapter 4

# Analysis of the Proper Motions of the SS 433 Radio Jets

## 4.1 Introduction

Spatially- and temporally resolved observations allow us to derive the proper motions of individual components within the jet structure. In this Chapter, we will outline a method for extracting intrinsic properties of the jet system from these measurements of the observed angular speeds across the celestial sphere. In particular, we will show that it is possible to extract all three components of the jet's velocity vector – the speed, the position angle projected onto the plane of the sky, and the angle to the line of sight. For the first time, this will give us unique measurements of the bulk speeds of the radio jets derived from milliarcsecond scale radio observations, which we will use to examine the behaviour of the system during flaring episodes.

To do this, we will use two data sets. Firstly, we will use the 2011-Dec-24 and 2012-Jan-28 observations outlined in the previous Chapter. Then, we will apply the same techniques to the wealth of data in the 2003 VLBA movie (Mioduszewski et al. (2004)) – a series of almost daily observations of SS 433 over seven weeks.

## 4.2 Calculating jet bulk speeds

### 4.2.1 Proper motions and line-of-sight velocities in ballistic jets

In Chapter 2, we showed that, accounting for the finite speed of light and the changing distance between source and observer for a moving source, the proper motion, $\mu$, of a light source across the sky is given by:

$$\mu = \frac{\mathrm{d}\xi}{\mathrm{d}T} = \frac{\beta_{\mathrm{apparent}} c}{D} = \frac{c}{D} \frac{\beta \sin \eta}{1 - \beta \cos \eta} \tag{4.1}$$

where $D$ is the distance to the source, $c$ is the speed of light, $\eta$ is the angle of the emitting source's intrinsic velocity to line-of-sight, and $v = \beta c$ is its speed. $\xi$ is the angular displacement on the sky, and $T$ denotes time passed according to the observer's clock on Earth (the epoch of observation).

Let us now consider a pair of symmetric, antiparallel, ballistic jets, launched from a common core, both travelling at speed $\beta$, with the jet and counterjet aligned at angles $\eta$ and $\pi - \eta$ to the line-of-sight. Inserting these into the definition of proper motion (Eqn 4.1) and rearranging, we can extract (e.g. Mirabel and Rodríguez (1994)) the line-of-sight component of the jet's velocity vector; i.e, $\beta_{\parallel} = \beta \cos \eta$. This is:

$$\beta_{\parallel} = \beta \cos \eta = \frac{\mu_{\mathrm{jet}} - \mu_{\mathrm{cjt}}}{\mu_{\mathrm{jet}} + \mu_{\mathrm{cjt}}} = \frac{\xi_{\mathrm{jet}} - \xi_{\mathrm{cjt}}}{\xi_{\mathrm{jet}} + \xi_{\mathrm{cjt}}} \tag{4.2}$$

where $\mu_{\mathrm{jet}}$ and $\mu_{\mathrm{cjt}}$ denote the proper motions of the jet and counterjet respectively. The final equality follows from the assumptions of ballistic motion and simultaneous launch, where $\xi_{\mathrm{jet}} = \mu_{\mathrm{jet}} \Delta T$ and $\xi_{\mathrm{cjt}} = \mu_{\mathrm{cjt}} \Delta T$ are the angular displacements from the launch point observed at the same epoch (according to the observatory clock), $\Delta T$ after their simultaneous launch.

### 4.2.2 Launch epoch and intrinsic jet speed

For ballistically moving ejecta, a further rearrangement is possible to allow us to extract both the launch epoch, $T_{\mathrm{launch}}$, and the intrinsic speed, $\beta$.

To find the launch epoch, we simply extrapolate back to the date on which the separation between jet and counterjet ejections was zero, under the assumptions that they were launched simultaneously and that they move ballistically and symmetrically. Hence, given two observations at epochs

$T$ and $T + \Delta T$, and defining the total angular separation $\xi_{\rm tot}(T) := \xi_{\rm jet}(T) + \xi_{\rm cjt}(T)$, we find:

$$T_{\rm launch} = T - \frac{\xi_{\rm tot}(T)}{\xi_{\rm tot}(T + \Delta T) - \xi_{\rm tot}(T)} \Delta T \,. \tag{4.3}$$

The quantity $\xi_{\rm tot}$ has the advantage that it is just the angular separation between the jet and counterjet bolides, and so can be determined independently of the absolute location of the centre. This is particularly useful for self-calibrated interferometric maps of symmetric jet sources (as is in our observations of SS 433), where the precise core location can be hard to identify.

Similarly, we can define a total proper motion $\mu_{\rm tot}(T) := \mu_{\rm jet}(T) + \mu_{\rm cjt}(T)$ as the rate at which the two bolides move apart. Using Equation 4.1, this total proper motion can be written:

$$\mu_{\rm tot} = \frac{\xi_{\rm tot}(T)}{T - T_{\rm launch}} = \frac{2c}{D} \frac{\beta_\perp}{1 - \beta_\parallel^2} \tag{4.4}$$

with $\beta_\perp = \beta \sin\eta$.

We can rearrange Equation 4.4 to find the velocity component perpendicular to the line-of-sight, $\beta_\perp$. Then, the jet speed itself can be written in terms of the total proper motion, $\mu_{\rm tot}$, and the line-of-sight velocity component, $\beta_\parallel$:

$$\beta = \sqrt{\beta_\perp^2 + \beta_\parallel^2} = \sqrt{\left[(D/2c)\,\mu_{\rm tot}\left(1 - \beta_\parallel^2\right)\right]^2 + \beta_\parallel^2} \tag{4.5}$$

where the line-of-sight velocity component, $\beta_\parallel$ is calculated using Equation 4.2.

The angle to the line-of-sight can be simply extracted from Equations 4.2 and 4.5 as:

$$\cos\eta = \frac{\beta_\parallel}{\beta} \tag{4.6}$$

If the position angle of the jet on the sky is also measured, then this calculation gives the complete velocity vectors of the jet and counterjet bolides. This calculation gives the best means of determining this vector; it returns a value for the angle rather than simply a constraint derived from the requirement that speeds are less than $c$ (Meyer et al. (2015)), and in principle allows examination of the three dimensional precession of jets such as SS 433.

If we further know the orientation of the jet precession cone (described by position angle $\chi_0$ and angle to the line of sight $i_0$ as in Figure 2.1), then by using the transformations outlined in

| Bolide | 2011-Dec-24 | | | 2012-Jan-28 | | | $T_{\rm launch}$ | Line-of-Sight | Bulk Speed |
|---|---|---|---|---|---|---|---|---|---|
| | $\xi_{\rm jet}$ | $\xi_{\rm cjt}$ | $\xi_{\rm tot}$ | $\xi_{\rm jet}$ | $\xi_{\rm cjt}$ | $\xi_{\rm tot}$ | (MJD) | Velocity $\beta_\parallel$ | $\beta = v/c$ |
| A | 162.2 | 173.9 | 336.1 | 488.9 | 480.5 | 969.4 | $55901.3 \pm 0.9$ | $0.009 \pm 0.029$ | $0.288 \pm 0.017$ |
| B | 12.7 | 18.7 | 31.2 | 318.3 | 343.8 | 662.0 | $55918.1 \pm 0.6$ | $-0.039 \pm 0.043$ | $0.289 \pm 0.017$ |

Table 4.1: Angular displacements and derived launch dates, line-of-sight velocities $\beta_\parallel = v_\parallel/c$, and launch speeds $\beta = v/c$ for bolides A and B in the 2011-12 observations. Angular displacements are given in milliarcseconds from the core (located at the origin of Figure 4.1). Speeds are given in units of $c$.

Section 2.2, we are also able to extract information about the launch vector's orientation on the precession cone. We can convert angles $\chi$ and $\eta$ into polar angles. That is, we can find the polar angle, $\theta$, representing the angle between the jet and cone axis about which the jet precesses as:

$$\cos\theta = \cos i_0 \cos\eta + \sin i_0 \sin\eta \cos(\chi_0 - \chi) \tag{4.7}$$

and we can find a "precession phase", which is the azimuthal angle, $\phi$, around the precession cone from closest approach to the line-of-sight):

$$\tan\phi = \frac{\sin\eta \sin(\chi_0 - \chi)}{\sin i_0 \cos\eta - \cos i_0 \sin\eta \cos(\chi_0 - \chi)} \tag{4.8}$$

(c.f., Result 2.2.6). We note, of course, that these last two results are dependent on the model used to determine $i_0$ and $\chi_0$.

## 4.3 Observations

### 4.3.1 2011-12 VLBA observations

SS 433 was observed with the Very Long Baseline Array (VLBA) on MJD 55919.83 and MJD 55954.75 (i.e. on 2011-Dec-24, and 35 days later on 2012-Jan-28). The data reduction involved in these two epochs was outlined in Chapter 3.

These two images show the milliarcsecond-scale jets of SS 433 in greater detail and over greater extent than any previous VLBI image of the system. We can trace the ejecta as they travel over $\gtrsim 0.4$ arcseconds on either side of the core, or $\gtrsim 50$ days from their initial launch, given that proper motions are of order of $8\,{\rm mas\,d^{-1}}$. In each epoch, we can identify a succession of pairs of bolides arising from antiparallel ejections of knots of jet plasma. The time-spacing of the two epochs is

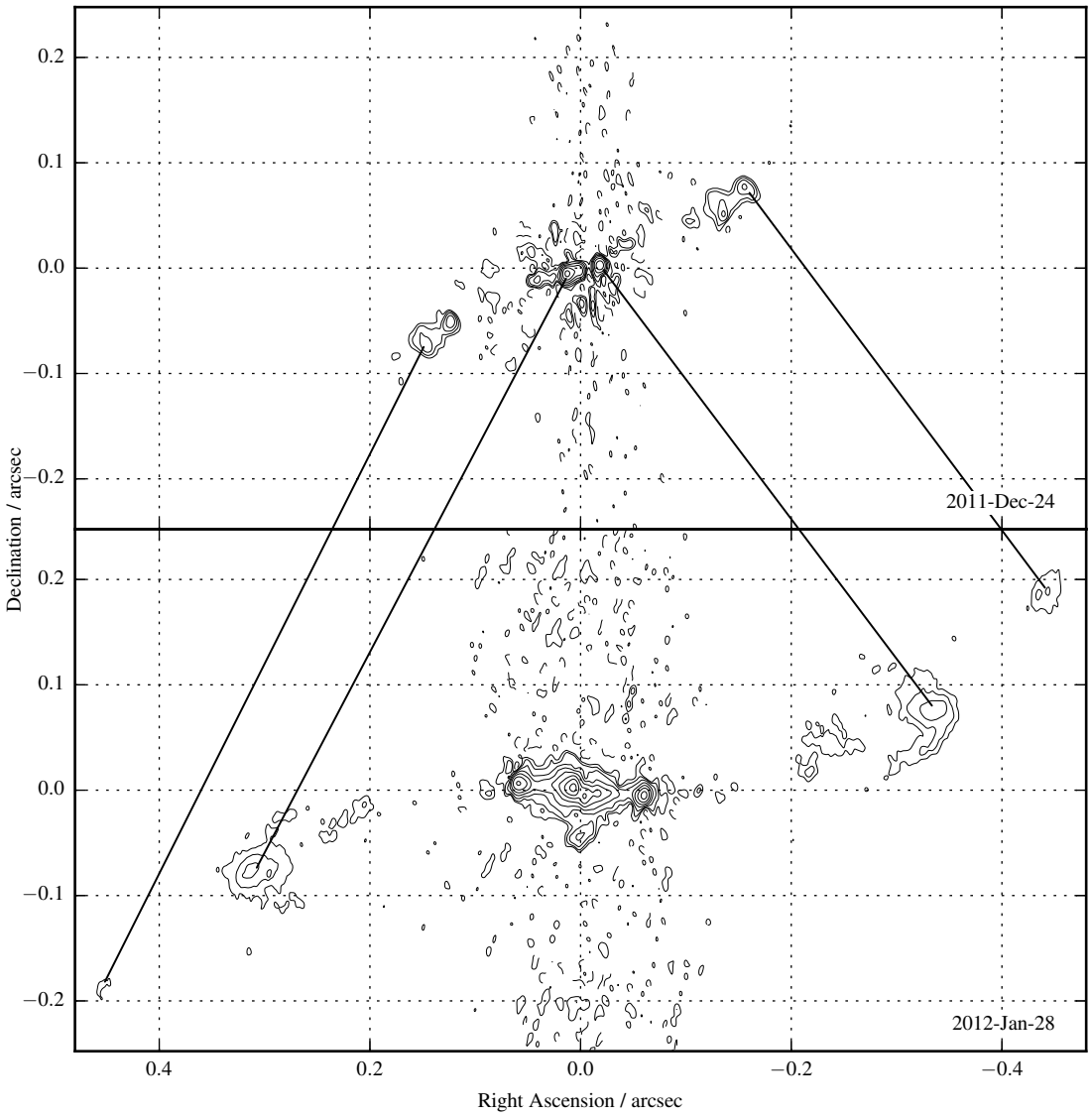


Figure 4.1: VLBA observations of SS 433 in 2011-12. Contour levels are at $2^n$ times the minimum contour level, which is $2.2\,\mathrm{mJy\,beam^{-1}}$ in the upper panel, and $0.22\,\mathrm{mJy\,beam^{-1}}$ in the lower panel. One negative contour (dashed) at $-1$ times the minimum contour level is also shown. The connecting lines identify the same ejections across the two epochs.

such that plasma that is launched shortly before the first observation has not had time to fade before the second, revealing for the first time the remarkable degree to which the jet knots expand as they fade (see Chapter 5).

For the two ejection complexes identified in both epochs, we can measure their angular displacements from an estimated core position, located at the origin in Figure 4.1. Then, we evaluate line-of-sight velocity, launch date, and jet bulk speed using Equations 4.2, 4.3, and 4.5 respectively.

The resulting values are given in Table 4.1. The two ejections occur on MJD $55901.3 \pm 0.9$ and MJD $55918.1 \pm 0.6$ (i.e., $18.5 \pm 0.9$ and $1.7 \pm 0.6$ days before the first observation). Both ejections launch bolides at speeds of almost $0.29c$. This is the first unique measurement of the bulk speeds of the radio jets on milliarcsecond scales. It is particularly noteworthy that the speeds lie at the upper end of the range of those fitted to the arcsecond-scale radio jets in Blundell and Bowler (2004), and also that they match the high optical jet speeds that Blundell et al. (2011) reported as being associated with flaring behaviour. We will discuss this further in Section 4.4.

### 4.3.2 Archival VLBA observations - the SS 433 movie

We can also apply the methods derived in Section 4.2 to historic VLBA observations of SS 433 in 2003.

SS 433 was observed on 39 out of the 42 days between 2003-June-26 and 2003-August-06, using 2 hour observation tracks with the VLBA at 1.4 GHz ($L$-Band). These data were prepared and reduced by Amy Mioduszewki of NRAO with the AIPS software using standard techniques for VLBI imaging (as discussed in the AIPS Cookbook), but truncating the inner regions at $200\,\mathrm{k}\lambda$ (private communication). As in our observations discussed in Chapter 3, multiscale CLEAN was used to assist with imaging, as was careful boxing, guided by the predicted jet loci generated from the kinematic model. A movie of the colour-scale images from this campaign has previously been released to the community (`http://www.nrao.edu/pr/2004/ss433/`; Mioduszewski et al. (2004)). The individual observations are plotted as contour maps in Figure 4.2. An animated version of these contour plots is available with the online edition of Jeffrey et al. (2016).

From a qualitative inspection of Figure 4.2, we can see that the jet consists mainly of a series of discrete ejection pairs, which we are able to track over multiple successive days' observing as they

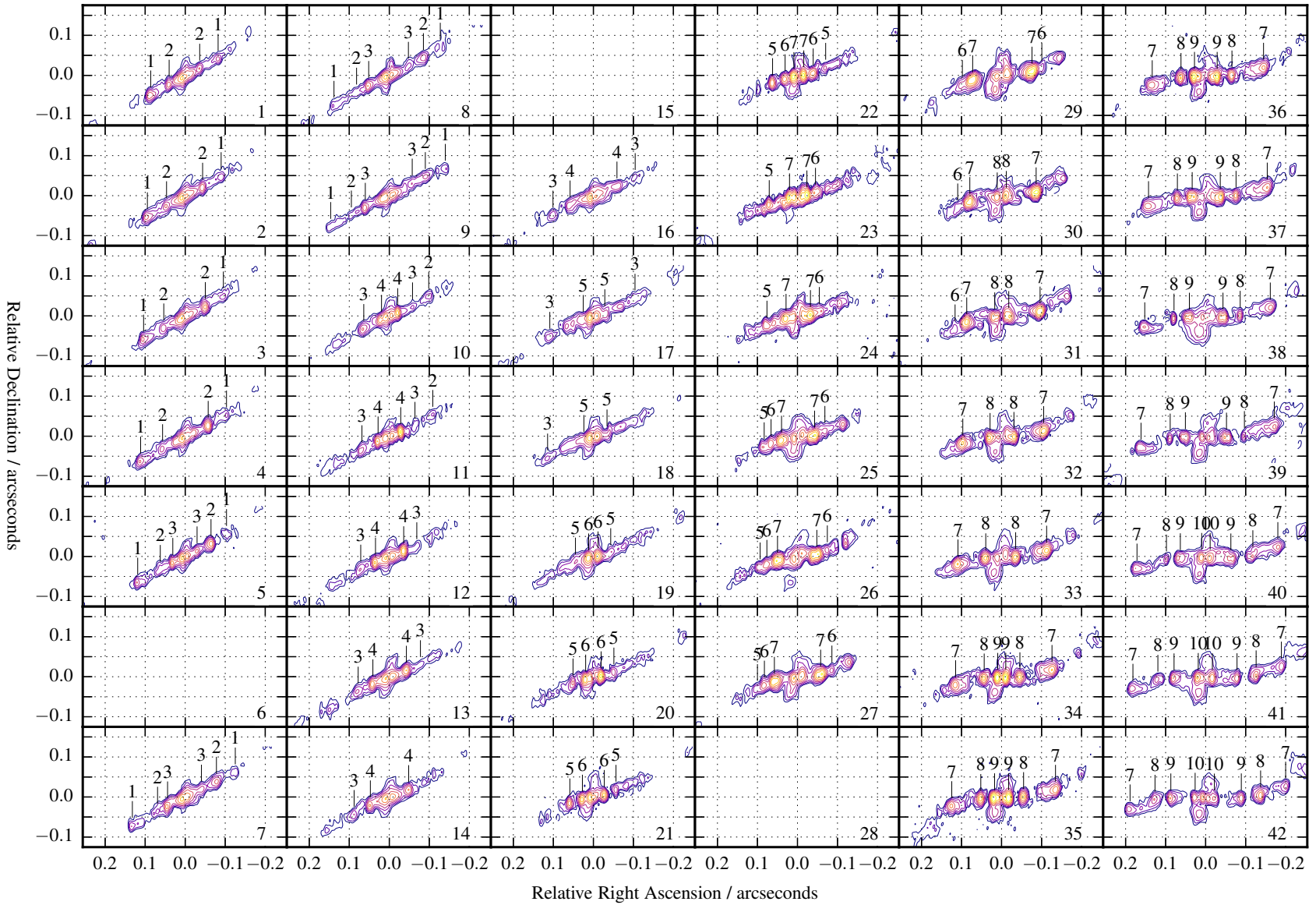


Figure 4.2: Contour Maps showing 2003 VLBA Observations of SS 433. Contour levels are identical across all frames, set at $2^n \times 0.7\,\mathrm{mJy\,beam}^{-1}$ for integer $n$. The frame number corresponds to number of days from 2003-June-25 (i.e. MJD − 52815.0). The crosses denote the Kinematic Model predictions for bolides launched at 5 day intervals.

travel away from the core in an apparently ballistic fashion. In each case, both components of a pair of bolides appear to be launched simultaneously. In the first observation, 2 bolide pairs can be distinguished. Over the course of the 6 week campaign, a further 8 pairs are launched.

Throughout the campaign, the jet shows deviations from the kinematic model predictions (i.e. the crosses in Figure 4.2, using the parameter fits of Eikenberry et al. (2001)), implying variations in launch angle or in jet speed (or in both) that are not described by this simple model. Schillemat et al. (2004) noted that the proper motions deviate from those predicted by the model. In Section 4.3.3 below, we apply Equation 4.5 to show how these correspond to variations in the physical jet launch speed.

It is also interesting to note that SS 433's behaviour over the course of the 2003 campaign appears to be divided into two distinct phases. During the first part of the campaign, we observe a period of relative quiescence. Discrete jet ejections can be identified, but they have low luminosities relative to later bolides, and appear to lie within a more continuous background jet flow.

From about day 19 (i.e. from 2003-Jul-14, MJD 52834) until the end of the observing campaign, the jet appears to move to a more active phase featuring more intense bolide ejections. The jet appears more fragmented, with more pronounced gaps in the jet flow between individual ejections (note that all frames of Figure 4.2 are contoured at the same levels). This fragmentation suggests that the continuous jet seen in earlier epochs is actually disrupted, although it may be a dynamic range or *uv*-plane sampling effect.

We believe this second phase of behaviour to be the milliarcsecond-scale manifestation of a radio flare, and in Section 4.4 we will discuss this hypothesis in relation to existing observations of SS 433.

### 4.3.3 Proper motion analysis of the 2003 data

We can determine the bulk launch speeds of the individual jet ejecta by using the analysis of Section 4.2. The peak positions of individual bolides were determined using the AIPS task `JMFIT`. At each epoch, a single Gaussian component was fitted to each bolide; the peak positions of these Gaussians served as the bolide locations.

Next, we determine the proper motions, $\mu_{\rm jet}$ and $\mu_{\rm cjt}$, of the bolides in the jet and counterjet. To do this, we fit the displacements of the bolides from the launch point in each epoch assuming

simultaneous and oppositely directed launch, followed by ballistic propagation. In Figure 4.2, each frame has been centred to the estimated launch point, taken to be the gap between the two stationary peaks that corresponds to the base of the jets. There are 4 parameters in this model: the proper motions $\mu_{\rm jet}$ and $\mu_{\rm cjt}$, together with the position angle of their trajectories on the sky, and the epoch of launch, $T_{\rm launch}$. That is,

$$\xi_{\alpha,\rm jet} = \mu_{\rm jet}\,(T - T_{\rm launch})\cos\chi\sec\delta_0 \tag{4.9}$$

$$\xi_{\delta,\rm jet} = \mu_{\rm jet}\,(T - T_{\rm launch})\sin\chi \tag{4.10}$$

$$\xi_{\alpha,\rm cjt} = -\mu_{\rm cjt}\,(T - T_{\rm launch})\cos\chi\sec\delta_0 \tag{4.11}$$

$$\xi_{\delta,\rm cjt} = -\mu_{\rm cjt}\,(T - T_{\rm launch})\sin\chi \tag{4.12}$$

where $\xi_\alpha$ and $\xi_\delta$ denote shifts in Right Ascension and Declination, the position angle, $\chi$, is the angle formed between the jet and the E-W axis, and $\delta_0$ is the Declination of the source ($+4°58'57\farcs764$ (J2000.0)).

#### 4.3.3.1 The fitting algorithm

To find the best-fitting parameters for this model, we use a modified least-squares fitting routine, making the simplifiying assumption that the unknown errors in the coordinates are independent and uniform. We also assume flat priors on the model parameters $\{\mu_{\rm jet}, \mu_{\rm cjt}, \chi, T_{\rm launch}\}$. This reasoning is similar to a problem in Sivia and Skilling (2006).

Let us suppose that we have data points $\{t_i, (x_i, y_i)\}$, where $t_i$ are the observation times, and $(x_i, y_i)$ are the measured coordinates of a (jet or counterjet) bolide. Let us suppose that we want to describe these points by a model which predicts that the coordinates at time $t$ will be $(\tilde{x}\,(t, \{m_j\})\,, \tilde{y}\,(t, \{m_j\}))$, where $\{m_j\}$ is the set of model parameters to be found. We will do this by exploiting Bayes' Theorem: $P_{\rm model\,|\,data} \propto P_{\rm data\,|\,model} P_{\rm model}$. Here, $P_{\rm model\,|\,data}$ is the probability density function (pdf) of a set of model parameters given data (the *posterior*), $P_{\rm data\,|\,model}$ is the pdf of a set of observed data given a set of model parameters (the *likelihood*), and $P_{\rm model}$ is the *a priori* pdf on the model parameters (the *prior*).

We make the assumptions that experimental uncertainties are independent, Gaussian and described by a single parameter, $\sigma$. Hence, the likelihood function on each measurement pair $(x_i, y_i)$

can be written:

$$P_{i^{\text{th}}\,\text{datum}\,|\,\text{model},\sigma}\left(x_i, y_i | t_i\left\{m_j\right\}, \sigma\right) = \frac{1}{2\pi\sigma^2}\,\exp\left(-\frac{\left(x_i - \tilde{x}\left(t_i, \{m_j\}\right)\right)^2 + \left(y_i - \tilde{y}\left(t_i, \{m_j\}\right)\right)^2}{2\sigma^2}\right) \tag{4.13}$$

and the assumption of independence gives us:

$$P_{\text{data}\,|\,\text{model},\sigma} = \prod_{i=1}^{N} P_{i^{\text{th}}\,\text{datum}\,|\,\text{model},\sigma} \propto \sigma^{-2N}\exp\left(-\frac{R^2}{2\sigma^2}\right) \tag{4.14}$$

where $N$ is the total number of data points (that is, the sum of the number of counterjet measurements and the number of jet measurements), and $R^2$ is the sum of squares of residuals:

$$R^2 := \sum_{i=1}^{N}\left[\left(x_i - \tilde{x}\left(t_i, \{m_j\}\right)\right)^2 + \left(y_i - \tilde{y}\left(t_i, \{m_j\}\right)\right)^2\right]. \tag{4.15}$$

To obtain $P_{\text{model}\,|\,\text{data}}$, we marginalise over $\sigma$, with an appropriately chosen prior on $\sigma$. Ignorance is expressed by a Jeffreys' prior: $P_\sigma \propto \frac{1}{\sigma}$ for positive $\sigma$. Thus, we have:

$$P_{\text{model}\,|\,\text{data}} = \int \mathrm{d}\sigma\, P_{\sigma,\text{model}\,|\,\text{data}} \tag{4.16}$$

$$\propto \int \mathrm{d}\sigma\, P_{\text{model}\,|\,\text{data},\sigma} P_\sigma \tag{4.17}$$

$$\propto \int \mathrm{d}\sigma\, P_{\text{data}\,|\,\text{model},\sigma} P_{\text{model}} P_\sigma \tag{4.18}$$

where, in the first step, we have used Bayes' Theorem to rearrange $\sigma$, and in the second, we have used Bayes' Theorem to rearrange the model parameters. Up to an appropriate choice of prior on the model parameter, we know all the terms in this expression. Hence,

$$P_{\text{model}\,|\,\text{data}} \propto P_{\text{model}} \int \mathrm{d}\sigma \sigma^{-1}\sigma^{-2N}\exp\left(-\frac{R^2}{2\sigma^2}\right). \tag{4.19}$$

To handle the integral, we make the substitutions $s = \sqrt{R^2}/\sigma$ and $\mathrm{d}\sigma = -\left(\sqrt{R^2}/s^2\right)\mathrm{d}s$. These give us

$$\int \mathrm{d}\sigma\, \sigma^{-(2N+1)}\exp\left(-\frac{R^2}{2\sigma^2}\right) = -\left(R^2\right)^{1/2}\left(R^2\right)^{-(2N+1)/2}\int \mathrm{d}s\, s^{(2N+1)}\exp\left(-\frac{s^2}{2}\right) \propto \left(R^2\right)^{-N} \tag{4.20}$$

since the integral over $s$ is now just an uninteresting constant which can be absorbed into the normalisation. This gives us our posterior pdf,

$$P_{\text{model}\,|\,\text{data}} \propto \left(R^2\right)^{-N} P_{\text{model}}\,. \tag{4.21}$$

Under the further assumption of a flat prior, $P_{\text{model}} = \text{constant}$, it is clear that the most likely model values, $\{m_{j,0}\}$, will be those which minimise the value of $R^2$. Hence, we obtain a slight variation on the *least-squares* method. We can use routines within Python's `scipy` package to find these optimal values.

**4.3.3.1.1 Uncertainties on model parameters** We can also find estimates of the uncertainties on these parameters by Taylor-expanding the posterior pdf about this minimum. This is most conveniently done using the logarithm of the posterior $L = \ln P_{\text{model}\,|\,\text{data}}$. Expanding $L$ in a Taylor Series in terms of the parameters $\{m_j\}$ about the maximum at $\{m_{0,j}\}$, we find:

$$L = L\left(\{m_{0,j}\}\right) + \tfrac{1}{2}\sum_i\sum_j \left(m_i - m_{0,i}\right)\left(m_j - m_{0,j}\right) \left.\frac{\partial^2 L}{\partial m_i \partial m_j}\right|_{\{m_{k,0}\}} + \ldots \tag{4.22}$$

where the first order term is identically zero because we are expanding about a stationary point and we have chosen to neglect terms of order $\mathcal{O}\left(\delta m^3\right)$. Exponentiating this, we recover the *quadratic approximation* to the posterior pdf: a multivariate Gaussian in the model parameters $\{m_j\}$, with covariance matrix $\boldsymbol{\sigma^2} = \mathbf{H}^{-1}$, where the Hessian matrix $\mathbf{H}$ has components $[\mathbf{H}]_{ij} := -\left.\frac{\partial^2 L}{\partial m_i \partial m_j}\right|_{\{m_{k,0}\}}$.

### 4.3.4 Derived launch speeds and vectors

The fitted proper motions are listed in Table 4.2 (there are too few data points for a reliable fit to the final ejection, giving a total of 9 fitted bolide pairs). Using equations (4.2) and (4.5), the line-of-sight velocity components and the bulk speeds were calculated for each ejecta pair. They are plotted against epoch of launch in Figure 4.3. The corresponding angles to the line-of-sight are also plotted, showing the precession of the jet launch vector. Uncertainties are estimated by drawing random samples from the Gaussian approximation to the posterior PDF on the fitted parameters, together with the distance to SS 433, $D = 5.5 \pm 0.2\,\text{kpc}$ (Blundell and Bowler (2004)). When propagated through equations (4.2) and (4.5), this gives estimates for the errors on the derived

| Bolide | $T_{\rm launch}$ | $\mu_{\rm jet}/{\rm mas\,d^{-1}}$ | $\mu_{\rm cjt}/{\rm mas\,d^{-1}}$ | $\chi/^\circ$ | $\beta_\parallel = v_\parallel/c$ | $\theta/^\circ$ | $\beta = v/c$ |
|---|---|---|---|---|---|---|---|
| 1 | $-10.740 \pm 0.385$ | $8.262 \pm 0.198$ | $7.611 \pm 0.184$ | $28.15 \pm 0.23$ | $0.041 \pm 0.004$ | $80.8 \pm 1.0$ | $0.255 \pm (0.006 + 0.005)$ |
| 2 | $-4.211 \pm 0.264$ | $7.449 \pm 0.209$ | $7.536 \pm 0.185$ | $27.15 \pm 0.41$ | $-0.006 \pm 0.008$ | $91.4 \pm 1.8$ | $0.238 \pm (0.006 + 0.004)$ |
| 3 | $0.561 \pm 0.301$ | $7.046 \pm 0.182$ | $6.683 \pm 0.192$ | $24.57 \pm 0.48$ | $0.026 \pm 0.009$ | $83.1 \pm 2.3$ | $0.220 \pm (0.005 + 0.004)$ |
| 4 | $6.962 \pm 0.118$ | $6.768 \pm 0.131$ | $6.916 \pm 0.133$ | $22.05 \pm 0.33$ | $-0.011 \pm 0.006$ | $92.9 \pm 1.5$ | $0.218 \pm (0.004 + 0.005)$ |
| 5 | $14.098 \pm 0.231$ | $7.894 \pm 0.211$ | $8.487 \pm 0.359$ | $16.25 \pm 0.56$ | $-0.036 \pm 0.013$ | $97.9 \pm 2.7$ | $0.262 \pm (0.010 + 0.004)$ |
| 6 | $18.247 \pm 0.112$ | $9.279 \pm 0.141$ | $9.400 \pm 0.183$ | $13.51 \pm 0.43$ | $-0.006 \pm 0.008$ | $91.3 \pm 1.5$ | $0.297 \pm (0.005 + 0.007)$ |
| 7 | $21.014 \pm 0.074$ | $8.891 \pm 0.056$ | $9.422 \pm 0.058$ | $8.74 \pm 0.15$ | $-0.029 \pm 0.003$ | $95.7 \pm 0.6$ | $0.292 \pm (0.002 + 0.009)$ |
| 8 | $29.654 \pm 0.126$ | $9.582 \pm 0.178$ | $10.443 \pm 0.189$ | $2.45 \pm 0.46$ | $-0.043 \pm 0.008$ | $97.7 \pm 1.5$ | $0.320 \pm (0.005 + 0.007)$ |
| 9 | $33.583 \pm 0.135$ | $9.602 \pm 0.269$ | $9.795 \pm 0.271$ | $-0.07 \pm 0.70$ | $-0.010 \pm 0.012$ | $91.8 \pm 2.2$ | $0.308 \pm (0.008 + 0.006)$ |

Table 4.2: Best fits to bolide launch dates, $T_{\rm launch}$; proper motions, $\mu_{\rm jet}$ and $\mu_{\rm cjt}$; and position angles projected on the plane of the sky, $\chi$, for the first 9 bolides seen in the 2003 campaign.. Also given are derived line-of-sight velocities, $\beta_\parallel$; angles $\theta$ to the line-of-sight; and bulk speeds $\beta$. $T_{\rm launch}$ is given as MJD $-$ 52815.0 (i.e. referred to 2003-June-25). The bolide numbers correspond to the labels in Figure 4.2. Uncertainties are at the $1\sigma$ level. For the bulk speed, $\beta$, the error is given as statistical uncertainty in the fit + systematic uncertainty in the distance $D$ to the source (see discussion in Section 4.4.5).

parameters. In fact, the uncertainty on distance $D$ is the largest source of uncertainty in the estimation of jet speed $\beta$. This is shown in Figure 4.3(b); we will return to this in Section 4.4.5.

Inspecting the derived speeds, we see clear and quantitative evidence for a change in behaviour during the campaign. Jet speeds are low ($\beta \lesssim 0.26$) for ejections before approximately day 15. In the later observations, jet speeds are high, exceeding $0.29c$.

#### 4.3.4.1 Jet orientation and the reliability of the precession model

We can use Equations 4.7 and 4.8 to make a determination of the launch angle and phase for each bolide, and compare to the predictions of the kinematic model. These are sketched in Figure 4.4. The solid lines show the kinematic model predictions for the position angle, jet cone angle and precession angle, obtained by using the ephemerides of Eikenberry et al. (2001), together with the nutation parameters given in Vermeulen (1989). Uncertainties given are $1\sigma$, and unlike in Figure 4.3, no distinction is made between the systematic uncertainty in distance $D$, and the statistical uncertainties in the data fits.

In all cases, the bolide angles clearly deviate significantly from the kinematic model's predictions. There are two interesting observations here:

1. there appears to be an offset between the data and the predictions obtained using the Eikenberry values of the kinematic model of between 5 and 10 days; and
2. while individual bolides appear to follow the shape of the basic kinematic model well, from the limited sampling here it is unclear whether the rapid $\sim 6\,\mathrm{d}$ variation introduced by the nutation is manifested in the radio bolides.

The apparent discrepancy between the historic kinematic model parameters and the data here need not be indicative that these parameter values have changed with time, or that the optical and radio jets follow different models. Indeed, a discrepancy of comparable size was reported by Stirling et al. (2002) in relation to MERLIN observations from 1992, where it was attributed to phase or velocity noise. However, Figure 4.4 (in particular the position and precession angles) suggest something more systematic.

A first contribution to the offset (perhaps $\sim 2\,\mathrm{d}$) may arise from the time taken for optical lines to appear after launch. A further part of this deviation can be accounted for by the uncertainties in the reference epoch introduced by the difference between conventions in Eikenberry et al. (2001)

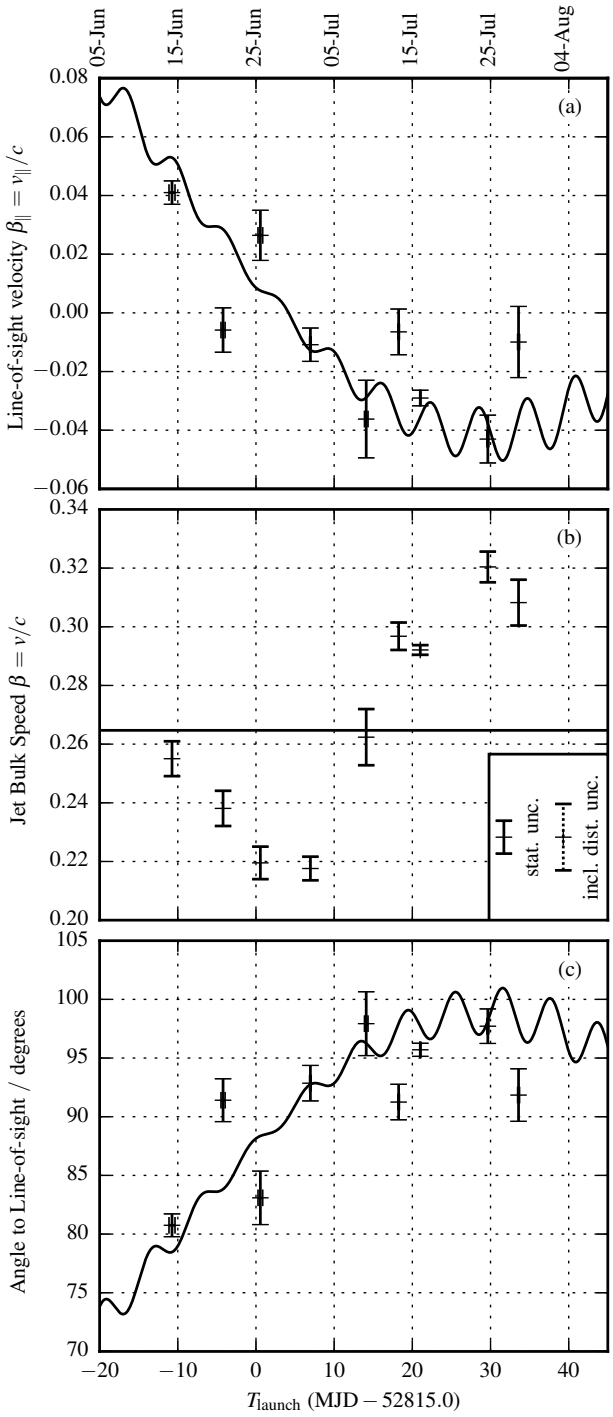


Figure 4.3: (a) Line-of-sight velocity component, $\beta_\parallel$, plotted against launch date. (b) Jet speed plotted against launch date. (c) Angle between jet bolide velocity vector and line-of-sight. In (a) and (c), the solid line shows the predicted values derived from the kinematic model, while the solid line in (b) shows the value of launch speed derived from optical spectroscopy by Eikenberry et al. (2001): $\beta = 0.2647c$. The systematic deviations from this constant value are clear. Uncertainties shown in (a) and (c) are $1\sigma$. The errorbars in (b) indicate only the uncertainty due to statistical variations in the fitted parameters. We have indicated the effect of the uncertainty in the distance to the object in the inset pane, where the mean statistical uncertainty in the fit (stat. unc.) and mean total uncertainty including that on the distance to SS 433 (incl. dist. unc.) are indicated. See Section 4.4.5. The errors in launch date are smaller than the marker width on this scale.

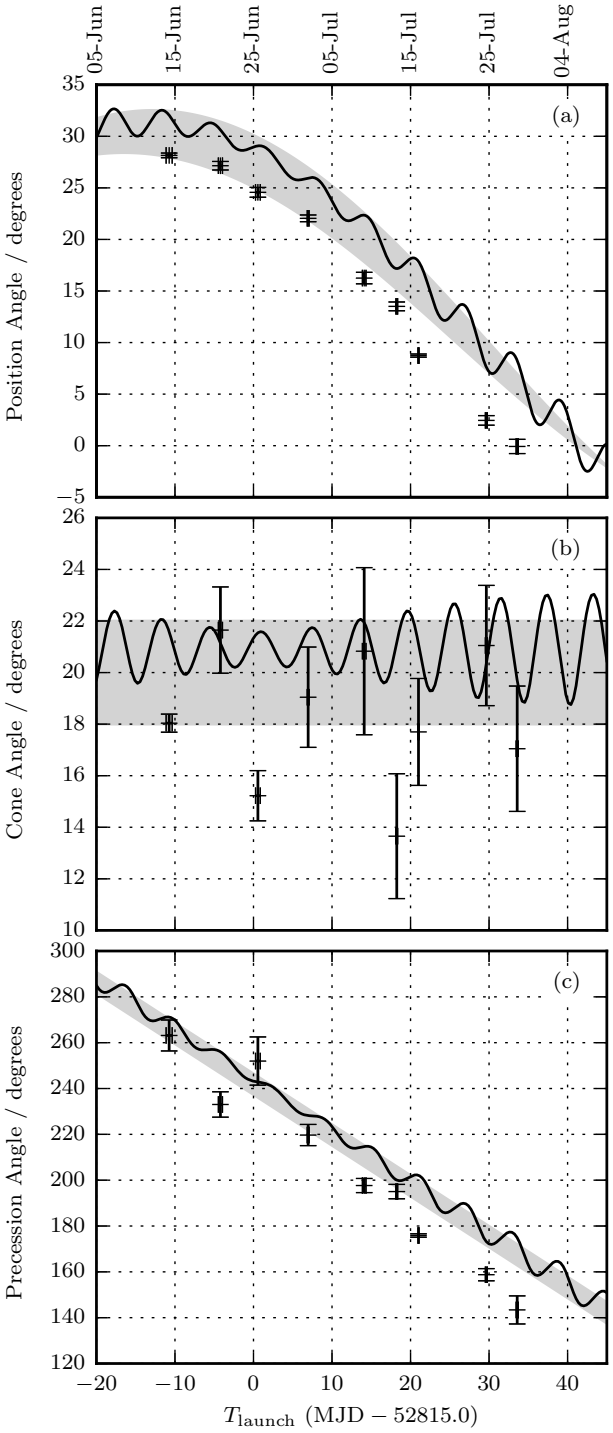


Figure 4.4: (a) Fitted position angle, $\chi$, for the trajectory of each bolide pair; (b) derived cone-opening angle, $\theta$; and (c) derived precession angle (i.e., azimuthal angle measured counter-clockwise from the point at which the jet is closest to the line-of-sight – c.f. $\Theta$ and $\Phi$ in Figure 2.1). In each case, plots are against the fitted launch date. The black lines show the kinematic model predictions obtained using the values of Eikenberry et al. (2001), and including nutation, while the grey bands show kinematic model predictions without nutation but varying the model mean cone angle between 18° and 22°.

and the present work. As previously noted (Section 2.4.1.1), in table 1 of Eikenberry et al. (2001), the convention used is that phases are measured from the point at which the (east) jet passes through the plane of the sky as it precesses away from us. We take zero phase to be the point at which the eastern jet is at its closest to the line-of-sight (maximally blue-shifted). The conversion between epoch of zero-phase in these two conventions is (non-linearly) dependent on the cone opening angle, $\Theta_0$. The grey bands indicate the effect of a variation in this cone opening angle between 18° and 22° - larger than the uncertainty stated by Eikenberry et al. (2001), but comparable with the variations introduced by both the nutation, and by stochastic variations (as reported by Blundell and Bowler (2005)). A new fit to the optical data archive, using a consistent zero-phase convention, may help to resolve this ambiguity.

On the second point, we note that, whereas new optical emission lines appear at a rate of about one a day, the radio bolides seen here are launched with a spacing of roughly 4 d between successive ejections. Given that the optical lines appear to obey the nutation model in an average sense (with stochastic variations of order of the same size as the nodding), we are not surprised that the effects of any nutation are not visible in this small sample of radio bolides.

In both cases, the present data are not sufficient to draw firm conclusions about the durability of the kinematic model or its nodding correction. A closer study of the optical spectra may help to clarify the discrepancies.

### 4.3.5 Do the jets undergo deceleration?

A number of authors (e.g., Stirling et al. (2004), Marshall et al. (2013)) have argued for deceleration in the jets of SS 433. Often this arises from the use of an erroneous distance measurement. If one assumes that SS 433 is closer than 5.5 kpc, then one finds that the same proper motion is associated with a jet speed lower than the $\sim 0.26c$ we find here. If one then wishes to compare to the speeds from optical spectra (also $\sim 0.26c$, and, crucially, determined independently of distance), then one must invoke a deceleration between the scale of the optical jets and the radio jets for consistency between their speeds.

If we are secure in using the distance of Blundell and Bowler (2004) and Lockman et al. (2007), then one finds the same jet speeds in the optical and radio jets, and so this deceleration is no longer necessary. Nevertheless, with the excellent temporal sampling of the 2003 archival VLBA observations, it is reasonable to ask: "how well do the radio bolides obey the ballistic model?"

To do this, we will examine a model in which we allow a non-zero first derivative to the proper motion:

$$\mu_i\left(T\right) = \mu_{i,0} + \dot{\mu}_{i,0}\left(T - T_{\rm launch}\right) \tag{4.23}$$

which we integrate to give expressions for the coordinates of jet and counterjet bolides:

$$\xi_{\alpha,\rm jet} = \left(\mu_{\rm jet,0}\left(T - T_{\rm launch}\right) + \tfrac{1}{2}\dot{\mu}_{\rm jet,0}\left(T - T_{\rm launch}\right)^2\right)\cos\chi\sec\delta_0 \tag{4.24}$$

$$\xi_{\delta,\rm jet} = \left(\mu_{\rm jet,0}\left(T - T_{\rm launch}\right) + \tfrac{1}{2}\dot{\mu}_{\rm jet,0}\left(T - T_{\rm launch}\right)^2\right)\sin\chi \tag{4.25}$$

$$\xi_{\alpha,\rm cjt} = -\left(\mu_{\rm cjt,0}\left(T - T_{\rm launch}\right) + \tfrac{1}{2}\dot{\mu}_{\rm cjt,0}\left(T - T_{\rm launch}\right)^2\right)\cos\chi\sec\delta_0 \tag{4.26}$$

$$\xi_{\delta,\rm cjt} = -\left(\mu_{\rm cjt,0}\left(T - T_{\rm launch}\right) + \tfrac{1}{2}\dot{\mu}_{\rm cjt,0}\left(T - T_{\rm launch}\right)^2\right)\sin\chi\,. \tag{4.27}$$

There are now 6 parameters in our model: $\{\mu_{\rm jet}, \mu_{\rm cjt}, \dot{\mu}_{\rm jet,0}, \dot{\mu}_{\rm cjt,0}, \chi, T_{\rm launch}\}$. We can use Monte-Carlo Markov Chain methods to examine the pdfs on each of these parameters.

Note that we no longer have the ability to extract physical parameters (e.g., launch speed, angle to the line-of-sight) from this model. The analysis in Section 4.2 was predicated on the assumption that the motion was ballistic. However, we can still make qualitative statements about acceleration/deceleration.

#### 4.3.5.1 Monte-Carlo sampling of the probability distribution with `emcee`

Perhaps the simplest example of an MCMC method is the Metropolis-Hastings algorithm (see e.g. Press et al. (2007)), which we will use to explain the basic principles. In this algorithm, we seek to sample some target pdf by drawing samples from a simpler trial probability distribution, which are then accepted or rejected with an appropriate weighting to recover the target and then accepted or rejected based on a weighting arising from the targeted probability distribution. More precisely, suppose our target pdf is $P_X\left(x\right)$, where $x$ is an $N$-dimensional draw from the space of the model parameters, $\mathbb{M}$. Let $Q_{X|Y}\left(x, y\right)$ be the trial distribution, returning the probability density at $x$ given some other value $y \in \mathbb{M}$. Often, we choose this to be a Gaussian distribution, with its centroid at $y$. At each iteration, we generate a new point $X_i$ based on the previous iteration $X_{i-1}$ using the trial distribution $Q_{X_i|X_{i-1}}$. Then we evaluate an acceptance ratio which (if $Q_{X|Y} = Q_{Y|X}$ is symmetric) is the ratio of the probability densities at $X_i$ and $X_{i-1}$; i.e.,

$P_X(x_i)/P_X(x_{i-1})$. If this ratio $a$ is greater than 1, the new point $x_i$ is accepted; if $a \in (0,1)$, the new point $x_i$ is accepted with probability $a$; if the point is not accepted, then a new test point is drawn from the sample distribution and its acceptance ratio calculated, repeating until a sample point is accepted. The algorithm is then iterated.

The dependence of each sample on its predecessor means that the series of samples forms a Markov chain. The acceptance criterion means that the Markov Chain will preferentially jump to regions of high probability, and draw fewer samples from less probable regions. The results will depend on the initial value, and on the choice of trial distribution (e.g., the width of the Gaussian in the above example). We can remove the initial condition by discarding a suitably long "burn-in" phase from the start of a sampling, while the distribution may need to be tuned appropriately - intuitively, the trial distribution should be at least as large as any structure in the target pdf.

Improvements on the basic Metropolis-Hastings algorithm are available. The `emcee` code (Foreman-Mackey et al. (2013)) is a Python-based implementation of an MCMC algorithm by Goodman and Weare (2010). In the Goodman & Weare algorithm, an ensemble of Markov chains (referred to as *walkers*) are used to explore the target pdf. Their positions are updated by using the positions of other walkers in the ensemble; at the $i^{\text{th}}$ iteration, for each walker in the ensemble (at position $X_{k,i}$) another walker (position $X_{j,i}$) is chosen at random, and a new trial position is chosen by moving to some appropriately randomly chosen point $X_{j,i+1} = X_{j,i} + Z(X_{k,i} - X_{j,i})$ along the line connecting $X_{j,i}$ and $X_{k,i}$, where $Z$ is a randomly chosen scalar[1]. This is referred to as a *stretch* move. Again, an acceptance ratio $a$ is defined[2], with the trial point $X_{j,i+1}$ definitely accepted if the move is to a more likely region of parameter space, or accepted with a probability $a$ if $X_{j,i+1}$ is in a less likely region.

[1] In `emcee`, the pdf on $Z$ is:

$$P_Z(z) := \begin{cases} z^{-1/2} & z \in [1/a, a] \\ 0 & \text{otherwise}. \end{cases}$$

[2] This acceptance ratio is $a := \min\left(1, z^{N-1}\frac{P_X(x_{j,i+1})}{P_X(x_{j,i})}\right)$

#### 4.3.5.2 Application to the decelerating jet model

The appropriate posterior pdf is as derived in Equation 4.21, and is passed to `emcee` as the log-posterior

$$\ln P_{\text{model}\,|\,\text{data}} = \text{constant} - N \ln R^2 + \ln P_{\text{model}}\,. \tag{4.28}$$

We briefly consider the choices for the model prior $P_{\text{model}}$. We choose uniform priors on $\dot{\mu}_{\text{jet},0}$, $\dot{\mu}_{\text{cjt},0}$, $\chi$, and $T_{\text{launch}}$, reflecting ignorance over the "direction" of these parameters (i.e., showing no preference for acceleration or deceleration, for a particular position angle, or for particular dates before or after the start of observations). For the proper motions, we choose priors that are uniform over positive real numbers and zero otherwise. Hence the log-prior is:

$$\ln P_{\text{model}} = \begin{cases} -\infty & \mu_{\text{jet}}, \mu_{\text{cjt}} < 0 \\ \text{constant} & \text{otherwise} \end{cases} \tag{4.29}$$

Figure 4.5 shows the model parameters plotted against launch date, $T_{\text{launch}}$. The markers indicate the peak of the posterior pdf marginalising over all other parameters, while the error bars give 95% confidence intervals. In Figure 4.6, we show the cross-correlations between the model parameters for one of the ejecta pairs (bolide pair 7). There are strong correlations between some of the parameters, especially between proper motion and launch date, and between proper motion and its derivative. These are intuitively obvious – a slower bolide launched earlier and a faster one launched later can reach the same point at the same time, and a bolide with a high acceleration (deceleration) launched slower (faster) will have approximately the same proper motion at the observation epoch. In fact, this is a very strong anti-correlation, explaining why even though uncertainties on deceleration are small, the uncertainties on proper motion are much larger than in the ballistic model used previously.

In almost all cases, $\dot{\mu}_{\text{jet}}$ and $\dot{\mu}_{\text{cjt}}$ are consistent with 0. Only bolide 4 shows evidence for deceleration, with bolides 8 and 9 apparently showing evidence for *acceleration*!

In fact, we can satisfy ourselves that the apparent acceleration in both bolides 8 and 9 is a result of subtle measurement errors. In the case of bolide 8, from day 38 of the campaign onwards, it appears to interact with bolide 7; this leads to an ambiguity in its position, meaning it appears to move slightly faster than its true motion.

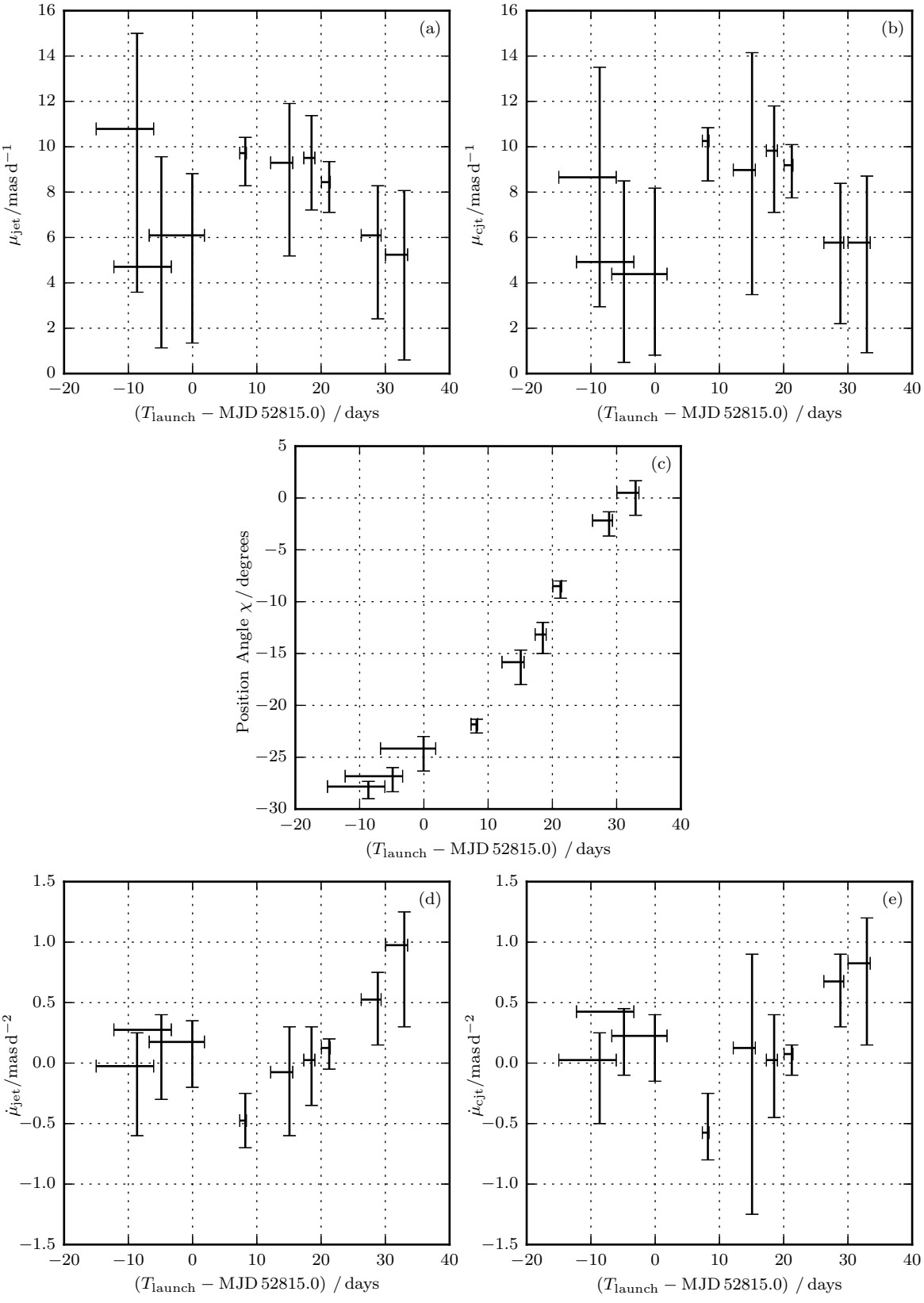


Figure 4.5: 90% confidence intervals for the parameters in the decelerating jet model, plotting (a)-(b) proper motions; (c) position angle from E-W; and (d)-(e) first order speed change terms against the fitted launch date for each of the 9 bolides seen in the 2003 observations. In panels (d)-(e), we see that all bolides except bolide 4 are consistent with no deceleration.

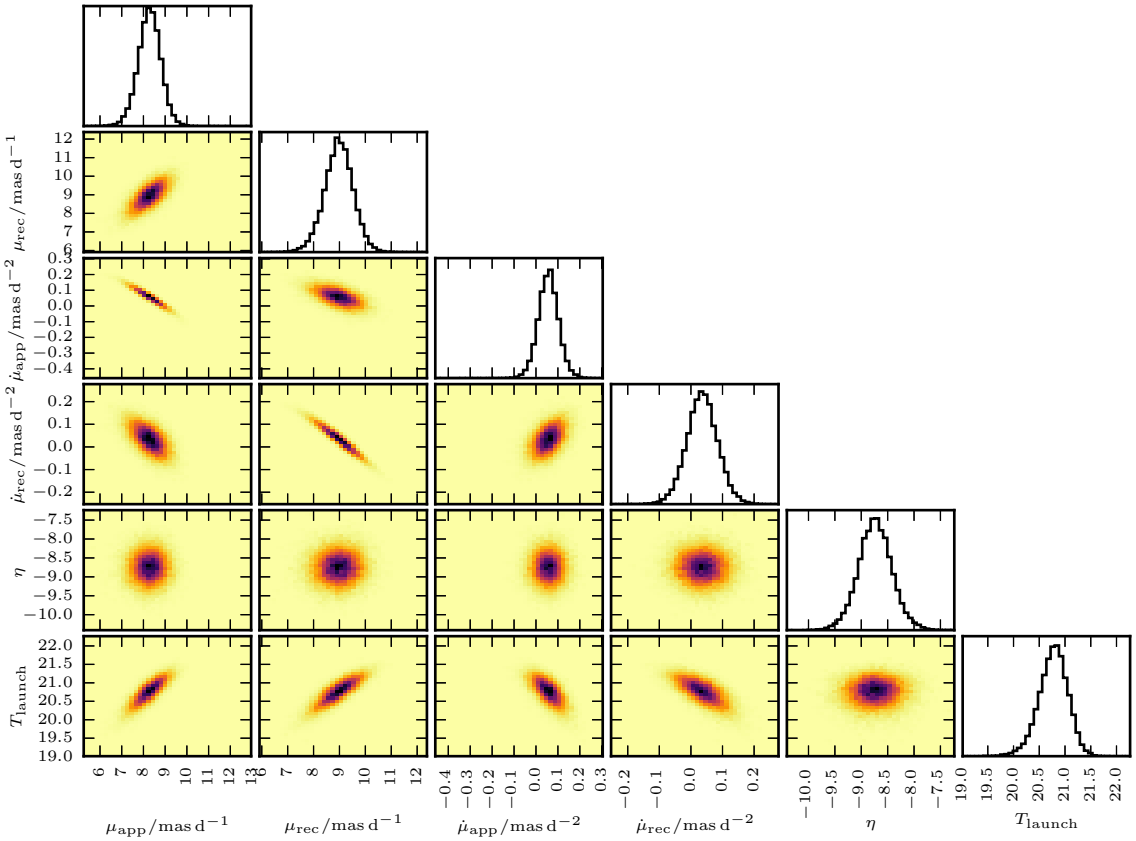


Figure 4.6: Cross-correlations between the 6 model parameters for the decelerating jet model, based on the data for bolide 7 - the best observed of the bolides in the 2003 VLBA movie. The parameters are the proper motions and their first derivatives for the jet and counterjet, the position angle $\eta$ of the jet motion, and the launch date. The 1D histograms on the diagonal represent the pdfs for each of the parameters in turn.

| Bolide | Bulk Speed $\beta = v/c$ | Flux on MJD 55919.83 / Jy | |
|---|---|---|---|
| | | Jet | Counterjet |
| A | $0.288 \pm 0.017$ | $0.126 \pm 0.003$ | $0.095 \pm 0.002$ |
| B | $0.289 \pm 0.017$ | $0.518 \pm 0.018$ | $0.226 \pm 0.008$ |

Table 4.3: The jet bulk speeds and deboosted fluxes for the two bolide pairs seen in the MJD 55919 (2011-Dec-24) observation. The reported fluxes are integrated fluxes measured using AIPS task `JMFIT`. Note that these fluxes are lower limits for the peak brightness these bolides reach, but that these bolides still obey the "bright-fast" pattern seen for other bolides launched during radio flares (c.f. Figure 4.7).

On the other hand, bolide 9 appears to accelerate because, in the early days after its launch (days 34-35), the brightening of the core makes determining a position difficult. If we remove the positions measured on these days from the data set, the acceleration term is consistent with 0.

In fact, we believe that similar ambiguities in the gaussian fits (e.g., the difficulty in disentangling the steady jet from discrete ejecta) can account for the slight accelerations seen in, for example, bolides 2 and 3.

This leaves bolide 4 as the only bolide for which there is significant evidence of deceleration. It is interesting that bolide 5 appears to undergo a brightening at a similar distance from the core to that at which bolide 4 appears to decelerate, stop, and fade. It may be that there is some cloud of (cold) gas that is sufficiently dense to stop and fragment bolide 4, but not to break up bolide 5, which instead shocks and brightens.

Excepting bolide 4, we conclude that a general bolide does indeed display no discernable deceleration on milli-arcsecond scales. This is reassuringly consistent with the fact that the speeds of both the radio jets on arcsecond scales (as determined by fitting the kinematic model to their shapes), and the optical jets at sub-milliarcsecond scales (as found from Doppler shift measurements) are approximately $0.26c$, and show no deceleration over the roughly 300 d post-launch that they are observed in e.g. Blundell and Bowler (2004).

## 4.4 Discussion

### 4.4.1 Do jet speeds and brightnesses rise in flaring episodes?

The 2003 VLBA observations allow us to characterise the distinction between the jets' behaviour in quiescent and flared periods of activity. From Figure 4.3, we can clearly see the distinct speed

distributions before and after day 15: launch speeds are higher during this flaring episode.

The 2003 VLBA observations make clear that more intensely radiating bolides travel faster than fainter bolides. This is plotted in Figure 4.7, where peak intensity is plotted against the calculated jet speed for the 9 bolide pairs in the 2003 data whose positions can be securely measured in more than 4 epochs. 'Intensity' here is a representative estimate; it is obtained by deboosting the total intensity within integrated fitted Gaussians returned by `JMFIT`, averaging over jet and counterjet ejections at each epoch, and then selecting the epoch for which this has its maximum value. For details on extracting the true deboosted brightness from a relativistic synchrotron source, see Miller-Jones et al. (2004); here, we have assumed optically-thin synchrotron emission from a jet composed of discrete plasmons, adiabatically expanding with a constant rate of change of radius, and with electron energy spectrum $\gamma^{-2.2}$, where $\gamma$ is the electron Lorentz factor (not the bulk Lorentz factor of the jet bolides). It is, however, worth remembering that for SS 433, whose jets are only mildly relativistic and lie close to the plane of the sky, Doppler boosting is a small correction (a few percent, rather than orders of magnitude). We will return to this point in Chapter 5

The two 2011 bolides also fit this pattern (Table 4.3). They are not plotted in Figure 4.7 because it is not possible to determine their peak brightnesses (since we do not have measurements of the evolution of their lightcurves). However, we can take the averaged and deboosted fluxes from the first of the two observations (MJD 55919, i.e., 2011-Dec-24) observation as lower limits. These bolides' properties (averaged flux densities 0.11 and 0.37 Jy for bolide pairs A and B, with speeds $0.288c$ and $0.289c$ respectively) are consistent with the "bright-fast", flare characteristics displayed by bolides 6, 7, 8, and 9 during the 2003 campaign, and with the behaviour observed in earlier optical observations (Blundell et al. (2011)).

So, the bolides from both the 2003 and 2011 campaigns display a clear trend: 'fast' ejections (those exceeding $0.28c$) can be as much as 8 times as luminous as those 'slow' ejections with speeds below $0.26c$.

Note that not all fast ejections are especially luminous (c.f. bolides 6 and 8). However, in Figure 4.7, we can again see the separation of the ejections in flaring episodes (bolides 6-9), and those in quiescence (bolides 1-5). This reinforces the conclusion that flaring episodes are characterised by generally faster and more luminous ejections, and that the fastest, most luminous ejections only occur during these periods of elevated activity.

This is entirely consistent with the conclusion of Blundell et al. (2011): high jet speeds as inferred from the *optical* emission lines (which are themselves more intense than usual) precede radio flares. Now, by using only radio maps to infer jet speeds completely independently of optical spectra, we also know that radio flares are characterised by high speeds in the *radio* jets. This further reinforces the tight link between the optical and radio ejecta.

### 4.4.2 How do these data compare with known properties of flares?

Our understanding of this phenomenon has been guided by the association of the behaviour seen on milliarcsecond scales in these maps with the flaring episodes seen in optical spectra and in photometric radio data. In the case of the 2011 data, we can make this comparison slightly more explicit.

It is unfortunate that there are not contemporaneous optical monitoring data for this object covering the periods of these two VLBA campaigns. However, for the 2011 observations, there is monitoring data from the RATAN telescope for the period up to 2011-Dec-15.[3] This overlaps with the launch of bolide pair A on 2011-Dec-06. In the total intensity radio data (Figure 4.8 lower panel), there is evidence that the radio intensity is quenched from 2011-Nov-26, and then rises by perhaps a factor of 3 over the 5 or so days preceding the ejection of bolide pair A (marked by the first grey bar). This pattern fits with the Type II flare described in Blundell et al. (2011), where Type II radio flares were associated with the launch of optical jets. This is the first time that we have seen direct evidence in SS 433 that a Type II radio flare corresponds to the launch of a radio-emitting jet bolide pair.

As an aside, we emphasise that not all radio flares seen in photometric monitoring are associated with the jets. Type I flares in Blundell et al. (2011) are characterised by a flat spectrum, and are associated with radio emission from an enhanced wind off the accretion disc. The peak in radio intensity at the end of the RATAN monitoring data on 2011-Dec-15 displays a flat radio spectrum, and does not appear to be associated with a bolide launch. 2011-Dec-15 is midway between the launches of bolides A and B – a bolide launched on this date would appear in the gap between these bolides in Figure 4.1, unless its initial brightness was so faint that it had faded completely before the observation on 2011-Dec-24 (which seems unlikely, given that the peaks in the RATAN data on days 33 and 40 in Figure 4.8 are of the same size). Consequently, we believe this peak

[3]These data were kindly provided by Sergei Trushkin (private communication); for more information about the RATAN microquasar monitoring program, see Trushkin et al. (2003)

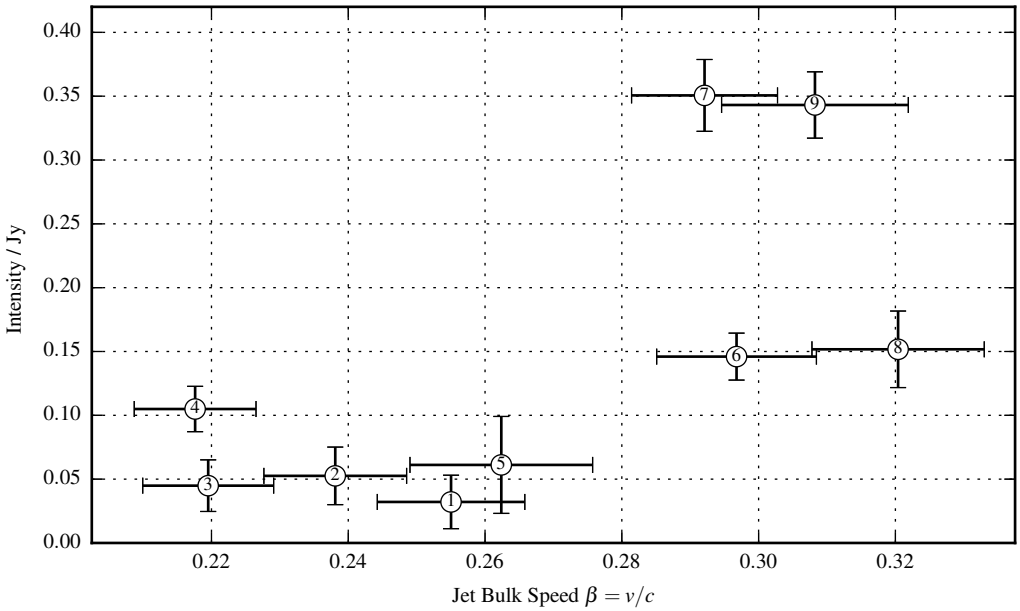


Figure 4.7: Jet launch speed plotted against intensity for the bolides seen in the 2003 campaign. Intensity is calculated as the peak of the mean of the deboosted intensities for the jet and counterjet. The numbers within the markers denote the bolide's number in the sequence of ejections 2003-Jun-14 to 2003-Jul-28 (see Figure 4.2 and Table 4.2).

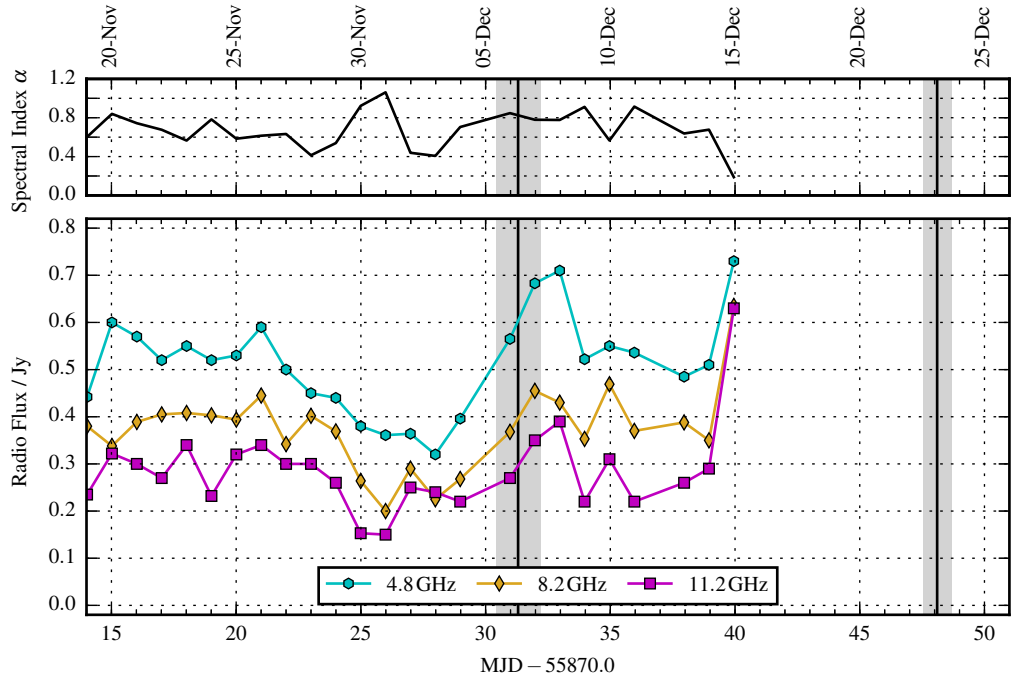


Figure 4.8: Bottom Panel: Daily radio-frequency fluxes for the period of the 2011 observations, as measured by the RATAN telescope. Top Panel: Corresponding spectral indices, $\alpha$, for the same period (note that flux $S \propto \nu^{-\alpha}$). The black vertical lines denote the launch dates of the two ejections A and B as calculated in Section 4.3.1, with the associated uncertainties in grey.

shows the hallmarks of a disc-wind-based radio flare, preceding the launch of a large jet ejection on 2011-Dec-23.

### 4.4.3 The circumbinary ruff during radio flares

We have previously noted the presence of a circumbinary ruff around the core of SS 433 – as identified by e.g., Paragi et al. (1999) and Blundell et al. (2001), and seen in our observations in Section 3.5. Doolin and Blundell (2009) explored the precession of this ruff using all existing VLBI data – including the observations from 2003 that are shown here in Figure 4.2. They suggested that the circumbinary ruff is a large scale manifestation of an outflow via a quasi-stable circumbinary disc. This circumbinary disc exists on scales comparable to a few times the orbital separation, and has been observed as static optical emission lines by Blundell et al. (2008)).

We comment that, during the 2003 observations, the ruff appears to grow significantly in size as the flare develops after day 19. We suggest that this may arise from one or more of the following: a) the observed variation is an artefact of changes in *uv*-coverage; b) the ruff appears larger because it is illuminated by more radiation from a brighter, flaring core; or c) the ruff is larger because of enhanced mass outflow from the circumbinary disc. In the first case, we note the apparent dimming of the ruff on days 23 and 26 is suggestive that the effect may be partly artefactual. We also note that the ruff's extent of $\gtrsim 50\,\mathrm{mas}$ is at the upper limit of angular scales to which the VLBA is sensitive, because the shortest VLBA baselines give only sparse coverage of the centre of the *uv*-plane. The third case is intriguing given optical observations of Blundell et al. (2011) that provided evidence that the inner circumbinary disc structure was disrupted during a flare in 2004-October. In the 2003-July observations, there are hints of detatchment between the core components and the radio ruff from day 31 onwards, raising the possibility that the enlarged ruff is a manifestation of an ejected circumbinary disc. However, this would require a very fast outflow speed – at 5.5 kpc, 50 mas corresponds to a physical size of $4 \times 10^{13}\,\mathrm{m}$. To cover this in $\sim 10\,\mathrm{d}$ would require an outflow speed exceeding $40,000\,\mathrm{km\,s^{-1}}$, which seems improbably high (though our estimated value is similar to that suggested by Mioduszewski et al. (2004)).

### 4.4.4 The unified picture

Despite the lack of contemporaneous optical and radio monitoring data, there are enough similarities between what we see in these milliarcsecond scale observations and what is seen at other

scales and frequencies that we can draw out some general characteristics.

In Figure 4.3, we see that jet launch speeds appear to fall over a period of about 30 days before the flare begins and jet speeds increase dramatically on or around day 15. A similar decline in speed is seen in the optical jet lines in figure 6(e) of Blundell et al. (2011), where jet speeds decline from $\sim 0.27c$ to $\sim 0.24c$ over the 20 days prior to a flare.

Both in the 2011-12 observations, and during the latter half of the 2003 campaign, we see bright, fast ejections, punctuated by gaps of 5 to 10 days. Again, almost identical behaviour is seen by Blundell et al. (2011) in the optical jet lines, where the intensity of the optical jet lines is lowest in the days immediately preceding the start of the flare. This stands in contrast to the behaviour of the jet in the early days of the 2003 campaign, where the jet has a more steady character. The difference is most clearly seen by comparing the first and last frame of Figure 4.2 (noting that the images of all epochs are contoured to the same minimum level): in the first frame we see faint bolides set against an apparently steady background flow, while in the last we see a succession of bright, compact bolides separated by gaps of low/no emission.

Taken together, we note that the variations in both the speeds of the optical emission lines and the speeds determined by the milliarcsecond scale bolides possess remarkably similar characteristics. In the absence of simultaneous, time-resolved optical and radio observations, this coincidence is intriguing evidence that the ejecta revealed by optical emission are indeed directly related to the ejecta seen through radio emission. That is, that both the optical emission lines and the radio continuum emission originate from the same jet moving ballistically and seemingly with the same speed, although this expectation remains to be tested with quasi-simultaneous radio imaging and optical spectroscopy.

### 4.4.5 The effect of uncertainty in the distance $D$

As noted in Section 4.3.2, the dominant contribution to the uncertainty in the calculations in Section 4.2 is the uncertainty in the distance $D$ (c.f. the discussion in Fender (2003)). For SS 433, we are fortunate to have a well measured distance value, confirmed by two entirely different methods. Firstly, fitting the precession model to the arcsecond-scale radio jets yields a distance of $5.5 \pm 0.2\,\mathrm{kpc}$ (Blundell and Bowler (2004)). This distance is consistent with the lower limit imposed on the distance by sensitive VLA measurements of HI in absorption at a line-of-sight speed of $75\,\mathrm{km\,s^{-1}}$; absorption at this speed precludes distances for SS433 below $5.5\,\mathrm{kpc}$ (Lockman et al.

(2007)), assuming the validity of Galactic gas rotation models (Dickey et al. (1983)). Moreover measurements of HI in emission, presented by Lockman et al. (2007) using the Green Bank Telescope, reveal interactions of gas at the same rotation speed (i.e. the same distance) with the W50 nebula that encloses SS 433. Most importantly, since this distance is inferred from HI and Galactic rotation curves, it is totally independent of any assumptions about SS 433's jet speeds; therefore our jet speed determinations on milliarcsecond-scales are not prejudiced by fits to the jet speeds on arcsecond scales. This gives us security in using the distance of Blundell and Bowler (2004).

In the inset panel to Figure 4.3(b) (and in Table 4.2), we have indicated the effect of the uncertainty in this distance $D$. The solid error bars assigned to each data point in the plot show the uncertainties only due to the statistical uncertainty (stat. unc.) in the fits to the proper motions $\mu_{\rm app}$ and $\mu_{\rm rec}$. The dotted error bar in the inset shows the scale of the uncertainties on each speed data point including the distance uncertainty (incl. dist. unc.), i.e., when the distance $D$ is allowed to be drawn from within the range $5.5 \pm 0.2\,$kpc. Since for all measurements, the object must lie at the same distance, the effect of this distance uncertainty is to give a systematic shift in the speed-axis values – the statistical error bars show the uncertainties on each point relative to one another, and give a truer reflection of our confidence that the jet bolides observed in the 2003 campaign show a significant variation in their launch speeds.

Figure 4.9 gives an alternative way to view this. Here, we plot the "distances" derived by inverting Equation 4.5 to obtain:

$$D = \frac{2c}{\mu_{\rm tot}} \frac{\sqrt{\beta_0^2 - \beta_\parallel^2}}{\left(1 - \beta_\parallel^2\right)}\,, \tag{4.30}$$

and then using the proper motions and line-of-sight velocities determined from the VLBA movie, and assuming that the bulk speed is a constant $\beta_0 = 0.2647$ for all bolides. In this picture, SS433 would have to move by $2\,$kpc in the course of these observations to explain the observed proper motions; it is a fairly safe bet that this does not happen. Instead, this shows that the intrinsic variation of the launch speed prevents the determination of the distance by assuming a fixed value of $\beta_0$.

The essential point here is that an error in distance measurement would manifest itself as a systematic error in the derived absolute launch speeds across all ejections. It would *not* change our most important overall conclusion: faster jet launch speeds occur during flaring episodes.

## 4.5 Summary & Conclusions

The two campaigns of VLBA observations have given us an unprecedented probe of SS 433's radio jet speeds on milliarcsecond scales. We have shown:

1. that flaring episodes are associated with faster launch speeds in the radio jets, just as their optical counterparts display elevated speeds in flares, as described in Blundell et al. (2011);
2. that there may be two quite different types of jet behaviour, with the 2003 campaign showing evidence for a flaring mode with a fast, bright jet consisting of compact, discrete ejections, and a quiescent jet consisting of slower bolides set within an apparently more continuous background ejection;
3. that the temporal resolution of the 2003 observations allows us to demonstrate that, in almost all cases, the jets show no evidence for deviations from ballistic motion; and
4. that the precession model parameters derived from optical jets by Eikenberry et al. (2001) do not provide a satisfactory description of the mean motion of the radio jets as seen in these observations.

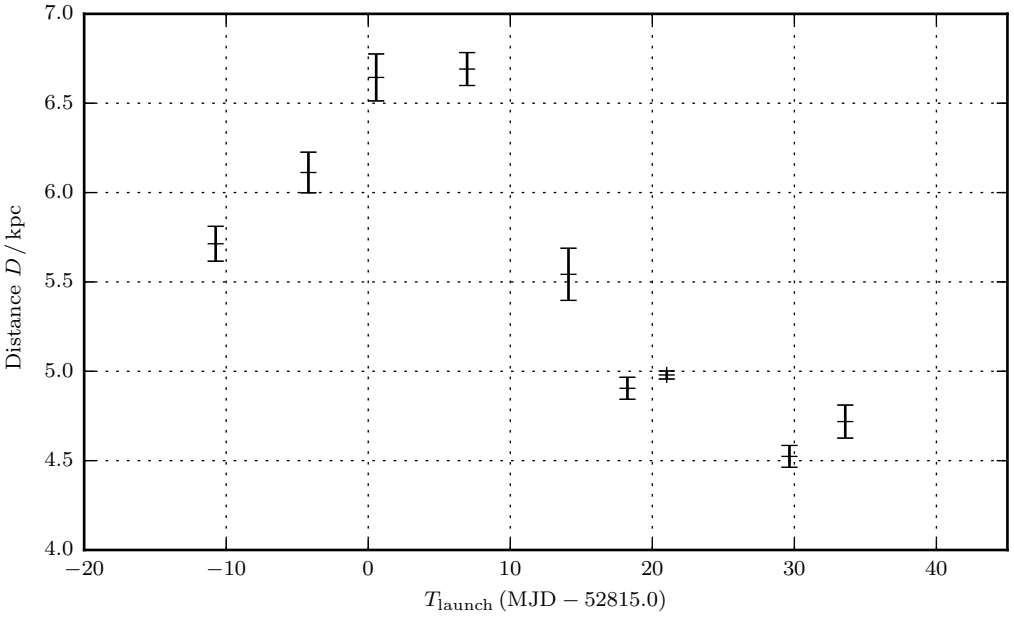


Figure 4.9: Supposing that the all bolides are launched with the same intrinsic speed $\beta = 0.2647$, the distance to the source as inferred from the observed proper motions would have to vary by 2 kpc. This not only comprehensively refutes the claim that all jet bolides possess the same intrinsic bulk speed, but also shows that closer distances (of perhaps 4.5 kpc) can easily be inferred if the bolides used to calculate these distances are launched with the slightly elevated speed of $0.3c$.

# Chapter 5

# The Evolution of Individual Jet Bolides I – A Resolved Pair of Bolides

## 5.1 Introduction

In the last Chapter, we used our time-resolved observations of the jets to uniquely determine the velocities of the ejected pairs of plasma bolides, under the assumption of symmetry between the jet and counterjet. We now want to explore the physical conditions within the bolides themselves. In particular, we will look at the nature of the emission at radio wavelengths, the mass of hydrogen in the bolides, and the evolution of the lightcurves of individual bolides as they expand and fade.

In Section 5.2, we use the spatially-resolved bolides seen in the 2012-01-08 observation to estimate the expansion rate of the jet bolides. We then consider the nature of the emission mechanism at work: in Section 5.3, we review some of the properties of synchrotron (magneto-bremsstrahlung) radiation; and in Section 5.4, we convert the observed flux densities into estimates of the internal number density and magnetic field, and discuss the implications for the assumption of equipartition of energies within the bolide.

## 5.2 The remarkable expansion of bolides in the 2012-Jan-28 map

The 2012-01-28 VLBA observation of SS 433 is shown in Figure 5.1. We have previously remarked on the remarkable degree to which the ejecta have expanded in the 36.7 days between the launch of these ejecta on MJD 55918.1 ± 0.6 and this observation on MJD 55954.75. Using the AIPS task `jmfit`, we have fitted Gaussians to the sky brightness distribution. The results are shown as the red ellipses in Figure 5.1, and are tabulated in Table 5.1.

### 5.2.1 The linear expansion rate of the bolides

We can estimate a linear expansion rate from these values. From the semi-major and semi-minor axes listed in Table 5.1, we see that a characteristic angular size for these particular bolides at $\Delta T = 36\,\mathrm{d}$ after launch is $\Delta\vartheta \sim 35\,\mathrm{mas}$. Converting this to a physical size at $5.5\,\mathrm{kpc} = 1.7\times10^{20}\,\mathrm{m}$ (the distance to SS 433), we find that these bolides are $\sim 2.8\times10^{13}\,\mathrm{m}$ in radius. By comparison, we expect the size of the bolides at launch to be of a similar scale to the inner regions of the accretion disc – i.e., a few times the Schwarzschild radius. For a black hole of $16\,\mathrm{M}_\odot$, the Schwarzschild radius $R_\mathrm{g} = 2GM/c^2 = (M/\mathrm{M}_\odot)\times 3\,\mathrm{km}$ is approximately $5\times10^4\,\mathrm{m}$. This is negligible in comparison with the radii observed in Figure 5.1, allowing us to estimate the expansion rate, assuming that the jets have initial size 0.[1]

Hence, given the distance to SS 433, we can estimate the expansion speed as:

$$v_\mathrm{exp} \simeq \frac{D\,\Delta\vartheta}{\Delta T} \simeq 0.032c \times \left(\frac{D}{5.5\,\mathrm{kpc}}\right) \times \left(\frac{\Delta T}{\mathrm{d}}\right)^{-1} \times \Delta\vartheta_\mathrm{mas} \tag{5.1}$$

where $\Delta T$ is the timestep between launch and observation, and $\Delta\vartheta_\mathrm{mas}$ is the angular size in milliarcseconds, and we have expressed this in terms of the speed of light, $c$. Note that we have neglected relativistic effects – for an object moving close to the speed of light, we would have to convert the observer time $T$ to a proper time in the rest frame of the jet, and then calculate the

[1] Modelling of the x-ray jets by, for example, Kotani et al. (1996) and Kotani et al. (2006) has been used to argue that the size of the base of the x-ray emitting jet may be perhaps 2-3 orders of magnitude larger than the Schwarzschild radius, with estimates of $\gtrsim 3\times10^7\,\mathrm{m}$. These are inferred by arguing that the jets must be optically thin at their base to explain the observed widths of the Fe XXV lines. This argument assumes that we see the base of the x-ray jets, which, as we discuss in Chapter 7, may not be the case. Irrespective of this, these estimates are still several orders of magnitude smaller than that observed in the 2012-01-28 observation – they are still negligible in comparison, and don't affect our estimates of the expansion speed.

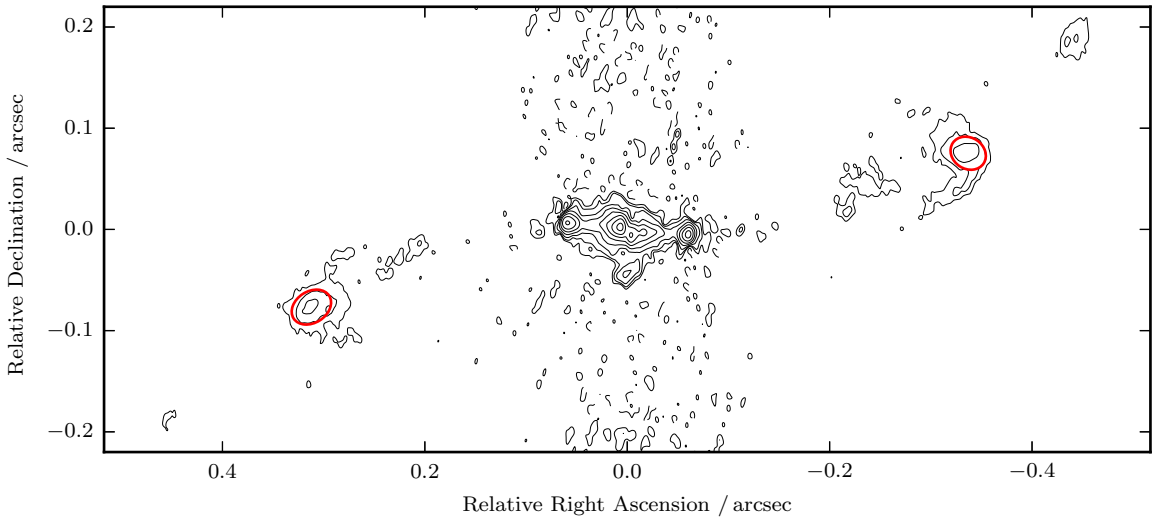


Figure 5.1: The 2012-01-28 observation. The bolide pair identified in Section 4.3.1 as pair B are resolved. The results of Gaussian fits to this radiance distribution obtained using AIPS task `JMFIT` are shown – the corresponding fit values are given in Table 5.1.

| | Jet | Counter-jet |
|---|---|---|
| Relative RA / mas | $312.11 \pm 0.47$ | $-336.92 \pm 0.33$ |
| Relative Dec / mas | $-76.77 \pm 0.42$ | $75.29 \pm 0.31$ |
| Peak intensity / mJy bm$^{-1}$ | $0.877 \pm 0.025$ | $1.218 \pm 0.027$ |
| Integrated intensity / mJy | $26.24 \pm 0.77$ | $31.68 \pm 0.73$ |
| Major Axis / mas | $41.7 \pm 1.2$ | $36.7 \pm 0.8$ |
| Minor Axis / mas | $31.1 \pm 0.9$ | $30.8 \pm 0.7$ |
| Position Angle | $122.7° \pm 3.9°$ | $56.2° \pm 5.2°$ |

Table 5.1: Gaussian fits to the pair of bolides indicated in Figure 5.1. The fits were obtained using the AIPS task `JMFIT`. Note that the position angle is here measured counter-clockwise from North, differing from the convention we have used elsewhere. The area of the clean beam used is 15.8 mas × 7.0 mas, at a position angle of 0.2° – i.e., the bolides, which are much larger than this, are resolved.

| | |
|---|---|
| Bulk speed $\beta = v/c$ | $0.289 \pm 0.017$ |
| Angle to line-of-sight $\eta$ | $97.5° \pm 8.8°$ |
| Jet position angle $\chi$ | $13.28° \pm 0.05°$ |

Table 5.2: The velocity vector of the jet bolide highlighted in Figure 5.1. The bulk speed $\beta$ is as derived in Section 4.3.1, the line-of-sight angle $\eta$ follows from $\beta_{\parallel} = \beta \cos \eta$, and the position angle (measured from the east parallel) is the angle connecting the two bolides.

expansion rate in the rest frame. For SS 433, whose jets are only mildly relativistic, this is a small correction.

So, from the angular size we see in Figure 5.1 ($\Delta\vartheta \simeq 30\,\mathrm{mas}$ at $\Delta T = 36\,\mathrm{d}$), we can see that the expansion speed of these bolides must be $v_{\mathrm{exp}} \simeq 0.03\,c$.

This is a remarkably high expansion rate. It is far in excess of any plausible thermal speed, but it is not completely unreasonable. High expansion speeds ($\sim 0.005c$) were estimated from the broadening of optical lines by Blundell et al. (2007), so, though our estimate here is almost an order of magnitude higher, there is existing evidence for supersonic expansion speeds. We also note the estimates of the opening angle for the conical outflow believed to form the X-ray emitting base of the jets. If the outflow is conical, then the expansion rate derived here can be converted to an equivalent opening angle of 6°. This is greater by a factor of 2-4 than existing estimates from Doppler-broadening of X-ray lines (e.g., 1.°22 (Marshall et al. (2002)), 1.°2 (Fabrika (2004)), 2.°5 (Kotani et al. (1996)), or 2.°7 (Lopez et al. (2006))). This would either require that the expansion rate increases after passing the X-ray and optically-emitting regions (and indeed, woiuld have to be even faster than the estimate above once the expansion begins), or suggest that these bolides are exceptional.

Lastly, we note that this is the first time that expansion of this size has been observed in VLBI observations of SS 433 – indeed in none of our other images have we seen bolides this extended, although we note the difficulties inherent in imaging extended objects with the sparse coverage of the inner regions of the $u$-$v$ plane given by the VLBA. This points towards this pair being somewhat anomalous in their high expansion rate. Even if so, then we have still shown that the bolides *can* expand as fast as $0.03c$.

### 5.2.2 The bolide emissivity

To probe the properties of the bolides, we would like to estimate the emissivity of the bolides (i.e., the energy per unit time per unit volume per unit frequency that is lost as radiation) from the integrated intensities.

#### 5.2.2.1 Doppler beaming

It is a well known result (e.g., Scheuer and Readhead (1979); see Rybicki and Lightman (1979), Begelman et al. (1984) or Longair (2011) for textbook treatments) that the flux density received from relativistically moving sources is strongly anisotropic. Relative to its angular distribution in the rest frame, the emission is boosted into a cone pointing along the direction of the motion, and is suppressed away from this axis. The form of this suppression is by some power of the *Doppler factor*, $\mathcal{D}$, where:

$$\mathcal{D} := \frac{1}{\gamma\left(1 - \beta\cos\eta\right)} \tag{5.2}$$

and where $\gamma = \left(1-\beta^2\right)^{-1/2}$ is the Lorentz factor, and $\eta$ is the angle between the line of sight and the velocity vector of the source as seen in the observer's rest frame. This is discussed in more detail in Box 5.1.

For ultrarelativistic objects, this effect can lead to several orders of magnitude difference between the apparent brightnesses of components in the approaching and receding jets (as seen, for instance, in imaging of quasars by Bridle et al. (1994), and the corresponding brightness ratios reported in Wardle and Aaron (1997)). However, with speeds of only $\beta c \simeq 0.26c$, the jets of SS 433 are only mildly relativistic sources. Consequently, the effect of Doppler beaming is only small. The flux ratio will vary as the jet and counterjet precess, and the range of flux ratios can be estimated from the Kinematic model. Using the geometry outlined in Section 2.2, we can see that the range of angles to the line of sight is $\eta \in [i_0 - \Theta_0, i_0 + \Theta_0]$, where $i_0$ is the angle between the jet cone axis and the line-of-sight, and $\Theta_0$ is the opening angle of the precession cone. Taking the canonical values of Eikenberry et al. (2001) (i.e., $\beta = 0.2647$, $i_0 = 78.05°$, and $\Theta_0 = 20.92°$), we have:

$$\frac{\mathcal{D}_{\rm jet}}{\mathcal{D}_{\rm cjt}} = \frac{1+\beta\cos\eta}{1-\beta\cos\eta} \in [0.92, 1.34] \tag{5.3}$$

This is illustrated more concretely in Table 5.3, where we calculate the values of the beaming factor using the known values of $\beta$ and $\beta\cos\eta$ that we calculated for the bolide pair highlighted in Figure 5.1. Since the bolide pair are launched close to orthogonal to the line-of-sight, the value of the beaming effect is on the order of 10% to 20% even for the most extreme exponents. This is a small enough effect that it will often prove to be almost negligible.

**Box 5.1: Doppler beaming of emission with a power law spectrum**

Doppler beaming is most easily explained for an unresolved point source. Then, we can define *spectral intensity* as the power received per unit solid angle per unit frequency:

$$I_\nu := \frac{\mathrm{d}\mathcal{E}}{\mathrm{d}\nu\,\mathrm{d}\Omega\,\mathrm{d}T}$$

where $\mathrm{d}\mathcal{E}$ is the energy received, $\mathrm{d}T$ is the time interval measured by the astronomer on Earth, $\mathrm{d}\nu$ is frequency, and $\mathrm{d}\Omega \equiv \sin\theta\,\mathrm{d}\theta\,\mathrm{d}\phi$ denotes solid angle. Note that here, as in the derivation in chapter 22 of Longair (2011), intensity is used in the strict radiometric sense, rather than in the more common usage in astronomy, namely flux density (power per unit area) per unit solid angle per unit frequency; the two definitions converge for a point source. In general, this will be a function of frequency $\nu$ and of the unit vector relating the source and the detector.

Suppose that the intensity of the (point) source in its own rest frame, $S'$ is $I'_\nu(\nu', \theta', \phi') = \mathrm{d}\mathcal{E}' / (\mathrm{d}\nu'\,\mathrm{d}\Omega'\,\mathrm{d}\tau)$, where $\tau$ denotes proper time. These quantites are related to their equivalents in frame $S$ by:

$$\mathrm{d}\nu' = \mathcal{D}^{-1}\,\mathrm{d}\nu \qquad \mathrm{d}\Omega' = \mathcal{D}^2\mathrm{d}\Omega$$
$$\mathrm{d}\tau = \mathcal{D}\,\mathrm{d}T \qquad \mathrm{d}\mathcal{E}' = \mathcal{D}^{-1}\,\mathrm{d}\mathcal{E}$$

where $\mathcal{D} := 1/(\gamma(1 - \beta\cos\eta))$ is the Doppler factor. Proofs of these results are given in Rybicki and Lightman (1979), pp140-1, or Begelman et al. (1984). Combining these four results with the definitions of intensity, we find:

$$I_\nu(\nu) = \frac{\mathrm{d}\mathcal{E}}{\mathrm{d}T\,\mathrm{d}\nu\,\mathrm{d}\Omega} = \frac{\mathcal{D}^{-1}\mathrm{d}\mathcal{E}}{\mathcal{D}^{-1}\mathrm{d}\tau\,\mathcal{D}^{-1}\mathrm{d}\nu'\,\mathcal{D}^{-2}\mathrm{d}\Omega'} = \frac{\mathcal{D}^{-1}}{\mathcal{D}^{-4}}\frac{\mathrm{d}\mathcal{E}'}{\mathrm{d}\tau\,\mathrm{d}\nu'\,\mathrm{d}\Omega'} = \mathcal{D}^3 I'_\nu(\nu')$$

where the frequencies $\nu' = \mathcal{D}^{-1}\nu$ are related by the Doppler shift. In particular, in the case where the intensity spectrum is a power law, i.e., $I'_\nu \propto \nu'^{-\alpha}$, then we can relate the emission in frame $S'$ at frequencies $\nu_{\mathrm{em}}$ and $\nu_{\mathrm{obs}}$ by:

$$\frac{I'_\nu(\nu' = \nu_{\mathrm{em}})}{I'_\nu(\nu' = \nu_{\mathrm{obs}})} = \left(\frac{\nu_{\mathrm{em}}}{\nu_{\mathrm{obs}}}\right)^{-\alpha} = \left(\frac{\mathcal{D}^{-1}\,\nu_{\mathrm{obs}}}{\nu_{\mathrm{obs}}}\right)^{-\alpha} = \mathcal{D}^{+\alpha}$$

allowing us to obtain the relationship between intensities at the same frequency $\nu_{\mathrm{obs}}$ in

frames $S$ and $S'$ as:

$$\frac{I_\nu\left(\nu=\nu_{\rm obs}\right)}{I'_\nu\left(\nu'=\nu_{\rm obs}\right)} = \frac{I_\nu\left(\nu=\nu_{\rm obs}\right)}{I'_\nu\left(\nu'=\nu_{\rm em}\right)}\frac{I'_\nu\left(\nu'=\nu_{\rm em}\right)}{I'_\nu\left(\nu'=\nu_{\rm obs}\right)} = \mathcal{D}^{3+\alpha}\,.$$

For an extended source, this becomes more complicated. In the case where a jet is a continuous beam, rather than a series of point sources, then the Doppler exponent is reduced to give $\mathcal{D}^{2+\alpha}$.

#### 5.2.2.2 Converting "Integrated Intensity" to emissivity

In Table 5.1, we give the "integrated intensities" of the bolides as returned by AIPS task `JMFIT`. This is the spectral radiance (often referred to as the specific intensity) integrated across the solid angle of sky containing the Gaussian fit to the bolide – i.e., it is the flux density received from the bolide. We want to convert this to an emissivity. Assuming that the emission in the rest frame is isotropic and that the source is optically thin, this can be written as:

$$S_\nu = \mathcal{D}^{3+\alpha}\frac{V\varepsilon_\nu}{4\pi D^2} \tag{5.4}$$

where $S_\nu$ is the integrated intensity, $\varepsilon_\nu$ is the spectral emissivity (power radiated per unit frequncy per unit volume: note that this quantity should appear in the primed frame; from here on we drop the primes), $\mathcal{D}$ is the Doppler beaming factor as defined above, $\alpha$ is the spectral index of the radiation such that $\varepsilon_\nu \propto \nu^{-\alpha}$, $V$ is the volume of the emitting region, and $D$ is the distance to the object.

We will approximate the volume by a sphere.[2] Expressing the radius of this region in terms of the angular size $\vartheta$ and the distance to the object $D$, we can write the volume:

$$V \simeq \frac{4\pi}{3}\left(\vartheta\, D\right)^3 \qquad\qquad \frac{V}{\rm m^3} \simeq 2.345\times10^{36}\times\vartheta^3_{\rm mas}\left(\frac{D}{5.5\,{\rm kpc}}\right)^3 \tag{5.5}$$

where $\vartheta_{\rm mas}$ is the angular radius of the bolide in milliarcseconds.[3] Then, inserting these into

[2]Strictly, this is an approximation that we can only make in relation to our source if it is either a) unresolved, or b) non-relativistic. In fact, we have been slightly casual in assuming that the integral over the solid angle subtended by the source of a quantity (i.e., the radiance) which is itself an integral over the depth along the line-of-sight is proportional to a volume integral (i.e., we have assumed that $\int {\rm d}^2\Omega \int {\rm d}x\, \varepsilon_\nu \propto \int {\rm d}^3{\rm Vol}\, \varepsilon_\nu$). Relativistic distortion can break this, but will only introduce a small error for a mildly relativistic source like SS 433.

[3]In the following, we will use the geometric mean of the semi-major and semi-minor axes of the fitted Gaussians reported by AIPS task `JMFIT` as the angular radius of the bolide. As can be seen from Figure 5.1, these fitted Gaussians give a reasonable approximation to the expanded components.

Equation 5.4, we have:

$$\frac{S_\nu}{\mathrm{Jy}} \simeq \mathcal{D}^{3+\alpha} \times 3.80 \times 10^{-6}\, \vartheta_{\mathrm{mas}}^3 \left(\frac{D}{5.5\,\mathrm{kpc}}\right) \frac{\varepsilon_\nu}{10^{-26}\,\mathrm{W\,m^{-3}\,Hz^{-1}}} \tag{5.6}$$

which can be inverted to express $\varepsilon_\nu$ in terms of known quantities $S_\nu$, $\mathcal{D}$, the distance $D = 5.5 \pm 0.2\,\mathrm{kpc}$, and $\vartheta_{\mathrm{mas}}$ (we will make appropriate assumptions when needed about the spectral index $\alpha$).

## 5.3 Review of synchrotron radiation

In the next section, we will interpret the emissivities derived above in terms of an optically-thin, quasi-neutral, magnetised, hydrogen plasma. Before doing so, let us briefly review the properties of synchrotron radiation.

### 5.3.1 Electron power law energy spectrum

We will assume that the synchrotron emission arises from a population of relativistic electrons with a power law distribution of energies. Here, we summarise what this means. Derivations of the essential physics here are also given in a number of sources (e.g., Longair (2011) or Rybicki and Lightman (1979)). Our purpose in reproducing the argument is to highlight the under-appreciated role of the low energy cutoff in the electron energy spectrum.

Let us begin by defining what we mean by the power law energy spectrum.

**Definition 5.3.1** (Electron Energy Spectral Index)**.** A power law electron energy spectrum, $n_\mathcal{E}$, with a spectral index $p$ is defined by the function:

$$n_\mathcal{E} = \begin{cases} \kappa\, \mathcal{E}^{-p} & \mathcal{E} \in [\mathcal{E}_0, \infty) \\ 0 & \text{otherwise} \end{cases} \tag{5.7}$$

where $n_\mathcal{E}$ is the number of electrons per unit volume per unit energy, $\mathcal{E}_0$ is the low-energy cutoff, and $\kappa$ is a normalisation constant.

We note that $\mathcal{E}_0$ can only take values greater than or equal to the electron rest energy $m_e c^2$ (i.e., $\gamma_0 \geq 1$), and we note that, for the energy spectrum to have a well-defined mean, the spectral index

must satisfy $p > 2$. We have also assumed that there is no high-energy cutoff. This should be ok if the spectral index is high enough that the highest energy electrons are a small correction. We can evaluate $\kappa$ by introducing the total electron number density, $n$, as follows.

**Result 5.3.2** (Total Electron Density)**.** The number density of electrons is the total number of electrons of all energies in a unit volume. i.e.,

$$n := \int_{m_e c^2}^{\infty} n_{\mathcal{E}} \, \mathrm{d}\mathcal{E} = \frac{1}{(p-1)} \frac{\kappa}{{\mathcal{E}_0}^{p-1}} \tag{5.8}$$

Equivalently, this can be rearranged to give the normalisation constant, $\kappa$:

$$\kappa = n \, (p-1) \, {\mathcal{E}_0}^{p-1} \tag{5.9}$$

*Proof.* From the definition of the spectral index:

$$n = \int_{m_e c^2}^{\infty} n_{\mathcal{E}} \, \mathrm{d}\mathcal{E} = \int_{\mathcal{E}_0}^{\infty} \kappa \, \mathcal{E}^{-p} \, \mathrm{d}\mathcal{E} = \left[ \frac{\kappa \mathcal{E}^{-p+1}}{-p+1} \right]_{\mathcal{E}_0}^{\infty} = \frac{1}{(p-1)} \frac{\kappa}{{\mathcal{E}_0}^{p-1}}$$

where in the second step we have used $n_{\mathcal{E}} = 0$ for $\mathcal{E} \in \left[ m_e c^2, \mathcal{E}_0 \right)$, and in the final step we have used $\lim_{\mathcal{E} \to \infty} \mathcal{E}^{-p+1} = 0$ for $p > 2$. □

In the calculations that follow, it will prove more useful to work in terms of the Lorentz factor. The electron energy spectrum in terms of the Lorentz factor is given by Result 5.3.3.

**Result 5.3.3.** The electron energy spectrum can be written in terms of the electron Lorentz factor, $\gamma = \frac{\mathcal{E}}{m_e c^2}$:

$$n_\gamma = \begin{cases} \frac{n \, (p-1)}{\gamma_0} \left( \frac{\gamma}{\gamma_0} \right)^{-p} & \gamma \in [\gamma_0, \infty) \\ 0 & \gamma \in [1, \gamma_0) \end{cases} \tag{5.10}$$

where $\gamma_0$ is the low energy cutoff, and $n$ is the total number of electrons per unit volume.

*Proof.* To change variables between $n_\gamma$ and $n_{\mathcal{E}}$, we note that $n_\gamma \, \mathrm{d}\gamma = n_{\mathcal{E}} \, \mathrm{d}\mathcal{E}$. Then, by considering

the non-zero part of $n_{\mathcal{E}}(\mathcal{E})$, we find

$$\begin{aligned} n_\gamma(\gamma) &= n_{\mathcal{E}}\left(\mathcal{E} = \gamma mc^2\right) \times \frac{\mathrm{d}\mathcal{E}}{\mathrm{d}\gamma} \\ &= \kappa\left(\gamma mc^2\right)^{-p} mc^2 \\ &= n(p-1)\left(\gamma_0 mc^2\right)^{p-1}\gamma^{-p}\left(mc^2\right)^{-(p-1)} \\ &= n(p-1)\gamma_0^{p-1}\gamma^{-p} \\ &= \frac{n(p-1)}{\gamma_0}\left(\frac{\gamma}{\gamma_0}\right)^{-p} \end{aligned}$$

where throughout we have used $\mathcal{E} = \gamma m_e c^2$. □

Finally, we will need the total energy density stored in the rest mass and kinetic energy of these relativistic electrons.

**Result 5.3.4** (Energy Density in Relativistic Electrons)**.** The total energy density in relativistic electrons for a power law energy spectrum of electrons is:

$$u_e = n\frac{p-1}{p-2}\gamma_0 m_e c^2 \tag{5.11}$$

*Proof.* The total energy density in relativistic electron is:

$$u_e = \int_1^\infty \gamma m_e c^2\, n_\gamma\, \mathrm{d}\gamma$$

where the integration is carried out over all possible values of Lorentz factor $\gamma$ (i.e., over the interval $[1,\infty)$). For a power law distribution of energy density as given in Result 5.3.3, the integrand is 0 below the minimum energy cutoff $\gamma_0$. The range of integration becomes $[\gamma_0,\infty)$, giving:

$$\begin{aligned} u_e &= \int_{\gamma_0}^\infty n(p-1)\, m_e c^2 \frac{\gamma}{\gamma_0}\left(\frac{\gamma}{\gamma_0}\right)^{-p}\mathrm{d}\gamma \\ &= n(p-1)\, m_e c^2\left[\frac{\gamma_0}{-p+2}\left(\frac{\gamma}{\gamma_0}\right)^{-p+2}\right]_{\gamma_0}^\infty \\ &= n\frac{p-1}{p-2}\gamma_0 m_e c^2 \end{aligned}$$

where we require that $p > 2$ for the integral to be bounded at infinity. □

It is worth considering certain limiting cases of this expression for a moment to examine its

meaning. In the case of a very steep power law spectrum (i.e., $p \to \infty$), then the population becomes sharply peaked at the cutoff energy, $\gamma_0 m_e c^2$, and the energy density is just the number density times this energy (as $\lim_{p\to\infty} \frac{p-1}{p-2} = 1$). If we further take the limit $\gamma_0 \downarrow 1$, this becomes the rest energy density. Indeed, since $\gamma_0 \frac{p-1}{p-2} > 1$ for $\gamma_0 > 1$, $p > 2$, the energy density is greater than the rest energy, as it ought to be. Lastly, if we consider the opposite limit of a flat spectrum, $p \downarrow 2$, then the total energy density becomes very large – there is a large population of very high energy electrons with $\gamma \gg 1$, making a large contribution to the total energy density.

### 5.3.2 Synchrotron emission

The derivation of the synchrotron spectrum from a power law distribution of electron energies can also be found in textbooks (e.g., Longair (2011), Rybicki and Lightman (1979)). The key result is as follows.

**Result 5.3.5** (Synchrotron Emissivity)**.** The emissivity due to synchrotron radiation from a hydrogen plasma with a power law of spectral energies is:

$$\varepsilon_\nu(\nu) = \frac{\sqrt{3}}{4} \frac{a(p)\,(p-1)}{(p+1)} \frac{e^2}{\epsilon_0 c} {\gamma_0}^{(p-1)}\, n \left(\frac{eB}{2\pi m_\mathrm{e}}\right) \left(\frac{\nu}{3}\frac{2\pi m_\mathrm{e}}{eB}\right)^{-(p-1)/2} \tag{5.12}$$

where

$$a(p) := \frac{\sqrt{\pi}\,\Gamma\left(\frac{3p+19}{12}\right)\Gamma\left(\frac{3p-1}{12}\right)\Gamma\left(\frac{p+5}{4}\right)}{\Gamma\left(\frac{p+7}{4}\right)}$$

$\nu = 1.6\,\mathrm{GHz}$ is the observation frequency, and $p$ and $\gamma_0$ are the spectral index and low energy cutoff in the energy distribution of relativistic electrons.

The full derivation is given on page 213 of Longair (2011) – the above equation is given there as equation 8.88, with the substitution $\kappa = n(p-1)\left(\gamma_0 m_e c^2\right)^{(p-1)}$ to replace the normalisation constant with the physically relevant quantities of electron number density and the energy spectrum cutoff (see Result 5.3.2).

It is worth pausing briefly to consider where this equation has come from. The power radiated per unit frequency interval for a single electron travelling with Lorentz factor $\gamma$ and at a pitch angle

$\zeta$ to the magnetic field is:

$$j_\nu(\nu,\gamma,\zeta) = \frac{\sqrt{3}}{2}\frac{e^2}{\epsilon_0 c}\frac{eB}{2\pi m_e}\sin\zeta\, F\left(\frac{\nu}{\nu_c(\gamma)}\right) \tag{5.13}$$

where $F(x) := x\int_x^\infty \mathrm{d}z\, K_{5/3}(z)$, and $\nu_c := \frac{3}{2}\gamma^2\frac{eB}{2\pi m_e}\sin\zeta$ (see equation 8.58 of Longair (2011) or equation 6.16 of Rybicki and Lightman (1979)). Then, the total energy emitted per unit volume per unit time per unit frequency is this integrated over all electron energies and averaged over all pitch angles. i.e.,

$$\varepsilon_\nu(\nu) = \int_0^\pi \mathrm{d}\zeta\, \tfrac{1}{2}\sin\zeta\int_{\gamma_0}^\infty \mathrm{d}\gamma\, n_\gamma(\gamma)\, j_\nu(\nu,\gamma,\zeta) \tag{5.14}$$

where the electron energy distribution, $n_\gamma(\gamma)$ is given by Result 5.3.3. This integration is usually performed by introducing a new variable $x := \nu/\nu_c = A\gamma^{-2}$, and changing variables in the integration to integrate over $x$ instead of $\gamma$. However, in both Rybicki and Lightman (1979) and Longair (2011) this is only solved approximately by setting the integration limits to $x \in [0,\infty)$. This is not valid for general values of the parameters $\nu$, $\gamma_0$, and $B$. The correct mapping of the integration limits should be $x(\gamma_0) = A{\gamma_0}^{-2}$ and $x(\infty) = 0$. Using $\nu_c = \frac{3}{2}\gamma^2\frac{eB}{2\pi m_e}\sin\zeta$, it is then clear that the upper limit of the integration can only be approximated by infinity if $A{\gamma_0}^{-2} \gg 1$, meaning that $\nu \gg \frac{3}{2}{\gamma_0}^2\frac{eB}{2\pi m_e}\sin\zeta$. Using $e/2\pi m_e = 27.992\,\mathrm{GHz\,T^{-1}}$, we have the rough condition that $(\nu\,/\,\mathrm{GHz}) \gg 40\,{\gamma_0}^2\,(B\,/\,\mathrm{T})$. Clearly, if $\gamma_0 \sim 10^3$ and $B \sim 10^{-10}\,\mathrm{T}$, then the approximation in Rybicki and Lightman (1979) is alright. If, on the other hand, $\gamma_0 \sim 10^3$ and $B \sim 10^{-6}\,\mathrm{T}$, we should probably revisit this integral.

Finally, we will need the numerical form for the emissivity. Rearranging Result 5.3.5, we can write:

$$\varepsilon_\nu(\nu) = \sqrt{3}\,b(p)\,{\gamma_0}^{(p-1)} n\,\alpha_{\mathrm{FS}}\,\mu_B\,B\left(\frac{h\nu}{6\mu_B B}\right)^{-(p-1)/2} \tag{5.15}$$

where $b(p) := \frac{a(p)\,(p-1)}{(p+1)}$. We have also introduced the Fine-Structure Constant, $\alpha_{\mathrm{FS}} = e^2/(4\pi\epsilon_0\hbar c)$, with value ${\alpha_{\mathrm{FS}}}^{-1} = 137.035999139(31)$ and the Bohr Magneton with value $\mu_B = e\hbar/(2m_e) = 927.4009994(57)\times10^{-26}\,\mathrm{J\,T^{-1}}$ (numerical values from Mohr et al. (2015)). Inserting these values,

and noting that $\mu_B/h = \frac{e}{4\pi m_e} = 13.996245042(86)\,\mathrm{GHz\,T^{-1}}$, we have:

$$\left(\frac{\varepsilon_\nu}{10^{-26}\,\mathrm{W\,m^{-3}\,Hz^{-1}}}\right) = 11.722\,b\,(p)\;{\gamma_0}^{(p-1)}\;\left(\frac{n}{\mathrm{m^{-3}}}\right)\left(\frac{\nu}{83.977\,\mathrm{GHz}}\right)^{-(p-1)/2}\left(\frac{B}{\mathrm{T}}\right)^{(p+1)/2} \tag{5.16}$$

Over the relevant range of values of $p$, $b\,(p) \simeq 1$.

## 5.4 What is the nature of the emission?

### 5.4.1 Synchrotron emissivity

In the preceding Section, we obtained an expression for the power radiated per unit volume per unit frequency interval as synchrotron emission in a quasi-neutral hydrogen plasma with a power law spectrum of electron energies. It contains 4 unknown quantities: electron energy index $p$, the low energy cutoff $\gamma_0$, the number density of relativistic electrons $n$, and the magnetic field $B$. We would like to make appropriate assumptions to allow us to estimate $n$ and $B$. As we are reducing 4 unknowns to 1, we will need 3 additional statements.

First, the electron index, $p$. This is related to the spectral index of the emissivity by $\alpha = (p-1)/2$. For SS 433, Stirling et al. (2004) found spectral indices that lay in the interval $[0.6, 0.8]$ for bolides further than $\sim 50\,\mathrm{mas}$ from the core. Blundell et al. (1999) find that many extragalactic radio sources possess spectral indices in the interval $[0.5, 0.8]$, though they also find ultra-steep spectra with indices as high as $\alpha = 1.6$. In much of what follows, we will take $\alpha = 0.6$ as a fixed value for the spectral index, and hence an electron energy power law index $p \simeq 2.2$. We return briefly to this in Sections 5.4.1.3 and 5.4.1.4.

The spectral cutoff is a significant unknown in this problem, and one which is ill-constrained. Often an arbitrary choice is made for $\gamma_0$, although there is no consensus around what value should be selected. Indeed, Blundell et al. (2006) cite examples in the literature where $\gamma_0$ is chosen to take values ranging from $\gamma_0 = 1$ all the way to $\gamma_0 = 10^3$. They themselves estimate an even higher value $\gamma_0$, perhaps as high as $10^4$. This is obtained from the consideration of inverse Compton scattering of CMB photons to X-ray energies by spent relativistic electrons in the lobe of a radio galaxy. Observing inverse compton scattered CMB photons at keV energies implies the presence of a population of electrons with $\gamma \sim 10^3$. Since they observe X-ray emission only from the lobe and

not from the hotspot, they argue that this requires the cutoff in the hotspot to exceed $\gamma_0 \gtrsim 10^4$, with the adiabatic expansion of the plasma as it moves away from the lobe reducing the cutoff such that $\gamma_0 \lesssim 10^3$. Notwithstanding this observation, equipartition of energy between a (non-relativistic, cold) population of protons and a relativistic population of electrons would suggest $\gamma_0 \sim m_p/m_e$ (Perlman et al. (2010)); simulations give some support for this value (Spitkovsky (2008)).

In our case, we are left with $\gamma_0$ as an essentially unconstrained parameter. In general, we will show explicit dependencies, rather than evaluating for an arbitrary choice of $\gamma_0$.

So, we have dealt with (or dodged the need to deal with) two of the three required constraints. For the third, we will consider the energetics of the plasma.

In Box 5.2, we outline two possible relations that enable us to relate magnetic energy $u_m$ and electron energy $u_e$. These are: 1) assuming equipartition of energy, such that $u_e = u_m$; and 2) seeking to minimise the total energy subject to the constraint that the emissivity at given frequency is fixed. In both cases, the resulting relation takes the form $u_m = A\,u_e$, where $A = 1$ in equipartion, and $A = \frac{p+1}{4}$ when the total energy is minimised. With this definition, we can write:

$$B = (2\mu_0\, A\, u_e)^{1/2} = \left(\gamma_0 \left(\frac{n}{\mathrm{m}^{-3}}\right) \times A\,\frac{p-1}{p-2}\right)^{1/2} \times 4.536 \times 10^{-10}\,\mathrm{T} \tag{5.17}$$

where $A = 1$ in the equipartition case, and $A = (p+1)/4$ in the minimum energy case.

Inserting this into Equation 5.16, we can eliminate $B$ (or $n$), and then evaluate $n$ (and hence $B$) as a function only of the electron energy cutoff $\gamma_0$. The (rather uninsightful) expressions are:

$$\begin{aligned}\left(\frac{n}{\mathrm{m}^{-3}}\right)\,{\gamma_0}^{(5p-3)/(p+5)} = &\left(A\,\frac{p-1}{p-2}\right)^{-(p+1)/(p+5)} \times \left(11.722 \times \left(2.130 \times 10^{-5}\right)^{p+1} \times b\,(p)\right)^{-4/(p+5)} \\ &\times \left(\frac{\nu}{83.977\,\mathrm{GHz}}\right)^{2(p-1)/(p+5)} \times \left(\frac{\varepsilon_\nu}{10^{-26}\,\mathrm{W\,m^{-3}\,Hz^{-1}}}\right)^{4/(p+5)}\end{aligned} \tag{5.21}$$

for the number density; and

$$\begin{aligned}\left(\frac{B}{\mathrm{T}}\right)\,{\gamma_0}^{(2p-4)/(p+5)} = &\frac{4.536 \times 10^{-10}}{\left(11.722 \times (2.130 \times 10^{-5})^{p+1} \times b\,(p)\right)^{2/(p+5)}} \times \left(A\,\frac{p-1}{p-2}\right)^{2/(p+5)} \\ &\times \left(\frac{\nu}{83.977\,\mathrm{GHz}}\right)^{(p-1)/(p+5)} \times \left(\frac{\varepsilon_\nu}{10^{-26}\,\mathrm{W\,m^{-3}\,Hz^{-1}}}\right)^{2/(p+5)}\end{aligned} \tag{5.22}$$

for the magnetic field density.

**Box 5.2: Energetic balance in a synchrotron radiating plasma**

The total energy density of our magnetised plasma is the sum of the magnetic energy $u_m$ and the energy (both rest mass and kinetic) in the relativistic electron population, $u_e$. i.e.,

$$u := u_m + u_e = \frac{B^2}{2\mu_0} + n\,\frac{p-1}{p-2}\,\gamma_0 m_e c^2 \tag{5.18}$$

where we have invoked Result 5.3.4 for the electron energy density. Note that we have disregarded the contribution to the energy from the (cold) proton population needed to ensure quasi-neutrality of the plasma bolide. This would introduce a term $u_p = nm_pc^2$.

Our observations constrain the synchrotron emissivity. This is given by Result 5.3.5, which we rewrite as:

$$\varepsilon_\nu = C\,(p,\nu)\;{\gamma_0}^{(p-1)}\,n\,B^{(p+1)/2} \tag{5.19}$$

where $C\,(p,\nu)$ encapsulates the variation with electron spectral index and observation frequency, and is not important in the present argument.

Both the total energy and the emissivity are functions of two physical quantities (magnetic field density $B$ and electron number density $n$), and the two parameters of the electron power law spectrum ($\gamma_0$ and $p$). In principle, $p$ is uniquely determined by the frequency spectral index of $\varepsilon_\nu$. We will treat $\gamma_0$ as a (given) constant.

Rearranging Equation 5.18, we can use Equation 5.19 to eliminate either $B$ or $n$, giving us an expression for the total energy density in terms of a single physical parameter. This is shown in Figure 5.2, where we plot the energy density as a function of $B$ (left panel), and $n$ (right panel). The various quantities are normalised to their values at equipartition of energy (i.e., $u_e = u_m$). The total energy has a minimum close to the values of $B$ and $n$ for which energy is equally divided between relativistic electrons and magnetic fields. The exact value of that minimum can be determined using a Lagrange multiplier.

**Result 5.4.1** (Minimum energy of the synchrotron spectrum)**.** For a given value of the emissivity $\varepsilon_\nu$ and a fixed low energy cutoff $\gamma_0$ in the electron energy spectrum, the total energy, $u$ is minimised when:

$$u_e = \frac{4}{p+1}\,u_m \tag{5.20}$$

where $p$ is the electron energy spectral index.

*Proof.* Write $u(n,B) = a_1 n + a_2 B^2$ and $g(n,B) = a_3\, n\, B^{(p+1)/2}$. Then, letting $f(n,B,\lambda) = u(n,B) + \lambda g(n,B)$, where $\lambda$ is a Lagrange multiplier, we look for minima of $f$, obtaining the equations:

$$\frac{\partial}{\partial n}(u+\lambda g) = 0 = a_1 + \lambda a_3 B^{(p+1)/2}$$
$$\frac{\partial}{\partial B}(u+\lambda g) = 0 = 2a_2 B + \lambda a_3 \tfrac{p+1}{2} n B^{(p-1)/2}$$

Eliminating $\lambda$, we see that:

$$\frac{a_1}{a_3 B^{(p+1)/2}} = -\lambda = \frac{4a_2 B}{a_3\,(p+1)\,n B^{(p-1)/2}}$$
$$\Rightarrow a_1 = \frac{4}{p+1}\, a_2\, \frac{B^2}{n}$$

which, since $u_e = a_1 n$ and $u_m = a_2 B^2$, has the required form. □

We note that this is slightly different from the form given in e.g., Longair (2011). The difference arises because we have imposed constraints on the electron energy spectrum, rather than on the emission spectrum.

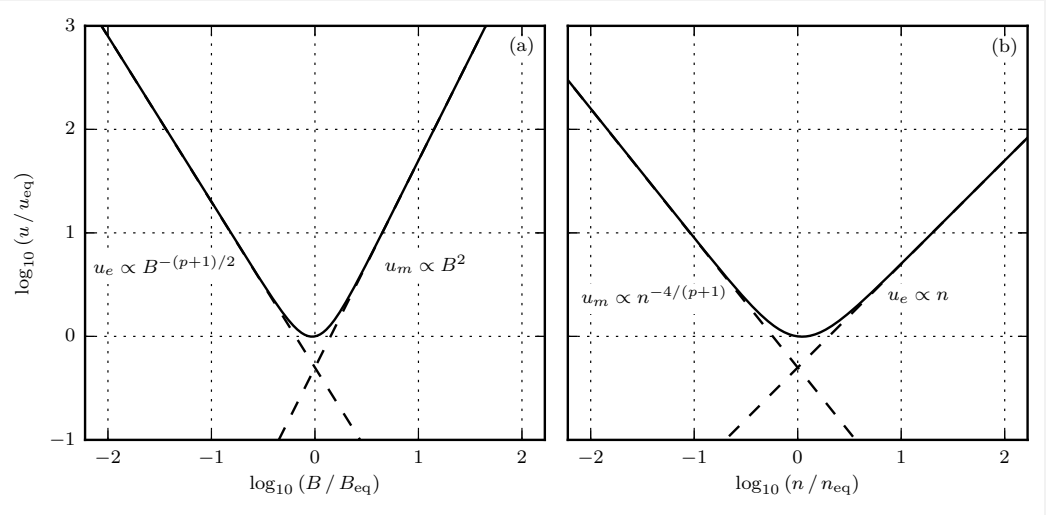


Figure 5.2: Total energy density plotted as a function of (a) magnetic field $B$, and (b) electron number density $n$. The dashed lines denote the individual behaviour of $u_e$ and $u_m$. The functions have minima close to equipartition of energy. Total energy density rises steeply as $u_m/u_e$ deviates from unity.

The values $n$ and $B$ derived from these in the equipartition case are listed in Table 5.4, together with an estimate of the bolide masses in Solar masses. We note that the two bolides are remarkably symmetrical. To within errors, the estimates of the values of $n$, $B$, and $M$ for jet and counterjet are the same.

There remains one free parameter in the model: the cutoff energy in the electron spectrum, $\mathcal{E}_0 = \gamma_0 m_e c^2$. The dependence of $n$ and $B$ on $\gamma_0$ are indicated in Equations 5.21 and 5.22. In Table 5.4, we show these explicitly evaluated, assuming an electron energy spectral index $p = 2.2$. Under this assumption, we see that $B$ is only very weakly dependent on this value ($B \propto {\gamma_0}^{0.056}$), while the number density (and hence the mass) are stronger functions of it ($n \propto {\gamma_0}^{1.111}$). Hence, if the power law cuts off at some energy (i.e., $\gamma_0 \gg 1$), the mass estimate and the number density will fall, but the magnetic field estimate will be largely unaffected.

However, these estimates of densities and massses seem remarkably low. $n \sim 10^6\,\mathrm{m}^{-3}$ is a comparable density to the interstellar medium, so it seems surprising to find that these bright jets have the same low density. Even more relevantly, the densities are far below those that would be extrapolated from estimates close to the base of the jet in the X-ray. For example, Kotani et al. (1996) find (from studies of iron line ratios) that the electron density at the base of the jet is $n_{e,0} < 5 \times 10^{21}\,\mathrm{m}^{-3}$, the base radius of a conical outflow is $R_0 > 3 \times 10^7\,\mathrm{m}$, and the mass loss rate in the jet is $\dot{M} > 5 \times 10^{-7}\mathrm{M}_\odot\,\mathrm{yr}^{-1}$. Extrapolating this as a conical outflow, we find $n_e = n_{e,0}\,(R_0/R)^2$, where we estimate a bolide radius $R \simeq 4 \times 10^{13}\,\mathrm{m}$. This would predict that densities should be on the order of 1000 times those we observe, with $n_e \sim 10^9\,\mathrm{m}$ rather than $n_e \sim 10^6\,\mathrm{m}$. And, as noted in the previous paragraph, this problem will only become *worse* if the energy cutoff $\gamma_0$ is greater than 1.

There is a similar disparity in the mass outflow rates. To match the outflow rate seen in, e.g., Kotani et al. (1996), bolides of the size seen here would have to be ejected at a rate of $1000\,\mathrm{pairs\,yr}^{-1}$. This is at least ten times the most generous estimate of the launch rate, which would be about one significant launch every 4 d (c.f., the launch rate in the 2003 VLBA observations; Chapter 4[4]). Given further that we suspect this to be a more massive ejection than average (suggested both by the elevated jet bulk speed derived in Section 4.3.2, and by the fact that this is the only ejection seen to expand so extensively), it seems that we are unable to account for the

[4]We stress again the ambiguous relationship between the radio and optical ejecta. Where radio ejections are seen at a launch rate of roughly one in four days, the appearance of optical lines happens perhaps 5 times more frequently. It is possible that the optical bolides merge into radio bolides, though it is not clear that this is the case.

mass loss rate purely through bolides in equipartition.

At the same time, the equipartition estimates of magnetic field densities – on the order of $10^{-5}$ T – are remarkably high. Magnetic field estimates are difficult to obtain, but fields of between $10^{-10}$ and $10^{-8}$ T are observed in the lobes of FRII radio galaxies (e.g., Blundell and Rawlings (2000), or estimates from synchrotron self-Compton radiation by Harris et al. (1994)).[5]

The combination of these two observations suggests that one (or more) of the following may be true: (a) our assumption of the equipartition of energy within the bolides is wrong; (b) our understanding of the geometry of the bolides is wrong; (c) our assumption that the $B$-field is internal to the bolides is wrong; or (d) the radio emission only comes from some fraction of the mass that is seen in the optical.

#### 5.4.1.1 Deviations from equipartition

We have already allowed for the possibility that equipartition may not hold by introducing $A := u_m/u_e$. We can see the scalings of $n$ and $B$ with $A$ in Equations 5.21 and 5.22, namely $n \propto A^{-(p+1)/(p+5)}$ and $B \propto A^{2/(p+5)}$. Therefore, if the energy in relativistic electrons exceeds the energy in magnetic fields, i.e., if $u_e > u_m$ and hence $A < 1$, we can increase the number density, and decrease the magnetic field.

We illustrate these dependencies in Figure 5.3. Here, the derived values of $n$ and $B$ are shown as a function of $A = u_m/u_e$. Logarithmically increasing values of $\gamma_0$ are indicated by lighter colours. To obtain number densities that are consistent with the mass injection rates of Kotani et al. (1996) (i.e., $n \sim 10^8$ – $10^9\,\mathrm{m}^{-3}$), the relativistic electron energy density must exceed the magnetic energy density by several orders of magnitude. This scales strongly with $\gamma_0$ – for $\gamma_0 \sim 1000$, the required ratio of energy densities is such that $u_m \lesssim 10^{-10} u_e$.

#### 5.4.1.2 Alternative solutions

Let's consider two other possibilities: that the synchrotron emitting plasma only fills some fraction of the apparent volume of the bolide, and that only part of the total mass of the bolide radiates.

Recall that $M \propto nV$, and that $\varepsilon_\nu \propto S_\nu/V$. Then by using Equation 5.21, we can write an

[5] For reference, our equipartition estimates for the bolide magnetic fields here are closer to stellar $B$-fields (measurements of $\gtrsim 10^{-4}$ T are made in the Sun) than to typical estimates of $B$-fields in jets or other synchrotron sources (e.g. the intracluster medium $B \sim 10^{-10}$ T (Leahy (1991))).

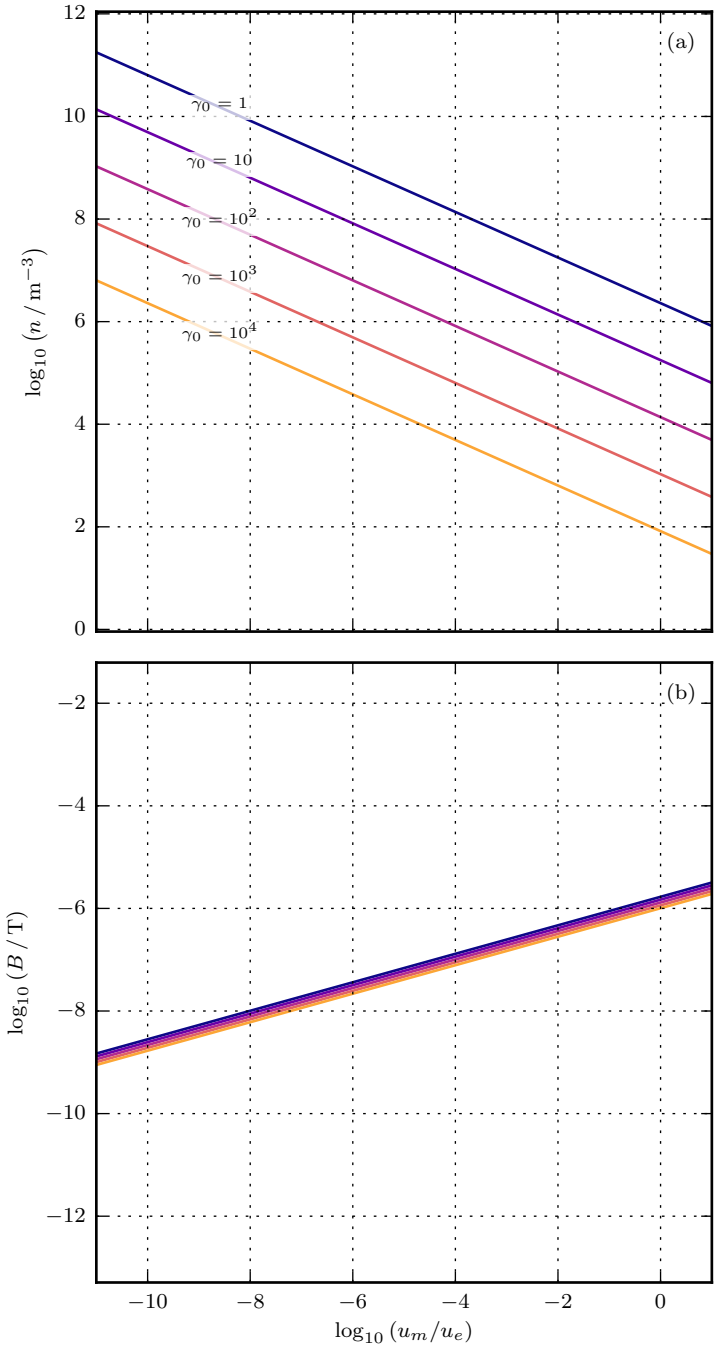


Figure 5.3: The derived number densities and magnetic field densities for the jet bolide as a function of the ratio between the magnetic and electron energy densities $A = u_m/u_e$. Only the (eastern) jet bolide is shown – the (western) counterjet matches to within experimental uncertainties. The different lines denote different values of $\gamma_0$, with lighter lines denoting higher $\gamma_0$. For definiteness, $p = 2.2$ is assumed for the electron spectral index – the corresponding weak dependence of $B$ on $\gamma_0$ is clear. For the derived number densities to be consistent with those inferred from X-ray spectra, there must be at least $10^4$ times, and possibly in excess of $10^{10}$ times, the energy density stored in the relativistic electron population as in the magnetic field.

expression for the variation of $M$ as a function of the volume $V$, at fixed flux density $S_\nu$. Since $n \propto V^{-4/(p+5)}$, this yields $M \propto V^{(p+1)/(p+5)}$. i.e., if the true volume of the bolide is only some fraction of the volume we have estimated in calculating the emissivity, then the mass of the volume will be even *lower* than the already low estimates we have here. Therefore, resorting to a geometry in which the synchrotron emission originates only in a thin shell doesn't allow us to reconcile the equipartition mass estimates with the mass loss rates derived from modelling of the x-ray jet.

This leaves us with the final suggestion, namely that we only observe some fraction of the bolide's total mass. In this picture, each bolide would consist of a small population of relativistic electrons, and then a much more massive contribution from cold baryonic matter. In practice, this would most likely have to be neutral atomic hydrogen at a temperature below $10^3$ K: this would both account for the lack of recombination lines at distances greater than about $10^{12}$ m (Vermeulen et al. (1993b)), and match with the adiabatic cooling model of Brinkmann et al. (1988) (though as a caveat we note the evidence from Migliari et al. (2002) for reheating of the jets to produce X-ray emission at about $10^{15}$ m). This unseen, cold population would have to be vastly dominant; by number, it would have to outnumber the relativistic population by perhaps as much as $10^4 : 1$, to allow us to reconcile the number densities derived assuming equipartition (and assuming $\gamma_0 \sim 10^3$) given in Table 5.4.

So, we have proposed two scenarios that would allow us to reconcile the low mass estimates obtained here with previous estimates for the mass loss rate in the SS 433 jets: either we must abandon the assumption of equipartition of energy between relativistic electrons and magnetic fields, or we must allow that the bolides contain a cold, invisible contribution that far exceeds the mass of the visible, relativistic, synchrotron-emitting component.

#### 5.4.1.3 Spectral properties

So far, we have assumed that the emission is optically-thin synchrotron in origin. In particular, we have assumed that the spectral index $\varepsilon_\nu \propto \nu^{-\alpha}$, with $\alpha \simeq 0.6$. This is in agreement with the spectral indices derived from VLA, arcsecond-scale maps of the system (e.g., Stirling et al. (2004) find bolides with indices $\alpha = 0.6$–$0.8$). Paragi et al. (1999) find spectral indices of 0.3 and 0.7 for two bolides seen in their 1.6 GHz and 5 GHz VLBA maps.[6] Do we have any evidence from these VLBA observations, in which individual bolides are resolved, to support this choice of spectral

[6] A spectral index $\alpha < 0.5$ is somewhat problematic for the synchrotron interpretation, as the electron spectrum as set out in Section 5.3, is no longer normalisable, without an additional upper energy limit.

index?

From the 6 frequency bands, we have a limited bandwidth with which to test the spectral index. This is shown in Figure 5.4. We have imaged each of the 6 frequency bands separately, and used `JMFIT` to fit the jet and counterjet bolides. The integrated intensities are then plotted against frequency, and a power law $S_\nu \propto \nu^{-\alpha}$ is fitted to the data.

The narrow frequency span (100 MHz) and large uncertainties mean that in neither case can we make useful statements. We are limited to saying that the spectral properties do not support or reject a synchrotron spectrum with a exponent in the range $0.5 \lesssim \alpha \lesssim 0.8$, as is canonically found for optically thin synchrotron sources. But equally, the data could be consistent with a flat spectrum. A wider frequency bandwidth is needed to determine this.

#### 5.4.1.4 Variation of electron energy spectral index

As well as not being able to rule out a flat or other spectrum, the lack of certainty in the spectral index, $\alpha$ gives us a similar lack of certainty in the electron energy spectral index, $p$ – as can be seen from Result 5.3.5, these are related by $\alpha = (p+1)/2$.

Allowing $p$ to vary gives us another free parameter in the model. The electron spectral index enters into the equations for $n$ and $B$ in a highly non-linear fashion, principally through its appearance in the exponents of the key variables (including implicitly, via the Doppler deboost, the emissivity). In Figure 5.5, we sketch its effect on the parameters as derived for the (eastern) jet bolide.

In the left-hand column of Figure 5.5, we assume that the magnetic and electron energies in the jet bolide are in fact in equipartition. Then, for different given values of the low energy electron spectrum cutoff, $\gamma_0$, we plot curves showing (top panel) the equipartition number density, and (bottom panel) the equipartition $B$-field as a function of the election energy index $p$. We want to determine whether deviating from $p = 2.2$ could *increase* the estimate of the number density, while simultaneously *decreasing* the magnetic field density. These two panels show that this is not possible. For low values of the low energy cutoff (i.e., $\gamma_0 \lesssim 100$), increasing $p$ increases both $n_{\rm eq}$ and $B_{\rm eq}$. For high values of the low energy cutoff (i.e., $\gamma_0 \gtrsim 100$), increasing $p$ decreases both $n_{\rm eq}$ and $B_{\rm eq}$.

In the right-hand column of Figure 5.5, we plot the dependences of the derived $B$ and $n$ values for a fixed value of $\gamma_0 = 1000$ and for different values of the energy ratio $A = u_m/u_e$. Here we see

| | Jet | Counterjet |
|---|---|---|
| $\mathcal{D}$ | $0.921 \pm 0.039$ | $0.995 \pm 0.045$ |
| $\mathcal{D}^2$ | $0.846 \pm 0.071$ | $0.988 \pm 0.089$ |
| $\mathcal{D}^3$ | $0.779 \pm 0.097$ | $0.981 \pm 0.132$ |
| $\mathcal{D}^{3+0.6}$ | $0.738 \pm 0.110$ | $0.979 \pm 0.157$ |

Table 5.3: The jet and counterjet Doppler beaming factors for a source moving at $\beta = 0.289 \pm 0.017$, with line-of-sight velocity component $\beta_{\parallel} = -0.039 \pm 0.043$.

| | | Jet | Counterjet |
|---|---|---|---|
| Integrated Intensity | $S_\nu \,/\, \mathrm{mJy}$ | $26.26 \pm 0.77$ | $31.68 \pm 0.73$ |
| Angular Radius | $\vartheta_{\mathrm{mas}}$ | $36 \pm 2$ | $33 \pm 2$ |
| Doppler Factor | $\mathcal{D}^{3+0.6}$ | $0.738 \pm 0.110$ | $0.979 \pm 0.157$ |
| Volume | $V \,/\, 10^{41}\,\mathrm{m}^3$ | $1.08 \pm 0.22$ | $0.84 \pm 0.18$ |
| Emissivity | $\varepsilon_\nu \,/\, 10^{-26}\,\mathrm{W\,m^{-3}\,Hz^{-1}}$ | $0.178 \pm 0.035$ | $0.231 \pm 0.049$ |
| Equipartition number density | $\left(n \,/\, 10^{6}\,\mathrm{m}^{-3}\right)\,{\gamma_0}^{1.111}$ | $2.29 \pm 0.26$ | $2.65 \pm 0.32$ |
| Equipartition $B$-field | $\left(B \,/\, 10^{-6}\mathrm{T}\right)\,{\gamma_0}^{0.056}$ | $1.68 \pm 0.09$ | $1.81 \pm 0.11$ |
| Equipartition bolide mass | $\left(M \,/\, 10^{-10}\mathrm{M}_\odot\right)\,{\gamma_0}^{1.111}$ | $2.11 \pm 0.28$ | $1.87 \pm 0.25$ |

Table 5.4: Synchrotron emission parameters for the jet and counterjet bolides identified in Figure 5.1. Note that the equipartition number density and $B$-fields are functions of the cutoff energy in the electron energy spectrum. Throughout, we have assumed that $p = 2.2$.

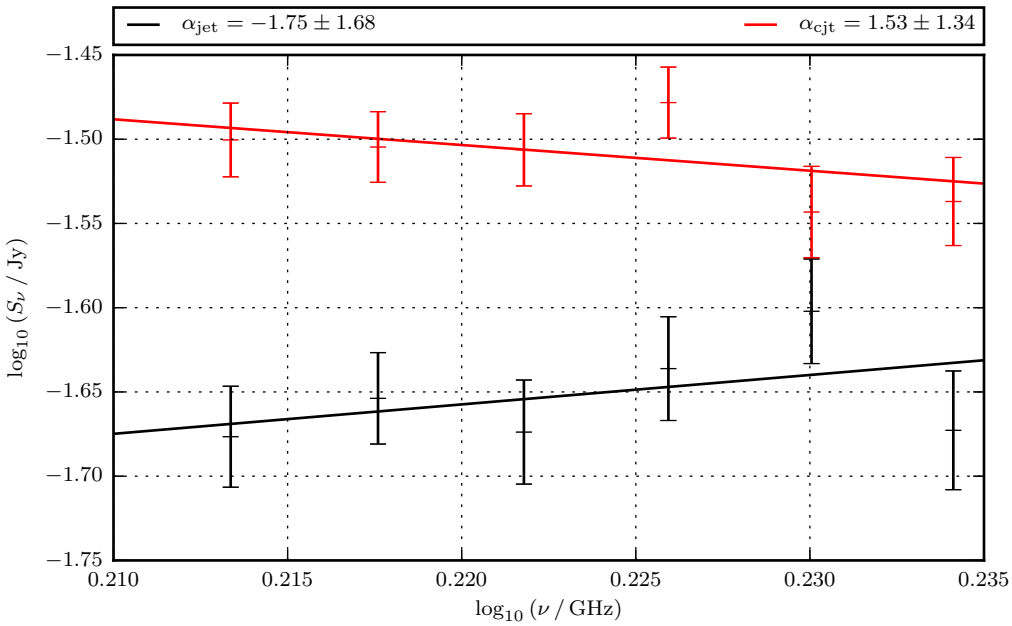


Figure 5.4: Plot showing the integrated intensity $S_\nu$ of the jet and counterjet bolides shown in Figure 5.1, as a function of frequency band, $\nu$. The data are not sufficient to distinguish between an optically-thin synchrotron source, a flat, thermal spectrum, or some other spectrum with any degree of significance. We note that there is no *a priori* reason to suppose that the spectral indices of the jet and counterjet bolides are different, let alone are of different sign.

the same pattern as outlined in the preceding section, namely that by decreasing $A$ (i.e., having less energy in magnetic fields than equipartition would suggest), we can *both* increase the number density and decrease the magnetic field density. There is no qualitatively important variation of this pattern as a function of $p$.

In summary, we can't explain the low densities and unexpectedly high $B$-fields simply by arguing that our choice of $p$ is incorrect.

#### 5.4.1.5 Proton energetics

Lastly, we return briefly to the energy stored in protons, which we noted previously we had neglected. Could this have a significant effect?

Simulations of shock acceleration in electon-ion plasmas suggest that the relativistic ion and electron populations tend to have energy densities that are comparable (e.g., Spitkovsky (2008)). Observations of Galactic cosmic rays suggest this ratio may be slightly greater, perhaps $u_p = 100u_e$ (Longair (2011)). In either case, this would not be sufficient to explain the more than 4 orders of magnitude difference between the energies in magnetic fields and relativistic particles.

#### 5.4.1.6 Summary

We have seen that there are three unknown parameters in the synchrotron sphere problem: the electron spectrum low energy cutoff, $\gamma_0$; the electron energy spectral index $p$; and the ratio between the magnetic and electron energy densities $A = u_m/u_e$. Assuming $A = 1$, $\gamma_0 = 1$, and $p = 2.2$, we obtain estimates of $B$ that are surprisingly high, and estimates of $n$ that are too low, and are inconsistent with the expected densities given previous estimates of the mass loss rates in the jets. Having considered each of these in turn, we have shown that only by allowing $A \ll 1$ can we obtain consistency between the electron number densities without requiring an even higher magnetic field. Hence, we are led to the conclusion that, if the emission is indeed optically thin synchrotron from a sphere, then the bolides cannot be in equipartition.

We have also discussed an alternative solution, in which the assumption of a filled sphere is sacrificed. However, we have shown that simply having a sphere that is only partially filled does not help – instead, we must include a massive, unseen component.

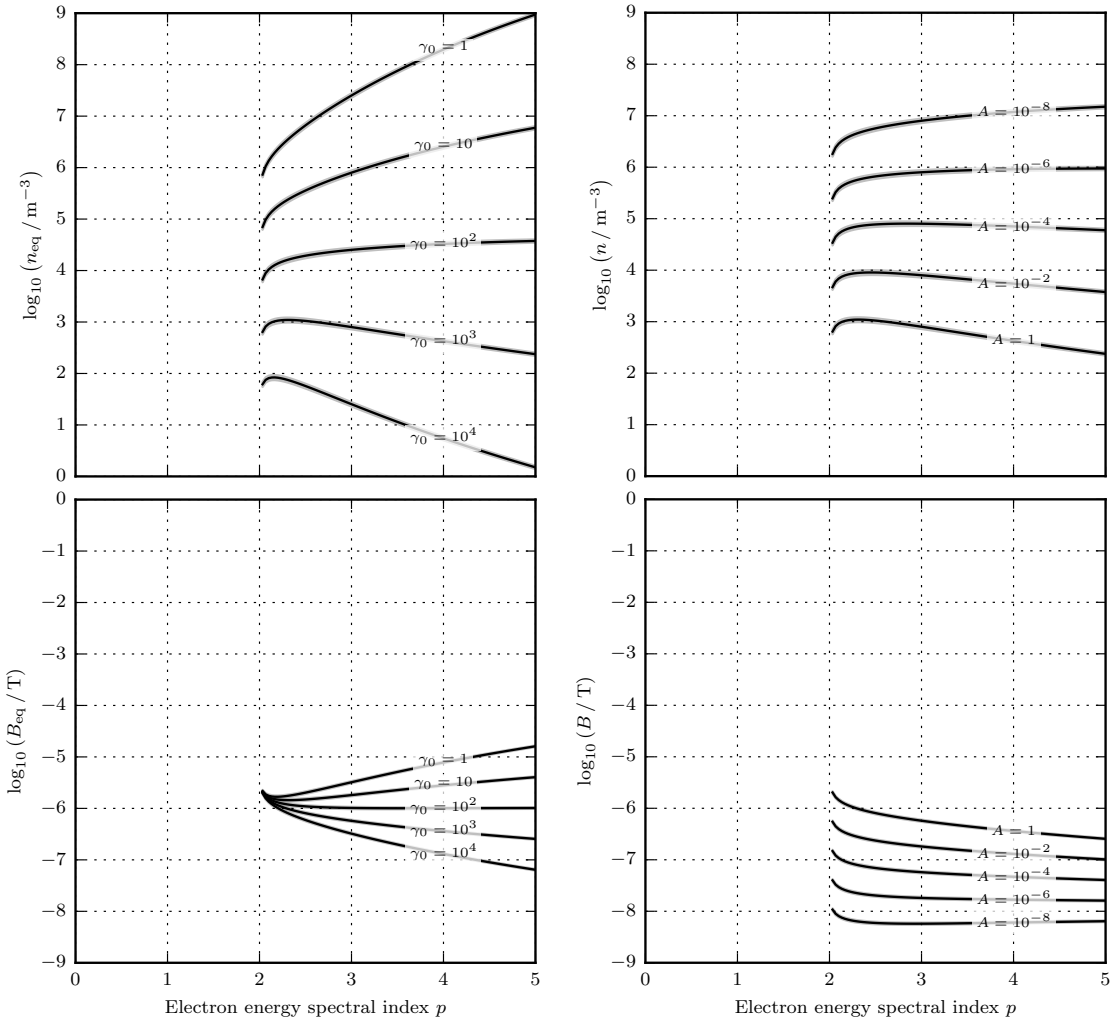


Figure 5.5: The variation of the number density and magnetic fields in the (eastern) jet bolide as a function of the electron energy spectral index $p = 2\alpha + 1$. In the left column, equipartition is assumed ($A = u_m/u_e = 1$), and the curves denote different values of the electron spectrum cutoff energy, $\gamma_0$. In the right column, $\gamma_0$ is held constant at $10^3$, while $A$ is varied. The curves are plotted for $p \in (2, 5]$ – note that for values of $p \leq 2$, the total energy cannot be defined without introducing a high energy cutoff to the electron spectrum as an additional parameter. Importantly, the left-hand column shows that choosing a steeper power law for the electron energy distribution can either increase (for $\gamma_0 \lesssim 100$) or decrease (for $\gamma_0 \gtrsim 100$) *both* of $n_{\rm eq}$ and $B_{\rm eq}$ from their values at $p = 2.2$ as shown in Table 5.4 – crucially, varying $p$ *cannot* increase $n_{\rm eq}$ while simultaneously decreasing $B_{\rm eq}$. The right-hand column, shows that the same qualitative variation with decreasing values of $A$ is followed at $p > 2$ as was outlined in Section 5.4.1.4 and in Figure 5.3 for $p = 2.2$.

### 5.4.2 Other emission mechanisms – thermal bremsstrahlung

In the previous Sections, we proved unable to unambiguously identify the emission from the resolved bolides as synchrotron radiation, let us briefly consider an alternative model. Could the emission arise purely from thermal bremsstrahlung? It is believed that this dominates the emission from the core regions (within $10^{12}\,\mathrm{m}$) in the X-ray band (see the discussion in Chapter 7). Could it still provide a significant contibution to the radio emission from individual bolides at distances on the order of $10^{14}\,\mathrm{m}$?

The emissivity due to bremsstrahlung of an ionised plasma in thermal equilibrium is given by:

$$\frac{\varepsilon_\nu}{\mathrm{W\,m^{-3}\,Hz^{-1}}} = 6.84\times10^{-51}\left(\frac{T}{\mathrm{K}}\right)^{-1/2} Z^2\left(\frac{n_i}{\mathrm{m^{-3}}}\right)\left(\frac{n_e}{\mathrm{m^{-3}}}\right)\overline{g_{\mathrm{ff}}} \times\exp\left(-4.799\times10^{-2}\frac{(\nu\,/\,\mathrm{GHz})}{(T\,/\,\mathrm{K})}\right) \tag{5.23}$$

where $Z$ is the atomic number, $T$ is the temperature, $n_i$ and $n_e$ are the electron and ion number densities, $\nu$ is the emission frequency, and $\overline{g_{\mathrm{ff}}}$ is the thermally-averaged Gaunt free-free factor. This is neither the time nor the place for an extended discussion of Gaunt factors. For the present, let it suffice to say that they encapsulate quantum-mechanical corrections to the classical scattering cross-section. For a more comprehensive discussion and explicit calculation, see the paper by Sutherland (1998). In general, the Gaunt factors can be approximated by a slowly varying function on a parameter space described by the dimensionless quantites:

$$\frac{h\nu}{k_{\mathrm{B}}T} \equiv 4.799\times10^{-2}\left(\frac{\nu}{\mathrm{GHz}}\right)\left(\frac{T}{\mathrm{K}}\right)^{-1} \qquad \frac{k_{\mathrm{B}}T}{Z^2\,\mathrm{Ry}} \equiv \frac{6.336\times10^{-6}}{Z^2}\left(\frac{T}{\mathrm{K}}\right) \tag{5.24}$$

In our case, with $\nu = 1.6\,\mathrm{GHz}$, we are always in the regime where $h\nu/k_{\mathrm{B}}T \ll 1$. As shown in figure 2(b) of Sutherland (1998), the thermally-averaged Gaunt factors in this regime are essentially logarithmic in $h\nu/k_{\mathrm{B}}T$, with little variation (a factor of order 2) due to $k_{\mathrm{B}}T/Z^2\,\mathrm{Ry}$. A reasonable approximation (see Novikov and Thorne (1973) or Rybicki and Lightman (1979)) is:

$$\overline{g_{\mathrm{ff}}}\,(\nu,T) = \frac{\sqrt{3}}{\pi}\left[\ln\left(\frac{4}{\zeta}\right) - \ln\left(\frac{h\nu}{k_{\mathrm{B}}T}\right)\right] \tag{5.25}$$

where $\zeta = 0.5772\ldots$ is the Euler-Mascheroni Constant. In fact, this can be approximated still further. If a plausible range of physical temperatures is $1\,\mathrm{K}$ to $10^8\,\mathrm{K}$, then over these 8 decades in temperature, $\overline{g_{\mathrm{ff}}}\,(\nu = 1.6\,\mathrm{GHz}, T)$ only varies from $\overline{g_{\mathrm{ff}}} \simeq 2.5$ to $\overline{g_{\mathrm{ff}}} \simeq 12.6$. We will see in a moment

that the Gaunt factor only enters the expression for number density as $\overline{g_{\rm ff}}^{-1/2}$, compressing this already small variation still further. For our purposes, it is sufficient to set $\overline{g_{\rm ff}} = 3$, which is true to within a factor of about 2.

Returning to Equation 5.23, we see that, under the assumption of quasi-neutrality (i.e., $n_i = n_e = n$), we can rearrange this to obtain an expression for the number density $n$:

$$\left(\frac{n}{\mathrm{m}^{-3}}\right) = 1.209 \times 10^{12} \times \frac{Z}{\overline{g_{\rm ff}}^{1/2}} \left(\frac{T}{\mathrm{K}}\right)^{1/4} \times \exp\left(2.400 \times 10^{-2} \frac{(\nu \,/\, \mathrm{GHz})}{(T \,/\, \mathrm{K})}\right) \left(\frac{\varepsilon_\nu}{10^{-26}\,\mathrm{W\,m^{-3}\,Hz^{-1}}}\right)^{1/2} \tag{5.26}$$

To a very reasonable approximation, the exponential is unity. Note also that temperature only enters at the 1/4th power, and therefore the resulting number densities are relatively insensitive to the size of $T$. In this picture, we have little basis to assume a value for the temperature. Hydrogen recombination lines are seen in the optical at a couple of days after launch (i.e., $10^{13}$ m from the core), but not afterwards indicating that the bolide temperature must have dropped through $10^4$ K long before these radio bolides are observed at 35 d after launch. To produce free-free emission, presumably we would need to reionise the bolides.[7] This does indeed happen, but at scales larger by a factor of 10 than those seen here (see Migliari et al. (2002)), and we have no evidence that this process is at play for bolides between distances of $10^{13}$–$10^{14}$ m from the core. However, the need to reionise plasma is not the major issue with this model.

In Table 5.5, we list the estimates of number density and bolide mass derived from the bremsstrahlung model. This time, the densities are too high. Bolide masses on the order of $10^{-5}\,\mathrm{M}_\odot$ would imply a total mass loss rate through the jets only that is perhaps as high as $10^{-3}\,\mathrm{M}_\odot\,\mathrm{yr}^{-1}$ – far in excess of that typically estimated from x-ray or optical measurements.

On this basis, it seems safe to conclude that bremsstrahlung is far too weak an emission mechanism to explain the observed radio emission from the resolved bolides at 35 d after launch (i.e., $10^{14}$ m from the core).

## 5.5 Summary

From the resolved bolide pair in the 2012-Jan-28 observation, we have:

[7] The same need to energise particles by some unknown mechanism is also present in the synchrotron picture.

| | | Jet | Counterjet |
|---|---|---|---|
| Number Density | $\left(n \,/\, 10^{11}\mathrm{m}^{-3}\right)\left(T \,/\, \mathrm{K}\right)^{1/2}$ | $3.03 \pm 0.32$ | $3.37 \pm 0.39$ |
| Mass | $\left(M \,/\, 10^{-5}\mathrm{M}_{\odot}\right)\left(T \,/\, \mathrm{K}\right)^{1/2}$ | $2.71 \pm 0.37$ | $2.37 \pm 0.33$ |

Table 5.5: Number density and mass estimates assuming the emission from the bolides identified in Figure 5.1 is thermal bremsstrahlung. The scaling with temperature is indicated. The mass loss rate implied by the masses derived in this table far exceed the mass loss rates estimated from the brightness of the optical and X-ray jets.

1. estimated an expansion rate of $0.03c$, which is found to be in excess of previous estimates for the expansion rate by a factor of $\gtrsim 2$;

2. estimated the masses of the bolides, under the assumption of optically thin synchrotron in equipartition, as $\lesssim 10^{-10}\,\mathrm{M}_{\odot}$, with associated magnetic fields $\lesssim 3 \times 10^{-5}\,\mathrm{T}$, and argued that the mass in particular is lower than necessary for consistency with other inferences of the mass loss rate;

3. explored possible solutions, ruling out bremsstrahlung, and instead suggesting that either (a) the bolides are significantly out of equipartition; or (b) they consist of a large, unseen, cold component, in addition to the relativistic component visible through its synchrotron emission.

# Chapter 6

# The Evolution of Individual Jet Bolides II – Unresolved Bolides

## 6.1 Introduction

In Chapter 4, we analysed the jet speeds of the 9 bolide pairs seen during the 42 day span of the 2003 VLBA movie (Mioduszewski et al. (2004)). In these images, we are able to track individual ejecta for as many as 21 days after their launch. This excellent temporal coverage means that we can study their evolution in some detail.

Although these images have been familiar within the community since 2004, until recently (Jeffrey et al. (2016)), there had been no analysis published in the scienitific literature. The initial press release (Mioduszewski et al. (2004)), however, contained two qualitative statements: that the circumbinary ruff appeared to take the form of a rapid ($10^7\,\mathrm{m\,s^{-1}}$) outflow; and that many of the bolides undergo a brightening as they move from the core. Mioduszewski et al. (2004) suggest that this brightening is due to the interaction between the jet bolides and the medium around SS 433, with an uneven replenishment of this medium explaining why different bolides undergo different levels of brightening.

In this Chapter, we will consider the second of these qualitative statements in more detail. We will show the lightcurves for the bolide pairs, discuss them in the context of existing VLBI images of SS 433, and comment on the nature of the fading.

## 6.2 Lightcurves for the 2003 VLBA movie

In Figure 6.1, we plot observed integrated intensity (determined using the AIPS task `jmfit`) against the number of days since launch (as calculated in Chapter 4 from their proper motions) for each of the 9 bolides.

### 6.2.1 Discussion of the 2003 VLBA movie images

Before we proceed to analyse these further, let us begin with a brief narrative description of SS 433 over the 42 day span of the 2003 observations. This should be read with reference to the movie images plotted in Figure 4.2, and the lightcurves in Figure 6.1). At the start of the campaign (Day 1), the system is in a relatively quiescent state. There is a reasonably continuous and relatively faint outflow, against which 2 bolide pairs can be identified. Their speeds, as shown in Chapter 4, are slightly slower than the mean speed ($\beta_0 = 0.255 \pm 0.11$ and $\beta_0 = 0.238 \pm 0.10$ for bolides 1 and 2 respectively). These two propagate outwards, and can be observed until about Day 9.

A third and fourth ejection pair appear on Days 5 and 10 respectively. These are the slowest of the 9 observed bolides. Pair 4 is initially relatively faint and disappears rapidly, becoming indistinguishable from the other bolides/the background flow by Day 16. A fifth ejection pair are visible by Day 17. This is the last of the pre-flare ejections, travelling slightly faster than its predecessors ($\beta_0 = 0.262 \pm 0.014$). The jet bolide from pair 5 fades over $\sim 10\,\mathrm{d}$ up to Day 27. However, as can be seen in Figure 6.1, it brightens significantly from about Day 19, before fading again, at a point close to that at which bolide 4 was last seen. Likewise, the counterjet bolide has mostly faded by Day 22. At this point, it becomes hard to distinguish between counterjet bolide 5, the remnants of counterjet bolide 4, and the background flow. However, there appears to be an interaction between these two – a "new" bolide, brighter than counterjet bolide 5 by perhaps a factor of 4, then emerges from this process, and continues to be identified until the last day of the observation. This rebrightening is not sketched in Figure 6.1, as it is ambiguous as to which bolide pair ought to be associated with the resulting plasmon.

At Day $\sim 18$, with the launch of pair 6, SS 433 appears to enter a flare. Pair 6 is fast ($\beta_0 = 0.297 \pm 0.012$), and can be tracked for $\sim 11\,\mathrm{d}$ until it can no longer be distinguished from the bolides of pair 7, which are fast and particularly bright. These are launched on Day 21, and can be tracked for the remaining 21 days of the campaign. Their peak brightness is obtained

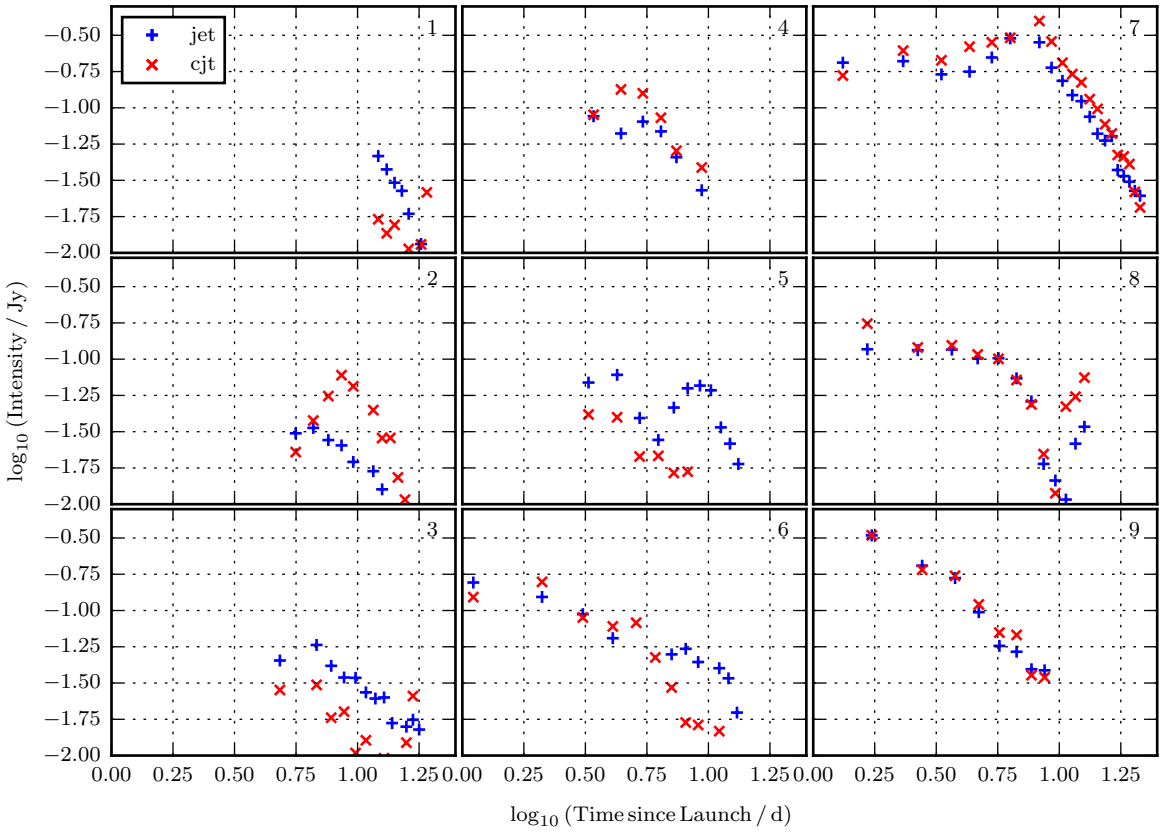


Figure 6.1: The lightcurves (integrated intensity as determined by `JMFIT` plotted against time since launch) for the 9 ejections in the 2003 VLBA data (Figure 4.2) for which launch dates are determined. The (eastern) jet is labelled by (blue) vertical crosses and the (western) counterjet by the (red) diagonal crosses. Many of the bolides display a marked asymmetry between the two components, often rebrightening and fading at different times post launch.

on Day 29, after which they fade. This fading occurs with a marked power law decay rate (see Figure 6.3). Indeed, pair 7 behaves in the most uniform fashion of all the ejections – much of the discussion in this Chapter will be devoted to these two bolides.

There follows the longest gap between successive ejections seen in this campaign (8.5 d) before the launch of bolide pair 8 – the fastest of the ejecta with $\beta_0 = 0.320 \pm 0.012$, though not as bright as either of bolide pairs 7 or 9. Most interestingly, the two bolides of pair 8 undergo fading, and then both the jet and the counterjet bolides of pair 8 brighten appreciably (by almost an order of magnitude) from Day 39 onwards. The reason is possibly clear from a study of the movie images for Days 39 to 42. Here, we see that the brightening of pair 8 occurs as it begins to catch/overlap with material trailing behind the bolides of pair 7. This leads to the same hypothesis as in respect of the rebrightening of counterjet bolide 5 – namely, that this rebrightening is caused by interactions between jet components moving with different velocities.

There are two more ejection events before the end of the campaign, though their lightcurves don't reveal anything new. The bolides of pair 9, launched on Day 33, are, like those of pair 7, fast and bright. Bolide pair 10 is only launched at about Day $\sim$ 39, giving too few data points to determine speeds and launchdates. It is also unclear how well we can disambiguate pair 10 from the core region.

So, how do these images relate to earlier VLBI observations of SS 433? There is evidence again for a core gap – a small region of lower emission around the object itself, surrounded by "wings" as the first visible parts of the radio jet – as seen previously in the multi-wavelength observations of Paragi et al. (1999). They attribute this to self-absorption of synchrotron emission in the radio jets. In the 2003 observations, this core gap is most clear in the early, pre-flare observations (i.e., before Day 16). We are unable to develop this further here, although we note briefly and qualitatively that there is a slight asymmetry in the earliest days of the campaign, that may be attributable to extinction by the circumbinary ruff. We note in particular that it is the western "wing" that appears fainter; this is intriguingly aligned with the orientation of the ruff at this epoch.

As noted by Mioduszewski et al. (2004) in their comments on these data, it is unclear that we see a regular and consistent "brightening zone" analagous to that seen by Vermeulen et al. (1987). This brightening zone was suggested to be a region covering about 50 mas either side of the core, within which jet bolides appear to brighten with time, before fading once they move beyond this region.

Corresponding to between 6 and 8 days travel by the bolides, the suggestion is that within the brightening region the bolides are either a) prevented from expanding by a confining medium, or b) expanding and becoming increasingly optically thin before fading once they have transitioned from an optically thick, self-absorbed regime to an optically thin regime. Looking at the lightcurves in Figure 6.1, it is certainly clear that this pattern is not followed uniformly. However, in the cases of bolide pairs 7 and 8, we do see a pattern in which there is 6-8 d of relatively flat flux evolution, followed by a transition to a steep fading. We are unable to rule out the existance of such a "brightening zone", but if the description is correct, its behaviour is more complex than the simple observation of Vermeulen et al. (1987).

Perhaps the most interesting observation here is the presence of a steep, power-law decay in several of the lightcurves. This is most prominent for bolide pair 7. There are hints of a similar pattern in some of the other curves, notably in bolide pair 8, in the jet bolide for bolide pair 1, and in the final fading of the jet bolide from pair 5. We will return to this in Section 6.3.

This discussion has led to two key points:

1. that the jet bolides appear to follow a power-law decay as they fade; and

2. that significant rebrightening of individual ejecta may well be attributable to interactions between different bolides.

### 6.2.2 Are the bolides resolved?

`jmfit` tries to determine whether a Gaussian component is resolved by attempting to deconvolve the beam from the fitted component. In the case of all the bolides seen here, it reports that the bolides are resolved. Is this in fact the case?

In Figure 6.2, we sketch the size of the fitted component as a function of time for bolide pair 7, which is the best behaved and longest tracked of the 9 pairs in Figure 6.1. Throughout the course of the observations, the fitted major axis is fairly constant at 20 mas, while the minor axis remains 15 mas. The restored clean beam is 16 mas $\times$ 7 mas, so the fitted Gaussians are slightly, but not much, in excess of this. We believe that this shows that the source is indeed unresolved, rather than that the source undergoes no expansion.

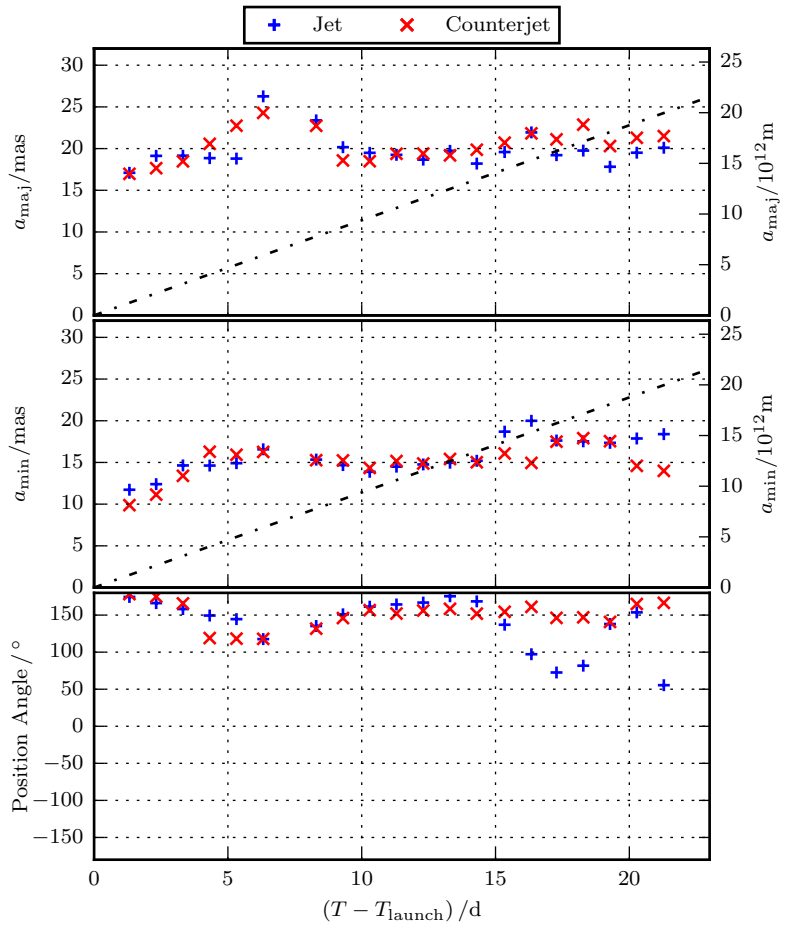


Figure 6.2: The semi-major and semi-minor axes ($a_{\mathrm{maj}}$ and $a_{\mathrm{min}}$ respectively) and the position angles of the fitted Gaussians for jet and counterjet bolides of pair 7 returned by `JMFIT`. The dashed lines denote the expansion rate of $1.14\,\mathrm{mas\,d^{-1}}$ determined for the 2012-Jan observation in Section 5.2. The beam size is $16\,\mathrm{mas} \times 7\,\mathrm{mas}$. The bolides must remain unresolved throughout the observations.

### 6.2.3 An upper limit on the expansion rate

The dashed line on the top two panels of Figure 6.2 indicates the expected angular size of the bolides if they expand at a rate that corresponds to that seen in the 2012-Jan-28 epoch (see Section 5.2). The bolides there expanded to a size of $\sim 40\,\mathrm{mas}$ in 35 d, corresponding to a physical speed $v_{\rm exp} \simeq 0.03c$. The bolides in Figure 6.2 must expand slower than this: there is no evidence that they transition from unresolved to resolved before the end of the observations, where the predicted size indicates that we should see such a transition.

Instead, we are only able to place an upper limit on the expansion rates of bolide pair 7. From their angular sizes (for this quick estimate, we simply take the mean of the major and minor axes) at the final epoch (i.e., 21.3 d after launch), these upper limits on their angular expansion rates are $0.90\,\mathrm{mas\,d^{-1}}$ and $0.83\,\mathrm{mas\,d^{-1}}$. From Equation 5.1, these are still on the order of $0.03c$, though the upper limits here require that the expansion rate be at least 25% lower than that seen in the 2012-Jan-28 epoch.

### 6.2.4 Lower limits on synchrotron parameters

Following the same reasoning as in Chapter 5, we can use Equations 5.21 and 5.22 to estimate the number density, magnetic fields, and masses of bolides. However, the situation is complicated by the lack of resolution: as we can only impose an *upper* limit on the volume of the bolides, we can only impose *lower* limits on the emissivity (from $\varepsilon_\nu \propto S_\nu/V$), and hence lower limits on number density $n$ and magnetic field density $B$.

In principle, since both flux density $S_\nu$ and bolide mass scale as $nV$, we can estimate the mass exactly. Unfortunately, our ignorance of the low energy cutoff to the electron spectrum, $\gamma_0$, prevents us from doing this. Indeed, we can now appreciate that this is even more complex than before, as the value of $\gamma_0$ evolves with time as the bolide expands. This will be discussed more fully in Section 6.3.

Let us briefly make an estimate of the properties for one bolide pair. To place the most restrictive lower limits, we want to choose observations that are as late as possible in the campaign, when the bolides will be closest to being resolved. We will consider pair 7 on the last day of the campaign (Day 42). Pair 7 are the oldest ejecta still detectable in the final observation. Their kinematic properties were determined in Chapter 4. These are given, together with the flux properties and

their fitted angular sizes in Table 6.1. We take the geometric mean of the major and minor axes to estimate the angular scale of the (spherical) bolide. We will assume equipartition of magnetic and particle energy, while remaining fully aware of the concerns raised in Section 5.4.1, and we leave $\gamma_0$ as an unknown parameter that will scale the values here to give the true values.

The numerical values reported here are not particularly insightful (they contain the same ambiguities discussed in Chapter 5). However, we note that the masses of the jet ($M_{\rm jet} = (8.8 \pm 0.8) \times 10^{-11}\,{\rm M}_\odot$) and counterjet ($M_{\rm cjt} = (6.4 \pm 0.6) \times 10^{-11}\,{\rm M}_\odot$) bolides are not quite consistent. We will return to this asymmetry shortly. First, let us consider the full lightcurve of the expanding plasmon.

## 6.3 The adiabatic expansion of a plasmon

In Figure 6.1, we noted that the lightcurves of several bolides decay with relatively steep power-laws. This is most clear for pair 7 (shown in Figure 6.3), where a power-law decay dominates the evolution of both jet and counterjet bolides. It can also be seen in parts of the evolution of jet bolide from pair 5, and both bolides of pair 8.

The fading rates for the jet and counterjet bolides in pair 7 can be calculated from Figure 6.3. We can see clearly that there is a break in the lightcurve: before this the intensity is relatively flat, while after this the lightcurve decays. This break appears to occur at or about 8 days post launch (i.e. $T - T_{\rm launch} > 8\,{\rm d}$, where $T_{\rm launch}$ = MJD 52836.014). Fitting a power law to the post-break lightcurve, we find exponents $\alpha_{\rm jet} = 2.57 \pm 0.09$ and $\alpha_{\rm cjt} = 2.94 \pm 0.12$, where $\alpha := -{\rm d}\log S_\nu / {\rm d}\log T$.

MERLIN observations of SS 433 by Spencer (1984) also showed evidence for a power law fading curve. Bolides were seen to fade with a $T^{-1.8}$ power law. This is shallower than that seen here, though we note that the higher angular resolution and more expansive time coverage of the 2003 observations reported here allows us to identify individual bolides with greater precision and certainty than in the earlier data.

To try to explain this fading rate, let us assume that the emission from each plasmon is entirely optically thin synchrotron radiation. Let us further assume that radiation losses are negligible, and that the plasmon's evolution is governed by an adiabatic expansion.

| | | Jet | Counterjet |
|---|---|---|---|
| Bulk speed | $\beta_0$ | $0.292 \pm 0.011$ | |
| (Jet) line-of-sight velocity | $\beta_0 \cos\eta$ | $-0.029 \pm 0.003$ | |
| Integrated Intensity | $S_\nu \,/\, \mathrm{mJy}$ | $24.75 \pm 0.63$ | $20.58 \pm 0.54$ |
| Angular major axis | $\vartheta_{\mathrm{max,mas}}$ | $20.1 \pm 0.4$ | $21.5 \pm 0.4$ |
| Angular minor axis | $\vartheta_{\mathrm{min,mas}}$ | $18.4 \pm 0.4$ | $14.0 \pm 0.3$ |
| Doppler Factor | $\mathcal{D}^{3+0.6}$ | $0.839 \pm 0.009$ | $0.964 \pm 0.011$ |
| Volume | $V \,/\, 10^{40}\,\mathrm{m}^3$ | $1.66 \pm 0.19$ | $1.22 \pm 0.14$ |
| Emissivity | $\varepsilon_\nu \,/\, 10^{-26}\,\mathrm{W\,m^{-3}\,Hz^{-1}}$ | $1.091 \pm 0.069$ | $1.076 \pm 0.067$ |
| Equipartition number density | $\left(n \,/\, 10^6\,\mathrm{m}^{-3}\right)\ {\gamma_0}^{1.111}$ | $6.26 \pm 0.22$ | $6.21 \pm 0.21$ |
| Equipartition $B$-field | $\left(B \,/\, 10^{-6}\mathrm{T}\right)\ {\gamma_0}^{0.056}$ | $2.78 \pm 0.05$ | $2.77 \pm 0.05$ |
| Equipartition bolide mass | $\left(M \,/\, 10^{-11}\mathrm{M}_\odot\right)\ {\gamma_0}^{1.111}$ | $8.8 \pm 0.8$ | $6.4 \pm 0.6$ |

Table 6.1: Synchrotron emission parameters for the jet and counterjet bolides for Pair 7 in the 2003 VLBA movie, using their fluxes on the final day of the campaign. Note that the equipartition number density and $B$-fields are functions of the cutoff energy in the electron energy spectrum. Note also that the bolides are unresolved, so the volume gives an upper limit, and $n$ and $B$ give lower limits. Throughout, we have assumed that $p = 2.2$.

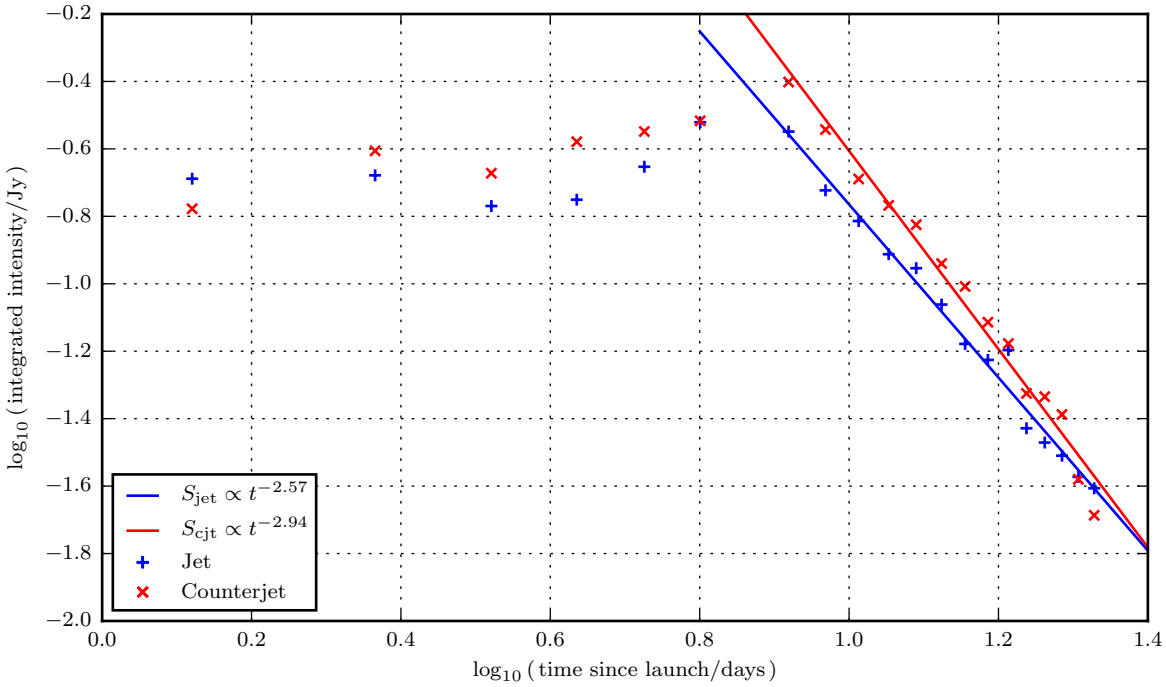


Figure 6.3: The lightcurves for the eastern jet (blue vertical crosses) and western counterjet (red diagonal crosses). A power law is fitted to the decaying lightcurve (i.e., for $T - T_{\mathrm{launch}} > 8\,\mathrm{d}$, where $T_{\mathrm{launch}} = \mathrm{MJD}\ 52836.014$). The exponents are $\alpha_{\mathrm{jet}} = 2.57 \pm 0.09$ and $\alpha_{\mathrm{cjt}} = 2.94 \pm 0.12$, where $\alpha := -\mathrm{d}\log S_\nu / \mathrm{d}\log T$.

These assumptions allow us to follow similar reasoning to that used by Miller-Jones et al. (2004). Their objective is to account for the flux ratio between simultaneously launched jet and counterjet bolides, accounting both for Doppler boosting, and for the different ages of the two bolides as seen at the same epoch according to an Earth-bound observer. The effect of Doppler boosting is to increase the brightness of the approaching bolide and to decrease the brightness of the receding one, while the fact that the speed of light is finite means that light from the receding bolide must set out earlier than from the approaching bolide to be observed at the same Earth epoch. Hence, they show that if the two bolides are fading with time, then the receding bolide, being observed earlier in its evolution, will appear brighter than Doppler beaming would predict, and hence the flux ratio $S_{\rm app}/S_{\rm rec}$ will be lower than would be expected from Doppler boosting alone.

It is important to note at this point that the relativistic motion of the bolide does not affect the shape of the lightcurve. To see this, note that the relationships between time of observation $T$, time of emission $t$, and proper time $\tau$, are linear:[1]

$$\mathrm{d}t = \frac{\mathrm{d}T}{1-\beta\cos\eta} = \gamma\,\mathrm{d}\tau \tag{6.1}$$

where $\gamma$ is the Lorentz factor and $\eta$ is the angle of the motion to the line of sight (c.f., the geometry in Figure 2.3). Consequently, if the bolide's luminosity in its rest frame evolves as a power law $L'(\tau) \propto \tau^{-\zeta}$, then the evolution of the luminosity as seen by the observer, $L(T)$ will be proportional to $T^{-\zeta}$. That is, the lightcurve will have the same *shape* according to the astronomer as its true evolution in its rest frame; the *rate* of its evolution (i.e., $\mathrm{d}L/\mathrm{d}T$ or $\mathrm{d}L'/\mathrm{d}\tau$) will change. The key point is that we can make arguments about the shape of the lightcurve in the rest frame, and by doing so we will explain the (identical) shape of the observed lightcurve.

As we assume the emission is optically thin synchrotron, our next task is to work out how the synchrotron emissivity scales with expansion geometry, and hence with time. From Result 5.3.5, we can write the spectral luminosity of the synchrotron emitting bolide as:

$$L_\nu = V\varepsilon_\nu \propto {\gamma_0}^{\xi-1}\,(nV)\;\nu^{-(\xi-1)/2}B^{(\xi+1)/2} \tag{6.2}$$

where $\xi$ is the spectral index of the electron energy power-law distribution,[2] $\gamma_0$ is the low energy

[1] Recall that $T$ and $t$ are measured in the common rest frame of the observer and the binary system; $\tau$ is measured in the bolide's rest frame.

[2] Note the change of notation from previous Chapters: here we use $\xi$ rather than $p$ for the electron index $n_\gamma \propto \gamma^{-\xi}$. We will shortly find ourselves working with both the momentum and the pressure of this electron population, giving us too many quantities traditionally labelled with the symbol $p$!

cutoff to the electron spectrum, $\nu$ is the observation frequency, $n_e$ is the electron number density, and $B$ is the magnetic field density.

We now need to determine the evolution of each of these parameters with the expansion. Let's suppose $R \propto t^{\lambda}$, where $R$ is the characteristic size of the bolide. How do $n_e V$, $\gamma_0$, and $B$ scale with $R$? The quantity $n_e V$ is the total number of electrons in the bolide, and must remain constant as the bolide expands. The scalings of $\gamma_0$ and $B$ are more complex, as discussed below.

### 6.3.1 Evolution of the particle distribution

In Section 5.3.1, we outlined some of the properties of an electron population with a power-law distribution of energies. Arguments for the evolution of this distribution in an expanding bolide are given by a number of workers (e.g., Scheuer and Williams (1968), Leahy (1991)). In Box 6.1, we demonstrate that, for the power-law distribution, with $\gamma_0 \gg 1$, the pressure $P_e$ and energy density $u_e$ are related by $P_e = u_e/3$. Using the expression for the energy density (Result 5.3.4), we can write the energy in the whole bolide as

$$U = u_e V = (n_e V)\,\gamma_0\,\frac{\xi - 1}{\xi - 2}\,m_e c^2\,, \tag{6.3}$$

and hence its derivative as:

$$\mathrm{d}U = (n_e V)\,\frac{\xi - 1}{\xi - 2}\,m_e c^2\,\mathrm{d}\gamma_0 = u_e V\,\frac{\mathrm{d}\gamma_0}{\gamma_0} \tag{6.4}$$

where $N = n_e V$ is a constant. Assuming the expansion is adiabatic ($\mathrm{d}Q = 0$), and that the only work done is by the internal pressure, the adiabatic losses are:

$$\mathrm{d}U = -P_e \mathrm{d}V = -\frac{u_e}{3}\mathrm{d}V\,. \tag{6.5}$$

Combining Equations 6.4 and 6.5, we obtain a differential equation for the low energy cutoff energy of the electron energy spectrum in terms of the volume:

$$\frac{\mathrm{d}\gamma_0}{\gamma_0} = -\frac{1}{3}\frac{\mathrm{d}V}{V} \tag{6.6}$$

which integrates to give $\gamma_0 \propto V^{-1/3}$. We now need to consider the shape of the expansion. Let's consider two cases. First, consider a 3-dimensional expansion (e.g., a sphere or an ellipsoid). Then,

we can write:

$$\frac{\mathrm{d}V}{V} = 3\frac{\mathrm{d}R}{R}\,. \tag{6.7}$$

Alternatively, we could consider a 2-dimensional expansion (e.g., a conical outflow or an expanding hollow shell). In this case, we have

$$\frac{\mathrm{d}V}{V} = 2\frac{\mathrm{d}R}{R}\,. \tag{6.8}$$

Combining Equations 6.7 and 6.8 with Equation 6.6, we find the scalings of the electron energy distribution with radius as:

$$\text{in 3D:} \qquad \gamma_0 \propto R^{-1} \tag{6.9a}$$

$$\text{in 2D:} \qquad \gamma_0 \propto R^{-2/3} \tag{6.9b}$$

### 6.3.2 Evolution of the magnetic field

The evolution of an expanding magnetic field is complex, and a full and correct treatment exceeds the scope of the present work. The scaling of the magnetic field density will be a strong function of the geometry of the expansion, and in particular, will depend on whether the flow expands along or parallel to the local magnetic field lines. The key assumption usually made is that the magnetic field is *frozen into* the flow. It can be shown that, in an inviscid and non-turbulent magnetohydrodynamic flow, the magnetic flux through a surface that follows the flow is constant.

Leahy (1991) gives, without proof, scalings for the steady adiabatic expansion of a magnetic field under different geometries (table 3.3 in Leahy (1991)). For our case, we consider a tangled magnetic field, in which case $B \propto \mathcal{R}^{-2}$, where $\mathcal{R}$ is the geometric mean of the expansions along each axis of a three dimensional space. Hence, for an expansion that is uniform along all three directions, $\mathcal{R} \sim R$, where $R$ is the radius, while for an expansion that is confined to two dimensions only, $\mathcal{R} \sim R^{2/3}$. Thus, we can write:

$$\text{in 3D:} \qquad B \propto R^{-2} \tag{6.10a}$$

$$\text{in 2D:} \qquad B \propto R^{-4/3} \tag{6.10b}$$

**Box 6.1: Pressure due to relativistic electrons**

The pressure from a thermal population of relativistic particles $P = u/3$ is a familiar result (Blundell and Blundell (2010)). We now demonstrate that the same result holds for a power-law distribution of electron energies.

From kinetic theory, we know that pressure can be written as an integral:

$$P = \frac{1}{3}\int \mathrm{d}p\, n_p\left(p\right)\, vp$$

where $n_p\left(p\right)$ is the number of electrons per unit volume per unit momentum, $p = \gamma m_e v$ is the modulus of the 3-momentum, and $v = \beta c$ is the velocity. This is obtained by calculating the momentum transfer per unit time per unit area on an imaginary surface. We can also write $\gamma^2\beta^2 = \gamma^2 - 1$ and we can use $n_p \mathrm{d}p = n_\gamma \mathrm{d}\gamma$ to recast the integral as one over $\gamma$, where the distribution $n_\gamma$ is given by Result 5.3.3. This gives:

$$\begin{aligned}
P &= \frac{1}{3}\int_{\gamma_0}^{\infty} \mathrm{d}\gamma\, n_\gamma\left(\gamma\right)\, \gamma m_e \beta^2 c^2 \\
&= \frac{1}{3} m_e c^2 \int_{\gamma_0}^{\infty} \mathrm{d}\gamma\, \frac{n\left(\xi-1\right)}{\gamma_0}\left(\frac{\gamma}{\gamma_0}\right)^{-\xi} \frac{\gamma^2-1}{\gamma} \\
&= \frac{1}{3}\, n\left(\xi-1\right) m_e c^2 \int_{\gamma_0}^{\infty} \frac{\mathrm{d}\gamma}{\gamma_0}\, \left(\frac{\gamma}{\gamma_0}\right)^{-\xi} \left[\gamma - \gamma^{-1}\right] \\
&= \frac{1}{3}\, n\left(\xi-1\right) m_e c^2 \left[\frac{\gamma_0}{\left(\xi-2\right)} - \frac{1}{\xi\,\gamma_0}\right] \\
&= \frac{u}{3}\left[1 - \frac{1}{{\gamma_0}^2}\frac{\xi-2}{\xi}\right].
\end{aligned}$$

This has the right limiting behaviour: we recover the ultra-relativistic case when $\gamma_0 \to \infty$, finding as advertised that $P = u/3$; the non-relativistic limit $P = 0$ is obtained in the case $\gamma_0 \to 1$ and $\xi \to \infty$, i.e., when the power law cutoff becomes very, very steep and there is no population of high $\gamma$ particles.

This discussion shows less rigour than we would like, reflecting the non-trivial physics, and especially the uncertainties over the geometries of both the expansion and the magnetic field. Scalings over the range $R^{-1}$ to $R^{-2}$ are possible depending on the relative orientation of the streamlines of the flow, the magnetic field, and the expansion. For instance, Miller-Jones et al. (2004) use $B \propto R^{-1}$, a scaling that could correspond to an expansion either perpendicular to or along the streamlines with a field purely orthogonal to that flow.

There are attempts to develop solutions for an expanding, magnetised sphere of plasma that display self-similarity (i.e., they undergo a simple scaling with time). These are generally confined to plasmons under an imposed external B-field: for example, a uniform field (Anderson et al. (1980), García-Rubio et al. (2016)), or a dipolar field (Winske and Omidi (2005), Nersisyan et al. (2011)). These are of limited applicability to our current case, and more work is certainly needed to understand this process.

### 6.3.3 Discussion

Now, we combine Equations 6.9 and 6.10 with Equation 6.2 for the spectral luminosity which must scale as the spectral flux density $S_\nu$. Hence, we can estimate the scalings for an expansion:

$$\text{in 3D:} \qquad S_\nu \propto \left(R^{-1}\right)^{(\xi-1)} \left(R^{-2}\right)^{(\xi+1)/2} \qquad \Rightarrow\ S_\nu \propto R^{-2\xi} \tag{6.11a}$$

$$\text{in 2D:} \qquad S_\nu \propto \left(R^{-2/3}\right)^{(\xi-1)} \left(R^{-4/3}\right)^{(\xi+1)/2} \qquad \Rightarrow\ S_\nu \propto R^{-4\xi/3} \tag{6.11b}$$

To convert these to lightcurves, we need to know the scaling of $R$ with time $T$. The simplest case is a free expansion, $R \propto T$. Then, we have a scaling purely expressed in terms of the electron energy power law index, $\xi$. If $\xi = 2.2$, corresponding to a spectral index of $\alpha = 0.6$ (see discussion in Section 5.4.1), then the two cases above give scalings $S_\nu \propto T^{-4.4}$ (3D) and $S_\nu \propto T^{-2.9}$ (2D). We compare these to the measured values: $\kappa_{\rm jet} = -2.57 \pm 0.09$ and $\kappa_{\rm cjt} = -2.94 \pm 0.12$. If our assumptions about the expansion of the magnetic field are correct, then the 3 dimensional expansion rate would be too rapid to explain that which we see here, unless there is a continuous acceleration of particles throughout the course of the observation.

Alternatively, an expansion geometry in two dimensions could be compatible with the observations. Such a two dimensional expansion could take the form of a conical outflow. However, the observations of optical emission lines suggest that the jet even if initially conical, has fragmented

into discrete balls of plasma long before reaching the scales we see here (Goranskii et al. (1998), Blundell and Bowler (2005)).; similarly, the stability analysis of Brinkmann et al. (1988) supports the fragmentation of the jet into discrete, cool blobs. These suggest a more promising geometry is a spherical expansion, but one in which the emitting region is confined to a thin shell at the surface of the bolide. This would allow the emitting region to scale in two dimensions only. It might also help to account for the apparent underestimation of the bolide masses in Section 5.4.1, by allowing a picture in which the bolide is cold, but it acceleration at its surface produces the observed population of relativistic electrons.

We note that this is only tentative evidence for such a geometry. Our remarks are highly dependent on the unknown geometry of the $B$-field, and the lack of a clear model for the joint scaling of $B$ and $\gamma_0$ makes drawing strong conclusions impossible at this time. However, the clear evidence from these real-time observations for the decay rates of the bolides in SS 433 should provide a strong result with which to test the predictions of such models.

## 6.4 Asymmetry between the jets

In Section 6.2.4 we noted that the mass estimates for the two bolides of pair 7 using the data from Day 42 were (slightly) inconsistent, with the jet bolide mass estimate about 30% greater than the counterjet . In Figure 6.3, we can see that this is actually an outlier. Throughout the decaying phase of the lightcurves, the counterjet is systematically brighter than the jet; only at the end does this pattern change. Let us examine this flux asymmetry in more detail.

In Figure 6.4, we plot the integrated intensities from the jet and the counterjet for bolide pair 7 against each other. There is a clear and almost linear relationship in the decaying part of the lightcurve. From Figure 6.3, we can identify 3 data points that deviate significantly from the otherwise almost linear decay curves: these are Days 37, 41, and 42. Removing these from the data set, we can fit a straight line to the $S_{\rm cjt} = a\, S_{\rm jet} + b$ where the slope $a = 1.437 \pm 0.035$ and the intercept $b\,/\,{\rm Jy} = -0.005 \pm 0.005$ – this offset term is consistent with zero.

Including the three discrepant data points makes only a small difference to the fitted line. The gradient is now $a = 1.461 \pm 0.035$ and the $y$-intercept is $b\,/\,{\rm Jy} = -0.010 \pm 0.004$ – this is still consistent with zero.

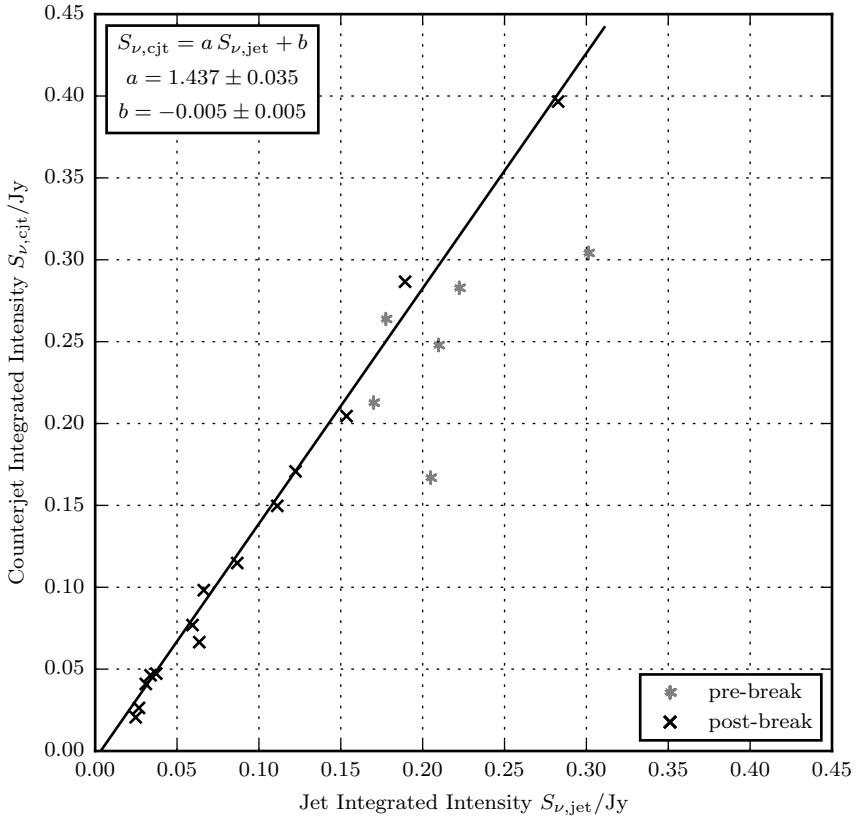


Figure 6.4: The integrated intensities as measured by `JMFIT` for the jet and counterjet bolides in pair 7 plotted against one another. Each marker represents one observation in the 2003 VLBA movie. The data are divided into pre-break and post-break. This refers to the point at which the bolides transition from a flat or slightly increasing lightcurve to a power-law decay – this occurs at approximately 8 d after launch, and corresponds to a very clear transition in this diagram, from a weak correlation to a tight, linear relationship. The linear fit (top left box) is consistent with passing through 0.

### 6.4.1 Doppler boosts and other light travel time effects

As already noted, a constant ratio between the fluxes of the two bolides is expected to account for the effects of Doppler beaming and the different ages of the (fading) bolides at the same observation epoch. The problem here is that the flux ratio found above (i.e., $S_{\nu,\mathrm{jet}}/S_{\nu,\mathrm{cjt}} = 0.696 \pm 0.017$ – note, it is the counterjet that is brighter here) is significantly lower than that expected by combining the work of Miller-Jones et al. (2004) with the kinematically derived velocities.

As set out in Miller-Jones et al. (2004), there are two contributions that set the flux ratio. Firstly, there is the ratio due purely to Doppler boosting, which is derived in e.g., Longair (2011). But, this assumes that the luminosities of the sources remain constant with time. As they manifestly don't stay constant, there is a second contribution to the flux ratio, namely the ratio of luminosities at the (different) times that light sets out from jet and counterjet to reach the Observer on Earth at the (same) time. Hence,

$$\frac{S_{\nu,\mathrm{jet}}}{S_{\nu,\mathrm{cjt}}} = \left(\frac{1+\beta\cos\eta}{1-\beta\cos\eta}\right)^{k+\alpha} \left(\frac{L_{\nu,\mathrm{jet}}\left(t_{\mathrm{jet}}\right)}{L_{\nu,\mathrm{cjt}}\left(t_{\mathrm{cjt}}\right)}\right) \tag{6.12}$$

where $k = 3$ is a geometric factor, $\alpha$ is the spectral index, $\beta$ is the jet launch speed, and $\eta$ is the angle between the jet and the line of sight (c.f., equation 2 of Miller-Jones et al. (2004)).[3] If, as we explored in the preceding Section, the spectral luminosities can be characterised by a power law evolution $L_\nu \propto t^\kappa$, then using

$$\frac{t_{\mathrm{jet}}}{t_{\mathrm{cjt}}} = \frac{1+\beta\cos\eta}{1-\beta\cos\eta} \tag{6.13}$$

(obtained by inspection of Equation 6.1; c.f., equation 4 of Miller-Jones et al. (2004)), we can write

$$\frac{S_{\nu,\mathrm{jet}}}{S_{\nu,\mathrm{cjt}}} = \frac{L_{\nu,0,\mathrm{jet}}}{L_{\nu,0,\mathrm{cjt}}} \left(\frac{1+\beta\cos\eta}{1-\beta\cos\eta}\right)^{k+\alpha+\kappa} \tag{6.14}$$

where $L_{\nu,0,\mathrm{jet}}$ and $L_{\nu,0,\mathrm{cjt}}$ denote the intrinsic luminosities of the bolides. We know from kinematic constraints that $\beta\cos\eta = -0.029 \pm 0.003$ for the jet of bolide pair 7. We now need a value for $\kappa$.

[3] A brief comment on the form of the equation given here. Sometimes, these ratios are given as $S_{\mathrm{app}}/S_{\mathrm{rec}}$ – the ratios of the approaching and receding bolides respectively. In this case, the value of $\eta$ must lie in the interval $[0, \pi/2]$, and the value of the fraction in brackets is definitely greater than 1. Here, as throughout this work, we prefer to use jet and counterjet to have fixed assignments in the jet system (east and west respectively in SS 433), to define $\eta$ as the angle between the *jet* and the line-of-sight, and to allow $\eta$ to lie in the interval $[0, \pi]$. i.e., there can be times when the counterjet approaches the observer and the jet points away from the observer, in which case it is the *counterjet* that undergoes boosting.

This is a source of some ambiguity, but we can follow two lines of reasoning.

#### 6.4.1.1 Using theoretical estimates for the fading rate

We can use the reasoning of Section 6.3 to find theoretical values for $\kappa$, and hence to predict the flux ratios. Miller-Jones et al. (2004) find that for synchrotron emission from an electron power law energy distribution with exponent $\xi$, then $\kappa = (1-3\xi)/2$, which combined with $\alpha = (1-\xi)/2$ gives an exponent $k+\alpha+\kappa = k-\xi$. Assuming $k=3$ and $\xi = 2.2$, and assuming that the intrinsic luminosities are the same, then for $\beta\cos\eta = -0.029 \pm 0.003$, we obtain $S_{\nu,\mathrm{jet}}/S_{\nu,\mathrm{cjt}} = 0.955 \pm 0.005$.

The value of $\kappa$ in Miller-Jones et al. (2004) is found by assuming $B \propto R^{-1}$. Taking instead the two values for $\kappa$ that we obtained by considering expansions in 2D and 3D, (i.e., $\kappa_{\mathrm{2D}} = -(4/3)\,\xi$ and $\kappa_{\mathrm{3D}} = -2\xi$), combined with a linear expansion ($R \propto t$), we obtain flux ratios:

$$\text{2D:} \qquad \frac{S_{\nu,\mathrm{jet}}}{S_{\nu,\mathrm{cjt}}} = \left(\frac{1+\beta\cos\eta}{1-\beta\cos\eta}\right)^{k-(1+5\xi)/6} = (0.944 \pm 0.006)^{1.0} \quad = 0.944 \pm 0.006 \tag{6.15}$$

$$\text{3D:} \qquad \frac{S_{\nu,\mathrm{jet}}}{S_{\nu,\mathrm{cjt}}} = \left(\frac{1+\beta\cos\eta}{1-\beta\cos\eta}\right)^{k-(1+3\xi)/2} = (0.944 \pm 0.006)^{-0.8} = 1.047 \pm 0.005 \tag{6.16}$$

In neither of these cases is the resulting flux ratio compatible with the observed value of $S_{\nu,\mathrm{jet}}/S_{\nu,\mathrm{cjt}} = 0.696 \pm 0.017$.

Note that in the second of these cases, the (approaching) counterjet appears fainter than the (receding) jet. This is because the fading of jet in this geometry is so rapid that the boosted approaching bolide has faded more in the time taken for light from the receding bolide to cover the distance along the line-of-sight than the Doppler boosting factor.

#### 6.4.1.2 Using observed values for the fading rate

We measured (Figure 6.3) the exponents of the lightcurves as $\kappa_{\mathrm{jet}} = -2.57 \pm 0.09$ and $\kappa_{\mathrm{cjt}} = -2.94 \pm 0.12$. Their different values indicate that the flux ratio will contain a time dependence. This will be a slow variation, $t^{\kappa_{\mathrm{jet}}-\kappa_{\mathrm{cjt}}}$, so we will neglect it. Instead, taking the mean of these two, we find $\kappa = -2.78 \pm 0.15$. This gives $k+\alpha+\kappa = 0.82$, and hence $S_{\nu,\mathrm{jet}}/S_{\nu,\mathrm{cjt}} = 0.954 \pm 0.010$. Again, this is inconsistent with the observed flux ratio.

### 6.4.2 An estimate of the density of obscuring circumbinary material

There are three immediately plausible explanations for the asymmetry. Firstly, it is possible that the observed flux asymmetries are representative of a true difference in the emissivities. That is, that the two bolides are intrinsically asymmetric at launch, carrying different masses and momenta. This would be surprising; the lack of evidence for a significant proper motion of the nucleus would suggest that simultaneously launched jet and counterjet bolides should carry equal and opposite momenta, though, of course, this strictly needs only be true in a time-averaged sense. With these data, we are unable to rule out the possibility of intrinsic asymmetry.

The second plausible explanation we propose is that the bolides are identical at birth, but that they accumulate or generate different magnetic fields as they propagate, or that the result of acceleration of electrons in each bolide is different. A clearer understanding of the evolution of both magnetic fields and the electron population is needed to examine this in any detail. However, we note that the estimates of the $B$-fields in Table 6.1 are virtually identical, which suggests that this is not the explanation.

Throughout this discussion, we have assumed that any extinction affects light from both bolides equally. However, we know that there are other outflows from the system: there are winds driven off the accretion disc (Blundell and Hirst (2011)), and outflow through the circumbinary ruff (Paragi et al. (1999) Blundell et al. (2001), Doolin and Blundell (2009)). Let us suppose that the difference in the jet and counter jet luminosities can be accounted for by an excess of obscuring material in front of the jet as opposed to the counterjet.

We will consider a simple model for this obscuring material. Let's assume (a) that there is a cloud of quasi-neutral ionised hydrogen plasma lying in front of one side of the system (in the current case, this will be in front of the jet, rather than the counterjet); (b) that this cloud has uniform density; (c) that it causes extinction by free-free absorption; (d) that radiation from the cloud is resolved out, and can be neglected; (e) that the original jet and counterjet bolides have the same intrinsic luminosities which are then affected by relativistic beaming and by different apparent fading rates; (f) that the bolides radiate via synchrotron radiation with a spectral index $\alpha = 0.6$ (g) that the bolides' luminosities evolve with $L \propto \tau^{\kappa}$ where $\kappa = -2.78 \pm 0.15$ (see above Section); and (h) that the obscuring region has a depth $l_0$, and covers the entire length of bolide 7's trajectory within the course of the observations.

From the theory of radiative transfer (see, e.g., Rybicki and Lightman (1979)), in the absence of emission, the flux density received from the jet bolide will be reduced by a factor $\mathrm{e}^{-\alpha^{\mathrm{ff}} l_0}$ where $\alpha^{\mathrm{ff}}$ is the free-free absorption coefficient and $l_0$ is the length of the absorbing region. Hence, we can write a modified expression for the flux ratio as:

$$\frac{S_{\nu,\mathrm{jet}}}{S_{\nu,\mathrm{cjt}}} = \mathrm{e}^{-\alpha^{\mathrm{ff}} l_0} \frac{L_{\nu,0,\mathrm{jet}}}{L_{\nu,0,\mathrm{cjt}}} \left(\frac{1+\beta\cos\eta}{1-\beta\cos\eta}\right)^{k+\alpha+\kappa} \tag{6.17}$$

Rearranging, we obtain an expression for the optical depth of the obscuring cloud:

$$\alpha_\nu l_0 = \ln\left[\frac{F_{\mathrm{cjt}}}{F_{\mathrm{jet}}}\left(\frac{1+\beta_\parallel}{1-\beta_\parallel}\right)^{k-p}\right]. \tag{6.18}$$

From equation 5.19 in Rybicki and Lightman (1979) the thermal free-free absorption coefficient is:

$$\alpha_\nu^{\mathrm{ff}} = \frac{4}{3}\left(\frac{2\pi}{3}\right)^{1/2} \frac{e^6}{(4\pi\epsilon_0)^3 {m_e}^{3/2} c} \frac{Z^2 n_e n_i \overline{g_{\mathrm{ff}}}}{(k_{\mathrm{B}}T)^{3/2}\nu^2} \tag{6.19}$$

where $T$ is the plasma temperature, $Z$ is the ion charge, $n_e$ and $n_i$ are electron and ion densities respectively, $\nu$ is the observation frequency, and $\overline{g_{\mathrm{ff}}}$ is the Gaunt Free-Free factor (we take $\overline{g_{\mathrm{ff}}} \simeq 1$). For an ionised hydrogen plasma ($Z = 1$, $n_e = n_i$), this evaluates to:

$$\frac{\alpha_\nu^{\mathrm{ff}}}{\mathrm{m}^{-1}} = 5.604\times10^{-35}\left(\frac{T}{1000\,\mathrm{K}}\right)^{-3/2}\left(\frac{n}{\mathrm{m}^{-3}}\right)^2\left(\frac{\nu}{\mathrm{GHz}}\right)^{-2}\overline{g_{\mathrm{ff}}} \tag{6.20}$$

Combining Equations 6.18 and 6.19, together with $Z = 1$ and $n_e = n_i = n$, we can obtain an expression for the number density of ionised hydrogen plasma in terms of the temperature and the depth of the plasma:

$$n^2 = \left(\frac{27}{32\pi}\right)^{1/2} \frac{(4\pi\epsilon_0)^3 {m_e}^{3/2} c}{e^6} \frac{(k_{\mathrm{B}}T)^{3/2}\nu^2}{\overline{g_{\mathrm{ff}}}} \times \ln\left[\frac{F_{\mathrm{cjt}}}{F_{\mathrm{jet}}}\left(\frac{1+\beta_\parallel}{1-\beta_\parallel}\right)^{k+\alpha+\kappa}\right] \tag{6.21}$$

which evaluates to:

$$\frac{n}{\mathrm{cm}^{-3}} = 2.625 \times 10^4 \times \left( \ln \left[ \frac{F_{\mathrm{cjt}}}{F_{\mathrm{jet}}} \left( \frac{1+\beta_{\parallel}}{1-\beta_{\parallel}} \right)^{k+\alpha+\kappa} \right] \right)^{1/2} \times \overline{g_{\mathrm{ff}}}^{-1/2} \left( \frac{T}{1000\,\mathrm{K}} \right)^{3/4} \left( \frac{l_0}{\mathrm{lightday}} \right)^{-1/2} \left( \frac{\nu}{\mathrm{GHz}} \right) . \quad (6.22)$$

Note that we do not have data for the temperature of the plasma, or the extent of the ruff material (either in depth, or by direct observation in area on the sky). Consequently, the determination of $n$ remains degenerate in $T$ and $l_0$. We can extract a representative order-of-magnitude estimate for $n$ by taking an estimate of the plasma temperature as $T \sim 1000\,\mathrm{K}$, and of the depth of the region as $l_0 \sim 1\,\mathrm{lightday}$. The first is commensurate with the temperature of ionised Hydrogen regions in the ISM. The $l_0$ estimate is more uncertain, representing our ignorance about the geometry of the circumbinary ruff. It corresponds to the distance travelled by the jet in $\sim 4\,\mathrm{d}$.

The resulting number density estimates are shown in Figure 6.5. The required density of obscuring matter is typically $n_e = 2 \times 10^{10}\,\mathrm{m}^{-3} \times (T\,/\,1000\,\mathrm{K})^{3/4}\,(l_0\,/\,\mathrm{lightday})^{-1/2}$. There is a slight residual time dependence, reflecting the difference in the power-laws describing the time dependences in Figure 6.3.

The three epochs on which we previously noted that the $S_{\nu,\mathrm{jet}}/S_{\nu,\mathrm{cjt}}$ flux ratio was inverted are even clearer here. These correspond to epochs on which there is apparently an excess of obscuring medium in front of the counterjet rather than the jet. Why these epochs should be so different is not clear at the present time, though we note the qualitative statements of Mioduszewski et al. (2004) that the component parts of the ruff may move as fast as $10^4\,\mathrm{km\,s}^{-1}$. It is clear from the images of the ruff in Figure 4.2 and in Paragi et al. (2002) that the ruff possesses a complex and uneven brightness distribution and hence a simple uniform covering is unlikely to be an accurate description of the observed asymmetry in the light decay. In exploring this, we are not helped by the insensitivity of the VLBA to large scale or extended structure, which helps to resolve out emission from the ruff.

With some further approximations, we can make an order-of-magnitude estimate a mass in the enveloping matter. Let's suppose that the density is constant in a region that is approximately cylindrical with $l_0 \simeq 1\,\mathrm{lightday}$ and a length corresponding to 20 d travel at $0.3c$ – i.e., 6 lightdays in length. Within this volume, assuming one proton per electron, the corresponding mass is $\sim 2 \times 10^{-6}\,\mathrm{M}_{\odot}$. By way of comparison, we note the estimates of mass loss via the accretion

disc wind – $10^{-4}\,\mathrm{M}_{\odot}\,\mathrm{yr}^{-1}$ (Perez and Blundell (2009)) – and via the jets – $5 \times 10^{-7}\,\mathrm{M}_{\odot}\,\mathrm{yr}^{-1}$ (Kotani et al. (1996)). If our mass estimate is correct, and if, most importantly, we are correct in attributing the asymmetry to extinction due to mass in the circumbinary ruff, this suggests that the mass loss through the circumbinary disc may be comparable in significance to that lost through the other known mechanisms.

We end on a note of caution: the nature of the outflow via the circumbinary ruff (including its velocity and geometry) is far from clear. Our calculation is predicated on the assumption that the bolides be intrinsically symmetric, but we have no evidence to support this claim, nor do we have evidence to discount the possibility that differences in the bolides' evolution post-launch may account for the observed asymmetry. Were we correct in identifying the obscuring matter with the ruff, the stability seen in the mass estimates in Figure 6.5 would require that the ruff be far greater in extent (by at least an order of magnitude) than any previous studies have shown. We do not know whether the jet and counterjet bolides are merely attenuated by the ruff, or whether their intrinsic evolution is moderated by passing through either the ruff or through the accretion disc wind. Indeed, Blundell and Hirst (2011) have shown that there are interactions between the jet and wind outflow. An eminently plausible alternative explanation – especially given that the fainter (eastern) jet is receding from the observer at this epoch – is that we see extinction due to the accretion disc wind rather than the ruff.

## 6.5 Summary

In this Chapter, we have qualitatively noted that the evolution of the flux densities of individual ejecta are complex – bolides appear to interact (either with each other or with other matter in the vicinity of the binary system) to cause significant dissipation of energy as radiation. We have discussed briefly the asymmetries that exist between bolides, and suggested a possible (though by no means certain) explanation in terms of extinction by a cicumbinary ruff containing as many as $2 \times 10^{10}$ electrons per cubic metre.

However, the most significant result is that, when given the opportunity to fade naturally, the bolides decay with a power law in time, with index $\sim 2.8$. Explaining this relationship could give a powerful probe of the internal thermodynamics.

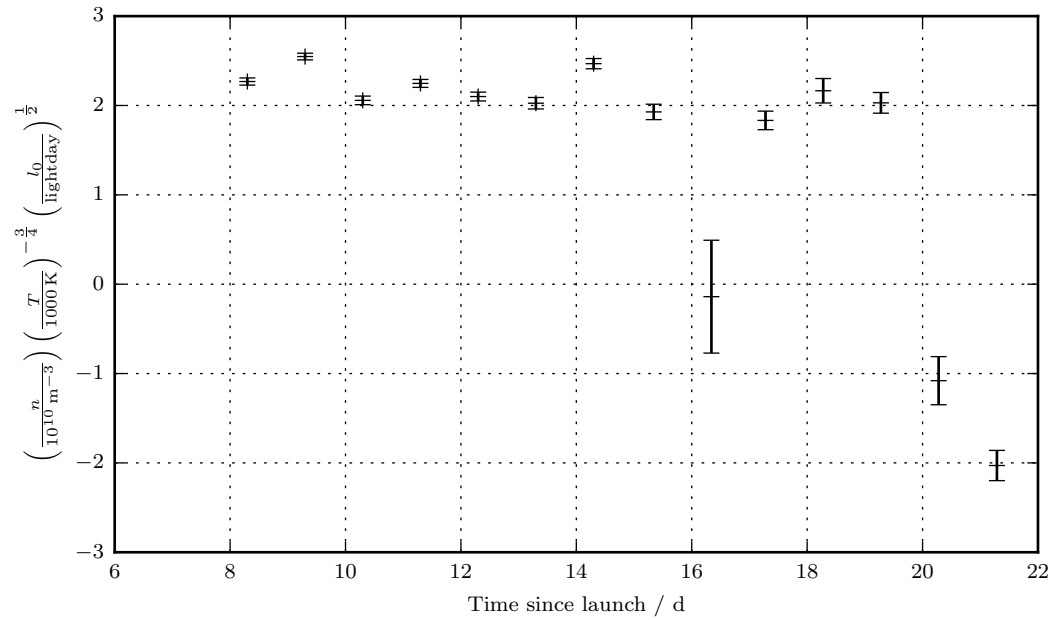


Figure 6.5: Estimated obscuring densities as described in Section 6.4.2. Degeneracies remain with the temperature and the depth of the obscuring medium, but these are expressed in terms of estimated characteristic values. Positive densities correspond to an excess of obscuring material in front of the jet. "Negative densities" correspond to an excess of obscuring material in front of the counter jet. Recall that we use "jet" and "counterjet" to mean the east and west jets respectively, and that at this epoch, the (western) counterjet is slightly angled towards the observer (by about 6° out of the plane of the sky).

# Chapter 7

# The X-Ray Behaviour of SS 433

## 7.1 Introduction

So far, we have used the power of high resolution VLBI imaging to probe the dynamics of the radio jets of SS 433 on scales of $10^{12}$-$10^{13}$ m. But, to explore the nature of the inner binary system itself, we must turn to higher energies. In this Chapter, we will review what is understood about SS 433 from observations at X-ray energies, and we will use new data from X-ray monitoring to examine the geometry and variability of the accreting binary. We will begin by reviewing the prevailing paradigm surrounding jet launch and variability in microquasars as inferred from their X-ray emission. We then outline the observational history of SS 433 at high energies (Section 7.1.2), describe monitoring data from the MAXI and Swift missions (Section 7.2), perform a time series analysis of these data (Section 7.3), and use the eclipse variation in the X-ray lightcurve to look at the binary geometry (Section 7.4). Finally, we will return to the standard paradigm and discuss SS 433's place within it (Section 7.5).

### 7.1.1 The standard picture of microquasar phenomenology

The prevailing paradigm around the interpretation of X-ray emission from accreting stellar-mass black holes is principally based on two key observations, namely:

1. that the X-ray emission from accreting black holes moves between two principal states – a low intensity, quiescent state, in which the emission is dominated by hard X-rays (a flat

spectrum extending up to perhaps 100 keV – this is referred to as the "low-hard" state), and a high intensity outburst state, where the emission is dominated by softer X-ray emission (the "high-soft" state); and,

2. that radio (and infra-red) emission is correlated with X-ray emission in the low intensity, hard X-ray state (seen in observations of V404 Cyg and GX339-4 by Gallo et al. (2003), Fender et al. (2004)), and is quenched when the system moves into the brighter, softer state (e.g., simultaneous radio observations and X-ray monitoring of the hard to soft state transition in GX339-4 by Fender et al. (1999)).

The first of these is encapsulated in the hardness-intensity diagram. This is constructed by analogy with the colour-magnitude plot in optical stellar photometry. The total intensity in the X-ray bands is plotted against some representation of its hardness. This is often the ratio of the X-ray flux in the hardest available waveband to that in the lowest (e.g., section 2.1 of Fender et al. (2004)). The transition between different states is traced by the evolution of the system around the hardness-intensity plane.

Somewhat conflicted terminology for the naming of these states is in use (see, for instance, Remillard and McClintock (2006)). The prevailing convention is that of, e.g., Fender et al. (2004), in which the system is categorised by its X-ray properties (i.e., a low-hard state and a high-soft state, separated by an intermediate or very-high state (intermediate spectral properties, very high photometric properties)).

In interpreting these observations, we have a number of physical pieces to consider. The accretion disc itself emits soft, thermal X-rays. It is usually understood to be geometrically thin but optically thick (e.g., from model-fits to X-ray spectra of Cyg X-1 by Gierliński et al. (1999)). Stable discs are theoretically possible to within a few gravitational radii of the black hole (with the innermost stable circular orbit (ISCO) dependent on the black hole's spin).[1] It is possible that these thin flows may be truncated at some radius $r > r_{\rm ISCO}$, changing to a different type of flow in the inner regions. The brightest emission in this thin flow comes from its hottest parts of the disc, close to its inner edge. The luminosity of the disc scales as the inverse of the inner radius, so a disc that is truncated far from the core (or which morphs into a radiatively inefficient accretion solution in

[1] The theory of such stable thin discs can be found in textbooks (e.g., Frank et al. (2002) or Beskin (2010)). Such discs consist of a fluid undergoing circular Keplerian orbits around the compact object. For mass to accrete inwards, angular momentum must be dissipated outwards. This is usually modelled by a viscosity which is proportional to the sound speed at radius $r$ and the scale height of the disc, or, equivalently, by a stress proportional to the gas pressure. This is the $\alpha$-prescription of Shakura and Sunyaev (1973).

its inner regions – see below) will make a smaller contribution to the system's emission.

A synchrotron-emitting jet typically emits at radio frequencies. Such jets are widely believed to come in two kinds: "compact" and discrete. The "compact" jets form continuous, conical, isothermal, and self-absorbed outflows, appearing with a flat spectrum (Fender (2001), Blandford and Königl (1979)). The jet appears discrete when it consists of distinct bolides more analogous to those we have seen in Chapter 4, and which have optically-thin, power-law spectra. The transition between these two regimes, characterised by their change in their spectral properties, has been observed (Fender (2001), Corbel et al. (2013)). A third type, more closely analogous to that which X-ray workers have seen in SS 433, is a continuous, optically thin outflow (Brinkmann et al. (1988), Kotani et al. (1996)).

Around the base of the jet may be a corona – a non-thermal plasma which upscatters soft X-rays by inverse Compton scattering (Gierliński et al. (1999)). The nature of this corona is unclear. Some workers attribute it to a hot accretion disc wind (e.g., Remillard and McClintock (2006)); others argue that a distinct corona may be unnecessary, and can instead be identified with the base of the jet (e.g., Markoff et al. (2005), who show that hard state spectra of GX339-4 and Cyg X-1 are consistent with both interpretations).

Lastly, outflows in the form of winds can disperse and expel matter from the disc, and may play an important role in the outbursts. These winds are inferred from iron line absorption measurements in 9 X-ray binaries (including GRS1915+105 and GX339-4) by Ponti et al. (2012). They are also observed by Muñoz-Darias et al. (2016) as P Cygni profiles in helium emission lines from V404 Cyg in outburst.

A qualitative understanding of the underlying physics of these phenomena follows the work of Fender et al. (1999) and Fender et al. (2004). This qualitative picture is best understood by following the evolution around the hardness-intensity diagram. In Figure 7.1, we reproduce figure 2 of Fender and Belloni (2012) to illustrate this point.

The system starts in quiescence in the low-hard state. Here accretion of matter occurs by a radiatively inefficient process. This accretion drives a compact jet, which radiates self-absorbed synchrotron emission at radio wavelengths. The X-ray emission consists of hard X-ray photons, perhaps arising from compton scattering off either a corona or off the jet itself. There may be a weak thermal contribution to the soft X-ray emission, arising from a geometrically thin, optically thick disc, but the heavy suppression of this thermal disc contribution indicates that the disc is

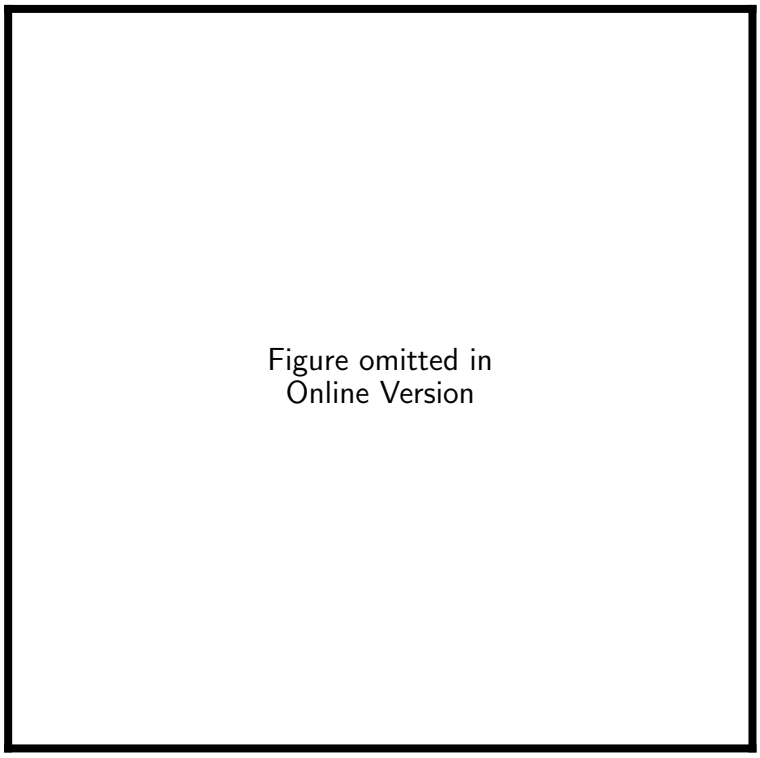


Figure 7.1: (Figure 2 in Fender and Belloni (2012)) Black hole accretion states in outburst, sketched in the hardness-intensity diagram. The $x$-axis represents the logarithm of the hardness ratio, and the $y$-axis represents the logarithm of the total intensity. The system starts in the hard state at A, brightens and moves to B as the outburst begins, softens to move from B to the soft state at D, with a discrete, relativistic, jet ejection as it passes through the intermediate state near C. The system may then repeatedly move between C and D, with repeated jet ejections. As the outburst ends, the system fades (E), hardens (F), and returns to quiescence (A). The cartoons at the bottom sketch the physical picture: in the hard state (right panel), there is a compact jet (pink), and the inner regions of the disc are dominated by a radiatively inefficient flow (blue); in the intermediate state (middle), the compact jet terminates and the inner radius of the radiatively efficient thin disc contracts; and in the soft state, there is a large outflow (accretion disc wind – yellow). The shape formed by the evolution around the hardness-intensity diagram is colloquially referred to as a "turtle-head" (e.g., Belloni (2010)).

truncated some distance from the compact object. The size of this suppression radius is highly uncertain, but is perhaps of the order of 10-100 gravitational radii from the core. Attempts have been made to estimate this for some systems (most notably GX339-4) by fitting to the faint thermal contribution made by the disc to the soft X-rays, and by modelling the effect of reflection of jet X-rays off the thin disc on the width of emission lines and the hard X-ray spectrum (for instance Tomsick et al. (2008) or García et al. (2015); see Narayan and McClintock (2008) for a review). At radii less than the truncation radius of the thin disc, there is believed to exist an optically thin but geometrically thick accretion flow. Candidates include advection dominated accretion flows (ADAFs; Narayan et al. (1998), Narayan and McClintock (2008)), or an advection dominated inflow-outflow solution (ADIOS; Blandford and Begelman (1999)).[2]

As the system moves into outburst its X-ray emission becomes first brighter and then softer. It is conjectured that this is due to some instability in the disc increasing the efficiency of accretion – for instance, a change in the hydrogen ionisation fraction increases the effective viscosity enabling transfer of angular momentum outwards and mass inwards within a Shakura-Sunyaev type disc (Fender (2010)). The inner radius of the disc contracts, increasing its temperature and the brightness of the thermal disc soft X-ray component (Remillard and McClintock (2006)). The system now approaches its peak brightness (this is identified in the literature as the Very High State or Intermediate State). As the spectrum continues to soften, the compact jet turns off, leading to a radio quench (as seen in GX339-4 by Fender et al. (1999)). Discrete, optically-thin, synchrotron emitting jet bolides are launched (e.g., observed by Corbel et al. (2000) as a power law spectral index in radio monitoring at the time of the X-ray state transition in GX339-4). These bolides typically have increased speeds over the continuous jet seen in quiescence (Fender et al. (2004)).

The system then settles into the high or soft state, in which it may reside for a timescale of the order of tens to a few hundred days. A thin accretion disc extends close to the innermost stable circular orbit, and there is a high accretion rate (Remillard and McClintock (2006)). The disc's soft thermal emission dominates the X-ray emission causing the soft spectrum. In some systems, the spectrum repeatedly hardens and softens at this point in the outburst – this appears to be the case in GRS1915+105 (e.g. Fender and Belloni (2004)), which has apparently remained in this

[2]Advection-dominated flows are radiatively inefficient – the ions and electrons in the flow are thermally decoupled, with the ions absorbing the excess heat liberated by viscous heating, and the electrons (which remain at a much lower temperature) dominating the emission. On the other hand, they are efficient accretion processes, carrying both matter and the liberated gravitational energy across the event horizon rapidly. In other words, they do their job properly, but they just don't tell us about it. There are, however, a number of outstanding problems relating to the consistency of these solutions. See Beskin (2010) for a summary discussion.

intermediate/mixed accretion state throughout its 20 yr observational history. While the system is in this soft state the disc is dissipated, partly through accretion onto the compact object, and partly through radiation driven winds (observed in optical spectroscopy of V404 Cyg in Muñoz-Darias et al. (2016)).

Once the disc has dissipated, the soft spectrum declines, the system's total emission becomes less intense, and it returns to the quiescent state. The radiatively inefficient accretion flow is reformed, and the radio emission from the compact jet reappears (e.g. Corbel et al. (2013)).

For more detailed discussions of this phenomenology, see the article by Fender et al. (2004) or the reviews by Remillard and McClintock (2006) and Belloni (2010). A brief overview is given in Fender and Belloni (2012). The review we have given here has been a necessarily cursory summary of the phenomena, and omits several key details. Most notably, we haven't discussed the changes in source variability, including the various quasi-periodic oscillations (QPOs; transient oscillations at timescales on the order of $10^{-1}$ Hz to $10^{2}$ Hz) that appear as the system evolves through its different states. These display a rich and varied phenomenology, with their short timescales suggesting that they may be related to the physical timescales of the inner regions of the accretion disc. A good discussion of the characteristic behaviour of the power spectra of these sources is given in Belloni (2011).

One of the most important claims of this "universal" paradigm is that it is able to describe jets across a wide range of scales. Similar hysteresis curves in the hardness-intensity plot are seen in a range of neutron star binaries (see e.g. Migliari and Fender (2006), Muñoz-Darias et al. (2014)). Likewise, active galactic nuclei with low accretion rates are seen to be radiatively loud, as predicted within this paradigm. Given an appropriate scaling with mass, their radio and X-ray brightnesses lie on the same correlation as seen in stellar mass black holes (Falcke et al. (2004), Fender (2010)). Lastly, Belloni (2011) finds evidence for similar spectral states in some ultraluminous X-ray sources (ULXs) – extra-Galactic sources with (highly) super-Eddington luminosities, which are conjectured to be accreting stellar-mass black holes whose Doppler-boosted jets lie close to the line-of-sight.

### 7.1.2 X-ray observations of SS 433

So, what do we know about the X-ray properties of SS 433? The first detections of X-ray emission associated with the object were made by Marshall et al. (1979) using the High Energy Astronomical Observatory (HEAO) satellite. They saw continuum emission consistent with thermal

bremsstrahlung from a plasma at 14.3 keV, as well as evidence for spectral line emission at 6.8 keV iron (associated with the hydrogen-like Fe XXVI or helium-like Fe XXV transitions), which was consistent with recombination in a thermal plasma of the same temperature. Using EXOSAT, Watson et al. (1986) resolved this line into a pair of precessing 6.7 keV lines. The Doppler shifts of these lines matched those predicted for the jet and counterjet by the kinematic model. They interpreted the line emission as dominated by Fe XXV, with both the line broadening and the continuum emission suggesting their origin lies in a thermal plasma that constitutes the lower regions of the jets.

In the subsequent decades, the system has been repeatedly observed by major X-ray observatories, with observations using Ginga (Brinkmann et al. (1991)), ASCA (Kotani et al. (1996)), the Chandra High Energy Transmission Grating Spectrometer (HETGS) (Marshall et al. (2002), Lopez et al. (2006), and Marshall et al. (2013)), the RXTE PCA (Filippova et al. (2006), Kotani et al. (2006), Seifina and Titarchuk (2010)), XMM-Newton (Brinkmann et al. (2005)), and INTEGRAL (Cherepashchuk et al. (2009), Cherepashchuk et al. (2013)). The general picture has remained largely unchanged. The emission is believed to be dominated by X-rays from the jet and counterjet, with the principal components being thermal bremsstrahlung and high-$Z$ recombination lines. There is also evidence for a Comptonization component, possibly associated with scattering off the disc, or with a corona (e.g. the INTEGRAL observations up to 100 keV by Cherepashchuk et al. (2009)).

Several workers have attempted to model the jets as radiatively cooled, adiabatically expanding, conical outflows. Under these assumptions, the emission is modelled as optically-thin, thermal bremsstrahlung radiation from a stable jet with a known temperature profile along its length. Versions of this profile are used in Kotani et al. (1996) and in Khabibullin et al. (2016); in both cases there are errors in their treatment (Khabibullin et al. are inconsistent in their use of the adiabatic index, and Kotani et al. make an error in their handling of the radiative cooling term), and we present a corrected derivation of this equation in Box 7.1. Brinkmann et al. (1988) gives a more general hydrodynamic treatment of a similar conical outflow, and argues that instabilities in the cooling of an initially nearly uniform flow will result in fragmentation of the flow into cool but still nearly ballistic clouds, which are in turn identified with the spectral line emitting hydrogen clouds seen at optical wavelengths, and possibly with those seen at radio wavelengths.

This model has allowed estimates of the properties of the base of the jets. Estimates for the temperature of the plasma near the base of the jets are typically 15-30 keV (e.g., $T = 17 \pm 2$ keV

**Box 7.1: Thermal evolution of a conical jet**

Kotani et al. (1996) and Khabibullin et al. (2016) both give, without proof, differential equations for the temperature variation $T(x)$ with distance $x$ along the jet. Both of their equations are wrong. The correct form for an adiabatically expanding, radiatively cooled, conical outflow is:

$$\frac{\mathrm{d}T}{\mathrm{d}x} = -\frac{n_\mathrm{e} n_\mathrm{i}}{n_\mathrm{e} + n_\mathrm{i}} \frac{(\Gamma - 1)}{\beta_\mathrm{jet} c} \Lambda(T) - 2(\Gamma - 1) \frac{T}{x} \tag{7.1}$$

where $\Gamma$ is the adiabatic index ($\Gamma = \frac{5}{3}$ for a non-relativistic monatomic plasma), and $\beta_\mathrm{jet} c$ is the jet bulk velocity. The derivation of this equation is as follows. The First Law of Thermodynamics gives us the change in the total internal energy of the jet:

$$\mathrm{d}U = \mathrm{d}Q + \mathrm{d}W_\mathrm{rad} + \mathrm{d}W_\mathrm{exp} \tag{7.2}$$

where $\mathrm{d}Q$ is the heat input, $\mathrm{d}W_\mathrm{rad}$ is the energy lost in radiation, and $\mathrm{d}W_\mathrm{exp}$ is the work done by expansion. From the assumption of adiabatic expansion, we have $\mathrm{d}Q = 0$ – i.e., there is no flow of heat. The radiative cooling term can be written:

$$\mathrm{d}W_\mathrm{rad} := -n_\mathrm{e} n_\mathrm{i} \Lambda(T) V \mathrm{d}t \tag{7.3}$$

where the emissivity (power radiated per unit volume) is defined to be $n_\mathrm{e} n_\mathrm{i} \Lambda(T)$. For optically thin bremsstrahlung, this will be proportional to $T^{1/2}$ – see e.g. Longair (2011) equation 6.46. We want to express this in terms of an emission per unit length. Neglecting a small relativistic correction due to length contraction of the jet, we can write $\mathrm{d}t = \mathrm{d}x / \beta_\mathrm{jet} c$. The expansion term $\mathrm{d}W_\mathrm{exp}$ is work done in pushing the volume outwards:

$$\mathrm{d}W_\mathrm{exp} = -p \, \mathrm{d}V \tag{7.4}$$

We let $x$ be the distance along the cone's axis from its apex (note that the base of the jet is not actually at the apex, but at some distance $x_0$ along the cone), and $\Theta$ be the half angle of the cone. The volume of a differential element at distance $x$ along the cone is

$V(x) = \lim_{\mathrm{d}x\to 0}\left[\pi\left(x\Theta\right)^2\mathrm{d}x\right]$, and its change with distance is:

$$\begin{aligned}\frac{\mathrm{d}V}{\mathrm{d}x} &= \lim_{\mathrm{d}x\to 0}\frac{V(x+\mathrm{d}x)-V(x)}{\mathrm{d}x} = \lim_{\mathrm{d}x\to 0}\pi\Theta^2\mathrm{d}x\,\frac{(x+\mathrm{d}x)^2-x^2}{\mathrm{d}x}\\ &= \lim_{\mathrm{d}x\to 0}\pi\Theta^2\mathrm{d}x\,\frac{2x\,\mathrm{d}x}{\mathrm{d}x} = 2\lim_{\mathrm{d}x\to 0}\left[\pi x\Theta^2\mathrm{d}x\right] = 2\frac{V}{x} \qquad (7.5)\\ \Rightarrow \frac{\mathrm{d}V}{V} &= 2\frac{\mathrm{d}x}{x} \qquad (7.6)\end{aligned}$$

For an electrically neutral, fully ionised plasma, we can write the pressure as: $p = \left(n_\mathrm{e}+n_\mathrm{i}\right)k_\mathrm{B}T$, giving for the expansion term:

$$\mathrm{d}W_\mathrm{exp} = -\left(pV\right)\frac{\mathrm{d}V}{V} = -\left(n_\mathrm{e}+n_\mathrm{i}\right)k_\mathrm{B}TV\times 2\frac{\mathrm{d}x}{x} \qquad (7.7)$$

Lastly, we use the heat capacity per unit volume of a gas $c_V = k_\mathrm{B}\left(n_\mathrm{e}+n_\mathrm{i}\right)/\left(\Gamma-1\right)$ (see e.g., Blundell and Blundell (2010)) to write:

$$\mathrm{d}U = c_V V\mathrm{d}T = V\frac{k_\mathrm{B}\left(n_\mathrm{e}+n_\mathrm{i}\right)\mathrm{d}T}{\left(\Gamma-1\right)} \qquad (7.8)$$

Combining these results we have:

$$V\frac{k_\mathrm{B}\left(n_\mathrm{e}+n_\mathrm{i}\right)\mathrm{d}T}{\left(\Gamma-1\right)} = -n_\mathrm{e}n_\mathrm{i}\Lambda\left(T\right)V\frac{\mathrm{d}x}{\beta_\mathrm{jet}c} - \left(n_\mathrm{e}+n_\mathrm{i}\right)k_\mathrm{B}TV\times 2\frac{\mathrm{d}x}{x} \qquad (7.9)$$

which can be rearranged to obtain the correct form of the temperature evolution equation – Equation 7.1.

(Brinkmann et al. (2005)); $T = 20 \pm 6\,\mathrm{keV}$ (Kotani et al. (1996)); $T \sim 30\,\mathrm{keV}$ (Filippova et al. (2006))). Estimates of the radius of the base of the jet are typically $\gtrsim 3 \times 10^7$ m (e.g., Brinkmann et al. (1991), Kotani et al. (1996), or Kotani et al. (2006), which, as we have previously noted, is large relative to the size of the event horizon of the black hole – perhaps as much as $200\,R_\mathrm{S}$.

The opening angle of this conical outflow[3] can be estimated by considering the broadening of spectral lines. For instance, using the Chandra HETGS, Marshall et al. (2002) estimate a jet opening angle of $1\overset{\circ}{.}23 \pm 0\overset{\circ}{.}06$, or equivalently an expansion speed of $\sim 0.5\%$ of the speed of light, for a jet travelling at $0.26c$.

More recently, spectra have been extended to higher energies (up to 100 keV) using the INTEGRAL observatory (Cherepashchuk et al. (2009), Seifina and Titarchuk (2010)). Here, emission is assumed to be inverse Compton scattered radiation from the disc or the jet, though the nature of the scattering region is unknown.

To explain the continuum emission up to 100 keV, Seifina and Titarchuk (2010) instead propose a model in which the continuum emission across the X-ray band is dominated by Comptonisation of soft outer disc photons off a thick thermal gas around the disk and off the converging accretion flow in the innermost region of the disc. This is able to explain the higher energy continuum, but produces poor agreement with the lower energy emission believed to be associated with the jets. Here, the earlier bremsstrahlung models give a better description of the thermal radiation from the jets.

Studies of lightcurves from the source have shown that the X-ray flux undergoes eclipses by the companion star and varies with the precession of the jets. Attempts to model this have been made by, for example, Antokhina et al. (1992), but the precise geometry remains unclear. Where attempts have been made to estimate binary parameters (e.g., Goranskii et al. (1998)), the mass estimates have been incompatible with optically derived values (e.g., Gies et al. (2002b)). We will return to this at greater length in Section 7.4 of this Chapter.

What is clear, however, is that no workers have hitherto seen evidence for direct X-ray emission from the accretion disc itself (Kotani et al. (1996), Brinkmann et al. (2005), Seifina and Titarchuk (2010)). This is in contrast to the optical disc (seen in observations immediately preceding a flare by Blundell et al. (2011)) – in the only X-ray observations known to coincide with a radio flare,

[3]Note, this angle describing the shape of the conical outflow is distinct from the opening angle of the precession cone used in the kinematic model (Section 2.2). The precession cone opening angle describes the shape of the cone about which the conical jet outflow precesses.

Kotani et al. (2006) attribute rapid (10 s) variability to shot-like behaviour in the jet outflow, rather than to variations in the disc itself.

As seen from Earth, SS 433 is a not particularly bright X-ray source, with an isotropic 2-10 keV X-ray luminosity of $\sim 10^{29}$ W (e.g., Watson et al. (1986) – by comparison, the nearby source GRS1915+105 is on the order of $\sim 3$ orders of magnitude brighter (Mirabel and Rodríguez (1994))). Due to the super-Eddington accretion rate in SS 433, it is believed that the isotropic X-ray luminosity as seen by an observer looking directly down the precession cone may be in excess of $10^{33}$ W (Fabrika (2004)). This leads to the identification of SS 433 as a misaligned, Galactic equivalent of the extra-Galactic ULXs, a conclusion strengthened by similarities in their optical spectra (Poutanen et al. (2007), Fabrika et al. (2015)). Indeed, Khabibullin and Sazonov (2016) claim to identify an excess of X-ray emission reflected off gas clouds in the Galactic plane supporting this estimate.

In summary, SS 433's X-ray behaviour presents a number of outstanding questions. Jet bremsstrahlung models like that of Kotani et al. (1996) describe the soft X-ray continuum and emission lines well, but do not integrate well with the Comptonisation models used to describe continuum emission at energies $\gtrsim 20$ keV. In particular, the geometry of both emitting and opaque matter is unknown, remains unclear, with no inconsistent eclipsing data and no estimate of the scale of the suspected Comptonisation region.

## 7.2 X-ray monitoring of SS 433

### 7.2.1 The MAXI Observatory on the International Space Station

The Monitor of All-sky X-ray Image (MAXI) is a Japanese-led observatory attached to the International Space Station (ISS). Since its installation in 2009, it has provided monitoring of the X-ray sky, using the Gas Slit Camera to look for variable sources and transients in the 2-20 keV energy range. Lightcurves are available in 3 energy bands (2-4 keV, 4-10 keV, and 10-20 keV) from `maxi.riken.jp`. Further details are available in Matsuoka et al. (2009).

In Figure 7.2, we plot the lightcurves for the combined energy band and the 3 sub-bands. We use the data from MJD 55058 to MJD 57294 (2009-Aug-15 to 2015-Sep-29). Each point represents data collected during one orbit of the ISS. From the plotted flux histograms, we can see that SS 433 is not detected in a significant fraction of the orbits. However, we will see in later sections

that we obtain sufficient signal-to-noise ratio to detect physical variations by averaging the data over many orbital and precessional periods.

### 7.2.2 The Swift/Burst Alert Telescope

The Swift/Burst Alert Telescope (Gehrels et al. (2004)) is another all-sky X-ray monitor, providing spectral coverage at higher energies. Designed to enable rapid detection of gamma-ray bursts and x-ray transients, Swift also provides monitoring of the light curves of known sources, including SS 433, in the 15-50 keV band. These data are processed and reduced by an automated pipeline (see Krimm et al. (2013) for details of the reduction process). They are then made available online at `swift.gsfc.nasa.gov/results/transients/SS433/`.

The Swift/BAT light curve for SS 433 is plotted in Figure 7.3 for the range of dates from MJD 53415 to MJD 57411 (2005-Feb-14 to 2016-Jan-24). Again, each observation represents one pointing (i.e., one orbit) of the telescope. As with the MAXI data, the histograms show that SS 433 is not consistently detected by Swift.

Before we can probe the physics of the system, there are two data analysis questions to resolve: 1) at individual epochs, the signal-to-noise ratio is too low to detect the source; and 2) the time series are irregular sampled, so their spectra cannot be obtained by simple use of the Fast Fourier Transform. To handle the first of these, we will see that it is sufficient to average the data over the periodicities of physical interest in the source. To find those periodicities, we must first consider the second point in more detail.

## 7.3 Time Series Analysis of X-Ray Lightcurves

### 7.3.1 Deconvolution of Irregularly Sampled Time Series

The problem of irregular sampling of a time series is recurrent across a wide range of data analysis problems in and beyond astronomy. An irregular sampling manifests itself by introducing spurious peaks into the spectrum. The problem is then how to separate the true spectrum from the effect of the irregular sampling. In Box 7.2, we show that this can be reduced to a deconvolution exercise.

Many workers have sought to avoid this complexity by interpolating data onto a regular grid to replicate a fixed “sampling” frequency, and then using Fast Fourier Transform methods to find the

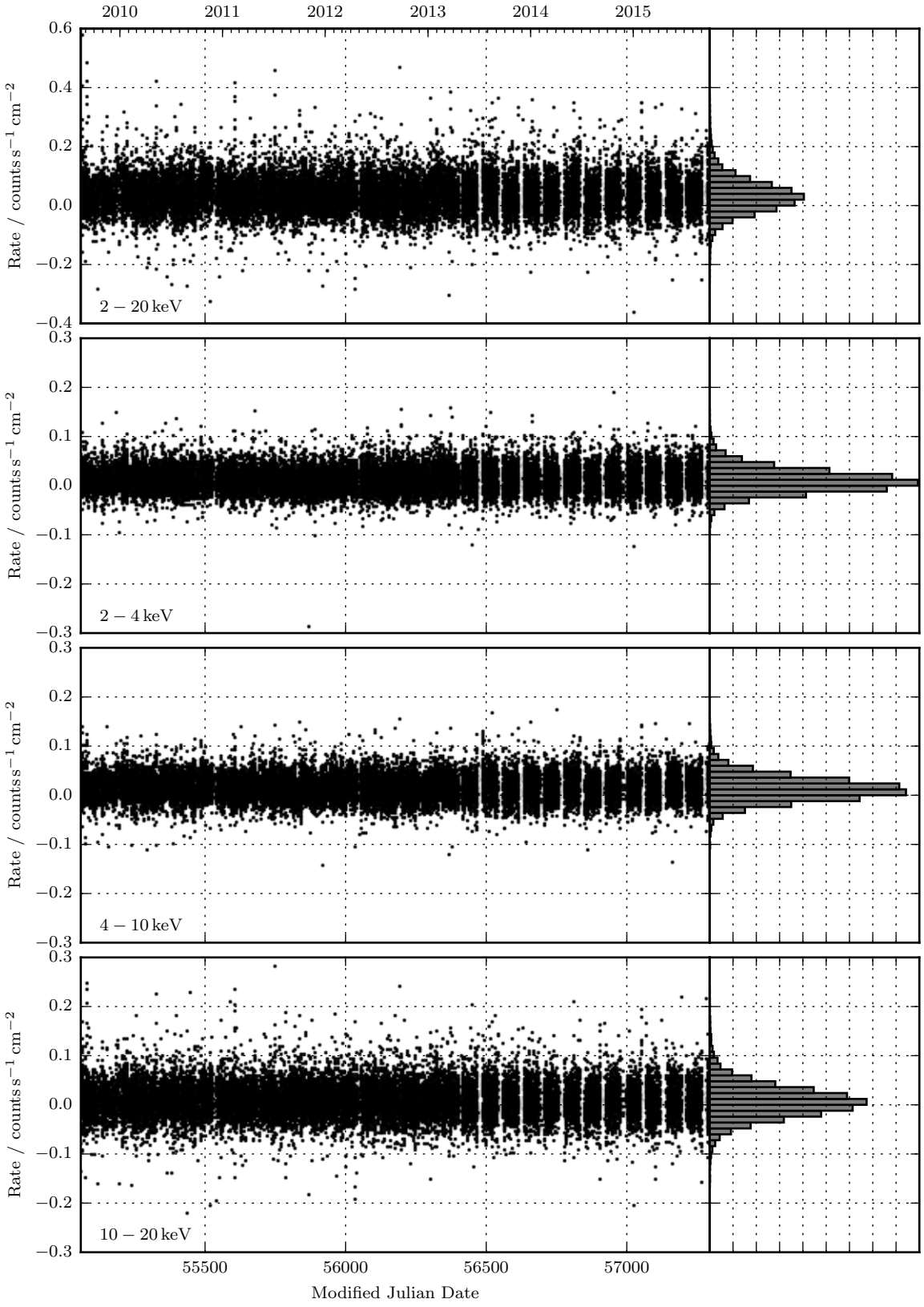


Figure 7.2: X-ray lightcurves of SS 433 from the MAXI Observatory, for the whole energy band, and 3 sub-bands (2-4 keV, 4-10 keV, and 10-20 keV). The data span the range MJD 55058 to MJD 57294. The subplots on the right show the same data binned into histograms by count rate.

spectrum. Maximum-Entropy based methods are sometimes used to try to recreate the spectrum. Others simply ignore the problem (cf., the Lomb-Scargle periodogram) – this approximation works satisfactorily if the time series consists of many samples, and if it is close to regular sampling.

Working in analogy to the CLEAN algorithm used in deconvolution of 2-dimensional radio maps, Roberts et al. (1987), developed a formulation that allows for the CLEANing of time series. As in radio interferometry, this proceeds by identifying the brightest points on the map, subtracting off the some fraction of the dirty beam (i.e., the point spread function (PSF), which is the response to a delta-function input) centred at that frequency, and then repeating the process by searching for the highest point in the residual map. The final spectrum is obtained by restoring a Gaussian beam to the residual map centred on each frequency from which a clean component was taken. This *clean beam* is obtained by fitting to the central maximum of the dirty beam. See Box 7.3 for further details.

Applying this algorithm to the (1-dimensional) photometric monitoring data, we can explore the periodicities present in the SS 433 system.

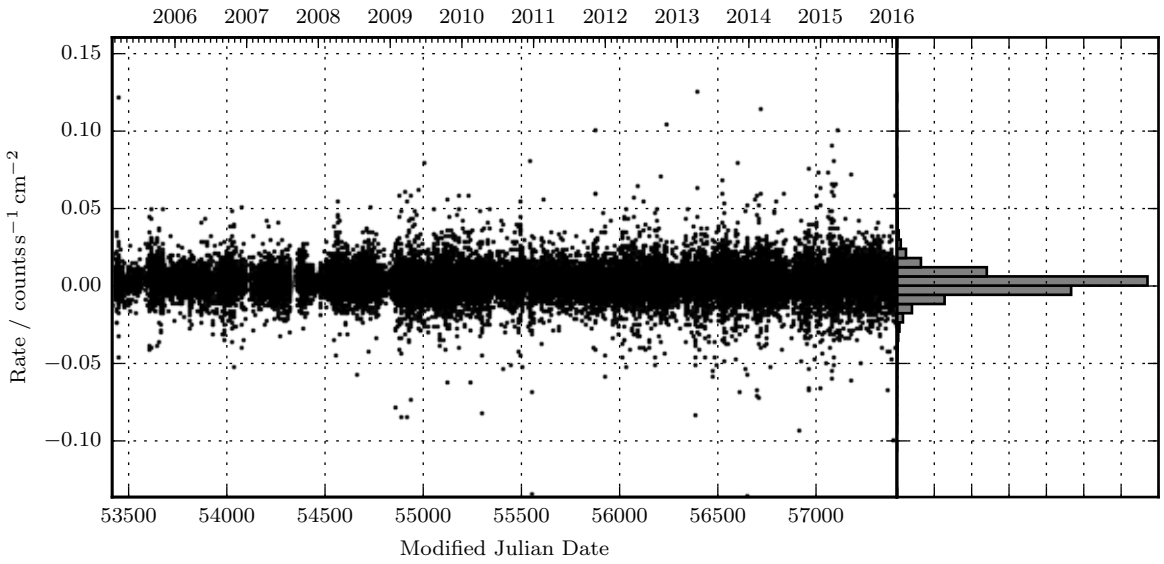


Figure 7.3: X-ray lightcurves of SS 433 at 15-50 keV from the Swift/BAT satellite. The data span the range MJD 53415 to MJD 57411. The subplot on the right shows the same data binned into a histogram by count rate.

**Box 7.2: The problem of irregular sampling - the Dirty Spectrum**

Suppose that we have a true signal $f(t)$, whose true spectrum Fourier theory tells us can be written as $\tilde{f}(\nu) = \int_{-\infty}^{\infty} \mathrm{d}t\, f(t)\, \mathrm{e}^{-2\pi i\nu t}$. We observe the signal at $N$ discrete times $\{t_i\}$ obtaining samples $\{f_i\}$. This can be represented as a sampled signal $s(t) := f(t)\, w(t)$, where $w(t) = \frac{1}{N}\sum_{i=1}^{N} \delta(t - t_i)$ is the sampling function, and so $s(t) = \frac{1}{N}\sum_{i=1}^{N} f_i \delta(t - t_i)$. The Fourier transform of the sampled signal is the *dirty spectrum*:

$$\tilde{s}(\nu) = \int_{-\infty}^{\infty} \mathrm{d}t\, s(t)\, \mathrm{e}^{-2\pi i\nu t} = \int_{-\infty}^{\infty} \mathrm{d}t\, \mathrm{e}^{-2\pi i\nu t} f(t)\, w(t) = \tilde{f}(\nu) * \tilde{w}(\nu) \tag{7.10}$$

where in the last step we have invoked the convolution theorem. That is, our dirty spectrum, $\tilde{s}(\nu)$, is the convolution of the true spectrum, $\tilde{f}(\nu)$, with the dirty beam, $\tilde{w}(\nu)$. The dirty beam and dirty spectrum can be written simply as Fourier sums:

$$\tilde{w}(\nu) = \frac{1}{N}\sum_{j=1}^{N} \mathrm{e}^{-2\pi i\nu t_j} \tag{7.11}$$

$$\tilde{s}(\nu) = \frac{1}{N}\sum_{j=1}^{N} f_j \mathrm{e}^{-2\pi i\nu t_j} \tag{7.12}$$

Then, by deconvolving $\tilde{w}$ from $\tilde{s}$, we can recover the true spectrum. In the special case of a regularly spaced sampling function, it is possible to avoid this problem by recalling the Nyquist sampling theorem. This tells us that the principal sidelobes will corrupt the data at frequencies greater than half the grid frequency, while the spectrum below this frequency forms a good approximation to the true spectrum (there is an interesting pedagogical analogue here with the free spectral range of the grating spectrometer). In the general case of irregularly drawn samples, there is no such simple rule for the location of principal sidelobes to help us interpret the dirty spectra – we must find a way to perform the deconvolution itself.

**Box 7.3: The Roberts, Lehar & Dreher [1987] spectral Clean algorithm**

The key insight underlying the Roberts, Lehar & Dreher [1987] algorithm is that the Fourier space expression of a single (positive) frequency component $f(t) = A\cos(2\pi\nu_0 t + \phi_0)$ is the sum of a positive and a negative frequency component. i.e.,

$$f(t) = a\,\mathrm{e}^{2\pi i\nu_0 t} + a^*\mathrm{e}^{-2\pi i\nu_0 t} \tag{7.13}$$

where $a := \frac{A}{2}\,\mathrm{e}^{i\phi_0}$ is the (complex) Fourier amplitude and $a^*$ is its complex conjugate. Therefore, by taking the Fourier transform, we find the true spectrum of this signal, $\tilde{f}(\nu)$, is:

$$\tilde{f}(\nu) = a\,\delta(\nu - \nu_0) + a^*\delta(\nu + \nu_0) \tag{7.14}$$

and consequently, the Fourier spectrum obtained from samples of such a monochromatic signal (Equation 7.10) is given by:

$$\tilde{s}(\nu) = \tilde{f}(\nu) * \tilde{w}(\nu) = a\,\tilde{w}(\nu - \nu_0) + a^*\tilde{w}(\nu + \nu_0) \tag{7.15}$$

where $\tilde{w}$ is the dirty beam. That is, at any frequency $\nu$, there will be contributions to the dirty spectrum from the sidelobes of *both* the positive frequency *and* the negative frequency parts of the spectrum.

For such a monochromatic signal, Roberts et al. obtain a unique expression for $a \equiv \tilde{f}(\nu_0)$ as follows. Note from Equations 7.11 and 7.12 that $\tilde{w}(-\nu) = \tilde{w}^*(\nu)$, $\tilde{w}(0) = \tilde{w}^*(0) = 1$, and $\tilde{s}(-\nu) = \tilde{s}^*(\nu)$. Then, considering Equation 7.15 and its complex conjugate, both evaluated at $\nu_0$, we have:

$$\tilde{s}(\nu_0) = a\,\tilde{w}(0) + a^*\tilde{w}(2\nu_0) \tag{7.16}$$

$$\tilde{s}^*(\nu_0) = a^*\tilde{w}^*(0) + a\,\tilde{w}(2\nu_0) \tag{7.17}$$

This means that the dirty spectrum at frequency $\nu_0$ is the sum of the dirty beam centred at $\nu_0$, *and* a contribution from the dirty beam centred at $-\nu_0$. Rearranging the second equation to find $a^*$, using $\tilde{w}(0) = \tilde{w}^*(0) = 1$, and then substituting into the first equation,

we find:

$$a^* = \tilde{s}^*(\nu_0) - a\,\tilde{w}(2\nu_0) \tag{7.18}$$

$$\Rightarrow \tilde{s}(\nu_0) = a + \tilde{s}^*(\nu_0)\,\tilde{w}(2\nu_0) - a\,|\tilde{w}(2\nu_0)|^2 \tag{7.19}$$

which finally yields:

$$a = \frac{\tilde{s}(\nu_0) - \tilde{s}^*(\nu_0)\,\tilde{w}(2\nu_0)}{1 - |\tilde{w}(2\nu_0)|^2} \tag{7.20}$$

Note that in the limiting case of a constant component in the spectrum, i.e., $\nu_0 \to 0$, we have $a = \frac{\tilde{s}(0)}{2}$. This can be shown by using $\tilde{w}(0) = \tilde{w}^*(0)$ and $\tilde{s}(0) = \tilde{s}^*(0)$ to factorise the denominator in Equation 7.20, and then canceling a term $(1 - \tilde{w}(0))$ from both numerator and denominator.

The challenge now is to expand this monochromatic reasoning to allow us to recreate a true polychromatic signal. By analogy with the CLEAN algorithm of Högbom (1974), Roberts et al. (1987) proceed by subtracting off a fraction of the contribution of the brightest monochromatic frequency in the dirty spectrum. This contribution is approximately given by Equation 7.20 where $\nu_0$ is the frequency of the component being subtracted. The algorithm is outlined in Appendix C of their paper.

### 7.3.2 Periodicities in X-ray photometric monitoring of SS 433

#### 7.3.2.1 The MAXI instrument – 2 - 20 keV waveband

The resulting spectrum is plotted in Figure 7.4. There is a very clear periodicity at around 160 d, and then a second complex of peaks at roughly half this period. As this is close to the kinematic model precession period, it is most likely that the two are associated. There are also a number of other peaks: these are approximately labelled in Fig. 7.4, and are fitted with (multiple) Gaussians in Figure 7.6. The resulting fits are listed in Table 7.1. Several of these can be associated with known periods of the system: there is a weak signal that appears to correspond to the 13.08 d orbital period (panel (d)), and a 12d period that could be associated with $\omega_{\rm orb} + |\omega_{\rm pre}|$ (panel (e)). This is the *synodic* period of the system – i.e., the time taken for the precessional and orbital orientations to stand in the same orientation relative to one another.

There are peaks that lie close to the 6d period associated with the nodding of the jet (panel (h)). However these are not consistent with the canonical beats at 5.83 d or 6.28 d obtained from optical spectroscopy. They are also not particularly significant.

We are not able to account for the broad complex of peaks at $\sim$ 18 d (panel (c)), or for the peak at $\sim$ 10 d (panel (f)). They do not appear to be un-cleaned side lobes of other signals (cf. Figure 7.5). As a check that these signals aren't purely artefactual, we repeated the spectral deconvolution dividing the data set randomly into two subsets. These are plotted in Figure 7.7. The broad 18 d peak remains particularly prominent. The signals associated with the orbital and precessional frequencies, $\omega_{\rm orb}$ and $\omega_{\rm pre}$, as well as $2\omega_{\rm pre}$ and $\omega_{\rm orb} + |\omega_{\rm pre}|$ also remain robust, but the possible frequencies around at $\sim$ 10 d and $\sim$ 6 d disappear. They can be discounted as statistical anomalies.

#### 7.3.2.2 Summary of results from the MAXI instrument – individual wavebands

As MAXI takes measurements in 3 sub-bands, we repeat the analysis on the flux densities in each of these. Again, we use the Roberts et al. (1987) CLEAN implementation. The fluxes given in the MAXI data products are normalised to mean flux densities by dividing each value by the bandwidth. The resulting spectra are plotted in Figure 7.8.

A number of interesting points arise:

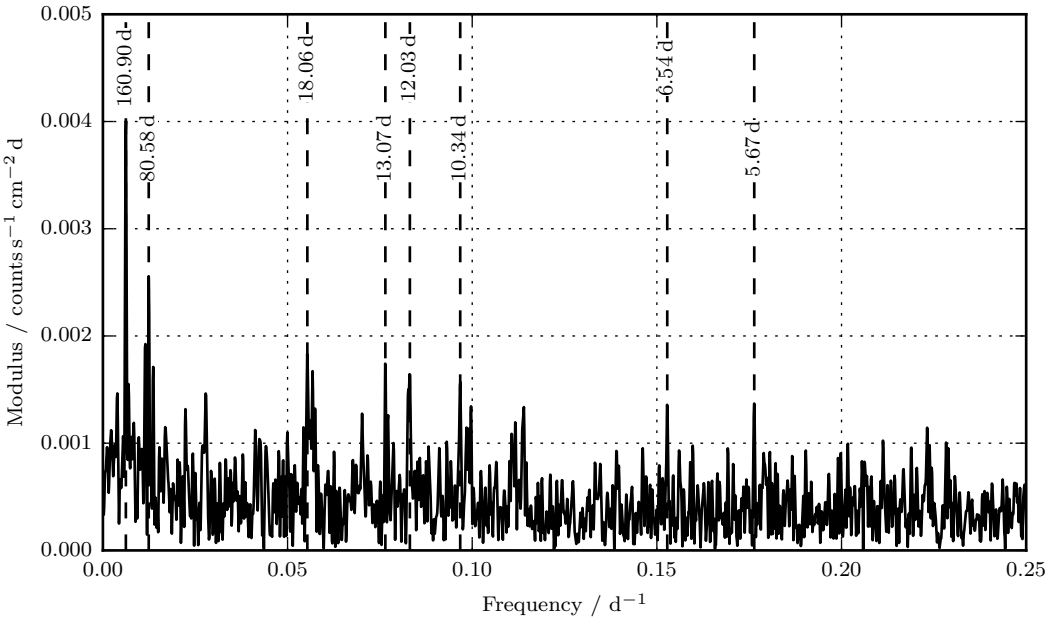


Figure 7.4: The positive-frequency spectrum of the MAXI X-ray data from the 2 keV − 20 keV band between dates MJD 55058 and MJD 57294. The most prominent periodicities are marked with dotted lines. The most prominent contribution is a variation at close to 161 d, which we identify with the precession of the accretion disc.

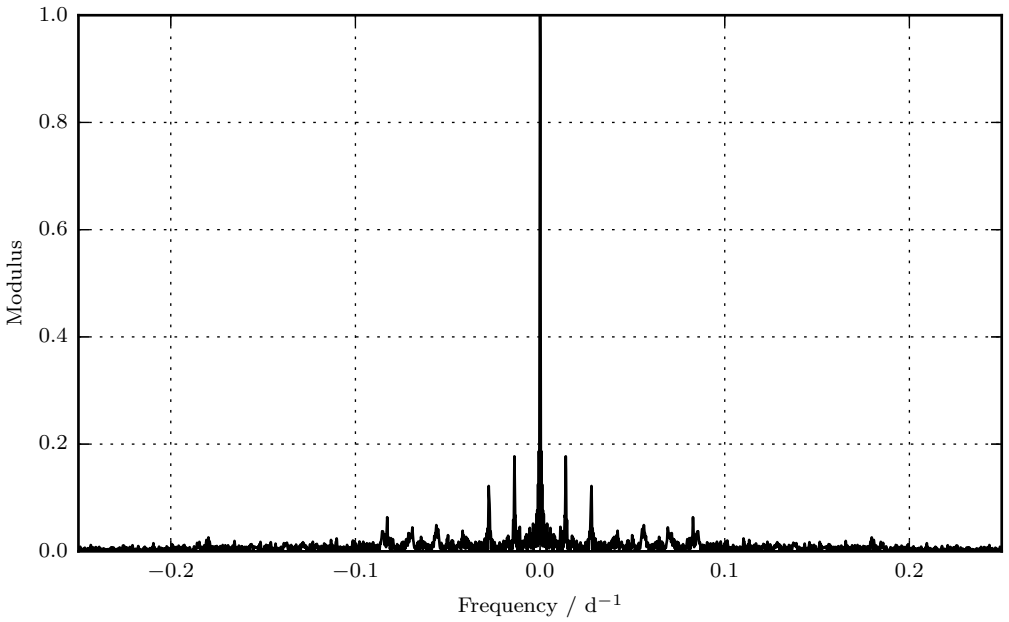


Figure 7.5: The "dirty beam" or point spread function for the single orbit MAXI observations between dates MJD 55058 to MJD 57294. The principal sidelobes are at 72 d (17%) and 36 d (12%), but are below the noise level arising from random variability of the source (see Figure 7.4). The key point is that the periodicities at 18 d cannot be accounted for by the effect of irregularly sampling the data.

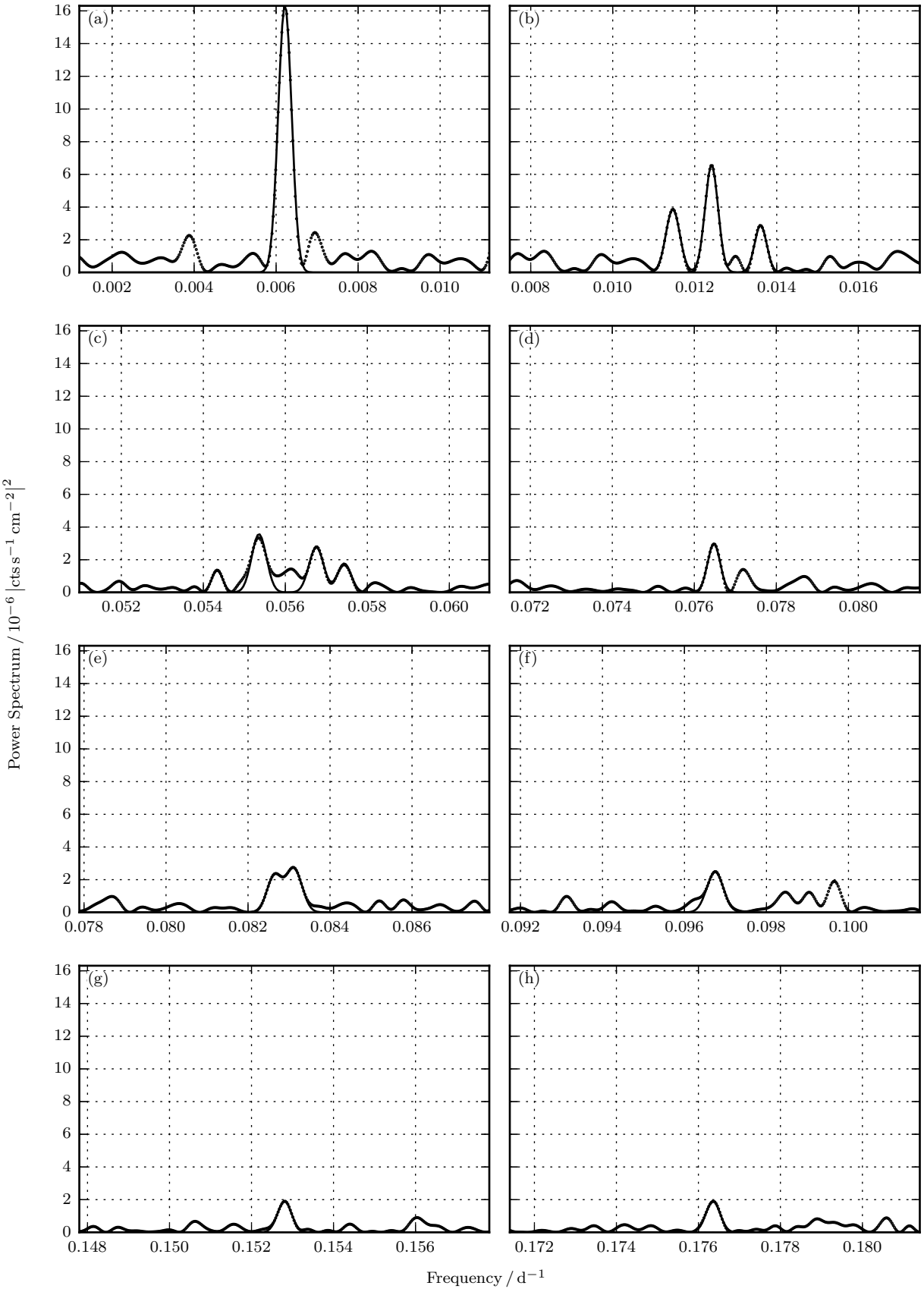


Figure 7.6: Gaussian fits to the most prominent peaks in the clean spectrum of the 2-20 keV data from the MAXI instrument (Fig. 7.4). The peaks are listed in Table 7.1. The dotted lines indicate the power spectrum, the thin lines are the Gaussian fits to the major peaks.

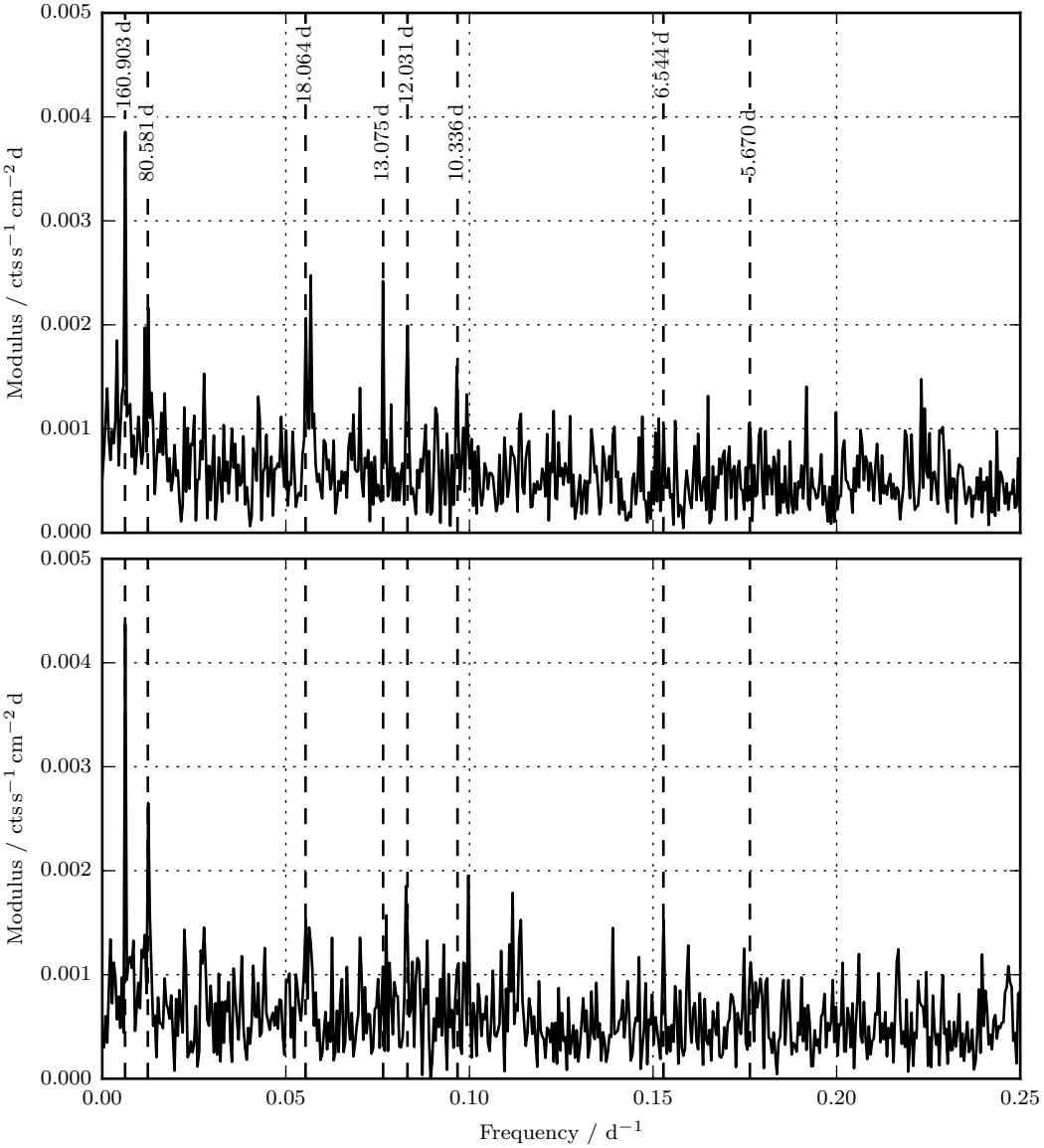


Figure 7.7: Modulus of the clean spectrum plotted against frequency for the MAXI 2-20 keV time series (cf. Figure 7.4). The data cover the same dates as in the earlier Figure (MJD 55058 to MJD 57294), but have been randomly divided in half, and each half-dataset analysed separately. The periodicities listed in Table 7.1 are highlighted. The unknown 18 d feature remains robust.

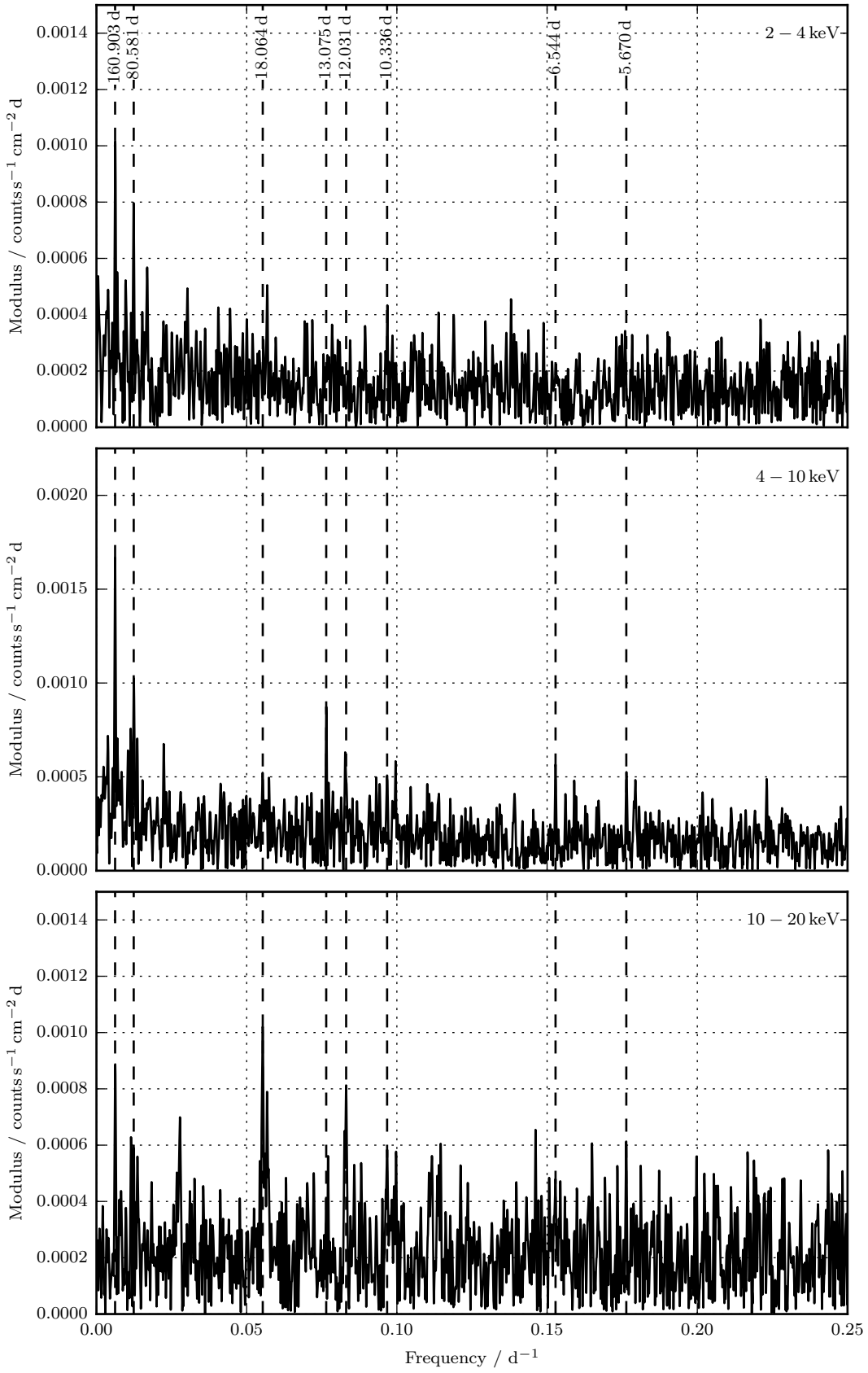


Figure 7.8: The modulus of the clean spectrum plotted against freqency for the three sub-bands of the MAXI monitoring data. The periodicities identified in the full band (Table 7.1) are marked. We note that the orbital periodicity at 13.08 d is only prominent in the middle band, and the unexplained 18 d period is only seen in the hardest, noisiest band.

- In all wavebands, the precessional periodicity is the clear and dominant signal, with a secondary signal at twice the precessional frequency.
- The orbital period is a strong signal in the middle waveband ($4-10\,\mathrm{keV}$), but is not strongly present in either the hardest or the softest bands.
- The hardest waveband ($10-20\,\mathrm{keV}$) displays the greatest random variability. This is not entirely surprising; the typical photon fluxes in this band are perhaps a factor of 2 lower than in the lower energy band meaning that the stochastic background makes a more significant contibution.
- It also appears that the broad 18 d feature seen in the total $2-20\,\mathrm{keV}$ arises almost entirely from this hard band. Its origin is unclear. It is not clearly associated with any known periodicity in the system. As the three wavebands have the same sampling function (cf. Figure 7.5), this periodicity cannot be associated with a windowing effect, or it would show up in all three bands. It is possible that this is a non-stochastic variation in the background; however, its origin remains unknown.

We note that the signal to noise, especially for the 10-20 keV band, is poor, although there is a clear precessional variation. As such, the data limit us, but we will still be able to make comments on the physics of the system.

#### 7.3.2.3 Summary of results from the Swift/BAT 15 - 50 keV waveband

The spectrum of the Swift/BAT photometry data is shown in Figure 7.9. The same periodicities as previously observed are marked. The precessional and orbital frequencies are clear, together with their harmonics at $2\,|\omega_{\mathrm{pre}}|$ and $2\,|\omega_{\mathrm{orb}}|$. There is no significant power attached to the spurious periodicities at 10 d and 6 d that we saw in the MAXI data. There is also no evidence for the unexplained 18 d periodicity seen in the MAXI 10-20 keV band – this gives further strength to our belief that this periodicity is not physically associated with the source.

#### 7.3.2.4 Summary

So, we have seen evidence for periodic behaviour in the X-ray photometry associated with the known physical, geometric variations of the system. We see no compelling evidence for nutational variation, or for any new physical periodicities – comparison between the different wavebands and

| | Frequency / $\mathrm{d}^{-1}$ | Width / $10^{-3}\mathrm{d}^{-1}$ | Amplitude / $10^{-6}$ | SNR | Period /d | Notes |
|---|---|---|---|---|---|---|
| (a) | 0.006215 | 0.162 | 16.404 | 23.22 | 160.902694 | $\lvert\omega_{\mathrm{pre}}\rvert$ |
| (b) | 0.011466 | 0.170 | 3.877 | 5.49 | 87.212707 | $2\,\lvert\omega_{\mathrm{pre}}\rvert$ |
| | 0.012410 | 0.159 | 6.579 | 9.31 | 80.580746 | |
| | 0.013606 | 0.147 | 2.906 | 4.11 | 73.497644 | |
| (c) | 0.054338 | 0.133 | 1.352 | 1.91 | 18.40348 | |
| | 0.055358 | 0.179 | 3.569 | 5.05 | 18.064372 | |
| | 0.056755 | 0.179 | 2.769 | 3.92 | 17.619685 | |
| | 0.057437 | 0.167 | 1.774 | 2.51 | 17.410469 | |
| (d) | 0.076477 | 0.153 | 2.994 | 4.24 | 13.075787 | $\lvert\omega_{\mathrm{orb}}\rvert$ |
| (e) | 0.082640 | 0.178 | 2.206 | 3.12 | 12.100731 | $\lvert\omega_{\mathrm{orb}}\rvert + \lvert\omega_{\mathrm{pre}}\rvert$ |
| | 0.083117 | 0.197 | 2.684 | 3.80 | 12.031182 | |
| (f) | 0.096746 | 0.202 | 2.481 | 3.51 | 10.336386 | |
| (g) | 0.152806 | 0.171 | 1.903 | 2.69 | 6.544259 | $2\,\lvert\omega_{\mathrm{orb}}\rvert$ |
| (h) | 0.176356 | 0.171 | 1.916 | 2.71 | 5.67034 | |

Table 7.1: Gaussian fits to the leading periodicites in the clean spectrum of the 2-20 keV MAXI photometric monitoring (see Figs. 7.4 and 7.6). SNR is the peak divided by the standard deviation of the power spectrum, $\sigma = 7.0651 \times 10^{-7}\ \left|\mathrm{cts\,s^{-1}\,cm^{-2}\,d}\right|^2$.

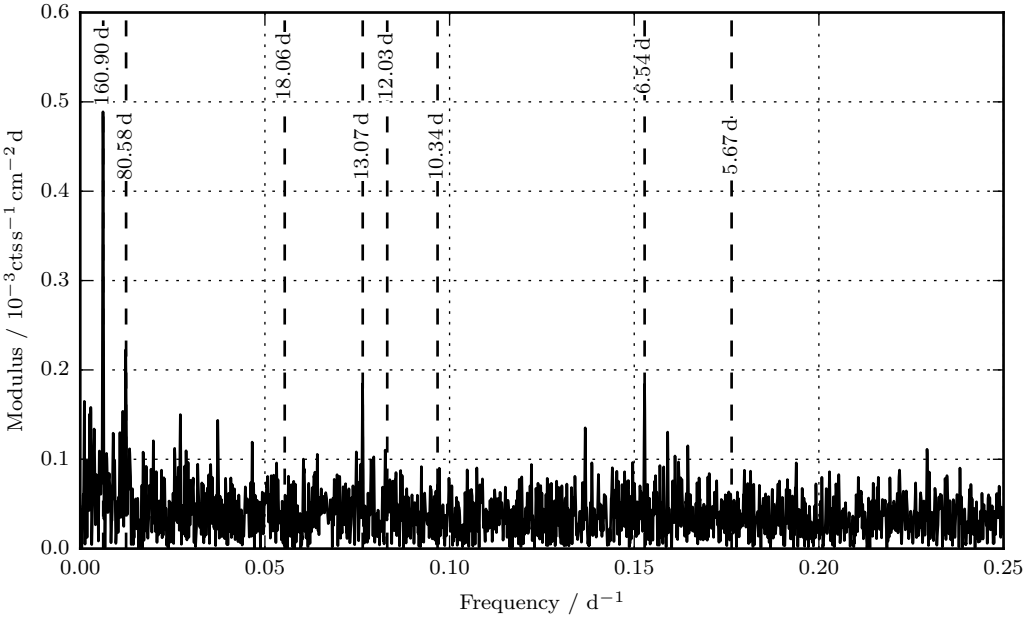


Figure 7.9: Modulus of the clean spectrum plotted against frequency for the Swift/BAT 15-50 keV time series (i.e., from dates MJD 53415 to MJD 57411). The peaks identified in the MAXI data are indicated. Those corresponding to $\omega_{\mathrm{pre}}$, $2\,\omega_{\mathrm{pre}}$, $\omega_{\mathrm{orb}}$, and $2\,\omega_{\mathrm{orb}}$ remain significant. We don't see a significant signal associated with the optically observed nutational periods at 5.83 d and 6.28 d.

instruments suggests that the unexplained signal detected in the MAXI data at 18 d is indeed spurious.

Now, let us examine two of these in more detail: the precessional and orbital variations. In the next section, we will use known ephemerides for these two periodicities to gain physical insights into the geometry of the system from an examination of the light curves.

## 7.4 X-Ray Variation with Precessional and Orbital Phases

### 7.4.1 Precession Phase

In Figure 7.10, we plot the X-ray fluxes from the MAXI instrument against jet precession phase, using the ephemerides of Eikenberry et al. (2001). Precession phase zero corresponds to the (eastern) jet lying at its closest to the line-of-sight. At precession phase 0.5, this jet lies at its furthest from the line-of-sight, while the (western) counterjet pointing slightly towards the observer. For each waveband, the data are binned by phase and then averaged within the bin. The precessional periodicity is clear.

Looking at the top panel (the complete 2-20 keV waveband), we see that at precession phases 0 and 1, there is an increase in the total X-ray flux by a factor of $\sim 2$. There are minima at precession phases of roughly 0.35 and 0.65, and there is a slight secondary maximum at precession phase 0.5. This lends itself to a very simple and intuitive interpretation: if the jet precession is simply a manifestation of the accretion disc precessing, then more of the emission from the disc can be seen when the jet (and accretion disc) lies closest to the line of sight (i.e., at phase 0); when the counterjet lies closest to the line of sight, we get a glimpse of the "back" of the disc, because the cone opening angle is greater than the angle between the jet and the plane of the sky, so at precession phase 0.5 the counterjet is pointed towards the observer. To put it succinctly: accretion discs have two sides.

Looking at each waveband in turn, we first note that the 10-20 keV band shows a low signal to noise ratio, and that there is only a weak variation of mean intensity with orbital phase. This is due to the limitations of the data products themselves, and leaves us unable to draw solid conclusions about this harder band.

Turning to the softer wavebands, we note that the secondary maximum is most clearly present

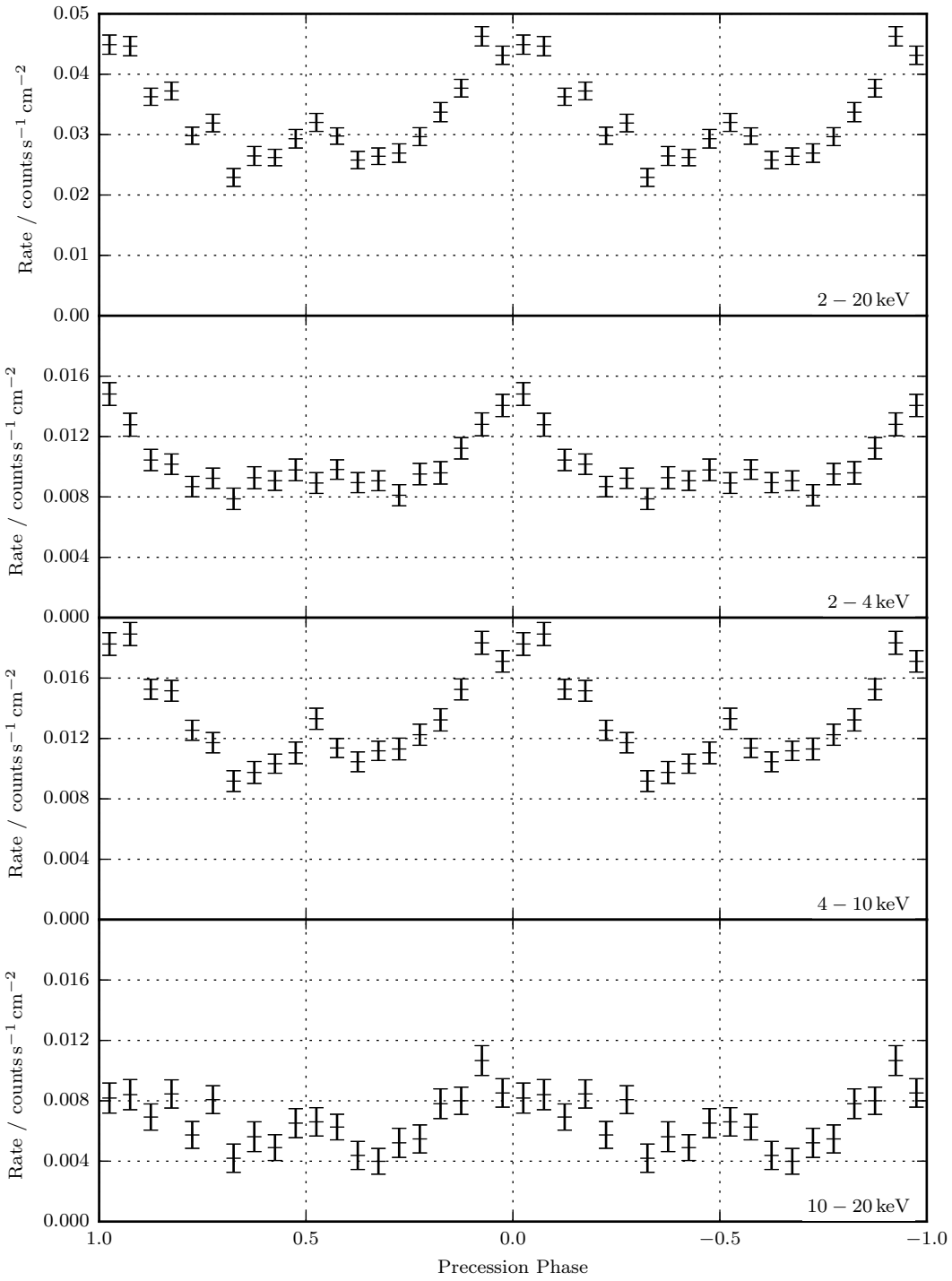


Figure 7.10: MAXI X-ray fluxes from SS 433 plotted against jet precession phase. Precession phases are evaluated using the ephemerides of Eikenberry et al. (2001) and averaged within bins. Note the inverted $x$-axis - the precessional evolution is in a negative sense (see Section 2.2) and so in this plot time advances from left to right.

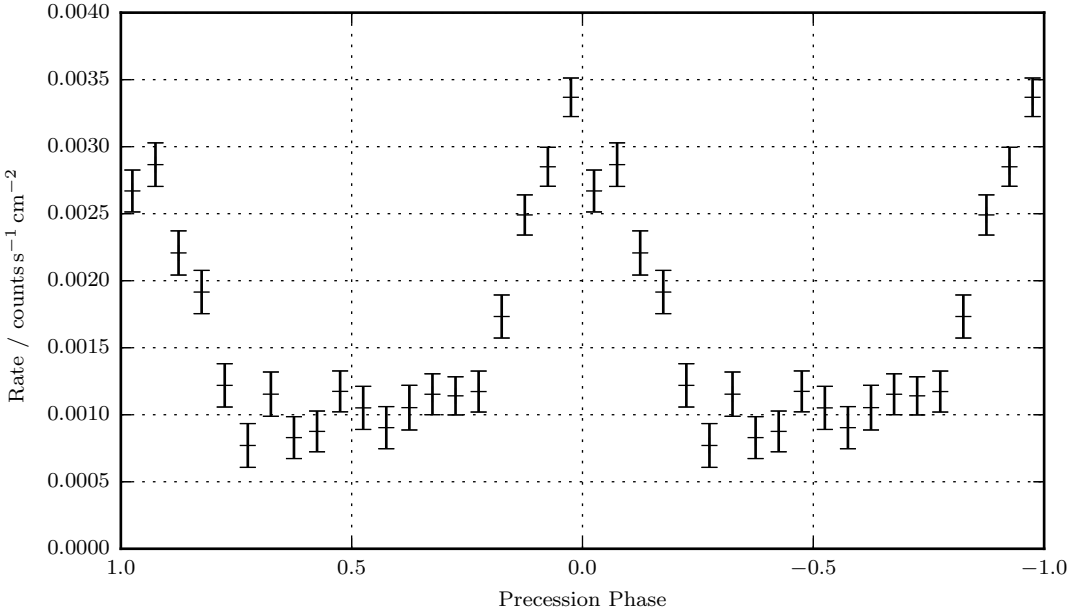


Figure 7.11: $15 - 50$ keV X-ray flux vs precession phase using data from the Swift/BAT satellite. The apparent brightening of the source at precessional phase zero is clear, but there is no evidence for a second peak at precession phase 0.5.

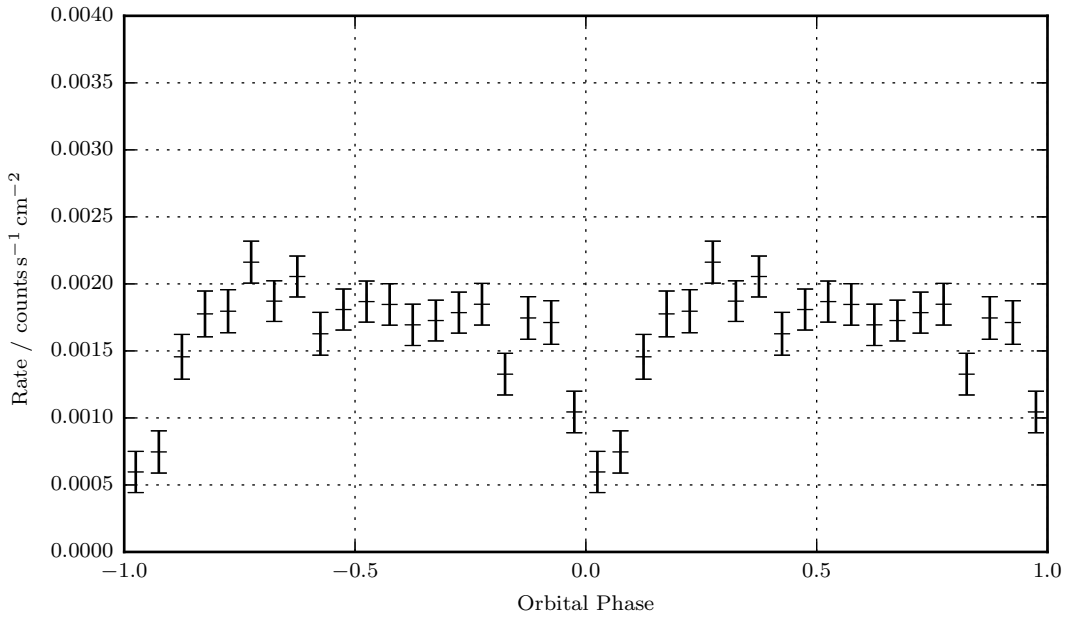


Figure 7.12: $15 - 50$ keV X-ray flux vs orbital phase using data from the Swift/BAT satellite. The eclipsing of the compact object by the companion star at precession phase zero is clear.

in the 4-10 keV data, with no strong signal in the softest 2-4 keV band. This indicates that the geometry of the thick, precessing, accretion disc is such that the source (or, perhaps, one of the sources) of the softest X-rays is still obscurred at precession phase 0.5.

The same pattern is also seen in the harder X-ray photometry from Swift (Figure 7.11). Again, there is a clear primary maximum, but there is no strong secondary maximum.

The two simplest plausible interpretations of this precessional variation are as follows:

1. The variation is purely a projection effect from the changing orientation of a (thin) disc. In this geometry, the observed flux would vary like $f_1 + f_2 |\cos \eta|$ where $f_1$ is a background flux, $f_2$ is the disc flux, and $\eta = \eta(\Phi_{\rm orb})$ is the angle to the line of sight as a function of the orbital phase (c.f. Equation 2.20). This approximately replicates the observed form of the variation seen, especially in the 4-10 keV band. However, it would not explain the apparent absence of a secondary maximum in the softest band. It is also without physical foundation – existing X-ray studies have seen *no* evidence for a disc contribution to SS 433's X-ray flux, and have modelled the spectrum successfully using only the flux from the jet.

2. A more believable geometry is one in which part of the jet (which is the main source of x-rays at 2-20 keV energies) is occulted by a thick, precessing, opaque accretion disc at phases when the jet lies in the plane of the sky, and revealed at those precession phases close to $\Phi_{\rm pre} = 0$ and $\Phi_{\rm pre} = 0.5$ where the funnel at pole of the disc around the jet (or counterjet) is most open to the observer.

In this second geometry, we can make an estimate of the necessary shape of the thick, occulting disc. At precession phase 0.0, the face of the disc is inclined at about 30° to the plane of the sky (from the sum of the orientation of the precession cone (12°) and the cone opening angle (21°) – see Section 2.2), while at precession phase 0.5, the "back" of the disc points about 10° out of the plane of the sky. This would suggest that the disc opening angle is somewhere between 10° and 30°. That is, the opening angle must be large enough to obscure the core at precession phase 0.5, but small enough not to obscure the core at precession phase 0.0.

Without a good model of the geometry of the disc, it is hard to make more qunatitative statements. The most complex attempt in the literature is that of Antokhina et al. (1992), who describe the thick accretion disc as an ellipsoid with conical sections removed about the poles. Here, we will limit ourselves to qualitative comments drawn from the interplay of the orbital and precessional

variations, to which we return after considering the orbital variability.

### 7.4.2 Orbital Phase

The variation of the photon fluxes in each of the MAXI bands as a function of orbital phase is plotted in Figure 7.13, using the orbital ephemerides derived from optical photometry by Goranskii et al. (1998), as reported in Fabrika (2004) (i.e., $\Phi = (T - T_0)/P_{\rm orb}$ with $T_0 = \text{MJD } 50023.62 \pm 0.26$, and $P_{\rm orb} = 13.082\,\text{d}$). The 15-50 keV Swift/BAT data are plotted with the same binning scheme in Figure 7.12. The convention here is such that at orbital phase 0, the relative coordinate vector between the black hole and the companion lies along the $x$-axis in the jet coordinate frame (i.e., the line in the $x$-$y$ plane closest to the line-of-sight – see Figure 2.1), with the companion lying closer to the observer. Hence, at orbital phase 0, the compact object and its accretion disc are eclipsed by the companion star.

For illustration, this geometry is sketched in Figure 7.14 for a system with the approximate parameters of SS 433 (i.e., with the normal to the orbital plane described by a position angle from East $\chi_0 = 10^\circ$ and an angle to line-of-sight $i_0 = 78^\circ$, and with a mass ratio $q = M_{\rm bh}/M_* = 16/22$; any orbital eccentricity is neglected). The red and blue surfaces correspond to the Roche lobes – the equipotential surfaces passing through the inner Lagrange point of the system for the companion star and the black hole respectively. The lobe surrounding the compact object is partially obscurred for about a quarter of the orbit, between orbital phases $\sim 0.875$ and $\sim 0.125$.

Looking again at the data in Figures 7.12 and 7.13, the eclipse can clearly be seen in the X-ray data from both satellites, though not at all wavebands. It is most clearly present in the hard 15-50 keV Swift data, with $\sim 60\%$ of the flux obscurred. It is also clear in the 4-10 keV MAXI band, where perhaps $\sim 30\%$ of the total photon flux is occluded. However, there is no significant signal in either the softest or the hardest of the MAXI bands. This tallies with Figure 7.8, where we saw significant power in the Fourier spectrum at 13.08 d only in the middle of the three bands. As with the precessional variation, the signal to noise ratio in the hardest MAXI band is probably too low for us to draw any scientific conclusions. On the other hand, the lack of signal in the 2-4 keV band is probably real.

We note at this point that a contradictory picture has emerged: in our discussion of the precessional variation, we speculated that the absence of a secondary peak in the soft band indicated that those emissions arose *close* to the core. Here, we seem to see that these emissions arise sufficiently *far*

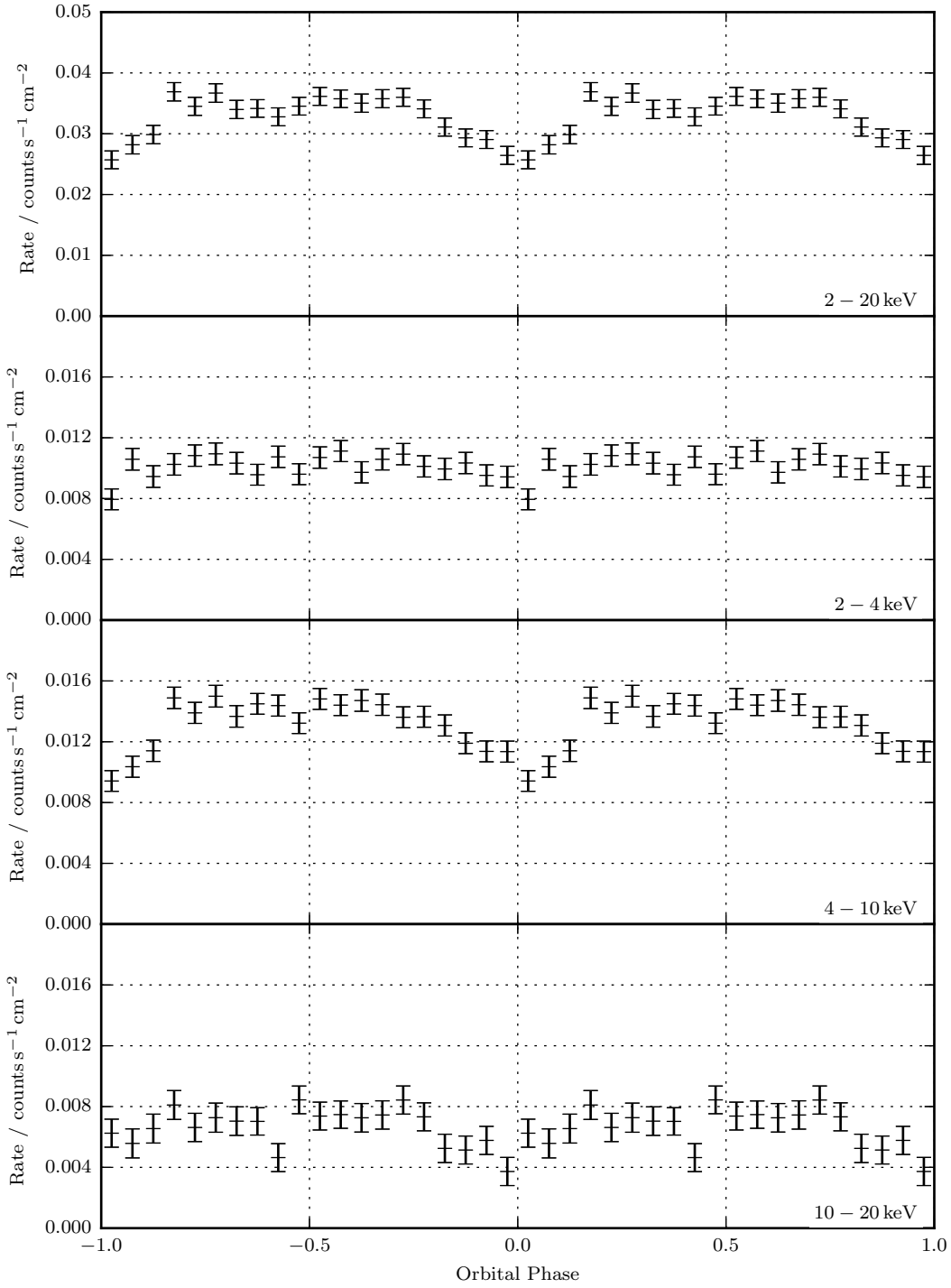


Figure 7.13: MAXI X-ray fluxes from SS 433 plotted against orbital phase. Orbital phases are evaluated using the ephemerides of Goranskii et al. (1998) as given in Fabrika (2004) and averaged within bins. In the 4-10 keV band, there is clear attenuation close to 0 phase - i.e., when the companion star partially obscures the compact object and accretion disc.

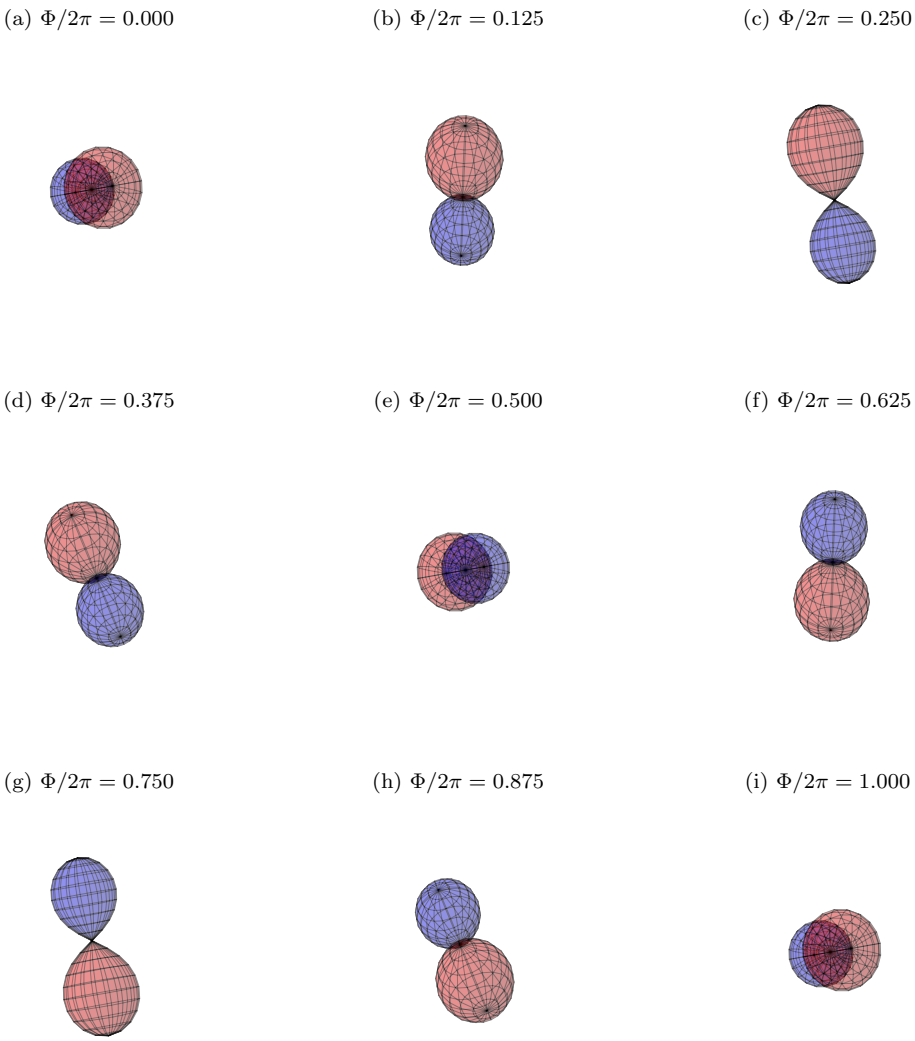


Figure 7.14: The Roche lobes for a $16\,M_\odot$ black hole and its $22\,M_\odot$ companion (cf. the masses of the components of the SS 433 system). The orientation of the orbital plane is set to match the mid-plane of the precession cone in the SS 433 geometry (c.f. Section 2.2), and the plane of the page matches the plane of the sky. At the primary eclipse ($\Phi_{\rm orb} = 0$), almost the entirety of the Roche lobe containing the compact object is eclipsed.

from the core such that they are not eclipsed by the orbital variation. This is the more intuitive picture – it fits with the adiabatic cooling model outlined in Section 7.1.2, in which lower energy emission arises further from the jet core. It is also consistent with the XMM Newton observations of Brinkmann et al. (2005), who saw little variation of the softest X-rays in their spectra. In both cases, the suggestion is that the X-ray emitting jets exceed the size of the eclipsed region.

#### 7.4.2.1 Eclipse fitting to the Swift data – a point source

We will now fit simple models of the geometry of eclipsing binary systems to these eclipse lightcurves. As the Swift data possess the best signal-to-noise, we will principally apply these models to the highest energy data. However, we will also see that the MAXI data 4-10 keV data are not well described by these toy models.

The simplest model to consider is a point source undergoing eclipse by a Roche-lobe filling companion. Allowing for a background, unocculted flux, there are then 3 parameters in the model: the mass ratio $q = M_{\rm bh}/M_*$, the background flux $f_1$, and the eclipsed source flux $f_2$. For simplicity, we approximate the Roche lobe of the companion star by a sphere of the same volume, using the approximation of Eggleton (1983) (see Box 7.4 for discussion). We also note that working within this formalism precludes the possibility of an eccentric orbit.

Assuming that the uncertainties are normally distributed, we again use the emcee implementation of the Goodman & Weare Monte-Carlo Markov Chain algorithm to explore the probability distribution for these model parameters (Goodman and Weare (2010); see Section 4.3.5.1). Since the parameters under consideration are of positive sign but unknown magnitude, we assume logarithmic priors on the parameters $q$, $f_1$, and $f_2$. We will also allow for a phase offset, $\Phi_0$, between the model and the orbital phases of the data as calculated from the Goranskii ephemerides – this will take a flat prior on the interval $\Phi_0 \in (-0.5, 0.5]$.

The resulting normalised, marginalised pdfs and associated covariances between the parameters as fitted to the Swift data are plotted in Figure 7.16. A subset of the samples of the posterior pdf produced by the MCMC algorithm are plotted against the binned data in Figure 7.17. The $5^{\rm th}$, $50^{\rm th}$, and $95^{\rm th}$ percentiles of the cumulative distribution function are given in Table 7.2.

The most important piece of information that can be gleaned from this model is the estimate of the mass ratio $q = M_{\rm bh}/M_*$. With these data (and this simple model), this is poorly constrained. Essentially all we can say is that the black hole is not less than 1% of the companion star mass, and

**Box 7.4: Approximating the Roche lobe**

In a frame corotating with the Keplerian orbit of a (circular) binary, the two masses appear stationary, and an effective potential, $U(x, y, z)$, can be written for a test mass combining the gravitational attraction of the two masses and the effect of the orbital motion. This effective potential is:

$$U(x, y, z) := -\frac{GM}{a}\left(\frac{m_1/M}{\rho_1} + \frac{m_2/M}{\rho_2}\right) - \frac{1}{2}\frac{GM}{a^3}\left(x^2 + y^2\right) \tag{7.21}$$

where $a$ is the separation of the two masses, $\rho_{1,2} = \left((x - x_{1,2})^2 + y^2 + z^2\right)^{1/2}/a$ is the distance of point $(x, y, z)$ from mass 1 or 2 in turn, and $x_{1,2} = \mp(m_{2,1}/M)\, a$ are the positions of masses 1 and 2. It can be shown that the Jacobi integral (the sum of the kinetic energy and this effective potential) is a constant of motion for test particles in this corotating frame (see, e.g., Binney and Tremaine (2008)), and so surfaces of constant $U$ correspond to surfaces at which a trapped test particle's velocity vanishes (zero-velocity surfaces).

The Roche lobes are described by the zero-velocity (i.e., the equipotential) surface that encloses both objects in the binary system, and that is just pinched shut on the axis between the two bodies (i.e., at the $L_1$ inner Lagrange point). Hence, the Roche lobes are the locus of points $\{x, y, z\}$ such that $U(x, y, z) = U(x_{L_1}, 0, 0)$, where $x_{L_1}$ is the position of the inner Lagrange point on the $x$ axis.

The Lagrange points and equipotential surfaces through them are sketched below, as viewed in the rotating frame. The Roche lobes are the innermost, yellow contours. Their shape – which the rotation elongates along the axis towards the centre of mass, and squashes in the $z$ direction perpendicular to the rotation – is non-analytic. A widely used approximation for their sizes is due to Eggleton (1983). This approximates the lobe around the mass $m_2$ by a sphere of the same volume as the true Roche lobe. Its radius is:

$$r_{\mathrm{L}}(q) = a\,\frac{0.49q^{2/3}}{0.6q^{2/3} + \ln\left(1 + q^{1/3}\right)} \tag{7.22}$$

where $q := m_2/m_1$ is the mass ratio and $a$ is the binary separation. This is sketched as the dashed line in the figure below. Using this spherical approximation has the significant computational advantage that there exists an analytic solution for the fraction of the source

eclipsed.

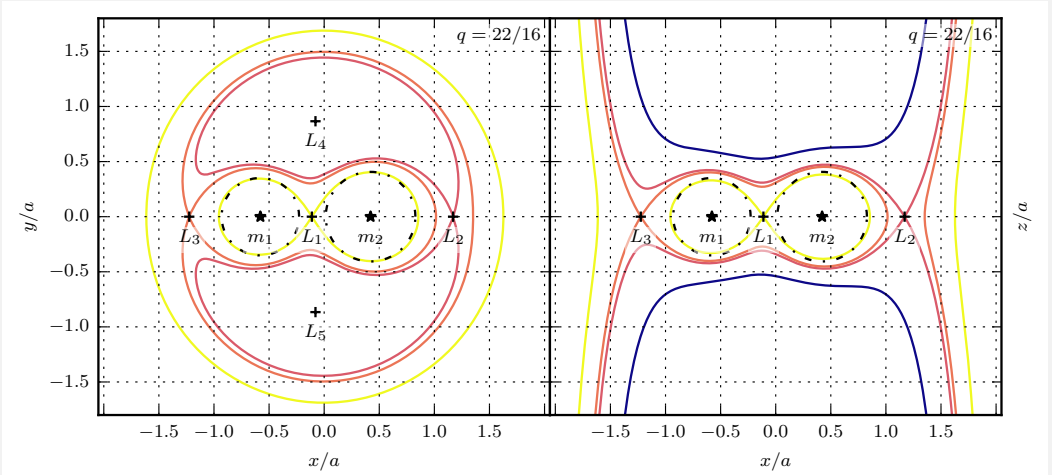


Figure 7.15: The equipotential curves for a two body system. The mass ratio $q = m_2/m_1 = 22/16$ is chosen to match that estimated for the SS 433 system by Blundell et al. (2008), where, in this case, $m_2 = m_* = 22\,\mathrm{M}_\odot$ and $m_1 = m_{\rm bh} = 16\,\mathrm{M}_\odot$.

is unlikely to be more massive than its companion. We note that the pdf is actually more sharply peaked than this (top left panel of Figure 7.17) – the bulk of the probability mass is concentrated in the range of mass ratios $0.3 \lesssim q \lesssim 1.0$, but with a broad tail that permits the smaller mass ratios.

The apparent preference for larger values of $q = M_{\rm bh}/M_*$ is interesting. Historically, there has existed a dichotomy between the mass ratios estimated from X-ray eclipses, and the mass ratios derived from optical spectra. Workers using X-ray observations tend to estimate mass ratios below $q \lesssim 0.25$, pointing to a less massive compact object and casting doubt on its identification as a black hole (rather than a neutron star). For instance, from fits to lightcurves from the Ginga satellite, both Brinkmann et al. (1989) and Antokhina et al. (1992) estimate $0.15 \lesssim q \lesssim 0.25$, while using a similar model with INTEGRAL observations, Cherepashchuk et al. (2009) support values $q \simeq 0.25$. On the other hand, attempts to infer masses from orbital velocities as derived from spectral lines point towards a more massive compact object, with typical estimates from $q \simeq 0.35$ (Hillwig and Gies (2008)) to $q \simeq 0.72$ (Gies et al. (2002b)). Consideration of the relative orbital speeds of the compact objecst and the circumbinary disc by Blundell et al. (2008) also points towards a mass ratio that is closer to parity (they estimate $q \gtrsim 0.4$). Here, we appear to see the eclipses of hard X-rays favouring a more massive compact object.

There are two other features of the fits to the Swift data that we can identify from this simple

Table 7.2: Eclipsing point model fitted to the Swift 15-50 keV data.

| Parameter | Percentile | | |
|---|---|---|---|
| | $5^{\rm th}$ | $50^{\rm th}$ | $95^{\rm th}$ |
| $M_{\rm bh}/M_*$ | 0.037 | 0.461 | 1.059 |
| $\log_{10}\left(f_1\,/\,{\rm cts\,s^{-1}\,cm^{-2}}\right)$ | $-3.306$ | $-3.146$ | $-3.017$ |
| $\log_{10}\left(f_2\,/\,{\rm cts\,s^{-1}\,cm^{-2}}\right)$ | $-3.089$ | $-2.980$ | $-2.897$ |
| $\phi_0$ | $-0.054$ | $-0.038$ | $-0.023$ |

Table 7.3: Eclipsing disc model fitted to the Swift 15-50 keV data

| Parameter | Percentile | | |
|---|---|---|---|
| | $5^{\rm th}$ | $50^{\rm th}$ | $95^{\rm th}$ |
| $M_{\rm bh}/M_*$ | 0.030 | 0.600 | 1.097 |
| $\alpha$ | $1.28\times10^{-4}$ | 0.922 | 1.422 |
| $\log_{10}\left(f_1\,/\,{\rm cts\,s^{-1}\,cm^{-2}}\right)$ | $-8.542$ | $-4.432$ | $-3.029$ |
| $\log_{10}\left(f_2\,/\,{\rm cts\,s^{-1}\,cm^{-2}}\right)$ | $-3.062$ | $-2.762$ | $-2.734$ |
| $\Phi_0$ | $-0.044$ | $-0.032$ | $-0.017$ |

Table 7.4: Eclipsing point model fitted to the Maxi 4-10 keV data

| Parameter | Percentile | | |
|---|---|---|---|
| | $5^{\rm th}$ | $50^{\rm th}$ | $95^{\rm th}$ |
| $M_{\rm bh}/M_*$ | $9.796\times10^{-5}$ | $4.444\times10^{-3}$ | $1.563\times10^{-2}$ |
| $\log_{10}\left(f_1\,/\,{\rm cts\,s^{-1}\,cm^{-2}}\right)$ | $-1.995$ | $-1.972$ | $-1.951$ |
| $\log_{10}\left(f_2\,/\,{\rm cts\,s^{-1}\,cm^{-2}}\right)$ | $-2.546$ | $-2.463$ | $-2.391$ |
| $\Phi_0$ | -0.016 | -0.007 | 0.008 |

point source model. Firstly, notice that the phase offset term is inconsistent with $\Phi_0 = 0$; we will return to this in the next Section. Secondly, we note that the abrupt transitions into and out of an eclipse produced by a small source are a poor description of the smooth variation of the averaged lightcurve. As we will now see, the quality of this fit can be improved by allowing an extended source.

#### 7.4.2.2 Eclipse fitting to the Swift data – an extended source

A simple generalisation to model an extended source is achieved by allowing the X-ray source surrounding the compact object to fill some fraction $\alpha$ of its Roche lobe. To reflect ignorance about the filling fraction, we impose a log-prior on $\alpha$, with the constraint that the combined sizes of the two objects, which within the Eggleton approximation is given by $\alpha r_{\rm L}\left(q\right) + r_{\rm L}\left(q^{-1}\right) < a$ (where a is the binary separation and $q = M_{\rm bh}/M_*$ is the mass ratio).

The resulting pdfs are displayed in Figure 7.18. From plotting representative random curves from the generated histograms against the data (Figure 7.19), it is clear that these provide a much better description of the shape of the eclipse curve than the point source model did. The key observation

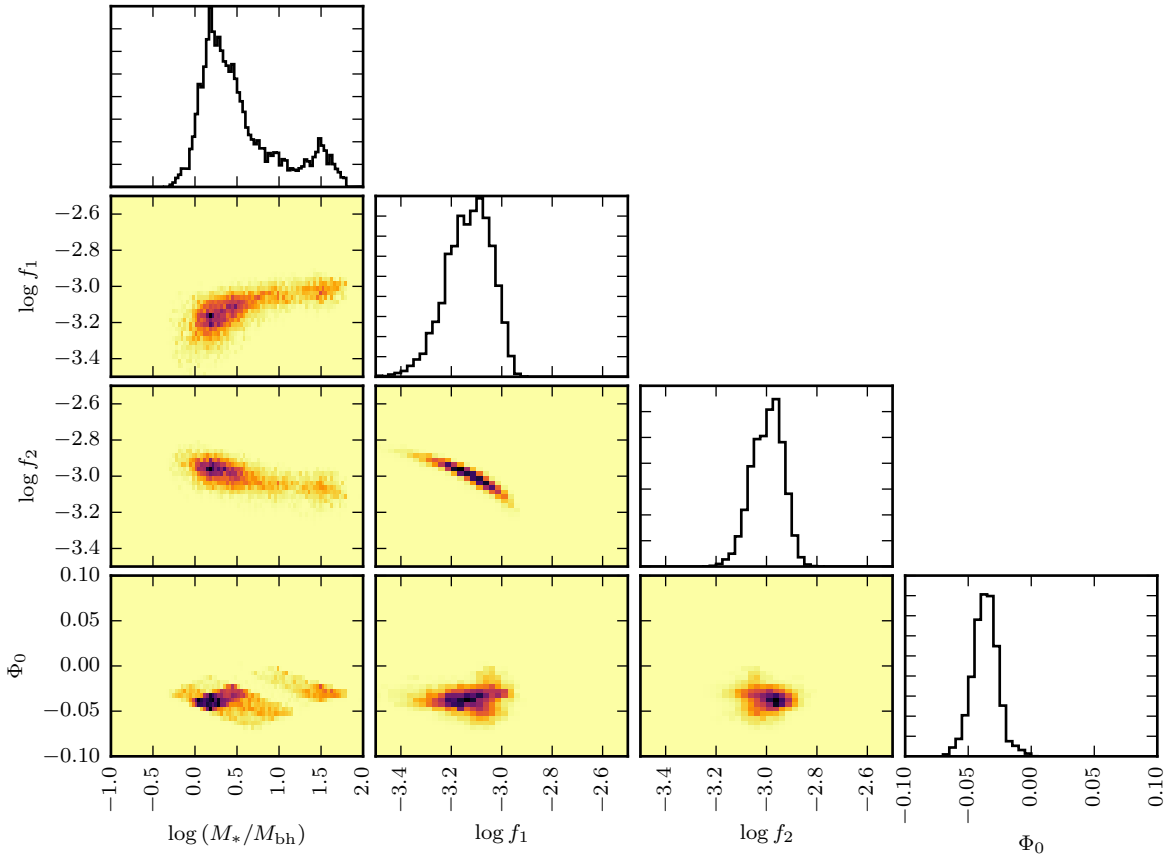


Figure 7.16: Plot showing the covariances between different parameters in the eclipsing point source model, as fitted to the Swift/BAT 15-50 keV data. The model parameters are the mass ratio $q^{-1} = M_*/M_{\rm bh}$, the background flux $f_1$, the eclipsed source flux $f_2$ (both in units of cts s$^{-1}$ cm$^{-2}$), and a phase offset $\Phi_0$. Confidence intervals are given in Table 7.2.

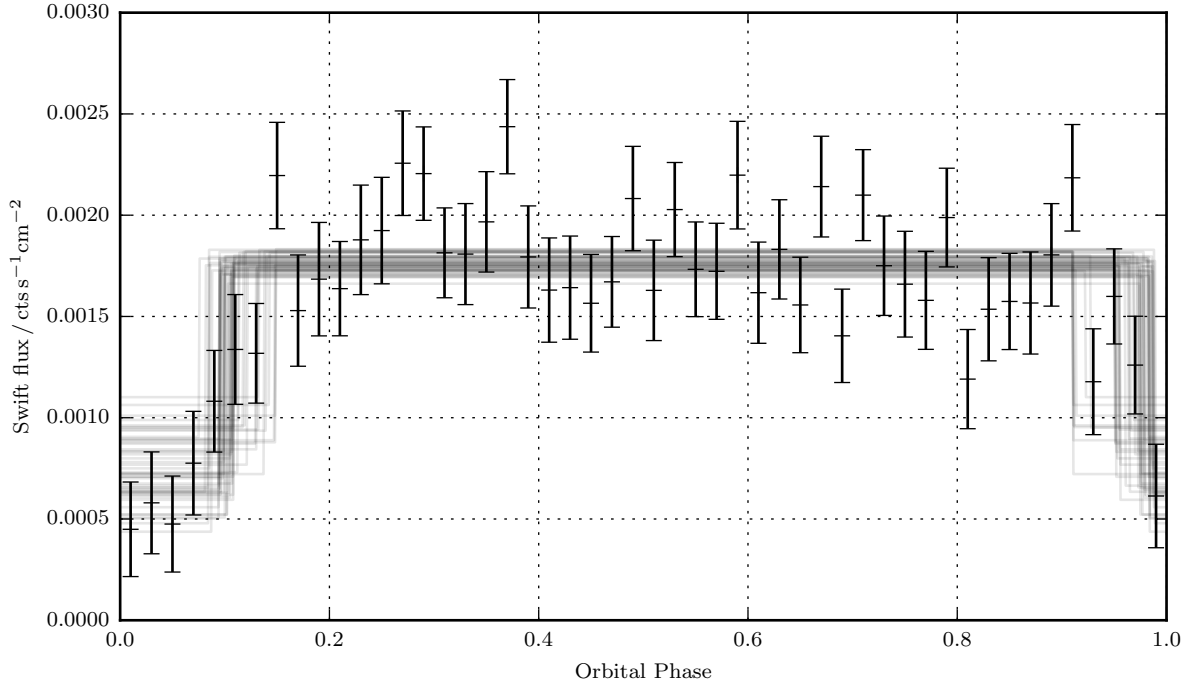


Figure 7.17: Binned Swift/BAT fluxes plotted against representative curves from the fitted eclipsing point source model parameters in Figure 7.16.

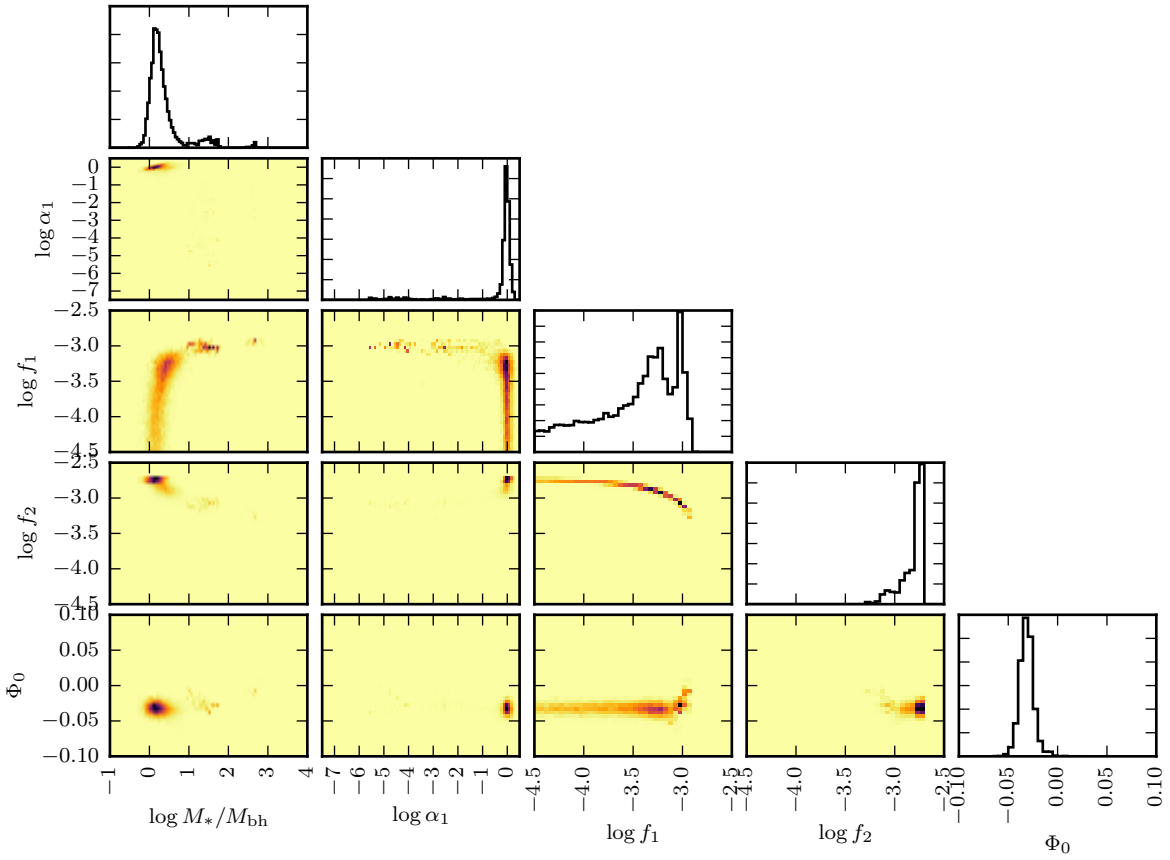


Figure 7.18: Plot showing the covariances between different parameters in the eclipsing disc model, as fitted to the Swift/BAT 15-50 keV data. The model parameters are the mass ratio $q^{-1} = M_*/M_{\rm bh}$, the filling factor $\alpha$, the background flux $f_1$, the eclipsed source flux $f_2$ (both in units of cts s$^{-1}$ cm$^{-2}$), and a phase offset $\Phi_0$. Confidence intervals are given in Table 7.3. Note that the filling factor is overwhelmingly consistent with $\alpha = 1$.

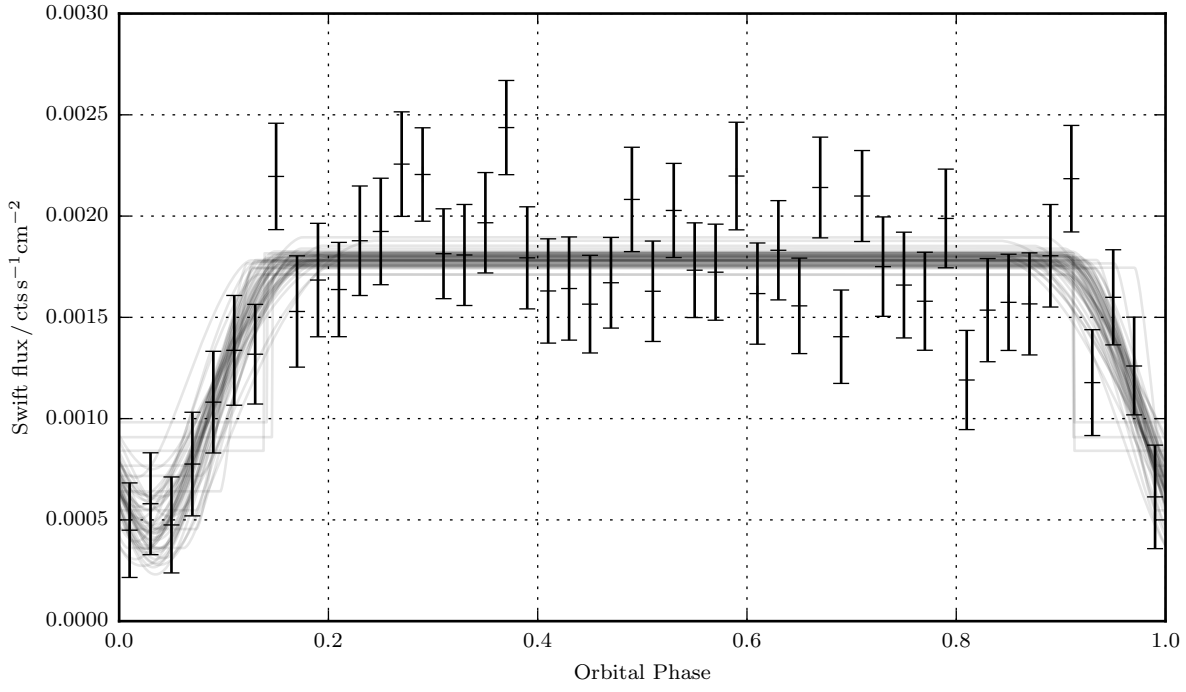


Figure 7.19: Binned Swift/BAT fluxes plotted against representative curves from the fitted eclipsing disc model parameters in Figure 7.18.

from inspection of the pdf on $\alpha$ in Figure 7.18 is that the data overwhelmingly support a filling factor of order unity. Although there is a small tail to the pdf extending to much smaller filling factors (Table 7.3), it appears that the X-ray source (at least for the hard X-rays observed by Swift) is not compact, but rather is on the order of the size of the Roche lobe surrounding the compact object.

Note also that, as we discussed in relation to the point source model, the mass ratio again points towards $q \gtrsim 0.3$ – indeed the pdf is even more heavily skewed towards parity in the masses.

We believe that the interpretation of these optical eclipses is that the hard X-rays are emitted (or come from Compton up-scattering of soft X-rays or optical photons) by a hot corona above the disc and around the base of the jet. This is the same picture as invoked by Cherepashchuk et al. (2009) and Cherepashchuk et al. (2013).

Combined with the estimates of the total system mass from the circumbinary ring observations of Blundell et al. (2008) we are able to estimate the approximate extent of this corona-like structure. From our fits, we take $q \simeq 0.7$ and $\alpha \simeq 1.0$. This value of $q = M_{\rm bh}/M_*$ matches that of Gies et al. (2002b) and is used in Blundell et al. (2008), to estimate the total system mass as $\sim 38\,{\rm M}_\odot$. Hence, given Kepler's law and a 13.08 d orbital period, the binary separation is $a \simeq 5.5 \times 10^{10}\,{\rm m}$. Then, using Equation 7.22, we find an estimate of the radius of this corona-like region as $r_{\rm cor} \simeq r_{\rm L}\,(q) \simeq 0.35a \simeq 1.9 \times 10^{10}\,{\rm m}$.

We stress that the interesting point here is that the corona-like emission is extended in origin, and comes from a region that is comparable with the size of the Roche lobe around the compact object. Its precise numerical value is of less interest to us here, and is strongly affected by both the true value of $q$ (which we are unable to constrain more precisely than a factor of 3 or so), and on the orbital separation $a$ as determined from the total mass of the system (for which there are conflicting values spanning a factor of 10 or so within the literature, although the value as determined by Blundell et al. (2008) is only weakly sensitive to $q$, and can be trusted so long as the identification of emission from the circumbinary ruff is correct).

We also note that, as in the point case, the Swift data appear not to be consistent with the eclipse ephemerides given in Fabrika (2004). This is shown by the non-zero values of $\Phi_0$. One possible explanation of this would be that the star (or, to be more precise, the X-ray opaque region which we have identified with the companion star) shows significant non-sphericity. This might perhaps be due to a high stellar wind, a tail of matter shed behind it as it passes through the

disc wind, or due to the overflow through the outer Lagrange point that is believed to drive the circumbinary outflow. Such a trailing opaque region would extend the eclipse in the sense seen in Figure 7.17. This is not the first evidence that the eclipsing region (and the companion star) may be more geometrically complex than the Roche lobe of the companion star. Gies et al. (2002b) also see evidence for a distorted eclipse in monitoring data from the RXTE observatory. Filippova et al. (2006) detect strong absorption in the X-ray spectra close to the eclipse; they argue that this represents a stellar wind that may increase the apparent size of the eclipsing star by 20%, although we note that Blundell et al. (2008) report no evidence for such a stellar wind in optical spectra. If such an attenuating region means that we are overestimating the physical size of the star's Roche lobe, this would mean that we overestimate the relative mass of the companion, $M_*$, and so *underestimate* the mass ratio. This may help explain the preference for lower values of $M_{\rm bh}/M_*$ in the existing X-ray literature than those we see here.

It is worth commenting on the degeneracies in this model. Most importantly, once the size of the source exceeds the size of the eclipsing star (achieved either at $\alpha > 1$ or $\log M_*/M_{\rm bh} < 0$), these parameters become degenerate with the background, uneclipsed flux $f_1$, and therefore the full projected area of the source is never fully eclipsed. This accounts for the long tail on the marginalised pdf of $f_1$.

#### 7.4.2.3 Eclipse Fitting to the MAXI 4 - 10 keV data – a point source

We have also attempted to fit the simple eclipse models to the MAXI 4-10 keV band, which displays the best signal-to-noise ratio and the strongest orbital signal. The pdfs for the point source model are shown in Figures 7.20 and 7.21.

The immediate observation is that the MAXI data appear to prefer vastly different mass ratios to those supported by the Swift data, with masses for the compact object any greater than 1% of its companion star apparently ruled out. Looking at Figure 7.21, it is easy to understand why. Unlike the Swift data, the eclipse edge appears more abrupt, but with a comparable mean width. This forces the fit to prefer a larger Roche lobe for the companion star (i.e., a to prefer a smaller mass ratio).

We are not inclined to believe these small mass ratios. The information content of a data point is dependent on its phase – we don't learn much from good coverage at orbital phase 0.5, but we gain a lot from increased sampling close to the start and end points of the eclipse. Hence, the fit is

heavily shaped by the few data points very close to the eclipse edge. With more data accumulated over a longer observation time improving the signal to noise, we might see the points at the first edge of the eclipse actually lie closer to the trend seen in the Swift data. This would allow us to reconcile the mass ratios estimated from these two data sets.

Notwithstanding our belief that more data are needed before we draw quantitative conclusions about the MAXI data, there remains another puzzle. If the soft X-rays, and especially the iron-dominated 4-10 keV band, are dominated by jet emission, and if the jet itself is geometrically thin, then we *do* indeed expect an abrupt edge (as seen here), but we expect a very narrow eclipse (which we very much don't see here). The solution to this dichotomy is not obvious.

### 7.4.3 Further Discussion

#### 7.4.3.1 Joint precessional and orbital variation

In Figures 7.22 and 7.23, we attempt to disentangle the effects of precessional and orbital variation further. Here, we plot the average flux variation with orbital phase for those precession phases near $\Phi_{\rm pre} = 0$, at which the jet is closest to the line of sight and its accretion disc is maximally oriented towards the observer (black), and for those precession phases when the disc is closer to edge-on, and so the disc itself obscures its inner X-ray emitting regions (red).

There are three qualitative features which we highlight:

1. In the 4-10 keV band, there is a broad eclipse feature that is most prominent close to precession phase 0, and which is not visible at those precessional phases such that the core regions are occulted by the thick disc. Tentatively, one might see a slow modulation with orbital phase outside the maximal opening phase, but these data are not strong enough to support this claim to a high level of significance. We also note that the eclipsed flux at $\Phi_{\rm pre} = 0$ is, to within errors, the same as the uneclipsed flux at the edge-on precession phases. This indicates that a similar fraction of the emitting region is covered by the companion as by the (thick) disc.

2. The 2-4 keV band displays a significant (narrow) eclipse only at epochs close to $\Phi_{\rm pre} = 0$. Given our earlier remarks about the surprising breadth of the 4-10 keV eclipse, the narrowness of the eclipse here suggests that the 2-4 keV X-rays are emitted within a rather narrow region. This is consistent with the view that they arise from a rather compact region

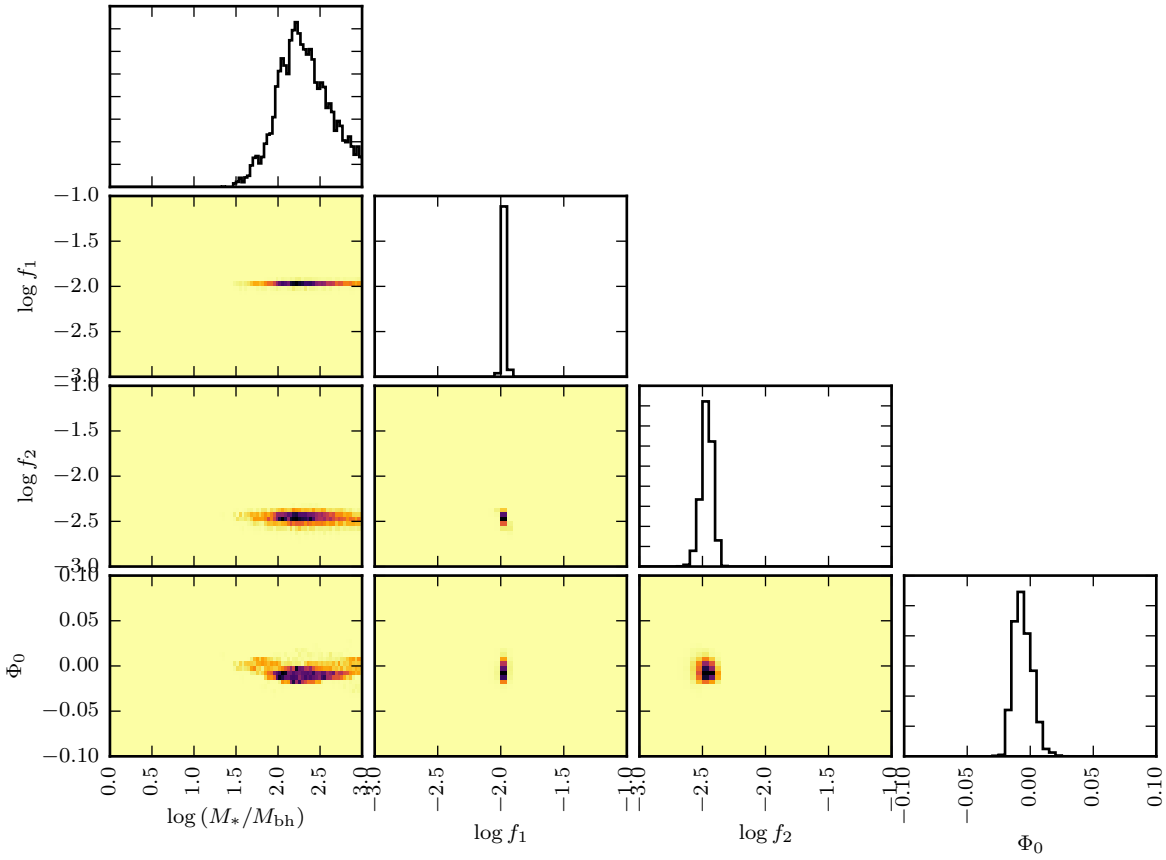


Figure 7.20: Plot showing the covariances between different parameters in the eclipsing point source model, as fitted to the MAXI 4-10 keV data. The model parameters are the mass ratio $q^{-1} = M_*/M_{\rm bh}$, the background flux $f_1$, the eclipsed source flux $f_2$ (both in units of cts s$^{-1}$ cm$^{-2}$), and a phase offset $\Phi_0$. Confidence intervals are given in Table 7.4.

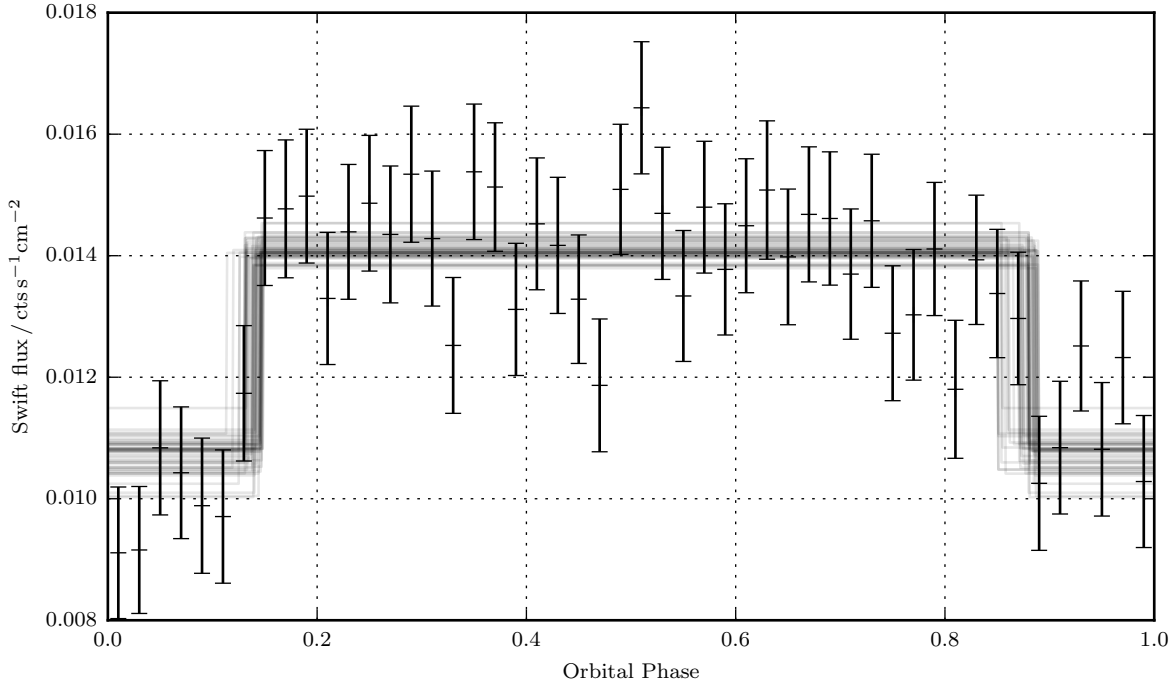


Figure 7.21: Binned MAXI 4-10 keV fluxes plotted against representative curves from the fitted eclipsing point source model parameters in Figure 7.20.

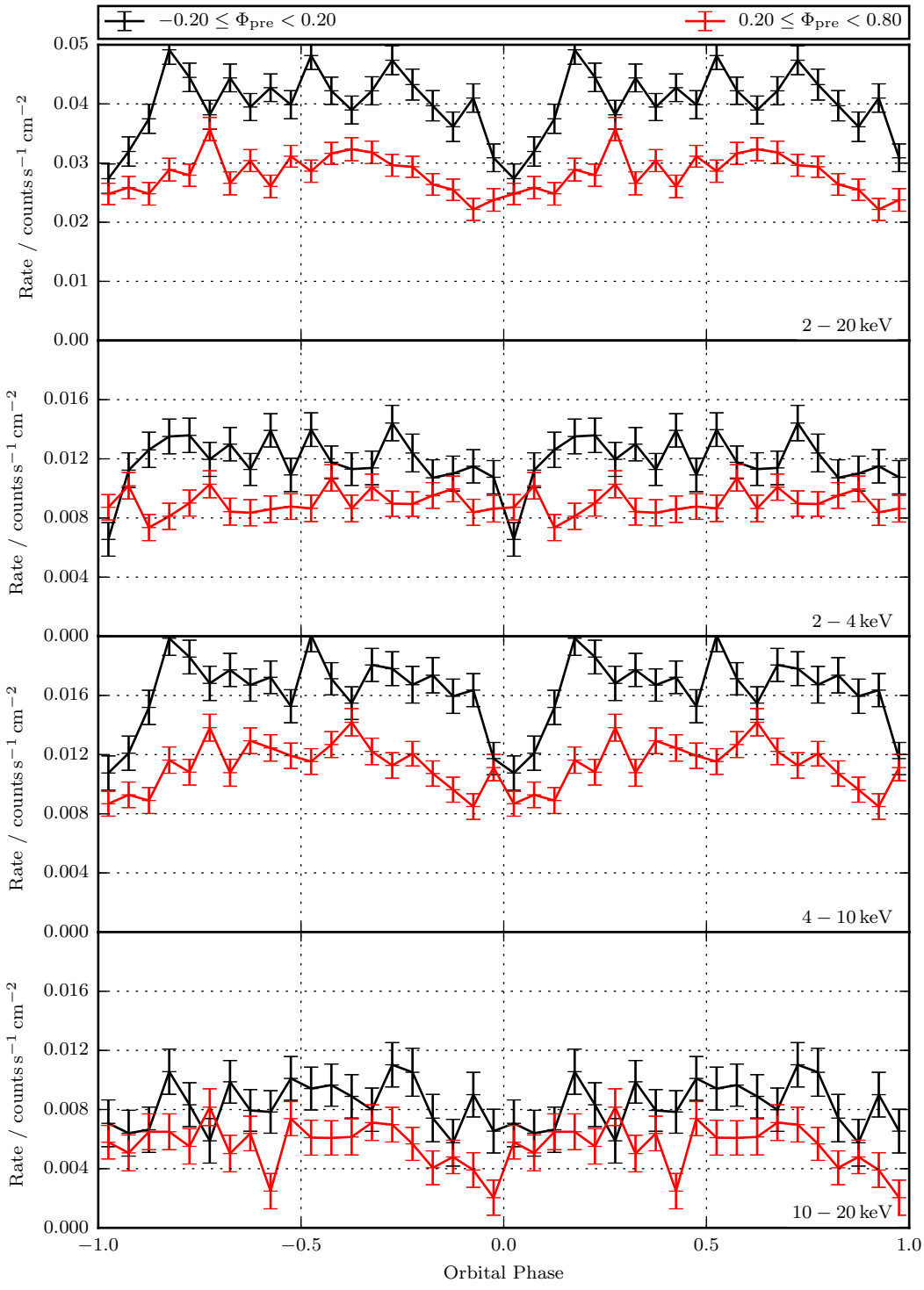


Figure 7.22: MAXI X-ray fluxes folded over orbital phase and averaged within bins. The data have been split by precession phase into two subsets - the black curve is centred on precession phase 0 (i.e., the disc maximally open to the line of sight), while the red curve contains observations at which the face of the disc is perpendicular to the line-of-sight.

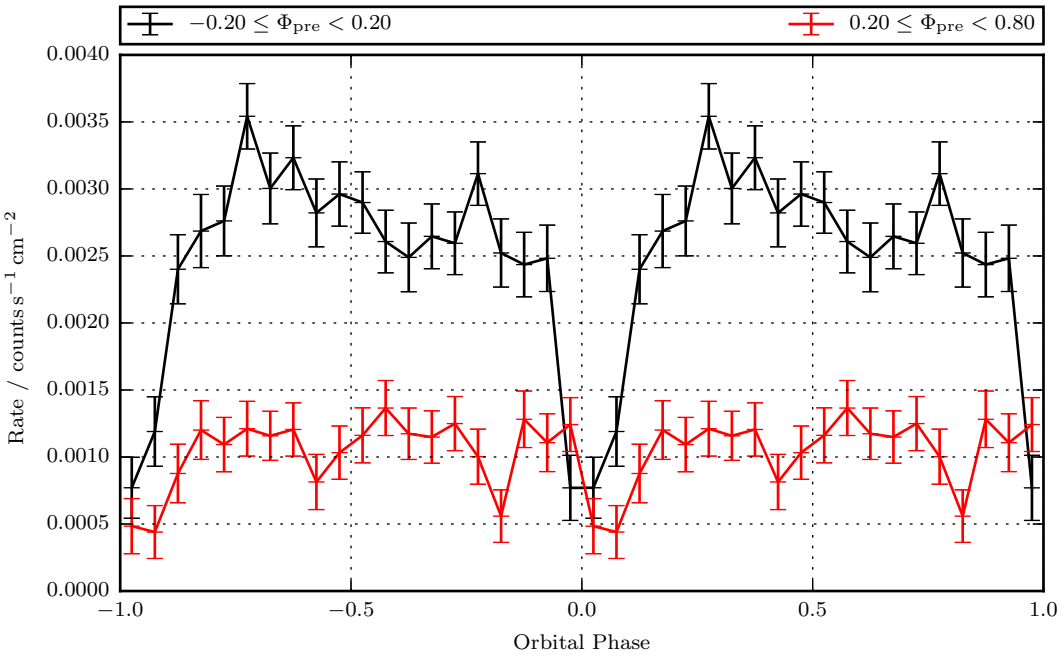


Figure 7.23: Swift 15-50 keV X-ray fluxes folded over orbital phase and averaged within bins. The data have been split by precession phase into two subsets - the black curve is centred on precession phase 0 (i.e., the disc maximally open to the line of sight), while the red curve contains observations at which the face of the disc is perpendicular to the line-of-sight.

(at least in the direction perpendicular to the orbital variation – a thin jet being a possible such solution). On the other hand, the absence of an eclipse signal at the edge-on precession phases suggests that the eclipsed X-rays must arise near the disc, and not in the extended jet (which is usually understood to be the origin of the soft X-rays).

3. In the Swift data, the uneclipsed mean flux when the disc is edge on is less than half that when the disc is open to the observer. This is consistent with a picture in which the hard X-ray emission arises in a corona close to a geometrically thick disc, or partly occulted by other high density outflows (e.g. winds). That the eclipsed fluxes in the open and the edge-on precession phases are comparable suggests that the extent of the corona is comparable with the scale of the compact object's Roche lobe.

#### 7.4.3.2 Other possible parameters – eccentricity and the companion's size

Within this simple model, there are two extensions that might prove insightful. Firstly, there are differing claims in the literature as to whether or not the companion star fills its Roche lobe, as we have assumed here. Most workers prefer a star that fills its Roche lobe (e.g., Antokhina et al.

(1992)), or even somewhat exceeds it (by perhaps 20% – e.g. Filippova et al. (2006)). However, since Lopez et al. (2006) observe recombination Si lines in eclipse from the eclipsed, receding counterjet, they contend that the very base of the counterjet must be uneclipsed, requiring that the companion star fill no more than 10% of its Roche lobe.

We have briefly experimented with allowing a filling factor for the companion star's Roche lobe, $\alpha_*$, as an additional parameter to those used in the MCMC analysis of Section 7.4.2.2. However, adding this parameter leaves us unable to obtain good fits to the data, most likely because the mass ratio $q$ and the two filling factors are degenerate in a non-trivial fashion. Both are essentially determined by the same variable (*viz.* the width of the eclipse) and only the very limited subset of the data around the eclipse transitions gives useful information with which to constrain the fits. Cautiously, the data do seem to point towards a reasonably full Roche lobe, but more careful analysis lies beyond the scope of the present discussion.

An important observation in this regard is that the Swift flux (which we suggest corresponds to quasi-coronal emission close to the compact object) is as occulted in eclipse at maximal disc opening as it is in the edge-on precession phase. This suggests that the companion must be great enough in size to completely obscure the centre of mass of the disc/compact object system. Crudely, this places a lower limit on the stellar radius of $R_* \gtrsim a \cos i_0 \simeq 0.2a$, where $a$ is the orbital separation and $i_0 = 78^\circ$ is the angle between the line-of-sight and the normal of the orbital plane.

Such a model precludes the geometry of Lopez et al. (2006). Plausibly, the lines observed could be emission from elsewhere within the system, misattributed to the receding red counterjet (perhaps a hot spot on the disc, though how this would avoid occultation in eclipse is similarly hard to explain).

Secondly, our formulation ignored the possiblity of an eccentric orbit. As noted in Section 1.5.2, there is evidence from the timing of flares and of jet speed variations that the binary orbit of SS 433 is eccentric. Handling this is non-trivial – for a start, the equivalent of the Roche lobe in an eccentric orbit is not simply calculated. Equipotential surfaces must distort, expanding and contracting as the masses orbit one another.

In our discussion of the eclipsing of the softer X-rays, we noted that the eclipses were "too long", leading us to overestimate $M_*$ relative to $M_{\rm bh}$. Can an eccentric orbit help us? We can get some handle on the effect of eccentricity on the eclipse as follows. The key parameter in eclipse

fitting is the duration of the eclipse as a fraction of the orbital period. From Kepler's laws, the orientation of the relative coordinate vector between the two masses varies as $\dot{\phi} \propto r^{-2}$, where $\phi$ is the orientation and $r$ the separation. Hence, the eclipse duration scales as $\delta t \sim r^2 \delta\phi$ where $\delta\phi$ is the angular size of the eclipsing companion star. Now, since $\delta\phi \sim R_*/r$, where $R_*$ is the radius of the companion star, the eclipse duration must scale as $\delta t \sim r R_*$.

If we assume that the semi-major axis is aligned close to the line-of-sight, then the eclipse occurs either at periastron or apastron. If the eclipse occurs at apastron (i.e., at maximum physical separation between the binary components), then since $r_{\rm apastron} = a\,(1+e)$, an eccentric orbit would indeed lead to an overestimate of the size of the eclipsing star. However, this is *only* true *if* the size of the companion star $R_*$ doesn't also scale with the eccentricity. If $R_*$ scales as $r_{\rm periastron} = a\,(1-e)$ (which is plausible if we want to avoid the objects colliding at their closest approach), then we find that $\delta t \sim a^2\left(1-e^2\right)$ – i.e., an eccentric orbit for fixed mass ratio would reduce the size of the companion, leading us to require an even more massive $M_*$ than the already high values suggested by the circular orbit. So, eccentricity helps, but *only* if the size of the companion is decoupled from the eccentricity of the system. As this seems an unlikely supposition, we conclude that eccentricity is unlikely to explain the apparently over-broad eclipses.

## 7.5 Spectral Properties

We began this Chapter by outlining the prevailing paradigm concerning X-ray outbursts in microquasars. Let us now consider SS 433 in view of this. The simplest test of the paradigm is to construct hardness-intensity diagrams from the MAXI and Swift monitoring data. Does the system soften as it enters into higher intensity states? Do we see evidence for a "turtle-head" like that in Figure 7.1?

In Figures 7.24 and 7.25, we show the hardness-intensity diagrams for SS 433. By analogy with those constructed using RXTE data for GX339-4 in Fender et al. (2004), we plot (the logarithm of) the ratio between the count rates in pairs of bands against the logarithm of the sum of those bands. The wavebands here are the hard (10-20 keV), medium (4-10 keV), and soft (2-4 keV) MAXI bands, and the very-hard (15-50 keV) Swift band, which we label as $h$, $m$, $s$, and $v$ respectively. As we noted in Section 7.2 (and is illustrated by the histograms in Figures 7.2 and 7.3), there is a large fraction of epochs in which it is not clear that the source is detected. To handle this, we simply

cut any epochs in which negative fluxes are reported. For Figure 7.24, each data point represents a single orbit of the MAXI satellite. For Figure 7.25, each data point represents a daily average, so as to allow comparison between the two satellites.

In panels (d) - (f) of each Figure, we have plotted the same hardness-intensity diagram, but imposing constraints on the precessional and orbital phase: we plot only uneclipsed (i.e., $\Phi_{\rm orb} \in [0.2, 0.8]$) data that are close to precession phase 0 (i.e, for $\Phi_{\rm pre} \in [-0.25, 0.25]$, when the jet's disc face is maximally open to the observer). These epochs are chosen because it is during these orbital and precessional phases that we expect to have the best chance to observe variation due to the disc, rather than the jet.

It is not clear that there is a relationship between hardness and intensity of the form predicted by the standard jet paradigm. Certainly, there is no such relationship seen in the MAXI data alone (Figure 7.24). If anything, the opposite is true: there is a slight (though probably insignificant) excess of hard X-rays during flares. This is noteworthy given that the state transitions in GX339-4 and in V404Cyg are seen by comparing X-rays where the "hard" band corresponds to 6.3-10.5 keV (Fender et al. (2004)).

Figure 7.25, on the other hand, does seem to show that there is an excess of soft X-rays at epochs of high intensity. A degree of caution is, however, required. Note that there is (especially in the softest band – panel (c)) a sharp termination with a slope of close to $-1$. This is probably artefactual, arising because the rates measured in the very-hard Swift band are lower than those measured in the softer MAXI bands. If one plots $\log_{10}(x+y)$ against $\log_{10}(x/y)$, then in the limiting case that $y \gg x$, one effectively plots $\log_{10} x$ against (constant $- \log_{10} x$) – i.e., a straight line. Nevertheless, the data in Figure 7.25 still appear to support the suggestion that on days when the system is brighter, it displays an excess of softer X-rays below 20 keV, and a deficit of the hardest X-rays, about 20 keV.

In interpreting these data, what help can we draw from archival observations? There are three examples in the literature which claim to observe SS 433 in an active X-ray state. Band (1989) attributes differences between the properties of the X-ray variability in 1979 observations made with the Einstein telescope and 1985 observations made with EXOSAT to SS 433 being in an active state in 1979, and a quiescent state in 1985. He notes rapid variation (with timescales of order days) in the 1979 observations, together with a varying spectral index (becoming flatter (i.e., harder) at epochs of higher intensity), which are absent in the later (sparsely sampled) data.

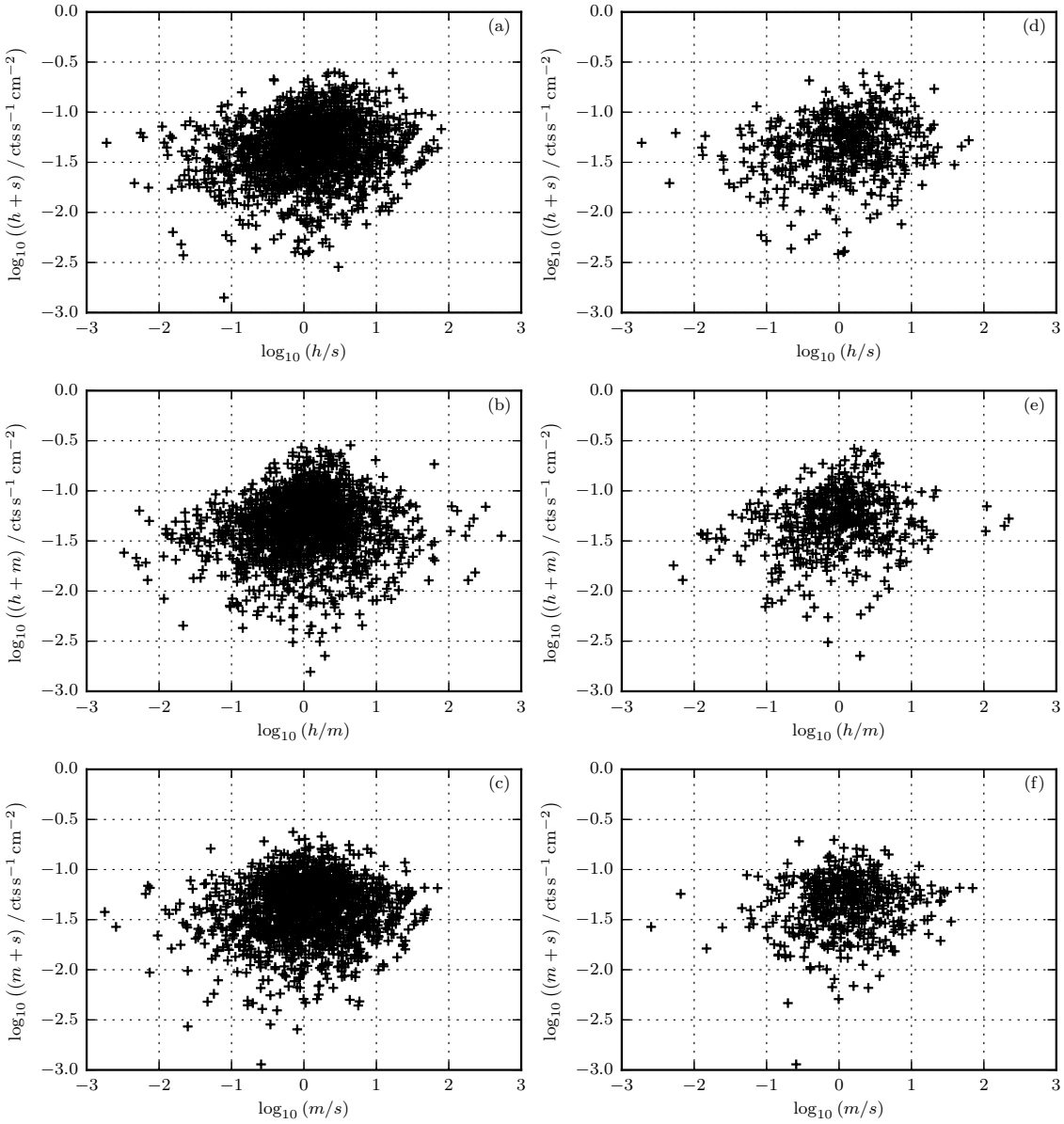


Figure 7.24: Hardness-intensity plots for SS 433 using X-ray data from the MAXI Observatory. The hard ($h$), medium ($m$), and soft ($s$) labels correspond to the fluxes in the 10-20 keV, 4-10 keV, and 2-4 keV wavebands respectively. Panels (a) - (c) plot hardness against intensity for all epochs with a possible source detection; in panels (d) - (f), the data selected to show only orbital phases $0.2 \leq \Phi_{\mathrm{orb}} \leq 0.8$ and precessional phases $-0.25 \leq \Phi_{\mathrm{orb}} \leq 0.25$. There is no evidence for an excess of *soft X-rays* during periods of *high intensity* X-ray activity.

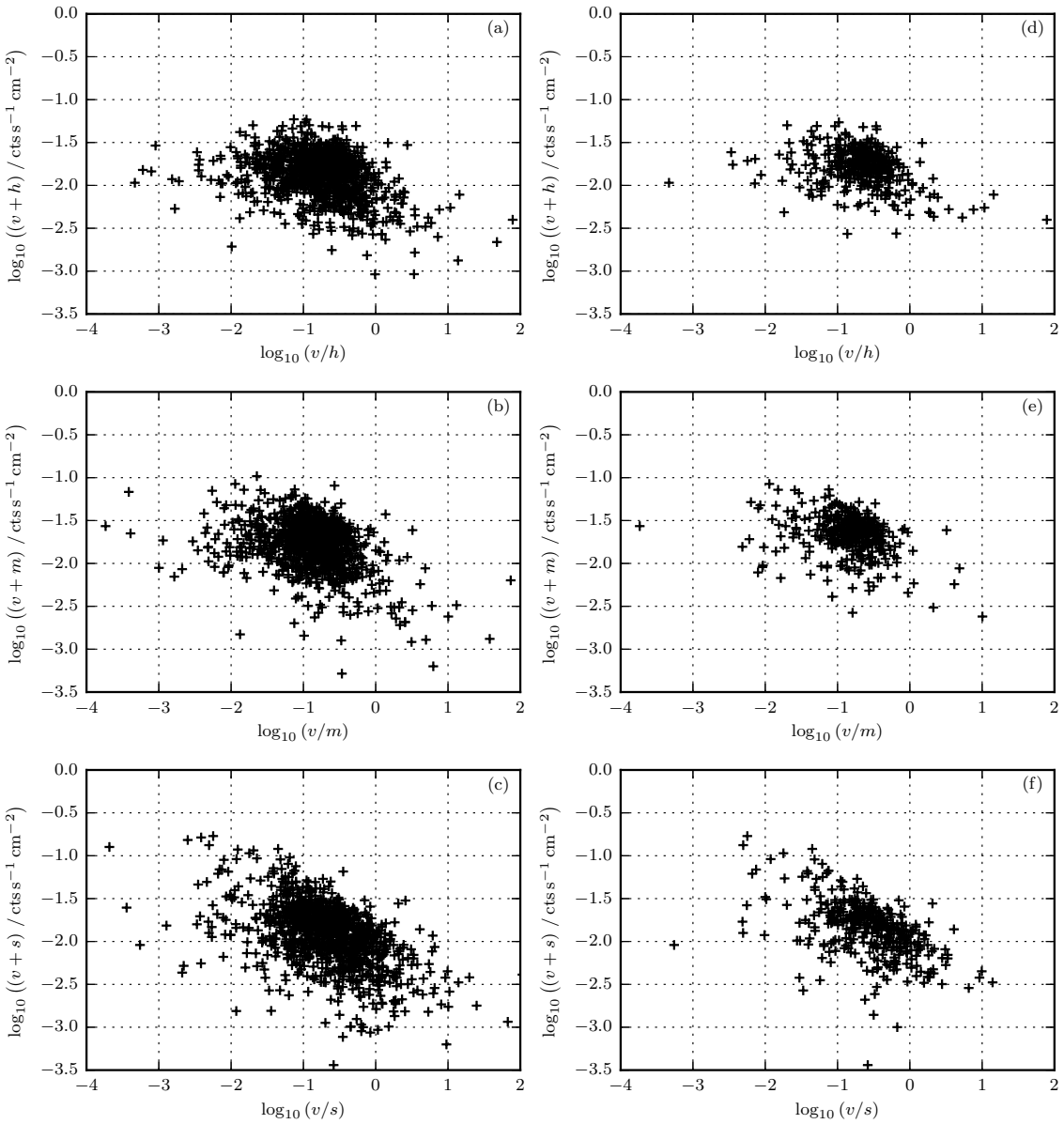


Figure 7.25: Hardness-intensity plots for SS 433 using X-ray data from the MAXI Observatory and the Swift/BAT satellite. The hard ($h$), medium ($m$), and soft ($s$) labels correspond to the fluxes in the 10-20 keV, 4-10 keV, and 2-4 keV wavebands of the MAXI instrument respectively, while $v$ ("very-hard") denotes the fluxes from the 15-50 keV band of the Swift satellite. Panels (a) - (c) plot hardness against intensity for all epochs with a possible source detection; in panels (d) - (f), the data selected to show only orbital phases $0.2 \leq \Phi_{\mathrm{orb}} \leq 0.8$ and precessional phases $-0.25 \leq \Phi_{\mathrm{orb}} \leq 0.25$.

However, the sparseness of the sampling and the lack of spectral resolution prevents us from drawing more solid conclusions.

Kotani et al. (2006) triggered observations with RXTE on a radio flare in 2001, to catch a follow up X-ray and radio flare 15-17 days later. The most significant observation is the detection of a relatively rapid $\sim 0.1$ Hz potential QPO in the time series during the $\sim 7$ d preceding the X-ray flare. Those authors suggest that this is related to the formation of more discrete ejecta in the jet outflow.

Lastly, Seifina and Titarchuk (2010) examined archival RXTE/PCA data (3-150 keV) at taken at uneclipsed orbital phases. They claim (without substantiation) that SS 433 displays the properties of an Intermediate State source in the categorisation of Fender et al. (2004), as discussed in Section 7.1.1, and that the source moves into and out of outburst in a fashion similar to that seen in sources that undergo repeated hardenings and softenings during flares while remaining in outburst. The most helpful insight may be offered by the spectra given in their figure 2, reproduced here as Figure 7.26. It appears that when SS 433 moves from quiescence to flare (where in SS 433's X-ray emission, these two states are most easily distinguished by the change from slow variability to rapid variability – cf., Band (1989) discussed above), this is accompanied by a slight increase in the soft bands (most noticeably in the 10-20 keV range), and a decrease in the very-hard X-rays (i.e., those above 20 keV). Within the soft range covered by MAXI, all bands, including the 6-10 keV range, dominated by the iron lines, rises slightly, but the most pronounced change is a steepening of the spectrum, such that there is an excess in the 10-20 keV band relative to the softest $< 6$ keV band. These two changes are not inconsistent with the picture we see in Figure 7.24 and particularly Figure 7.25.

It is tempting to argue that the behaviour that we see (both here and in Seifina and Titarchuk (2010)) is analogous to the standard picture, but at higher energies, perhaps due to SS 433's higher, super-Eddington accretion rate (Fabrika (2004)), compared with the sub-Eddington accretion rate of sources such as GX339-4. In this case, there are other intriguing parts of the picture. In particular, in both the standard picture and in SS 433, the transition from quiescence to the active state appears to be associated with a massive, possibly discrete jet launch – in SS 433, this is seen in the simultaneous X-ray and radio observations of Kotani et al. (2006) and in the simultaneous optical and radio observations of Blundell et al. (2011), while it is seen in radio/X-ray monitoring of a range of microquasars by Fender et al. (2004). There are also qualitative similarities between

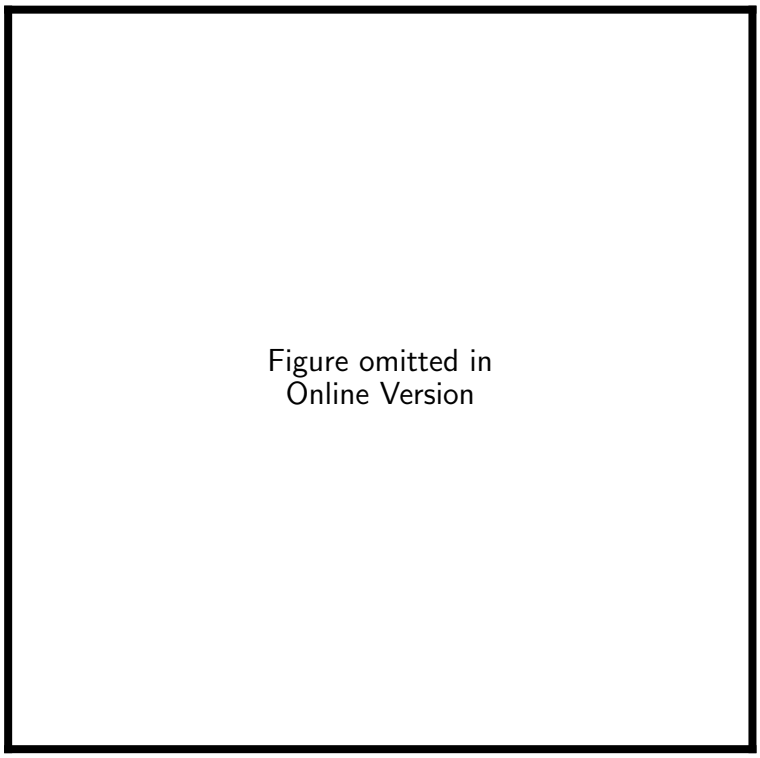


Figure 7.26: Figure 3 from Seifina and Titarchuk (2010). Here, they plot representative x-ray spectra from the INTEGRAL observatory which they claim to depict an "active" and a "quiet" state. The unhelpful units of energy × counts per unit time per unit area per unit energy bandwidth are used, which makes interpretation more difficult; we can, however, identify the presence of the iron lines in the 5-10 keV band. The blue line denotes their model, consisting of Comptonized X-rays from a surrounding corona. For our purposes, we point out that the ratio of the 20-100 keV flux to the 10-20 keV flux is lower in the "active" state than in the "quiet" state. Note the qualitative similarity with the soft-high and hard-low states described in Section 7.1.1.

the differences seen in the radio jet in hard and soft states (slow and continuous vs fast and discrete) with the picture that we outlined in Chapter 4 in relation to the observations in the 2003 movie of VLBA data, where we saw a similar transition from "slow" knots against a continuous flow to a seemingly discrete jet made of "fast" bolides as the jet began to flare.

The biggest problem with this reasoning is that we have no evidence to support the view that we are actually able to directly observe the disc. The standard model accounts for the softening of the spectrum as an enhanced disc contribution from a radiatively efficient accretion flow, together with reduced coronal emission. In SS 433, we don't see a disc component (most likely hidden by either the thick disc or by the disc wind), so this cannot be the cause.

Instead, we must attribute this variability to either the jet, whose bremsstrahlung emission is believed to dominate the soft X-ray spectrum (Kotani et al. (1996), Brinkmann et al. (2005)) or the extended corona, which the eclipse modelling of the Swift data in Section 7.4.2.2 suggested may be comparable in size with the Roche lobe of the compact object. A plausible qualitative picture is that during flaring episodes, the putative, corona-like structure is dispersed or at least reduced (perhaps partially expelled by an enhanced wind or radiation pressure) while the jet emission component rises (with a higher temperature or higher density at the jet base accounting for the increase in 10-20 keV X-rays). Any interplay between matter outflow as a disc wind and the possible corona is a highly unknown parameter in our understanding of this system.

This reasoning would seem to predict that the behaviour of hardness ratio should vary with precession phase – if the enhanced $\lesssim 20$ keV emission is due to enhanced emission close to the base of the jet, one would expect a stronger signal (i.e., a more prominent soft excess) at precessional phases close to 0, when our view of the jet's inner regions is obstructed by less of the thick disc. However, we don't see any clear change in the distibution of points in the hardness-intensity diagram at precesion phases close to $\Phi_{\rm orb} = 0$ (panels (d)-(f) in Figures 7.24 and 7.25), though perhaps we are limited by the relatively poor signal to noise of the MAXI data.

One would also expect to see a change in the spectral line properties, particularly of blue and redshifted iron from the jet and counterjet (c.f., the analysis of flux ratios in the jet and counterjet by Kotani et al. (1996)). The present data do not allow us to analyse these ratios – high resolution spectral data during outbursts would be necessary to allow us to follow this reasoning further.

We stress again that without some probe of the accretion disc itself, it is very difficult to fully compare the X-ray properties of SS 433 with those of other Galactic microquasars. The solution to

this probably lies in a better understanding of the timing properties of high frequency oscillations in SS 433's power spectrum. We refer to the QPO-like structure seen by Kotani et al. (2006), and also to the disc-reprocessing arguments of Atapin et al. (2015), which may allow an indirect probe of the variability of the core regions, which are otherwise obscured by the funnel of the thick disc. However, we have noted that the qualitative picture seen by studying hardness ratios cannot be simply explained within the existing paradigm of microquasar phenomenology – a more complete understanding of the behaviour of SS 433's core is needed.

## 7.6 Final Discussion

Over the course of this Chapter, we have followed two significant lines of enquiry. Firstly, we have used X-ray measurements to probe the geometry of the SS 433 binary system, concluding that the eclipse data support a binary system where the companion star is more massive than the compact object (i.e., $q = M_{\rm bh}/M_* < 1$ – see Section 7.4.2.2). Secondly, we examined the spectral properties and found no evidence that SS 433 conforms to the paradigm of X-ray state transitions.

So, let us make one final speculation as to why SS 433 displays differing accretion behaviour to other accreting stellar mass black-holes. We have found compelling evidence for one particular difference betwen SS 433 and other Galactic black hole systems. This is illustrated by figure 2 of Fender and Muñoz-Darias (2016), which sketches estimated binary parameters for 20 black hole systems. This includes several of those sources known to display state transitions (e.g., GX339-4, GRS1915+105, XTE J1859+226, and XTE J1550-564; see Fender et al. (2004)). Unfortunately, references to precise values are not given, but qualitatively there is a clear pattern: in all of the systems cited, the black hole is more massive than its companion (i.e., $q = M_{\rm bh}/M_* \gtrsim 1$). In SS 433 though, this is *not* the case.

Following this reasoning further, we note the discussion in section 4.4 of Frank et al. (2002) regarding the evolution of Roche lobes during mass transfer from the companion to the black hole. Crucially, there is a critical mass ratio $q_{\rm crit} = M_{\rm bh}/M_* \simeq 6/5$. Below this value ($q < q_{\rm crit}$), mass transfer causes the Roche lobe of the companion will contract, sustaining the mass transfer, while above it ($q > q_{\rm crit}$), mass transfer expands the companion's Roche lobe, potentially suppressing the accretion flow.

It is interesting to note that SS 433's mass ratio places it into the first category, while GX339-4 and

the other sources mentioned fall into the second. It is also interesting to note that unlike the other sources listed, SS 433 has a persistently super-Eddington accretion rate. King et al. (2000) discuss these points briefly, arguing that this may point to a future common envelope evolution phase in SS 433. Further development of this idea lies beyond the scope of this thesis. However, it is plausible that the presence of a dynamically self-sustaining flow could help explain the differences between SS 433 and other Galactic microquasars.

## 7.7 Summary

X-ray data allows us to probe the physics of the innermost regions of the SS 433 binary system. Using the monitoring archives from the Swift and MAXI observatories, we have:

- seen evidence for orbital and precessional flux variations, and, by fitting the eclipse shapes, estimated the mass ratio of the system;
- used the high energy Swift data to argue for the presence of an extended corona-like region of emission around the compact object, perhaps comparable in size to the companion;
- seen that SS 433 does not obey the standard paradigm of microquasar activity, although we have not been able to preclude the existence of limit cycles appearing in higher energy X-rays.

There are several avenues along which further work is needed. To account for the anomalously broad eclipses in the MAXI data, we need better geometrical models of obscurring matter in the system – this will also allow an interpretation of the precession variability. Extending the time baseline of the monitoring data will allow us to constrain the eclipse shapes better variability, and hence to obtain better estimates of the binary parameters and to reconcile the disparities between the two data sets.

From an observational perspective, the future lies in X-ray timing. We deliberately only looked at long timescale variations here, but the time series may also contain information about variability on sub-day scales (limited here by the weak SNR of the all-sky monitors). Examination of the timing properties to look for QPOs or for other disc signatures (following the work of Atapin et al. (2015)) lies beyond the scope of this work, but may offer the best chance to observe the disc itself.

# Chapter 8

# Conclusions

There are several important developments that have emerged from this study of SS 433's remarkable outflows. The most significant result is the first unique determination of the velocities of individual bolide pairs in the jets of SS 433 purely from radio images. Where previous estimates of these speeds have been dependent on the assumptions of the kinematic model (at least in the radio jets – unique determinations of jet speeds are of course possible from the optical redshifts (Blundell and Bowler (2005))), here we have only assumed the distance to SS 433, and that the jets are symmetrical and move ballistically to calculate the jet speeds. As a corollary of this, we have shown conclusively that different bolide pairs can be launched with different speeds, and that the launch speed can vary from as low as $0.22c$ to as high as $0.32c$ within a few days. That these launch speeds vary is entirely consistent with previous observations of variation in the speeds of the optical jets and are highly suggestive of a common underlying phenomenology.

We accept that our method is still dependent on having prior information about the distance to the object. We have argued that the work of Blundell and Bowler (2004) and Lockman et al. (2007) gives us good reason to assume a distance of $5.5 \pm 0.2$ kpc. Moreover, we have been shown that the variation in the distance estimates can be entirely accounted for as an artefact of the true intrinsic variation in the jet speeds themselves. The varying proper motions within the 2003 VLBA observations preclude the consistent estimation of a distance by assuming a fixed launch speed for all ejecta. A distance of close to 4.5 kpc is eminently consistent with some of the extreme low launch speeds seen in the earlier part of the 2003 VLBA observations (Figure 4.9). That the extreme high proper motions also seen in these observations would correspond to distances well

beyond the usual distance estimates further strengthens our confidence in the value of 5.5 kpc.

The similar characteristics of the jet speed variation seen in these radio observations and in previous optical data (especially by Blundell et al. (2011)) extends to the behaviour of the system in its flaring mode. We have argued that the 2003 data reveal (supported to some degree by the 2011-Dec-24 and 2012-Jan-28 images) that SS 433 occasionally enters a flaring mode, in which the bolides launched tend to be brighter (i.e., more massive), and to possess faster launch speeds. This displays qualitative similarities to the correlation between the optical jet emission lines and the radio flux seen in Blundell et al. (2011), with evidence in both cases for a dip in the launch speed immediately before the flare.

However, our attempts to relate this flaring behaviour to variability in the system's X-ray emission were only partially successful. Certainly SS 433 does not display the same characteristic pattern of X-ray variation during flares as is seen in many other microquasars (GRS1915+105, V404 Cyg, GX339-4, and others). There is no evidence in the data from the MAXI All-Sky Monitor for systematic variability in the soft X-ray bands (below 20 keV), though a tentative anti-correlation may exist between the harder X-rays (about 20 keV as observed by Swift) and the MAXI bands (i.e., an excess of soft-band X-rays during flaring episodes), though the limited sensitivity of the all-sky monitor data and the corresponding low SNR restricts our ability to draw firm conclusions from this.

More useful information may be obtainable from multi-epoch spectra from high-energy X-ray observatories (e.g., the INTEGRAL data, some of which is given in Seifina and Titarchuk (2010)). The main challenge in doing this is that our understanding of the actually geometry of the system on scales between the size of the accretion disc and the size of the binary system remains remarkably poor – it is hard to interpret variations in the spectra without a clear understanding of which parts of the disc, jet, wind, or possible corona dominate (or obscure) different parts of the spectra. For instance, the consensus among those workers who have taken X-ray spectra or photometry is that the disc itself is obscured and not directly observed (e.g., Kotani et al. (2006), Atapin et al. (2015)); if this is so, and if (as is assumed within the canonical microquasar flaring phenomenology), the x-ray variation is due to changes in the disc, then without a clear understanding of the geometry of the system, we are unable to interpret any reprocessed variations that we may see.

The all-sky monitor light curves given here are unable to strongly constrain the geometry, though certain key points are worth stressing. There are clear variations with precession and orbital phase

in the 4-10 keV MAXI band and in the Swift data. We see no variation with nutation in the data here, though we are almost certainly limited by low signal-to-noise. In the all-sky monitor data, we see no evidence to claim that the disc is directly observed: we note that while the precessional variability may be described by a simple picture in which the flux varies as the projected area of a thin accretion disc, the fact that the uneclipsed flux at precessional phases when the jets are close to the plane of the sky (i.e., the edge of the disc is aligned with the line of sight) is comparable to the eclipsed flux at those precession phases when the disc is at its most open to the observer suggests that a large part of the x-ray flux is obscured by a geometrically thick and opaque disc-like structure. This observation also indicates that a significant fraction of both the hard and soft x-rays are emitted close to the compact object/disc. The shape of the hard eclipse data is consistent with a picture in which the X-ray emission above 20 keV is dominated by an extended corona-like emitting region. The smooth transition into and out of eclipse indicates that this region must be comparable in extent to the size of the Roche surface around the compact object. For a mass ratio $M_{\rm bh}/M_*$ that is probably between 0.1 and 1, and with an estimate of the orbital separation $a \simeq 5.5 \times 10^{10}$ m (assuming a total mass of 38 $\mathrm{M}_\odot$ (Blundell et al. (2008)) and an orbital period of 13.08 d), then is region must be on the order of 1-2 $\times 10^{10}$ m in radius. Importantly, the width of the eclipse also allows us to estimate the mass ratio, hence the values given above – the large uncertainty in our determination means we are unable to constrain the mass ratio more precisely than previous workers, though we note that the value we derive is consistent with some of the higher mass ratio estimates derived from optical data ($q \simeq 0.7$; Gies et al. (2002b)), though we are not able to exclude lower values (e.g., $q \lesssim 0.3$ Antokhina et al. (1992)).

Less clear is the interpretation of the low energy (4-10 keV) light curves. Here, the eclipses are broader than we would expect. The logarithmic dependence of the Roche radius in Equation 7.22 means that a small change in the width of the eclipse (and hence the radius of the eclipsing object) can equate to orders of magnitude change in the mass ratio estimated – the low mass ratio estimates ($q = 10^{-2}$ is perhaps an upper limit here) suggest that we probably overestimate the width of the eclipse, and hence the size of the Roche lobe of the companion star, by at least a factor of a few.

On the other hand, the sharpness of the eclipse edges could be consistent with a very thin emitting region (a thin jet, as expected in models where the soft x-rays are jet dominated). We are not helped because in essence only a tiny fraction of the orbital period (around the edges of the eclipse) carries useful information. With already limited sensitivity in the MAXI ASM, we find ourselves

with an insufficient number of data points to constrain the model reliably. Hence, disentangling mass ratio and the size of the eclipsed object is difficult.

Again, the most likely way to answer these questions is with broadband, high sensitivity X-ray data. Achieving the necessary temporal coverage to disentangle natural fluctuations from precessional and orbital variation will not be easy, but offers the best chance of both identifying both the flaring behaviour of SS 433 and the geometry of the emitting regions.

Though there are still ambiguities about the geometry of the inner jets and binary as revealed by the X-ray data, the 2012-Jan-28 VLBA observation allows us, for the first time been able to make measurements of the properties of resolved bolides on milliarcsecond scales. It is clear that at least some of the bolides expand very rapidly – our estimate of the expansion rate ($\sim 0.03c$) is faster than previous estimates of the expansion of optical bolides by at least a factor of 5, and is equivalent to perhaps 3 times the expansion rate estimated from the opening angle of the X-ray jet. Having some volume estimate for the bolide allowed us to make estimates of the bolide masses and magnetic fields, assuming equipartition of energy. The estimates so derived, especially for the masses, were far too low to be consistent with the mass outflow rates estimated from the strengths of X-ray emission lines. We estimated that the masses of individual bolides were $M \sim 2 \times 10^{-10}\,\mathrm{M}_\odot\,\gamma_0^{-(5p-3)/(p+5)}$ where $\gamma_0$ is the low energy cut off in the electron spectrum, and $p$ is the electron energy index. As a value of $\gamma_0 \sim 10^3$ would not be unreasonable, this means that the mass as estimated within these assumptions may be as low as $10^{-13}\,\mathrm{M}_\odot$. For consistency with existing mass outflow rates ($\dot{M}_{\rm jets} \sim 10^{-6}$ – $10^{-7}\,\mathrm{M}_\odot\,\mathrm{yr}^{-1}$), we would require these to be launched at a rate of at least $10^6\,\mathrm{yr}^{-1}$ – at least four orders of magnitude higher than observations suggest is the case. Crucially, we showed that because the number density depends on the volume of the emitting region as $n \propto V^{-4/(p+5)}$, and as this exponent lies between $-1$ and 0, the estimate of the mass in the bolide $M \propto nV \propto V^{(p+1)/(p+5)}$ will *decrease* further if we have overestimated the volume (i.e., if the bolide is not resolved). Instead, we argued that this gives evidence for one of two plausible explanations: either (a) the bolides are significantly out of equipartition (with perhaps $10^{10}$ times as much energy in the electron population than the magnetic field); or (b) there is a large population of unobserved, cold baryons in the jet (perhaps $10^4$ times the mass in these unseen particles than in the relativistic electron population and its associated cold protons). Importantly, this second possibility means we are only required to accelerate a small fraction of the total mass to form the relativistic particle distribution.

This may be related to the tentative and provisional results that emerged from our discussion of the lightcurves of individual bolides. Although we have not performed a full analysis of the coupled evolution of magnetic fields and electron energies in an evolving bolide, we offered some simple arguments based on handling their evolutions independently. These suggested that a 3-dimensional expansion geometry would result in more rapid fading of the lightcurve than that seen here, while a 2-dimensional geometry – such as a spherical shell with the emission concentrated in a thin outer layer – might be able to match the observed decay rate. This would be consistent with a picture in which quasi-thermal bolides cool rapidly over the first 3 or 4 days after launch (emitting first bremsstrahlung and recombination lines in the X-ray, then recombination lines in the optical as it cools). Then, from about 2 days after launch, particles are accelerated to relativistic speeds on the outer edges of the bolide, producing the synchrotron radiation seen at scales greater than milliarcseconds (i.e., greater than $10^{12}$ m).

Though we have offered several insights into SS 433's behaviour, there remain many outstanding questions. Among these are the big questions, which we have not attempted to tackle here. For instance how to explain the two accelerations in the system, namely the accelerations of particles and bolides? We need to accelerate the bolides to $\sim 0.26c$, and we need to so in such a way as to produce a significant distribution in speeds. Why should the speed vary? Why should the more massive ejecta seen in flares travel faster? But, we also need to accelerate the relativistic electron population that produces the synchrotron emission on scales of $\gtrsim 10^{13}$ m. Are these present at launch, or are they accelerated later? If both the electrons and the magnetic fields are present at launch, can their properties be constrained from the contribution of inverse Compton scattering to the X-ray spectra, and what should be the synchrotron contribution? A more thorough review of existing X-ray data may help to constrain these two contributions to the spectra further.

We also still have significant ignorance about the shape and nature of the accretion flow. This is closely linked to our earlier remarks about the uncertainty around the geometry of the system. Again, the most profitable approach to this problem lies in high energy observations. Again, studies of X-ray variability (and particularly a search for high frequency oscillations and QPOs) may allow us to indirectly probe the structure of the accretion disc.

This work has pointed to three very specific individual observational questions, for which theoretical explanations are needed.

Firstly, in Section 7.6, we noted that SS 433 was unique in the sample of well-studied microquasars

in having a more massive companion star than its black hole. We cited the arguments of Frank et al. (2002) and King et al. (2000) showing that the accretion of mass in such a system could be rapid and self-sustaining, and could explain SS 433's super-Eddington accretion behaviour. A full study of this process lies beyond the remit of the current work, but more thorough analysis of this question must offer important insights into the structure of the accretion flow in SS 433.

Secondly, we discussed the nodding of the accretion disc (Section 2.6). We noted that the Katz et al. (1982) prescription predicts three frequencies of interest, namely $2\left(|\omega_{\rm orb}| + |\omega_{\rm pre}|\right)$, $2|\omega_{\rm orb}| + |\omega_{\rm pre}|$, and $2|\omega_{\rm orb}| + 3|\omega_{\rm pre}|$ corresponding to periods of 6.06 d, 6.28 d, and 5.83 d respectively (see Appendix A). These are observed with the ratios of their amplitudes $A_{5.83\,\rm d} : A_{6.06\,\rm d} : A_{6.28\,\rm d}$ in the Fourier spectra given approximately by $1 : 0 : 4$ (figure 3 of Katz et al. (1982), and figure 3(a) of Blundell and Bowler (2005)). Although the small relative amplitude of the 5.83 d peak makes its detection hard (e.g., Cherepashchuk et al. (2013)), this ratio has been seen in multiple optical data sets (Katz et al. (1982), Blundell and Bowler (2005)).

However, theoretical models of this system have yet to successfully predict these relative amplitudes. Though there is a significant literature on warped discs (e.g., Ogilvie and Dubus (2001)), attempts to apply this is SS 433 (e.g., Begelman et al. (2006)), fail to explain the presence of the 5.83 d periodicity – which is often left out of the treatment entirely – and fail to explain the lack of a signal at 6.06 d (half the synodic period). If this could be explained, it would contain a powerful constraint on the dynamically precession of the tilted or warped accretion disc.

The third open question concerns the evolution of magnetic fields in expanding plasmons, as discussed in Section 6.3. Here again we have a quantitative observation that cannot be understood in terms of the existing theory as outlined in this thesis. In particular, our treatment decoupled the evolutions of the relativistic electrons from the magnetic fields, where a more complete solution would allow for transfer of energy between the two. This might take the form of the generataion of magnetic fields (the magnetic dynamo), or the slowing of the expansion by the internal magnetic forces. It should also be able to handle the way in which different expansion geometries can affect different components of the magnetic field in different ways, meaning that an initially tangled field may come to be dominated by one component either parallel to or perpendicular to the flow. Again, this is a significant analytical (and, most likely, computational) problem which goes far beyond the work here.

Throughout this work, we have seen that the most powerful tool for understanding the behaviour

of SS 433, and hence of accretion processes around other compact objects is through time resolved observations. It was time-resolution that allowed us to uniquely measure the speeds of the jets. It was time resolution that allowed us to demonstrate that jet bolides fade in a regular and systematic fashion. And it was temporal monitoring of X-ray photometry that enabled us to probe the geometry of this remarkable system. From an observational standpoint, we now need quasi-simultaneous coverage at multiple wavebands, to allow us to show how the same phenomena manifest themselves at different observational frequencies, and to allow us to confirm that the qualitative similarities we have noted between different wave bands correspond to the same underlying physics (for example, by looking for correlated variation between the jets as seen in the optical and radio). We have also proposed three very specific questions – relating to the super-Eddington accretion, the nutation of the accretion flow, and the energetic evolution within individual expanding jet bolides – where theoretical predictions are needed to illuminate existing observational facts. There is much work still to be done, and much more to be learnt.

# Appendix A

# The Slaved Disc Model

In Chapter 2, we briefly discussed some of the results of the slaved disc model as set out in Katz et al. (1982). In the first Section of this Appendix, we present our own derivation of the key results of the Katz et al. (1982) paper, emphasising the sequence of approximations made. Then, in the second Section, we perform the derivation of equations 7 (a)-(c) from Vermeulen (1989) (given in a corrected form as Equations 2.39 in this work).

## A.1 The slaved disc model

### A.1.1 The Lagrangian & equations of motion

The model used by Katz et al. (1982) is of a rigid ring, at rest at the origin of some coordinate system and subject to a time-dependent potential from an orbiting point mass. The key approximations in this model are:

1. that the rotation frequency of the disc is much faster than the orbital frequency of the massive companion, which is much faster than the precessional frequency;
2. that the ring radius is much less than the binary separation;
3. that the perturbations to the mean, driven motion may be treated as small.

The first of these is the most important, because (a) it allows us to treat the disc as a rigid ring (see Collins and Scher (2002) for comments on this); (b) it allows us to neglect inertial (centrifugal)

forces and treat the centre of mass of the ring as being at rest, rather than the centre of mass of the ring–companion system being at rest; and (c) will allow us to greatly simplify the linearised equations of motion. The second approximation will allow us to use the dipole expansion to write down the potential up to the quadrupole (tidal) term.

In Section 2.2, we defined the jet cone opening angle and precession angles $\{\theta, \phi\}$ by analogy with the polar and azimuthal angles. Let us add a third angle, labelled $\varpi$, denoting the rotation of the ring about the unit vector described by $\{\theta, \phi\}$. This forms a set of Euler Angles (see, e.g., Kibble and Berkshire (2004)). We can then write down the two parts of the Lagrangian.

**Result A.1.1** (Kinetic energy of an axisymmetric body)**.** The rotational kinetic energy of an axisymmetric rigid body with moment of inertia

$$T = \tfrac{1}{2} I_{\perp} \left( \dot{\theta}^2 + \dot{\phi}^2 \sin^2 \theta \right) + \tfrac{1}{2} I_{\parallel} \left( \dot{\varpi} + \dot{\phi} \cos \theta \right)^2 \tag{A.1}$$

*Proof.* See, e.g., Kibble and Berkshire (2004). □

For a rigid ring, it can be shown that $I_{\parallel} = m_d {r_d}^2 = 2 I_{\perp}$. Now, we calculate the potential energy for a ring under the influence of a point mass.

**Result A.1.2** (Potential energy of rigid ring)**.** Consider a rigid ring inclined at an angle $\theta$ to the orbital plane, with the normal to the ring as projected onto the orbital plane making an angle $\phi$ with the $x$-axis (c.f., the jet coordinate system in Section 2.2), and with the companion mass at distance $R$ and at an angle $\psi$ to the $x - axis$. Then,

$$V(\theta, \phi; \psi) = V_0 - \tfrac{1}{4} I_{\parallel} {\omega_{\mathrm{orb}}}^2 \left( 1 - 3 \sin^2 \theta \cos^2 (\psi - \phi) \right) \tag{A.2}$$

*Proof.* We write the potential as:

$$V(\boldsymbol{R}) = -\int \frac{G\, m_{\mathrm{c}}\, \mathrm{d}m}{|\boldsymbol{R} - \boldsymbol{r}|} = -\frac{G\, m_{\mathrm{c}}\, m_{\mathrm{d}}}{2\pi} \int |\boldsymbol{R} - \boldsymbol{r}(\alpha)|^{-1}\, \mathrm{d}\alpha$$

where $m_{\mathrm{c}}$ is the mass of the companion, and we have used $\alpha$ to parametrize the points on the ring, and where $\mathrm{d}m = (m_{\mathrm{d}}/2\pi r_{\mathrm{d}})\, \mathrm{d}\alpha$. Then, expanding the term $|\boldsymbol{R} - \boldsymbol{r}(\alpha)|^{-1}$ and neglecting terms $\mathcal{O}\left( [r_{\mathrm{d}}/R]^3 \right)$, we have:

$$|\boldsymbol{R} - \boldsymbol{r}(\alpha)|^{-1} = R^{-1} \left( 1 - \frac{r_{\mathrm{d}}}{R} \frac{\boldsymbol{r} \cdot \boldsymbol{R}}{r_{\mathrm{d}} R} + \frac{1}{2} \left( \frac{r_{\mathrm{d}}}{R} \right)^2 \left( \frac{3}{2} \left( \frac{\boldsymbol{r} \cdot \boldsymbol{R}}{r_{\mathrm{d}} R} \right)^2 - 1 \right) \right)$$

But, from the geometry of the jet coordinate frame, we can write

$$\boldsymbol{r}\cdot\boldsymbol{R} = r_{\rm d}\,R\,\left(\cos\alpha\cos\theta\cos\left(\psi-\phi\right)+\sin\alpha\sin\left(\psi-\phi\right)\right)$$
$$\left(\boldsymbol{r}\cdot\boldsymbol{R}\right)^2 = \left(r_{\rm d}\,R\right)^2\,\left(\cos^2\alpha\cos^2\theta\cos^2\left(\psi-\phi\right)+\sin^2\alpha\sin^2\left(\psi-\phi\right)+\tfrac{1}{2}\sin 2\alpha\cos\theta\sin 2\left(\psi-\phi\right)\right)$$

Performing the integration over $\alpha$, only the terms in $\cos^2\alpha$ and $\sin^2\alpha$ survive. This yields:

$$V\left(\theta,\phi;\psi\right) = -\frac{Gm_{\rm c}\,m_{\rm d}}{2\pi R}\left[1+\frac{1}{4}\left(\frac{r_{\rm d}}{R}\right)^2\left[3\left(\cos^2\theta\cos^2\left(\psi-\phi\right)+\sin^2\left(\psi-\phi\right)\right)-2\right]\right]$$

The final form is obtained by rearranging the trigonometric identities in the last square bracket. □

**Result A.1.3** (Equations of motion)**.** The equations of motion for the slaved disc model can be written:

$$\dot{\varpi}+\dot{\phi}\cos\theta = \text{constant} = \frac{p_\varpi}{I_\parallel} \tag{A.3a}$$
$$\ddot{\theta} = \tfrac{1}{2}\dot{\phi}^2\sin 2\theta - 2\dot{\phi}\sin\theta\left(\dot{\varpi}+\dot{\phi}\cos\theta\right) - \tfrac{3}{2}\,\omega_{\rm orb}^2\,\sin 2\theta\cos^2\left(\psi-\phi\right) \tag{A.3b}$$
$$\ddot{\phi} = \frac{2\dot{\theta}\dot{\varpi}}{\sin\theta} - \tfrac{3}{2}\,\omega_{\rm orb}^2\,\sin 2\left(\psi-\phi\right) \tag{A.3c}$$

*Proof.* Using the Lagrangian $L = T - V$, we can write down the Euler-Lagrange equations:

$$\frac{\rm d}{{\rm d}t}\,I_\parallel\left(\dot{\varpi}+\dot{\phi}\cos\theta\right) = 0 \tag{A.4a}$$
$$\frac{\rm d}{{\rm d}t}\,\left(I_\perp\dot{\theta}\right) = \frac{1}{2}I_\perp\dot{\phi}^2\sin 2\theta - I_\parallel\dot{\phi}\sin\theta\left(\dot{\varpi}+\dot{\phi}\cos\theta\right) - \frac{\partial V}{\partial\theta} \tag{A.4b}$$
$$\frac{\rm d}{{\rm d}t}\,\left(I_\perp\dot{\phi}\sin^2\theta + I_\parallel\cos\theta\left(\dot{\varpi}+\dot{\phi}\cos\theta\right)\right) = -\frac{\partial V}{\partial\phi} \tag{A.4c}$$

where

$$\frac{\partial V}{\partial\theta} = \frac{3}{4}\,I_\parallel\,\omega_{\rm orb}^2\,\sin 2\theta\cos^2\left(\psi-\phi\right)$$
$$\frac{\partial V}{\partial\phi} = \frac{3}{4}\,I_\parallel\,\omega_{\rm orb}^2\,\sin^2\theta\sin 2\left(\psi-\phi\right).$$

Then, integrating Equation A.4a, we see that $I_\parallel\left(\dot{\varpi}+\dot{\phi}\cos\theta\right)$ is a constant, which we label $p_\varpi$.

Differentiating Equation A.4b, and remembering that $I_\parallel = 2I_\perp$, we can write:

$$\begin{aligned}\ddot{\theta} &= \frac{1}{2}\dot{\phi}^2 \sin 2\theta - \frac{I_\parallel}{I_\perp}\dot{\phi}\sin\theta\left(\dot{\varpi} + \dot{\phi}\cos\theta\right) - \frac{3}{4}\frac{I_\parallel}{I_\perp}{\omega_{\rm orb}}^2 \sin 2\theta \cos^2(\psi - \phi) \\ &= \frac{1}{2}\dot{\phi}^2 \sin 2\theta - 2\dot{\phi}\sin\theta\left(\dot{\varpi} + \dot{\phi}\cos\theta\right) - \frac{3}{2}\,\omega_{\rm orb}^2\, \sin 2\theta \cos^2(\psi - \phi)\end{aligned}$$

completing the $\theta$ equation of motion. For the $\phi$ equation of motion, we see that Equation A.4c can be written:

$$\frac{\mathrm{d}}{\mathrm{d}t}\left(\dot{\phi}\sin^2\theta\right) + \frac{I_\parallel}{I_\perp}\frac{\mathrm{d}}{\mathrm{d}t}\left(\cos\theta\left(\dot{\varpi} + \dot{\phi}\cos\theta\right)\right) = -\frac{3}{4}\,\frac{I_\parallel}{I_\perp}\,\omega_{\rm orb}^2\, \sin^2\theta \sin 2(\psi - \phi)$$

but $\left(\dot{\varpi} + \dot{\phi}\cos\theta\right) = \text{constant}$, so

$$\frac{\mathrm{d}}{\mathrm{d}t}\left(\cos\theta\left(\dot{\varpi} + \dot{\phi}\cos\theta\right)\right) = -\left(\dot{\varpi} + \dot{\phi}\cos\theta\right)\, \sin\theta\,\dot{\theta}$$

and we can write

$$\frac{\mathrm{d}}{\mathrm{d}t}\left(\dot{\phi}\sin^2\theta\right) = \ddot{\phi}\, \sin^2\theta + \dot{\phi}\dot{\theta}\, \sin 2\theta\,.$$

Combining the last three equations, we find:

$$\begin{aligned}\ddot{\phi}\, \sin^2\theta &= -\dot{\phi}\dot{\theta}\, 2\sin\theta\cos\theta + 2\dot{\theta}\left(\dot{\varpi} + \dot{\phi}\cos\theta\right)\, \sin\theta - \frac{3}{2}\,\omega_{\rm orb}^2\, \sin^2\theta \sin 2(\psi - \phi) \\ \Rightarrow \ddot{\phi} &= \frac{2\dot{\theta}}{\sin\theta}\left(\left(\dot{\varpi} + \dot{\phi}\cos\theta\right) - \dot{\phi}\cos\theta\right) - \frac{3}{2}\,\omega_{\rm orb}^2\, \sin 2(\psi - \phi) \\ &= \frac{2\dot{\theta}\dot{\varpi}}{\sin\theta} - \frac{3}{2}\,\omega_{\rm orb}^2\, \sin 2(\psi - \phi)\end{aligned}$$

□

### A.1.2 Frequency ordering & mean driven precession

We now introduce the ordering of frequencies. These follow from the approximation above, namely that:

$$|\dot{\varpi}| \gg |\omega_{\rm orb}| \gg |\Omega_0| \tag{A.5}$$

i.e., the ring rotates much faster than the companion orbits, and the companion orbits much faster than the (driven) precession.

Let us then use our equations of motion to reproduce the mean driven precession (equation 7c in Katz et al. (1982)). This is the frequency at which the normal to the ring will precess steadily if the ring is able to respond immediately to the tidal forcing.

**Result A.1.4** (Mean driven precession)**.** The mean driven precession frequency, obtained by averaging over the orbital motion, is:

$$\Omega_0 := \langle \dot{\phi} \rangle = -\frac{3}{4} \frac{\omega_{\rm orb}^2}{\dot{\varpi}} \cos\theta_0 \tag{A.6}$$

where $\theta_0$ is the inclination of the disc to the orbital plane, $\omega_{\rm orb}$ is the Keplerian orbital frequency, and $\dot{\varpi}$ is the rotational frequency of the disc.

*Proof.* Let $\theta = \theta_0 =$ constant, and hence $\dot{\theta} = \ddot{\theta} = 0$. Then, in Equation A.3b, we have:

$$\begin{aligned} 0 &= \dot{\phi}^2 \sin\theta_0 \cos\theta_0 - 2\dot{\phi} \sin\theta_0 \left( \dot{\varpi} + \dot{\phi} \cos\theta_0 \right) - \tfrac{3}{2}\, \omega_{\rm orb}^2 \, \sin 2\theta_0 \cos^2(\psi - \phi) \\ &\Rightarrow \dot{\phi} \sin\theta_0 \left( 2\dot{\varpi} + \dot{\phi} \cos\theta_0 \right) = -\tfrac{3}{2}\, \omega_{\rm orb}^2 \, \sin 2\theta_0 \cos^2(\psi - \phi)\,. \end{aligned}$$

Now, invoking $|\dot{\varpi}| \gg |\dot{\phi}|$, we can write:

$$\begin{aligned} \dot{\phi}\dot{\varpi}\, 2 \, \sin\theta_0 &= -\tfrac{3}{2}\, \omega_{\rm orb}^2 \, 2 \, \sin\theta_0 \cos\theta_0 \cos^2(\psi - \phi) \\ \Rightarrow \dot{\phi} &= -\frac{3}{2} \, \frac{\omega_{\rm orb}^2}{\dot{\varpi}} \, \cos\theta_0 \cos^2(\psi - \phi)\,. \end{aligned}$$

Finally, we average over the orbital phase $\psi$, using $\langle \cos^2(\psi - \phi) \rangle = \frac{1}{2}$ to obtain the result. □

This is in agreement with the Katz et al. (1982) result.

### A.1.3 Linearised equations of motion

We now consider small perturbations about the mean motion. Katz et al. (1982) allow for a slaved, rather than a driven precession – i.e., the precession occurs at $\Omega_{\rm s} \neq \Omega_0$. In the slaved disc picture, the companion star also undergoes precession, which can couple to the precessing accretion disc (see also Roberts (1974), Cherepashchuk (2002)). This complicates the algebra slightly, so we will precede without this generalisation.

We do, however, follow the approximation made by Katz et al. (1982) in keeping the first order terms in the expansion of the inertial terms in the equations of motion, but only retaining the zeroth order terms in the expansion of the tidal force terms. This assumes that the nutational motion makes only a small correction to the size of the tidal forcing terms.

**Result A.1.5.** If the precessing ring is perturbed from the mean motion by:

$$\theta = \theta_0 + \delta\theta$$

$$\phi = \phi_0 + \Omega_0 t + \delta\phi$$

then the perturbations obey:

$$\delta\theta = -\frac{\Omega_0 \tan\theta_0}{2\left(\omega_{\rm orb} - \Omega_0\right)} \cos 2\left[\left(\omega_{\rm orb} - \Omega_0\right) t + \psi_0 - \phi_0\right] \tag{A.7a}$$

$$\delta\phi = \frac{\Omega_0}{2\left(\omega_{\rm orb} - \Omega_0\right)} \sin 2\left[\left(\omega_{\rm orb} - \Omega_0\right) t + \psi_0 - \phi_0\right] \tag{A.7b}$$

*Proof.* The derivatives of $\theta$ and $\phi$ are:

$$\dot{\theta} = \dot{\delta\theta} \qquad \dot{\phi} = \Omega_0 + \dot{\delta\phi}$$

$$\ddot{\theta} = \ddot{\delta\theta} \qquad \ddot{\phi} = \ddot{\delta\phi}$$

We start with Equation A.3c:

$$\begin{aligned} \sin\theta\ddot{\phi} - 2\dot{\theta}\dot{\varpi} &= -\tfrac{3}{2}\,\omega_{\rm orb}^2 \sin\theta \sin 2\left(\psi - \phi\right) \\ \Rightarrow \left(\sin\theta_0 + \delta\theta\, \cos\theta_0\right)\ddot{\delta\phi} - 2\dot{\varpi}\,\dot{\delta\theta} &= -\tfrac{3}{2}\,\omega_{\rm orb}^2 \sin\theta_0 \sin 2\left(\psi - \Omega_0 t - \phi_0\right). \end{aligned}$$

Now, we neglect terms that are second order in small quantities, and we neglect the $\ddot{\delta\phi}$ term – we will shortly see that $|\dot{\varpi}\,\dot{\delta\theta}| \gg |\ddot{\delta\phi}|$, with the approximation justified because $\dot{\delta\phi} \sim \dot{\delta\theta} \sim \Omega_0$, and $\ddot{\delta\phi} \sim \Omega_0\omega_{\rm orb}$, leading to $\dot{\varpi} \gg \omega_{\rm orb}$, which is true from our frequency ordering (the disk rotates much more rapidly than the orbital period of the companion). Therefore,

$$\begin{aligned} \dot{\theta} &= \frac{3}{4}\frac{\omega_{\rm orb}^2}{\dot{\varpi}} \sin\theta_0 \sin 2\left(\psi - \Omega_0 t - \phi_0\right) \\ \Rightarrow \dot{\delta\theta} &= -\Omega_0 \tan\theta_0 \sin 2\left(\psi - \Omega_0 t - \phi_0\right) \end{aligned} \tag{A.8}$$

which agrees with Katz et al. (1982) (up to a minus sign). Now, we linearise Equation A.3b:

$$\ddot{\theta} - \tfrac{1}{2}\dot{\phi}^2 \sin 2\theta + 2\dot{\phi}\sin\theta\left(\dot{\varpi} + \dot{\phi}\cos\theta\right) = -\tfrac{3}{2}\,\omega_{\rm orb}^2\,\sin 2\theta\cos^2(\psi-\phi)\,.$$

Considering the terms on the left, we have $\dot{\phi} \sim \Omega_0$ (to be seen in a moment) and $\ddot{\theta} \sim \Omega_0\,\omega_{\rm orb}$ (from our expression for $\dot{\delta\theta}$ above). Recalling the frequency ordering, we have:

$$2\dot{\phi}\,\dot{\varpi}\,\sin\theta \gg \frac{1}{2}\dot{\phi}^2\sin 2\theta \gg \ddot{\theta}$$

and can therefore neglect all terms apart from $2\dot{\phi}\,\dot{\varpi}\,\sin\theta$. Inserting $\dot{\phi} = \dot{\delta\phi} + \Omega_0$, we find:

$$\begin{aligned}\left(\dot{\delta\phi} + \Omega_0\right)\dot{\varpi}\sin\theta_0 &= -\tfrac{3}{4}\omega_{\rm orb}^2\,\left(2\sin\theta_0\cos\theta_0\right)\,\tfrac{1}{2}\left(1+\cos 2\left(\psi - \Omega_0 t - \phi_0\right)\right)\\ \Rightarrow \dot{\delta\phi} + \Omega_0 &= \Omega_0\left(1+\cos 2\left(\psi-\Omega_0 t-\phi_0\right)\right)\end{aligned}$$

Cancelling out the mean precessional motion, we obtain the linearised equation:

$$\dot{\delta\phi} = \Omega_0\cos 2\left(\psi - \Omega_0 t - \phi_0\right) \tag{A.9}$$

The last step is to integrate the linearised equations of motion (Equations A.8 and A.9), taking $\psi = \psi_0 + \omega_{\rm orb} t$. This yields the final Result. □

## A.2 First-order velocity perturbations

**Result A.2.1.** Consider small perturbations to the polar, cone opening angle $\theta$, and the azimuthal, precession angle $\phi$ of the launch velocity vector of a precessing jet. If these perturbations are at twice the synodic frequency, then the first order perturbations to the three components of the launch velocity vector in the Observer's reference frame are:

$$\beta_{\tilde{x}}^{(1)} = A_{63}\cos\psi_{63} + A_{58}\cos\psi_{58} \tag{A.10a}$$

$$\beta_{\tilde{y}}^{(1)} = \frac{A_{63}}{\sin i_0}\left(\cos\chi_0\sin\psi_{63} + \cos i_0\sin\chi_0\cos\psi_{63}\right) - \frac{A_{58}}{\sin i_0}\left(\cos\chi_0\sin\psi_{58} - \cos i_0\sin\chi_0\cos\psi_{58}\right) \tag{A.10b}$$

$$\beta_{\tilde{z}}^{(1)} = \frac{A_{63}}{\sin i_0}\left(\sin\chi_0\sin\psi_{63} - \cos i_0\cos\chi_0\cos\psi_{63}\right) - \frac{A_{58}}{\sin i_0}\left(\sin\chi_0\sin\psi_{58} + \cos i_0\cos\chi_0\cos\psi_{58}\right) \tag{A.10c}$$

*Proof.* In Section 2.4, we showed that the components of the velocity vector may be written:

$$\beta_{\tilde{x}} = \beta\sin\Theta\cos\Phi\sin i_0 + \beta\cos\Theta\cos i_0 \tag{A.11a}$$

$$\beta_{\tilde{y}} = \beta\sin\Theta\cos\Phi\cos i_0\sin\chi_0 + \beta\sin\Theta\sin\Phi\cos\chi_0 - \beta\cos\Theta\sin i_0\sin\chi_0 \tag{A.11b}$$

$$\beta_{\tilde{z}} = -\beta\sin\Theta\cos\Phi\cos i_0\cos\chi_0 + \beta\sin\Theta\sin\Phi\sin\chi_0 + \beta\cos\Theta\sin i_0\cos\chi_0 \tag{A.11c}$$

where $\beta_{\tilde{x}}$ is the velocity component along the line-of-sight, and $\beta_{\tilde{y}}$ and $\beta_{\tilde{z}}$ are the velocity components in the directions of increasing Declination and Right Ascension respectively.

Let us consider small sinusoidal perturbations about the mean jet cone opening angle $\theta_0$ and the mean precession phase angle $\bar{\phi}$ as follows:

$$\theta = \theta_0 + \delta\theta = \theta_0 + \varepsilon_\theta\cos 2\left(\psi - \phi\right) \tag{A.12a}$$

$$\phi = \bar{\phi} + \delta\phi \ = \bar{\phi} + \varepsilon_\phi\sin 2\left(\psi - \phi\right) \tag{A.12b}$$

Recall the Taylor expansions of the sine and cosine functions:

$$\cos A = \cos A_0\cos\delta A - \sin A_0\sin\delta A = \cos A_0 - \delta A\,\sin A_0$$

$$\sin A = \sin A_0\cos\delta A + \cos A_0\sin\delta A = \sin A_0 + \delta A\,\cos A_0$$

As we will only work to first order, these allow us immediately to write $\delta\theta = \varepsilon_\theta \cos 2\left(\psi - \bar{\phi}\right)$ and $\delta\phi = \varepsilon_\phi \sin 2\left(\psi - \bar{\phi}\right)$

Then, recall also the trigonometric identities:

$$\cos A \cos B = \tfrac{1}{2}\left(\cos\left(A - B\right) + \cos\left(A + B\right)\right)$$
$$\sin A \sin B = \tfrac{1}{2}\left(\cos\left(A - B\right) - \cos\left(A + B\right)\right)$$
$$\sin A \cos B = \tfrac{1}{2}\left(\cos\left(A + B\right) + \cos\left(A - B\right)\right)$$
$$\cos A \sin B = \tfrac{1}{2}\left(\cos\left(A + B\right) - \cos\left(A - B\right)\right)$$

which we can use to write:

$$\delta\theta\ \cos\bar{\phi} = \varepsilon_\theta \cos 2\left(\psi - \bar{\phi}\right)\cos\bar{\phi} = \tfrac{1}{2}\,\varepsilon_\theta\ \left[\cos\left(2\psi - 3\bar{\phi}\right) + \cos\left(2\psi - \bar{\phi}\right)\right] \tag{A.13a}$$
$$\delta\phi\ \sin\bar{\phi} = \varepsilon_\phi \sin 2\left(\psi - \bar{\phi}\right)\sin\bar{\phi} = \tfrac{1}{2}\,\varepsilon_\phi\ \left[\cos\left(2\psi - 3\bar{\phi}\right) - \cos\left(2\psi - \bar{\phi}\right)\right] \tag{A.13b}$$
$$\delta\theta\ \sin\bar{\phi} = \varepsilon_\theta \cos 2\left(\psi - \bar{\phi}\right)\sin\bar{\phi} = \tfrac{1}{2}\,\varepsilon_\theta\ \left[\sin\left(2\psi - \bar{\phi}\right) - \sin\left(2\psi - 3\bar{\phi}\right)\right] \tag{A.13c}$$
$$\delta\phi\ \cos\bar{\phi} = \varepsilon_\phi \sin 2\left(\psi - \bar{\phi}\right)\cos\bar{\phi} = \tfrac{1}{2}\,\varepsilon_\phi\ \left[\sin\left(2\psi - \bar{\phi}\right) + \sin\left(2\psi - 3\bar{\phi}\right)\right] \tag{A.13d}$$

Now we will use these to expand each component of the velocity vector, keeping terms up to first order in the perturbed quantities. First, we write the line-of-sight component, $\beta_{\tilde{x}}$:

$$\begin{aligned}
\beta_{\tilde{x}} &= \beta\left(\sin\theta_0 + \delta\theta\ \cos\theta_0\right)\left(\cos\bar{\phi} - \delta\phi\ \sin\bar{\phi}\right)\sin i_0 + \beta\left(\cos\theta_0 - \delta\theta\ \sin\theta_0\right) \\
&= \beta\left(\sin\theta_0\cos\bar{\phi}\sin i_0 + \cos\theta_0\cos i_0\right) \\
&\quad + \beta\left[\delta\theta\left(\cos\theta_0\cos\bar{\phi}\sin i_0 - \sin\theta_0\cos i_0\right) - \delta\phi\sin\theta_0\sin\bar{\phi}\sin i_0\right] \\
&= \beta^{(0)}_{\tilde{x}} + \beta^{(1)}_{\tilde{x}}
\end{aligned} \tag{A.14}$$

where we have identified the first term as the unperturbed line-of-sight velocity component (Equation A.11a). Then, using Equations A.13a and A.13b, we can write the perturbation to the velocity

vector, $\beta_{\tilde{x}}^{(1)}$, as:

$$\begin{aligned}
\beta_{\tilde{x}}^{(1)} &= \beta \left[\cos\theta_0 \sin i_0 \, \delta\theta \cos\bar{\phi} - \delta\theta \sin\theta_0 \cos i_0 - \sin\theta_0 \sin i_0 \, \delta\phi \sin\bar{\phi}\right] \\
\Rightarrow \beta_{\tilde{x}}^{(1)} &= \tfrac{1}{2}\,\beta\,\varepsilon_\theta \, \cos\theta_0 \sin i_0 \, \left(\cos\left(2\psi - 3\bar{\phi}\right) + \cos\left(2\psi - \bar{\phi}\right)\right) \\
&\quad - \beta\,\varepsilon_\theta \, \cos i_0 \sin\theta_0 \cos\left(2\psi - 2\bar{\phi}\right) \\
&\quad - \tfrac{1}{2}\,\beta\,\varepsilon_\phi \, \sin\theta_0 \sin i_0 \, \left(\cos\left(2\psi - 3\bar{\phi}\right) - \cos\left(2\psi - \bar{\phi}\right)\right) \\
\Rightarrow \beta_{\tilde{x}}^{(1)} &= \left[\tfrac{1}{2}\beta \sin i_0 \, (\varepsilon_\theta \cos\theta_0 - \varepsilon_\phi \sin\theta_0)\right] \cos\left(2\psi - 3\bar{\phi}\right) \\
&\quad + \left[-\beta\,\varepsilon_\theta \cos i_0 \sin\theta_0\right] \cos\left(2\psi - 2\bar{\phi}\right) \\
&\quad + \left[\tfrac{1}{2}\beta \sin i_0 \, (\varepsilon_\theta \cos\theta_0 + \varepsilon_\phi \sin\theta_0)\right] \cos\left(2\psi - \bar{\phi}\right) \\
\Rightarrow \beta_{\tilde{x}}^{(1)} &= A_- \cos\left(2\psi - 3\bar{\phi}\right) + A_0 \cos\left(2\psi - 2\bar{\phi}\right) + A_+ \cos\left(2\psi - \bar{\phi}\right) \qquad \text{(A.15)}
\end{aligned}$$

where:

$$A_- = \tfrac{1}{2}\beta \sin i_0 \, (\varepsilon_\theta \cos\theta_0 - \varepsilon_\phi \sin\theta_0) \qquad \text{(A.16a)}$$

$$A_0 = -\beta\varepsilon_\theta \cos i_0 \sin\theta_0 \qquad \text{(A.16b)}$$

$$A_+ = \tfrac{1}{2}\beta \sin i_0 \, (\varepsilon_\theta \cos\theta_0 + \varepsilon_\phi \sin\theta_0) \qquad \text{(A.16c)}$$

This reproduces equations 20 and 21 of Katz et al. (1982), with $A_-$ and $A_+$ here corresponding to $A_{58}$ and $A_{63}$ in that paper, and representing the amplitudes of the line-of-sight velocity variation at 5.83 d and 6.28 d. We also include $A_0$, the amplitude of the variation with the synodic period, 6.06 d.

Vermeulen (1989) states, without derivation and with a sign error, the result of extending this to the perturbations in the other two velocity components, $\beta_{\tilde{y}}^{(1)}$ and $\beta_{\tilde{z}}^{(1)}$. The corrected derivations are as follows.

First, using Equation A.11b for $\beta_{\tilde{y}}$, we have:

$$\begin{aligned}
\beta_{\tilde{y}} &= \beta\left(\sin\theta_0 + \delta\theta\,\cos\theta_0\right)\left(\cos\bar{\phi} - \delta\phi\,\sin\bar{\phi}\right)\cos i_0 \sin\chi_0 \\
&\quad + \beta\left(\sin\theta_0 + \delta\theta\,\cos\theta_0\right)\left(\sin\bar{\phi} + \delta\phi\,\cos\bar{\phi}\right)\cos\chi_0 \\
&\quad - \beta\left(\cos\theta_0 - \delta\theta\,\sin\theta_0\right)\sin i_0 \sin\chi_0 \\
&= \beta\sin\theta_0\cos\bar{\phi}\sin\chi_0\cos i_0 + \beta\sin\theta_0\sin\bar{\phi}\cos\chi_0 - \cos\theta_0\sin i_0\sin\chi_0 \\
&\quad + \beta\left(\delta\theta\,\cos\bar{\phi}\cos\theta_0 - \delta\phi\,\sin\bar{\phi}\sin\theta_0\right)\sin\chi_0\cos i_0 \\
&\quad + \beta\left(\delta\theta\,\sin\bar{\phi}\cos\theta_0 + \delta\phi\,\cos\bar{\phi}\sin\theta_0\right)\cos\chi_0 \\
&\quad + \beta\,\delta\theta\,\sin\theta_0\sin i_0\sin\chi_0 \\
&= \beta^{(0)}_{\tilde{y}} + \beta^{(1)}_{\tilde{y}}\,,
\end{aligned} \tag{A.17}$$

where, using Equations A.13, the pertubation term, $\beta^{(1)}_{\tilde{y}}$, is

$$\begin{aligned}
\beta^{(1)}_{\tilde{y}} &= \beta\Big(\tfrac{1}{2}\,\varepsilon_\theta\,\left[\cos\left(2\psi - 3\bar{\phi}\right) + \cos\left(2\psi - \bar{\phi}\right)\right]\cos\theta_0 \\
&\qquad - \tfrac{1}{2}\,\varepsilon_\phi\,\left[\cos\left(2\psi - 3\bar{\phi}\right) - \cos\left(2\psi - \bar{\phi}\right)\right]\sin\theta_0\Big)\sin\chi_0\cos i_0 \\
&\quad + \beta\Big(\tfrac{1}{2}\,\varepsilon_\theta\,\left[\sin\left(2\psi - \bar{\phi}\right) - \sin\left(2\psi - 3\bar{\phi}\right)\right]\cos\theta_0 + \\
&\qquad + \tfrac{1}{2}\,\varepsilon_\phi\,\left[\sin\left(2\psi - \bar{\phi}\right) + \sin\left(2\psi - 3\bar{\phi}\right)\right]\sin\theta_0\Big)\cos\chi_0 \\
&\quad + \beta\,\tfrac{1}{2}\,\varepsilon_\theta\,\sin\theta_0\sin i_0\sin\chi_0 \\
&= \tfrac{1}{2}\beta\left(\varepsilon_\theta\cos\theta_0 - \varepsilon_\phi\sin\theta_0\right)\cos\left(2\psi - 3\bar{\phi}\right)\sin\chi_0\cos i_0 \\
&\quad + \tfrac{1}{2}\beta\left(\varepsilon_\theta\cos\theta_0 + \varepsilon_\phi\sin\theta_0\right)\cos\left(2\psi - \bar{\phi}\right)\sin\chi_0\cos i_0 \\
&\quad + \tfrac{1}{2}\beta\left(\varepsilon_\theta\cos\theta_0 + \varepsilon_\phi\sin\theta_0\right)\sin\left(2\psi - \bar{\phi}\right)\cos\chi_0 \\
&\quad - \tfrac{1}{2}\beta\left(\varepsilon_\theta\cos\theta_0 - \varepsilon_\phi\sin\theta_0\right)\sin\left(2\psi - 3\bar{\phi}\right)\cos\chi_0 \\
&\quad + \beta\,\varepsilon_\theta\cos\left(2\psi - 2\bar{\phi}\right)\sin\theta_0\sin i_0\sin\chi_0 \\
&= \frac{A_-}{\sin i_0}\left(\cos\left(2\psi - 3\bar{\phi}\right)\sin\chi_0\cos i_0 - \sin\left(2\psi - 3\bar{\phi}\right)\cos\chi_0\right) \\
&\quad + \frac{A_+}{\sin i_0}\left(\cos\left(2\psi - \bar{\phi}\right)\sin\chi_0\cos i_0 + \sin\left(2\psi - \bar{\phi}\right)\cos\chi_0\right) \\
&\quad - A_0\cos\left(2\psi - 2\bar{\phi}\right)\tan i_0\sin\chi_0
\end{aligned} \tag{A.18}$$

which agrees with Vermeulen (1989) up to the convention on $\chi_0$ and an overall minus sign. Lastly,

the $\beta_{\tilde{z}}$ component yields:

$$\begin{aligned}
\beta_{\tilde{z}} = & -\beta\left(\sin\theta_0 + \delta\theta\,\cos\theta_0\right)\left(\cos\bar{\phi} - \delta\phi\,\sin\bar{\phi}\right)\cos i_0\cos\chi_0 \\
& +\beta\left(\sin\theta_0 + \delta\theta\,\cos\theta_0\right)\left(\sin\bar{\phi} + \delta\phi\,\cos\bar{\phi}\right)\sin\chi_0 \\
& +\beta\left(\cos\theta_0 - \delta\theta\,\sin\theta_0\right)\sin i_0\cos\chi_0 \\
= & -\beta\sin\theta_0\cos\bar{\phi}\cos\chi_0\cos i_0 + \beta\sin\theta_0\sin\bar{\phi}\sin\chi_0 + \cos\theta_0\sin i_0\cos\chi_0 \\
& +\beta\left(-\delta\theta\,\cos\bar{\phi}\cos\theta_0 + \delta\phi\,\sin\bar{\phi}\sin\theta_0\right)\cos\chi_0\cos i_0 \\
& +\beta\left(\delta\theta\,\sin\bar{\phi}\cos\theta_0 + \delta\phi\,\cos\bar{\phi}\sin\theta_0\right)\sin\chi_0 \\
& -\beta\,\delta\theta\,\sin\theta_0\sin i_0\sin\chi_0 \\
= & \beta_{\tilde{y}}^{(0)} + \beta_{\tilde{y}}^{(1)}\,,
\end{aligned} \tag{A.19}$$

where again we can use Equations A.13 to write the pertubation term, $\beta_{\tilde{z}}^{(1)}$, as

$$\begin{aligned}
\beta_{\tilde{z}}^{(1)} = & \beta\Big(\tfrac{1}{2}\,\varepsilon_\phi\,\left[\cos\left(2\psi - 3\bar{\phi}\right) - \cos\left(2\psi - \bar{\phi}\right)\right]\sin\theta_0 \\
& \qquad -\tfrac{1}{2}\,\varepsilon_\theta\,\left[\cos\left(2\psi - 3\bar{\phi}\right) + \cos\left(2\psi - \bar{\phi}\right)\right]\cos\theta_0\Big)\cos\chi_0\cos i_0 \\
& +\beta\Big(\tfrac{1}{2}\,\varepsilon_\theta\,\left[\sin\left(2\psi - \bar{\phi}\right) - \sin\left(2\psi - 3\bar{\phi}\right)\right]\cos\theta_0 + \\
& \qquad +\tfrac{1}{2}\,\varepsilon_\phi\,\left[\sin\left(2\psi - \bar{\phi}\right) + \sin\left(2\psi - 3\bar{\phi}\right)\right]\sin\theta_0\Big)\sin\chi_0 \\
& -\beta\,\tfrac{1}{2}\,\varepsilon_\theta\,\sin\theta_0\sin i_0\cos\chi_0 \\
= & \tfrac{1}{2}\beta\left(-\varepsilon_\theta\cos\theta_0 + \varepsilon_\phi\sin\theta_0\right)\cos\left(2\psi - 3\bar{\phi}\right)\cos\chi_0\cos i_0 \\
& -\tfrac{1}{2}\beta\left(\varepsilon_\theta\cos\theta_0 + \varepsilon_\phi\sin\theta_0\right)\cos\left(2\psi - \bar{\phi}\right)\cos\chi_0\cos i_0 \\
& +\tfrac{1}{2}\beta\left(\varepsilon_\theta\cos\theta_0 + \varepsilon_\phi\sin\theta_0\right)\sin\left(2\psi - \bar{\phi}\right)\sin\chi_0 \\
& -\tfrac{1}{2}\beta\left(\varepsilon_\theta\cos\theta_0 - \varepsilon_\phi\sin\theta_0\right)\sin\left(2\psi - 3\bar{\phi}\right)\sin\chi_0 \\
& -\beta\,\varepsilon_\theta\cos\left(2\psi - 2\bar{\phi}\right)\sin\theta_0\sin i_0\sin\chi_0 \\
= & -\frac{A_-}{\sin i_0}\left(\cos\left(2\psi - 3\bar{\phi}\right)\cos\chi_0\cos i_0 + \sin\left(2\psi - 3\bar{\phi}\right)\sin\chi_0\right) \\
& -\frac{A_+}{\sin i_0}\left(\cos\left(2\psi - \bar{\phi}\right)\cos\chi_0\cos i_0 - \sin\left(2\psi - \bar{\phi}\right)\sin\chi_0\right) \\
& +A_0\cos\left(2\psi - 2\bar{\phi}\right)\tan i_0\cos\chi_0
\end{aligned} \tag{A.20}$$

The final steps to complete the proof are to set $A_0 = 0$ (determined by experiment), and to

introduce

$$\psi_{58} := 2\psi - 3\phi = (2\omega_{\rm orb} + 3\,|\omega_{\rm pre}|)\,t + \text{constant}$$

$$\psi_{58} := 2\psi - \phi \;\; = (2\omega_{\rm orb} + |\omega_{\rm pre}|)\,t + \text{constant}$$

Inserting these into Equations A.15, A.18, and A.20 completes the proof.

□

# Bibliography

G. O. Abell and B. Margon. A kinematic model for SS433. *Nature*, 279:701–703, June 1979. doi: 10.1038/279701a0.

D. Anderson, M. Bonnedal, and M. Lisak. Effects of magnetic field of self-similar plasma expansion into vacuum. *Phys. Scr*, 22:507–509, January 1980. doi: 10.1088/0031-8949/22/5/015.

S. F. Anderson, B. Margon, and S. A. Grandi. Precession instability in SS 433. *ApJ*, 273:697–701, October 1983. doi: 10.1086/161404.

É. A. Antokhina, E. V. Seifina, and A. M. Cherepashchuk. Analysis of x-ray eclipses in SS 433. *Soviet Ast.*, 36:143, April 1992.

K. Atapin, S. Fabrika, A. Medvedev, and A. Vinokurov. X-ray variability of SS 433: effects of the supercritical accretion disc. *MNRAS*, 446:893–910, January 2015. doi: 10.1093/mnras/stu2134.

D. L. Band. Comparison of Einstein and EXOSAT X-ray observations of SS 433. *ApJ*, 336: 937–948, January 1989. doi: 10.1086/167063.

M. C. Begelman, R. D. Blandford, and M. J. Rees. Theory of extragalactic radio sources. *Reviews of Modern Physics*, 56:255–351, April 1984. doi: 10.1103/RevModPhys.56.255.

M. C. Begelman, A. R. King, and J. E. Pringle. The nature of SS433 and the ultraluminous X-ray sources. *MNRAS*, 370:399–404, July 2006. doi: 10.1111/j.1365-2966.2006.10469.x.

T. Belloni. "states and transitions in black hole binaries". In T. "Belloni, editor, *"The Jet Paradigm: From Microquasars to Quasars"*, pages 53–84, Berlin, Heidelberg, 2010. Springer Berlin Heidelberg. ISBN 978-3-540-76937-8. doi: 10.1007/978-3-540-76937-8_3. URL `http://dx.doi.org/10.1007/978-3-540-76937-8_3`.

T. M. Belloni. Black-hole states in external galaxies. *Astronomische Nachrichten*, 332:324, May 2011. doi: 10.1002/asna.201011492.

V. S. Beskin. *MHD Flows in Compact Astrophysical Objects*. Springer-Verlag Berlin Heidelberg, 2010. doi: 10.1007/978-3-642-01290-7.

J. Binney and S. Tremaine. *Galactic Dynamics: Second Edition*. Princeton University Press, 2008.

R. D. Blandford and M. C. Begelman. On the fate of gas accreting at a low rate on to a black hole. *MNRAS*, 303:L1–L5, February 1999. doi: 10.1046/j.1365-8711.1999.02358.x.

R. D. Blandford and A. Königl. Relativistic jets as compact radio sources. *ApJ*, 232:34–48, August 1979. doi: 10.1086/157262.

K. M. Blundell and M. G. Bowler. Symmetry in the Changing Jets of SS 433 and Its True Distance from Us. *ApJ*, 616:L159–L162, December 2004. doi: 10.1086/426542.

K. M. Blundell and M. G. Bowler. Jet Velocity in SS 433: Its Anticorrelation with Precession-Cone Angle and Dependence on Orbital Phase. *ApJ*, 622:L129–L132, April 2005. doi: 10.1086/429663.

K. M. Blundell and P. Hirst. Jet Propulsion of Wind Ejecta from a Major Flare in the Black Hole Microquasar SS433. *ApJ*, 735:L7, July 2011. doi: 10.1088/2041-8205/735/1/L7.

K. M. Blundell and S. Rawlings. The Spectra and Energies of Classical Double Radio Lobes. *AJ*, 119:1111–1122, March 2000. doi: 10.1086/301254.

K. M. Blundell, S. Rawlings, and C. J. Willott. The Nature and Evolution of Classical Double Radio Sources from Complete Samples. *AJ*, 117:677–706, February 1999. doi: 10.1086/300721.

K. M. Blundell, A. J. Mioduszewski, T. W. B. Muxlow, P. Podsiadlowski, and M. P. Rupen. Images of an Equatorial Outflow in SS 433. *ApJ*, 562:L79–L82, November 2001. doi: 10.1086/324573.

K. M. Blundell, A. C. Fabian, C. S. Crawford, M. C. Erlund, and A. Celotti. Discovery of the Low-Energy Cutoff in a Powerful Giant Radio Galaxy. *ApJ*, 644:L13–L16, June 2006. doi: 10.1086/504839.

K. M. Blundell, M. G. Bowler, and L. Schmidtobreick. Fluctuations and symmetry in the speed and direction of the jets of SS 433 on different timescales. *A&A*, 474:903–910, November 2007. doi: 10.1051/0004-6361:20077924.

K. M. Blundell, M. G. Bowler, and L. Schmidtobreick. SS 433: Observation of the Circumbinary Disk and Extraction of the System Mass. *ApJ*, 678:L47–L50, May 2008. doi: 10.1086/588027.

K. M. Blundell, L. Schmidtobreick, and S. Trushkin. SS433's accretion disc, wind and jets: before, during and after a major flare. *MNRAS*, 417:2401–2410, November 2011. doi: 10.1111/j.1365-2966.2011.18785.x.

S. Blundell and K. M. Blundell. *Concepts in Thermal Physics*. Oxford University Press, 2010. ISBN 0-19-956209-1.

M. G. Bowler. SS 433: the accretion disk revealed in H$\alpha$. *A&A*, 516:A24, June 2010a. doi: 10.1051/0004-6361/200913859.

M. G. Bowler. Interpretation of observations of the circumbinary disk of SS 433. *A&A*, 521:A81, October 2010b. doi: 10.1051/0004-6361/201014711.

A. H. Bridle, D. H. Hough, C. J. Lonsdale, J. O. Burns, and R. A. Laing. Deep VLA imaging of twelve extended 3CR quasars. *AJ*, 108:766–820, September 1994. doi: 10.1086/117112.

D. S. Briggs. *High Fidelity Deconvolution of Moderately Resolved Sources*. PhD thesis, New Mexico Institute of Mining and Technology, 1995.

W. Brinkmann, H. H. Fink, S. Massaglia, G. Bodo, and A. Ferrari. The thermal evolution of the jets in SS 433. *A&A*, 196:313–326, May 1988.

W. Brinkmann, N. Kawai, and M. Matsuoka. SS433 - The puzzle continues. *A&A*, 218:L13–L16, July 1989.

W. Brinkmann, N. Kawai, M. Matsuoka, and H. H. Fink. The X-ray emission of SS 433. *A&A*, 241:112–126, January 1991.

W. Brinkmann, T. Kotani, and N. Kawai. XMM-Newton observations of SS 433 I. EPIC spectral analysis. *A&A*, 431:575–586, February 2005. doi: 10.1051/0004-6361:20041768.

B. W. Carroll and D. A. Ostlie. *An Introduction to Modern Astrophysics: Pearson New International Edition*. Pearson Education, 3 edition, 2014. ISBN 9781292022932.

P. Charles, W. Clarkson, R. Cornelisse, and C. Shih. Observational properties of accretion discs: Precessing and warped? *New A Rev.*, 51:768–774, May 2008. doi: 10.1016/j.newar.2008.03.025.

A. Cherepashchuk. Observational Manifestations of Precession of Accretion Disk in the SS 433 Binary System. *Space Sci. Rev.*, 102:23–35, October 2002.

A. M. Cherepashchuk, R. A. Sunyaev, K. A. Postnov, E. A. Antokhina, and S. V. Molkov. Peculiar nature of hard X-ray eclipse in SS433 from INTEGRAL observations. *MNRAS*, 397:479–487, July 2009. doi: 10.1111/j.1365-2966.2009.14948.x.

A. M. Cherepashchuk, R. A. Sunyaev, S. V. Molkov, E. A. Antokhina, K. A. Postnov, and A. I. Bogomazov. INTEGRAL observations of SS433: system's parameters and nutation of supercritical accretion disc. *MNRAS*, 436:2004–2013, December 2013. doi: 10.1093/mnras/stt1715.

B. G. Clark. Coherence in Radio Astronomy. In G. B. Taylor, C. L. Carilli, and R. A. Perley, editors, *Synthesis Imaging in Radio Astronomy II*, volume 180 of *Astronomical Society of the Pacific Conference Series*, page 1, 1999.

D. H. Clark. *The Quest for SS433*. New York, N.Y. : Viking, 1985., 1985.

D. H. Clark and P. Murdin. An unusual emission-line star/X-ray source/radio star, possibly associated with an SNR. *Nature*, 276:44, November 1978. doi: 10.1038/276044a0.

G. W. Collins and R. W. Scher. A revised dynamical model for SS433 and the nature of the system. *MNRAS*, 336:1011–1020, November 2002. doi: 10.1046/j.1365-8711.2002.05844.x.

G. W. Collins, II and G. H. Newsom. SS 433. *IAU Circ.*, 3547, December 1980.

G. W. Collins, II and G. H. Newsom. A dynamical model for SS 433. *ApJ*, 308:144–151, September 1986. doi: 10.1086/164485.

G. W. Collins, II, G. H. Newsom, and R. N. Boyd. An interpretation of the SS433 phenomenon. *Ap&SS*, 76:417–440, May 1981. doi: 10.1007/BF00687504.

S. Corbel, R. P. Fender, A. K. Tzioumis, M. Nowak, V. McIntyre, P. Durouchoux, and R. Sood. Coupling of the X-ray and radio emission in the black hole candidate and compact jet source GX 339-4. *A&A*, 359:251–268, July 2000.

S. Corbel, H. Aussel, J. W. Broderick, P. Chanial, M. Coriat, A. J. Maury, M. M. Buxton, J. A. Tomsick, A. K. Tzioumis, S. Markoff, J. Rodriguez, C. D. Bailyn, C. Brocksopp, R. P. Fender, P. O. Petrucci, M. Cadolle-Bel, D. Calvelo, and L. Harvey-Smith. Formation of the compact jets in the black hole GX 339-4. *MNRAS*, 431:L107–L111, April 2013. doi: 10.1093/mnrasl/slt018.

T. Cornwell, R. Braun, and D. S. Briggs. Deconvolution. In G. B. Taylor, C. L. Carilli, and R. A.

Perley, editors, *Synthesis Imaging in Radio Astronomy II*, volume 180 of *Astronomical Society of the Pacific Conference Series*, page 151, 1999.

W. D. Cotton. Fringe Fitting. In J. A. Zensus, P. J. Diamond, and P. J. Napier, editors, *Very Long Baseline Interferometry and the VLBA*, volume 82 of *Astronomical Society of the Pacific Conference Series*, page 189, 1995.

D. Crampton and J. B. Hutchings. The SS 433 binary system. *ApJ*, 251:604–610, December 1981. doi: 10.1086/159505.

D. Crampton, A. P. Cowley, and J. B. Hutchings. The probable binary nature of SS 433. *ApJ*, 235:L131–L135, February 1980. doi: 10.1086/183176.

M. Díaz Trigo, J. C. A. Miller-Jones, S. Migliari, J. W. Broderick, and T. Tzioumis. Baryons in the relativistic jets of the stellar-mass black-hole candidate 4U1630-47. *Nature*, 504:260–262, December 2013. doi: 10.1038/nature12672.

J. M. Dickey, S. R. Kulkarni, J. H. van Gorkom, and C. E. Heiles. A survey of H I absorption at low latitudes. *ApJS*, 53:591–621, November 1983. doi: 10.1086/190903.

S. Doolin and K. M. Blundell. The Precession of SS433's Radio Ruff on Long Timescales. *ApJ*, 698:L23–L26, June 2009. doi: 10.1088/0004-637X/698/1/L23.

S. Doolin and K. M. Blundell. The dynamics and stability of circumbinary orbits. *MNRAS*, 418: 2656–2668, December 2011. doi: 10.1111/j.1365-2966.2011.19657.x.

G. M. Dubner, M. Holdaway, W. M. Goss, and I. F. Mirabel. A High-Resolution Radio Study of the W50-SS 433 System and the Surrounding Medium. *AJ*, 116:1842–1855, October 1998. doi: 10.1086/300537.

P. P. Eggleton. Approximations to the radii of Roche lobes. *ApJ*, 268:368, May 1983. doi: 10.1086/160960.

S. S. Eikenberry, P. B. Cameron, B. W. Fierce, D. M. Kull, D. H. Dror, J. R. Houck, and B. Margon. Twenty Years of Timing SS 433. *ApJ*, 561:1027–1033, November 2001. doi: 10.1086/323380.

S. Fabrika. The jets and supercritical accretion disk in SS433. *Astrophysics and Space Physics Reviews*, 12:1–152, 2004.

S. Fabrika, Y. Ueda, A. Vinokurov, O. Sholukhova, and M. Shidatsu. Supercritical accretion

disks in ultraluminous X-ray sources and SS 433. *Nature Physics*, 11:551–553, July 2015. doi: 10.1038/nphys3348.

S. N. Fabrika. The Supercritical Accretion Disk of SS 433. *Ap&SS*, 252:439–450, 1997.

S. N. Fabrika and L. V. Bychkova. The mass function of SS 433. *A&A*, 240:L5–L7, December 1990.

H. Falcke, E. Körding, and S. Markoff. A scheme to unify low-power accreting black holes. Jet-dominated accretion flows and the radio/X-ray correlation. *A&A*, 414:895–903, February 2004. doi: 10.1051/0004-6361:20031683.

R. Fender. "'disc–jet' coupling in black hole x-ray binaries and active galactic nuclei". In T. Belloni, editor, *"The Jet Paradigm: From Microquasars to Quasars"*, pages 115–142, Berlin, Heidelberg, 2010. Springer Berlin Heidelberg. ISBN 978-3-540-76937-8. doi: 10.1007/978-3-540-76937-8_5. URL `http://dx.doi.org/10.1007/978-3-540-76937-8_5`.

R. Fender and T. Belloni. GRS 1915+105 and the Disc-Jet Coupling in Accreting Black Hole Systems. *ARA&A*, 42:317–364, September 2004. doi: 10.1146/annurev.astro.42.053102.134031.

R. Fender and T. Belloni. Stellar-Mass Black Holes and Ultraluminous X-ray Sources. *Science*, 337:540, August 2012. doi: 10.1126/science.1221790.

R. Fender and T. Muñoz-Darias. The Balance of Power: Accretion and Feedback in Stellar Mass Black Holes. In F. Haardt, V. Gorini, U. Moschella, A. Treves, and M. Colpi, editors, *Lecture Notes in Physics, Berlin Springer Verlag*, volume 905 of *Lecture Notes in Physics, Berlin Springer Verlag*, page 65, 2016. doi: 10.1007/978-3-319-19416-5_3.

R. Fender, S. Corbel, T. Tzioumis, V. McIntyre, D. Campbell-Wilson, M. Nowak, R. Sood, R. Hunstead, A. Harmon, P. Durouchoux, and W. Heindl. Quenching of the Radio Jet during the X-Ray High State of GX 339-4. *ApJ*, 519:L165–L168, July 1999. doi: 10.1086/312128.

R. P. Fender. Powerful jets from black hole X-ray binaries in low/hard X-ray states. *MNRAS*, 322:31–42, March 2001. doi: 10.1046/j.1365-8711.2001.04080.x.

R. P. Fender. Uses and limitations of relativistic jet proper motions: lessons from Galactic microquasars. *MNRAS*, 340:1353–1358, April 2003. doi: 10.1046/j.1365-8711.2003.06386.x.

R. P. Fender, T. M. Belloni, and E. Gallo. Towards a unified model for black hole X-ray binary jets. *MNRAS*, 355:1105–1118, December 2004. doi: 10.1111/j.1365-2966.2004.08384.x.

E. Filippova, M. Revnivtsev, S. Fabrika, K. Postnov, and E. Seifina. Diagnostics of SS433 with the RXTE. *A&A*, 460:125–131, December 2006. doi: 10.1051/0004-6361:20054784.

D. Foreman-Mackey, D. W. Hogg, D. Lang, and J. Goodman. emcee: The MCMC Hammer. *PASP*, 125:306–312, March 2013. doi: 10.1086/670067.

J. Frank, A. R. King, and D. J. Raine. *Accretion Power in Astrophysics*. Cambridge University Press, 3 edition, 2002. ISBN 0521620538.

Y. Fuchs, L. Koch-Miramond, and P. Abraham. A 2.4-80,mum Spectrophotometric Study of SS,433 with ISO. In P. O. Slane and B. M. Gaensler, editors, *Neutron Stars in Supernova Remnants*, volume 271 of *Astronomical Society of the Pacific Conference Series*, page 369, 2002.

E. Gallo, R. P. Fender, and G. G. Pooley. A universal radio-X-ray correlation in low/hard state black hole binaries. *MNRAS*, 344:60–72, September 2003. doi: 10.1046/j.1365-8711.2003.06791.x.

J. A. García, J. F. Steiner, J. E. McClintock, R. A. Remillard, V. Grinberg, and T. Dauser. X-Ray Reflection Spectroscopy of the Black Hole GX 339–4: Exploring the Hard State with Unprecedented Sensitivity. *ApJ*, 813:84, November 2015. doi: 10.1088/0004-637X/813/2/84.

F. García-Rubio, A. Ruocco, and J. Sanz. Plasma expansion into a vacuum with an arbitrarily oriented external magnetic field. *Physics of Plasmas*, 23(1):012103, January 2016. doi: 10.1063/1.4939476.

N. Gehrels, G. Chincarini, P. Giommi, K. O. Mason, J. A. Nousek, A. A. Wells, N. E. White, S. D. Barthelmy, D. N. Burrows, L. R. Cominsky, K. C. Hurley, F. E. Marshall, P. Mészáros, P. W. A. Roming, L. Angelini, L. M. Barbier, T. Belloni, S. Campana, P. A. Caraveo, M. M. Chester, O. Citterio, T. L. Cline, M. S. Cropper, J. R. Cummings, A. J. Dean, E. D. Feigelson, E. E. Fenimore, D. A. Frail, A. S. Fruchter, G. P. Garmire, K. Gendreau, G. Ghisellini, J. Greiner, J. E. Hill, S. D. Hunsberger, H. A. Krimm, S. R. Kulkarni, P. Kumar, F. Lebrun, N. M. Lloyd-Ronning, C. B. Markwardt, B. J. Mattson, R. F. Mushotzky, J. P. Norris, J. Osborne, B. Paczynski, D. M. Palmer, H.-S. Park, A. M. Parsons, J. Paul, M. J. Rees, C. S. Reynolds, J. E. Rhoads, T. P. Sasseen, B. E. Schaefer, A. T. Short, A. P. Smale, I. A. Smith, L. Stella, G. Tagliaferri, T. Takahashi, M. Tashiro, L. K. Townsley, J. Tueller, M. J. L. Turner, M. Vietri, W. Voges, M. J. Ward, R. Willingale, F. M. Zerbi, and W. W. Zhang. The Swift Gamma-Ray Burst Mission. *ApJ*, 611:1005–1020, August 2004. doi: 10.1086/422091.

M. Gierliński, A. A. Zdziarski, J. Poutanen, P. S. Coppi, K. Ebisawa, and W. N. Johnson. Radiation mechanisms and geometry of Cygnus X-1 in the soft state. *MNRAS*, 309:496–512, October 1999. doi: 10.1046/j.1365-8711.1999.02875.x.

D. R. Gies, W. Huang, and M. V. McSwain. The Spectrum of the Mass Donor Star in SS 433. *ApJ*, 578:L67–L70, October 2002a. doi: 10.1086/344436.

D. R. Gies, M. V. McSwain, R. L. Riddle, Z. Wang, P. J. Wiita, and D. W. Wingert. The Spectral Components of SS 433. *ApJ*, 566:1069–1083, February 2002b. doi: 10.1086/338335.

P. T. Goodall, F. Alouani-Bibi, and K. M. Blundell. When microquasar jets and supernova collide: hydrodynamically simulating the SS 433-W 50 interaction. *MNRAS*, 414:2838–2859, July 2011. doi: 10.1111/j.1365-2966.2011.18388.x.

J. Goodman and J. Weare. Ensemble samplers with affine invariance. *Communications in Applied Mathematics and Computational Science*, 5:65–80, 2010. doi: 10.2140/camcos.2010.5.65.

V. P. Goranskii, V. F. Esipov, and A. M. Cherepashchuk. Optical variability of SS 433 in 1978-1996. *Astronomy Reports*, 42:209–228, March 1998.

V. Goranskij. Photometric Mass Estimate for the Compact Component of SS 433: And Yet It Is a Neutron Star. *Peremennye Zvezdy*, 31, October 2011.

E. W. Greisen. AIPS, the VLA, and the VLBA. *Information Handling in Astronomy - Historical Vistas*, 285:109, March 2003. doi: 10.1007/0-306-48080-8_7.

E. W. Greisen, K. Spekkens, and G. A. van Moorsel. Aperture Synthesis Observations of the Nearby Spiral NGC 6503: Modelling the Thin and Thick H I Disks. *AJ*, 137:4718–4733, June 2009. doi: 10.1088/0004-6256/137/6/4718.

D. E. Harris, C. L. Carilli, and R. A. Perley. X-ray emission from the radio hotspots of Cygnus A. *Nature*, 367:713–716, February 1994. doi: 10.1038/367713a0.

T. C. Hillwig and D. R. Gies. Spectroscopic Observations of the Mass Donor Star in SS 433. *ApJ*, 676:L37, March 2008. doi: 10.1086/587140.

T. C. Hillwig, D. R. Gies, W. Huang, M. V. McSwain, M. A. Stark, A. van der Meer, and L. Kaper. Identification of the Mass Donor Star's Spectrum in SS 433. *ApJ*, 615:422–431, November 2004. doi: 10.1086/423927.

R. M. Hjellming and K. J. Johnston. An analysis of the proper motions of SS 433 radio jets. *ApJ*, 246:L141–L145, June 1981. doi: 10.1086/183571.

J. A. Högbom. Aperture Synthesis with a Non-Regular Distribution of Interferometer Baselines. *A&AS*, 15:417, June 1974.

J. D. Hunter. Matplotlib: A 2d graphics environment. *Computing In Science & Engineering*, 9 (3):90–95, 2007.

R. M. Jeffrey, K. M. Blundell, S. A. Trushkin, and A. J. Mioduszewski. Fast launch speeds in radio flares, from a new determination of the intrinsic motions of SS 433's jet bolides. *MNRAS*, 461:312–320, September 2016. doi: 10.1093/mnras/stw1322.

J. I. Katz. Thirty-five-day Periodicity in Her X-1. *Nature Physical Science*, 246:87–89, December 1973. doi: 10.1038/physci246087a0.

J. I. Katz and T. Piran. Jitter in SS 433-A clue to the collimation mechanism. *Astrophys. Lett.*, 23:11–15, 1982.

J. I. Katz, S. F. Anderson, S. A. Grandi, and B. Margon. Nodding motions of accretion rings and disks - A short-term period in SS 433. *ApJ*, 260:780–793, September 1982. doi: 10.1086/160297.

M. Kettenis, H. J. van Langevelde, C. Reynolds, and B. Cotton. ParselTongue: AIPS Talking Python. In C. Gabriel, C. Arviset, D. Ponz, and S. Enrique, editors, *Astronomical Data Analysis Software and Systems XV*, volume 351 of *Astronomical Society of the Pacific Conference Series*, page 497, July 2006.

I. Khabibullin and S. Sazonov. Is SS 433 a misaligned ultraluminous X-ray source? Constraints from its reflected signal in the Galactic plane. *MNRAS*, 457:3963–3974, April 2016. doi: 10.1093/mnras/stw266.

I. Khabibullin, P. Medvedev, and S. Sazonov. Thermal X-ray emission from a baryonic jet: a self-consistent multicolour spectral model. *MNRAS*, 455:1414–1427, January 2016. doi: 10.1093/mnras/stv2432.

T. Kibble and F. Berkshire. *Classical Mechanics*. Imperial College Press, 2004. ISBN 9781860944352. URL `http://books.google.co.uk/books?id=0a8dk0eDxgEC`.

A. R. King, R. E. Taam, and M. C. Begelman. The Evolutionary Status of SS 433. *ApJ*, 530: L25–L28, February 2000. doi: 10.1086/312475.

T. Kotani, N. Kawai, M. Matsuoka, and W. Brinkmann. Iron-Line Diagnostics of the Jets of SS 433. *PASJ*, 48:619–629, August 1996. doi: 10.1093/pasj/48.4.619.

T. Kotani, S. A. Trushkin, R. Valiullin, K. Kinugasa, S. Safi-Harb, N. Kawai, and M. Namiki. A Massive Jet Ejection Event from the Microquasar SS 433 Accompanying Rapid X-Ray Variability. *ApJ*, 637:486–493, January 2006. doi: 10.1086/498387.

H. A. Krimm, S. T. Holland, R. H. D. Corbet, A. B. Pearlman, P. Romano, J. A. Kennea, J. S. Bloom, S. D. Barthelmy, W. H. Baumgartner, J. R. Cummings, N. Gehrels, A. Y. Lien, C. B. Markwardt, D. M. Palmer, T. Sakamoto, M. Stamatikos, and T. N. Ukwatta. The Swift/BAT Hard X-Ray Transient Monitor. *ApJS*, 209:14, November 2013. doi: 10.1088/0067-0049/209/1/14.

K. Kubota, Y. Ueda, S. Fabrika, A. Medvedev, E. A. Barsukova, O. Sholukhova, and V. P. Goranskij. Subaru And Gemini Observations Of SS 433: New Constraint On The Mass Of The Compact Object. *ApJ*, 709:1374–1386, February 2010. doi: 10.1088/0004-637X/709/2/1374.

J. P. Leahy. Interpretation of large scale extragalactic jets. In P. A. Hughes, editor, *Beams and Jets in Astrophysics*, pages 100–185. Cambridge University Press, 1991.

F. J. Lockman, K. M. Blundell, and W. M. Goss. The distance to SS433/W50 and its interaction with the interstellar medium. *MNRAS*, 381:881–893, November 2007. doi: 10.1111/j.1365-2966.2007.12170.x.

M. Longair. *High Energy Astrophysics*. Cambridge University Press, 2011. ISBN 9780521756181. URL `http://books.google.co.uk/books?id=0qUrmQEACAAJ`.

L. A. Lopez, H. L. Marshall, C. R. Canizares, N. S. Schulz, and J. F. Kane. Determining the Nature of the SS 433 Binary from an X-Ray Spectrum during Eclipse. *ApJ*, 650:338–349, October 2006. doi: 10.1086/506174.

B. Margon and S. F. Anderson. Ten years of SS 433 kinematics. *ApJ*, 347:448–454, December 1989. doi: 10.1086/168132.

B. Margon, S. Anderson, and S. Grandi. V1343 Aquilae. *IAU Circ.*, 3649, December 1981.

S. Markoff, M. A. Nowak, and J. Wilms. Going with the Flow: Can the Base of Jets Subsume the Role of Compact Accretion Disk Coronae? *ApJ*, 635:1203–1216, December 2005. doi: 10.1086/497628.

F. E. Marshall, J. H. Swank, E. A. Boldt, S. S. Holt, and P. J. Serlemitsos. X-ray observations of H1908+050 /=SS 433/. *ApJ*, 230:L145–L148, June 1979. doi: 10.1086/182980.

H. L. Marshall, C. R. Canizares, and N. S. Schulz. The High-Resolution X-Ray Spectrum of SS 433 Using the Chandra HETGS. *ApJ*, 564:941–952, January 2002. doi: 10.1086/324398.

H. L. Marshall, C. R. Canizares, T. Hillwig, A. Mioduszewski, M. Rupen, N. S. Schulz, M. Nowak, and S. Heinz. Multiwavelength Observations of the SS 433 Jets. *ApJ*, 775:75, September 2013. doi: 10.1088/0004-637X/775/1/75.

J. J. Matese and D. P. Whitmire. The 6-day photometric and spectroscopic periods in SS433. *A&A*, 106:L9–L11, February 1982.

M. Matsuoka, K. Kawasaki, S. Ueno, H. Tomida, M. Kohama, M. Suzuki, Y. Adachi, M. Ishikawa, T. Mihara, M. Sugizaki, N. Isobe, Y. Nakagawa, H. Tsunemi, E. Miyata, N. Kawai, J. Kataoka, M. Morii, A. Yoshida, H. Negoro, M. Nakajima, Y. Ueda, H. Chujo, K. Yamaoka, O. Yamazaki, S. Nakahira, T. You, R. Ishiwata, S. Miyoshi, S. Eguchi, K. Hiroi, H. Katayama, and K. Ebisawa. The MAXI Mission on the ISS: Science and Instruments for Monitoring All-Sky X-Ray Images. *PASJ*, 61:999–1010, October 2009. doi: 10.1093/pasj/61.5.999.

E. T. Meyer, M. Georganopoulos, W. B. Sparks, E. Perlman, R. P. van der Marel, J. Anderson, S. T. Sohn, J. Biretta, C. Norman, and M. Chiaberge. A kiloparsec-scale internal shock collision in the jet of a nearby radio galaxy. *Nature*, 521:495–497, May 2015. doi: 10.1038/nature14481.

S. Migliari and R. P. Fender. Jets in neutron star X-ray binaries: a comparison with black holes. *MNRAS*, 366:79–91, February 2006. doi: 10.1111/j.1365-2966.2005.09777.x.

S. Migliari, R. Fender, and M. Méndez. Iron Emission Lines from Extended X-ray Jets in SS 433: Reheating of Atomic Nuclei. *Science*, 297:1673–1676, September 2002. doi: 10.1126/science.1073660.

J. C. A. Miller-Jones, K. M. Blundell, and P. Duffy. Jet Evolution, Flux Ratios, and Light-Travel Time Effects. *ApJ*, 603:L21–L24, March 2004. doi: 10.1086/382954.

A. J. Mioduszewski, M. P. Rupen, R. C. Walker, and G. B. Taylor. VLBA "Movie" Gives Scientists New Insights On Workings of Mysterious Microquasars. *National Radio Astronomy Observatory Press Release*, page 1, January 2004. URL `http://www.nrao.edu/pr/2004/ss433/`.

I. F. Mirabel and L. F. Rodríguez. A superluminal source in the Galaxy. *Nature*, 371:46–48, September 1994. doi: 10.1038/371046a0.

P. J. Mohr, D. B. Newell, and B. N. Taylor. Codata recommended values of the fundamental physical constants: 2014. *ArXiv e-prints*, July 2015.

T. Muñoz-Darias, R. P. Fender, S. E. Motta, and T. M. Belloni. Black hole-like hysteresis and accretion states in neutron star low-mass X-ray binaries. *MNRAS*, 443:3270–3283, October 2014. doi: 10.1093/mnras/stu1334.

T. Muñoz-Darias, J. Casares, D. Mata Sánchez, R. P. Fender, M. Armas Padilla, M. Linares, G. Ponti, P. A. Charles, K. P. Mooley, and J. Rodriguez. Regulation of black-hole accretion by a disk wind during a violent outburst of V404 Cygni. *Nature*, 534:75–78, June 2016. doi: 10.1038/nature17446.

R. Narayan and J. E. McClintock. Advection-dominated accretion and the black hole event horizon. *New A Rev.*, 51:733–751, May 2008. doi: 10.1016/j.newar.2008.03.002.

R. Narayan, R. Mahadevan, and E. Quataert. Advection-dominated accretion around black holes. In M. A. Abramowicz, G. Björnsson, and J. E. Pringle, editors, *Theory of Black Hole Accretion Disks*, pages 148–182, 1998.

H. B. Nersisyan, K. A. Sargsyan, D. A. Osipyan, M. V. Sargsyan, and H. H. Matevosyan. Self-similar analytical model of plasma expansion in a magnetic field. *Phys. Scr*, 84(6):065003, December 2011. doi: 10.1088/0031-8949/84/06/065003.

G. H. Newsom and G. W. Collins. SS 433. *IAU Circ.*, 3459, March 1980.

G. H. Newsom and G. W. Collins, II. Short-period variations in the moving line spectrum of SS 433. *AJ*, 86:1250–1258, August 1981. doi: 10.1086/113005.

G. H. Newsom and G. W. Collins, II. Period and cone-angle changes in SS 433. *AJ*, 91:118–124, January 1986. doi: 10.1086/113990.

I. D. Novikov and K. S. Thorne. Astrophysics of black holes. In C. Dewitt and B. S. Dewitt, editors, *Black Holes (Les Astres Occlus)*, pages 343–450, 1973.

NRAO. *AIPS Cookbook*. National Radio Astronomy Observatory, 1990. URL `http://www.aips.nrao.edu/cook.html`.

G. I. Ogilvie and G. Dubus. Precessing warped accretion discs in X-ray binaries. *MNRAS*, 320: 485–503, February 2001. doi: 10.1046/j.1365-8711.2001.04011.x.

J. C. B. Papaloizou and J. E. Pringle. The time-dependence of non-planar accretion discs. *MNRAS*, 202:1181–1194, March 1983. doi: 10.1093/mnras/202.4.1181.

J. C. B. Papaloizou and C. Terquem. On the dynamics of tilted discs around young stars. *MNRAS*, 274:987–1001, June 1995. doi: 10.1093/mnras/274.4.987.

Z. Paragi, R. C. Vermeulen, I. Fejes, R. T. Schilizzi, R. E. Spencer, and A. M. Stirling. The inner radio jet region and the complex environment of SS433. *A&A*, 348:910–916, August 1999.

Z. Paragi, I. Fejes, R. C. Vermeulen, R. T. Schilizzi, R. E. Spencer, and A. M. Stirling. The Equatorial Outflow of SS 433. In E. Ros, R. W. Porcas, A. P. Lobanov, and J. A. Zensus, editors, *Proceedings of the 6th EVN Symposium*, page 263, June 2002.

S. M. Perez and K. M. Blundell. Inflow and outflow from the accretion disc of the microquasar SS433: UKIRT spectroscopy. *MNRAS*, 397:849–856, August 2009. doi: 10.1111/j.1365-2966.2009.14979.x.

E. S. Perlman, M. Georganopoulos, E. M. May, and D. Kazanas. Chandra Observations of the Radio Galaxy 3C 445 and the Hot Spot X-Ray Emission Mechanism. *ApJ*, 708:1–8, January 2010. doi: 10.1088/0004-637X/708/1/1.

G. Ponti, R. P. Fender, M. C. Begelman, R. J. H. Dunn, J. Neilsen, and M. Coriat. Ubiquitous equatorial accretion disc winds in black hole soft states. *MNRAS*, 422:11–15, May 2012. doi: 10.1111/j.1745-3933.2012.01224.x.

J. Poutanen, G. Lipunova, S. Fabrika, A. G. Butkevich, and P. Abolmasov. Supercritically accreting stellar mass black holes as ultraluminous X-ray sources. *MNRAS*, 377:1187–1194, May 2007. doi: 10.1111/j.1365-2966.2007.11668.x.

W. H. Press, S. A. Teukolsky, W. T. Vetterling, and B. P. Flannery. *Numerical Recipes 3rd Edition: The Art of Scientific Computing*. Cambridge University Press, New York, NY, USA, 3 edition, 2007. ISBN 0521880688, 9780521880688.

M. J. Rees. Appearance of Relativistically Expanding Radio Sources. *Nature*, 211:468–470, July 1966. doi: 10.1038/211468a0.

R. A. Remillard and J. E. McClintock. X-Ray Properties of Black-Hole Binaries. *ARA&A*, 44: 49–92, September 2006. doi: 10.1146/annurev.astro.44.051905.092532.

D. H. Roberts, J. Lehar, and J. W. Dreher. Time Series Analysis with Clean - Part One - Derivation of a Spectrum. *AJ*, 93:968, April 1987. doi: 10.1086/114383.

W. J. Roberts. A slaved disk model for Hercules X-1. *ApJ*, 187:575–584, February 1974. doi: 10.1086/152667.

G. B. Rybicki and A. P. Lightman. *Radiative Processes in Astrophysics*. Wiley, 1979.

M. Ryle, J. L. Caswell, G. Hine, and J. Shakeshaft. A new class of radio star. *Nature*, 276:571–573, December 1978. doi: 10.1038/276571a0.

P. A. G. Scheuer and A. C. S. Readhead. Superluminally expanding radio sources and the radio-quiet QSOs. *Nature*, 277:182–185, January 1979. doi: 10.1038/277182a0.

P. A. G. Scheuer and P. J. S. Williams. Radio Spectra. *ARA&A*, 6:321, 1968. doi: 10.1146/annurev.aa.06.090168.001541.

K. Schillemat, A. Mioduszewski, V. Dhawan, and M. Rupen. Exploring the Jet Proper Motions of SS433. In *American Astronomical Society Meeting Abstracts*, volume 36 of *Bulletin of the American Astronomical Society*, page 104.01, December 2004.

F. R. Schwab. Relaxing the isoplanatism assumption in self-calibration; applications to low-frequency radio interferometry. *AJ*, 89:1076–1081, July 1984. doi: 10.1086/113605.

E. R. Seaquist, P. C. Gregory, and P. C. Crane. Nonthermal Radio Emission from H-alpha-Emission Object. *IAU Circ.*, 3256, August 1978.

E. Seifina and L. Titarchuk. On the Nature of the Compact Object in SS 433: Observational Evidence of X-ray Photon Index Saturation. *ApJ*, 722:586–604, October 2010. doi: 10.1088/0004-637X/722/1/586.

N. I. Shakura and R. A. Sunyaev. Black holes in binary systems. Observational appearance. *A&A*, 24:337–355, 1973.

D. S. Sivia and J. Skilling. *Data analysis : a Bayesian tutorial*. Oxford Science Publications. Oxford University Press, Oxford, New York, 2006. ISBN 0-19-856831-2.

R. E. Spencer. A radio jet in SS433. *Nature*, 282:483, November 1979. doi: 10.1038/282483a0.

R. E. Spencer. Flux density and structure variations in SS 433. *MNRAS*, 209:869–879, August 1984. doi: 10.1093/mnras/209.4.869.

A. Spitkovsky. On the Structure of Relativistic Collisionless Shocks in Electron-Ion Plasmas. *ApJ*, 673:L39, January 2008. doi: 10.1086/527374.

C. B. Stephenson and N. Sanduleak. New H-alpha emission stars in the Milky Way. *ApJS*, 33: 459–469, April 1977. doi: 10.1086/190437.

A. M. Stirling, F. H. Jowett, R. E. Spencer, Z. Paragi, R. N. Ogley, and T. V. Cawthorne. Radio-emitting component kinematics in SS433. *MNRAS*, 337:657–665, December 2002. doi: 10.1046/j.1365-8711.2002.05944.x.

A. M. Stirling, R. E. Spencer, T. V. Cawthorne, and Z. Paragi. Polarization and kinematic studies of SS 433 indicate a continuous and decelerating jet. *MNRAS*, 354:1239–1254, November 2004. doi: 10.1111/j.1365-2966.2004.08285.x.

R. S. Sutherland. Accurate free-free Gaunt factors for astrophysical plasmas. *MNRAS*, 300: 321–330, October 1998. doi: 10.1046/j.1365-8711.1998.01687.x.

G. B. Taylor, C. L. Carilli, and R. A. Perley, editors. *Synthesis Imaging in Radio Astronomy II*, volume 180 of *Astronomical Society of the Pacific Conference Series*, 1999.

C. E. J. M. L. J. Terquem. The Response of Accretion Disks to Bending Waves: Angular Momentum Transport and Resonances. *ApJ*, 509:819–835, December 1998. doi: 10.1086/306505.

J. A. Tomsick, E. Kalemci, P. Kaaret, S. Markoff, S. Corbel, S. Migliari, R. Fender, C. D. Bailyn, and M. M. Buxton. Broadband X-Ray Spectra of GX 339-4 and the Geometry of Accreting Black Holes in the Hard State. *ApJ*, 680:593-601, June 2008. doi: 10.1086/587797.

S. A. Trushkin, N. N. Bursov, and N. A. Nizhelskij. The multifrequency monitoring of microquasars. SS433. *Bulletin of the Special Astrophysics Observatory*, 56:57–90, 2003.

R. C. Vermeulen, V. Icke, R. T. Schilizzi, I. Fejes, and R. E. Spencer. Evolving radio structure of the binary star SS433 at a resolution of 15 MARC S. *Nature*, 328:309–313, July 1987. doi: 10.1038/328309a0.

R. C. Vermeulen, W. B. McAdam, S. A. Trushkin, S. R. Facondi, R. L. Fiedler, R. M. Hjellming, K. J. Johnston, and J. Corbin. Daily spectra of radio flares from SS 433 in May/June 1987. *A&A*, 270:189–199, March 1993a.

R. C. Vermeulen, P. G. Murdin, E. P. J. van den Heuvel, S. N. Fabrika, B. Wagner, B. Margon, J. B. Hutchings, R. T. Schilizzi, M. H. van Kerkwijk, L. B. van den Hoek, E. Ott, L. P. Angebault, G. K. Miley, S. D'Odorico, and N. Borisov. Monitoring of very rapid changes in the optical spectrum of SS 433 in May/June 1987. *A&A*, 270:204–222, March 1993b.

R. C. Vermeulen, R. T. Schilizzi, R. E. Spencer, J. D. Romney, and I. Fejes. A series of VLBI images of SS433 during the outbursts in May/June 1987. *A&A*, 270:177–188, March 1993c.

R. Vermeulen. *Multi-Wavelength Studies of SS 433*. PhD thesis, Leiden University, 1989.

J. F. C. Wardle and S. E. Aaron. How fast are the large-scale jets in quasars? Constraints on both Doppler beaming and intrinsic asymmetries. *MNRAS*, 286:425–435, April 1997. doi: 10.1093/mnras/286.2.425.

M. G. Watson, G. C. Stewart, A. R. King, and W. Brinkmann. Doppler-shifted X-ray line emission from SS433. *MNRAS*, 222:261–271, September 1986. doi: 10.1093/mnras/222.2.261.

D. P. Whitmire and J. J. Matese. The slaved disc model for SS 433. *MNRAS*, 193:707–712, December 1980. doi: 10.1093/mnras/193.4.707.

D. Winske and N. Omidi. Plasma expansion in the presence of a dipole magnetic field. *Physics of Plasmas*, 12(7):072514, July 2005. doi: 10.1063/1.1947487.